UNIVERSITY OF LODZ

Developing low-energy data analysis methods for Large-Sized Telescopes and observations of Flat-Spectrum Radio Quasars with Cherenkov telescopes

Doctoral thesis

Author:

Pawel Gliwny

University of Lodz
Doctoral School of Exact and Natural Sciences

Supervisor:

Prof. Dr. Hab. Julian Sitarek

University of Lodz, Department of Astrophysics

21/03/2024

Developing low-energy data analysis methods for Large-Sized Telescopes and observations of Flat-Spectrum Radio Quasars with Cherenkov telescopes

Author:
Pawel Gliwny (University of Lodz
Doctoral School of Exact and Natural Sciences)

Supervisor:
Prof. Dr. Hab. Julian Sitarek (University of Lodz, Department of Astrophysics)

Abstract

My doctoral thesis is focused on the exciting field of gamma-ray astrophysics, which deals with the study of the highest-energy part of the electromagnetic spectrum. Ground-based observations via Cherenkov telescopes are the primary tool used for investigation in this area. My research endeavors to contribute to this field in two ways. Firstly, I have made a number of contributions to the standard analysis chain of LST-1 data. The new analysis methods that I developed involve low-level calibration techniques such as raw signal correction to reduce noise and time calibration to improve time resolution. I have also developed special cleaning methods that account for noise from calibration runs to improve the accuracy of my analysis further. Secondly, I have undertaken a detailed study of FSRQs (Flat Spectrum Radio Quasars) using MAGIC telescopes.

The thesis is divided into the following chapters:

Chapter 1 presents a short introduction to gamma-ray astronomy and observation techniques. It also describes physics processes such as particle and photon interaction with matter and describes the formation of Extensive Air Showers in the Earth atmosphere.

Chapter 2 In this chapter, I present an introduction to active galaxies, focusing on blazars, especially on FSRQ. I will cover the current standard model of such objects and highlight the open questions. For instance, I will explore the uncertainty of the emission region's location and how I can derive physical parameters from observations to describe the source.

Chapter 3 Presents the Cherenkov technique and current Cherenkov telescopes, focusing on the MAGIC and LST-1 experiments I am involved in. I also describe the analysis methods and the corresponding software packages used for the analysis of the data from different Cherenkov telescopes, from analyzing raw signals to deriving physical results. Additionally, I provide a detailed description of the low-level calibration process I have been working on for LST-1.

Chapter 4 In this chapter I describe my analysis of LST-1 data obtained from the direction of the BL Lac source for the BL Lac source, detailing each step of the data processing in the LST-1 pipeline. I use this source as an example to check the performance of the LST-1 telescope analysis with how the performance is dependent on the used Monte Carlo simulations.

Chapter 5 The chapter describes VHE gamma-ray observations, data analysis, and findings from studies of nine FSRQs observed by the MAGIC telescopes and *Fermi*-LAT from 2008 to 2020. It includes details about the study that led to establishing upper limits on their gamma-ray emission and constructing a theoretical broadband emission model that incorporates the MAGIC upper limits and *Fermi*-LAT data. It also discusses my enhancements to the `agnpy` software to allow me to perform a more reliable emission modeling, including a more realistic BLR model.

Chapter 6 This chapter summarizes my thesis and includes a discussion of the future of gamma-ray astronomy and my future plans.

Abstrakt

Moja praca doktorska skupia się na dziedzinie astrofizyki gamma bardzo wysokich energii, która zajmuje się badaniem najbardziej energetycznej części widma elektromagnetycznego. Podstawowym narzędziem używanym w tych badaniach są teleskopy czerenkowskie, która pozwalają na naziemne obserwacje.

Mój wkład do dziedziny astronomii gamma, który opisuje w tej pracy jest dwojaki:

Po pierwsze, rozwijałem standardową bibliotekę analizy danych LST-1. Opracowałem nowe metody analizy, które obejmują techniki kalibracji niskiego poziomu, takie jak korekcja surowego sygnału z systemu odczytu danych, aby zmniejszyć szumy sygnału, oraz kalibrację czasową, aby poprawić rozdzielczość czasową. Opracowałem również specjalne metody czyszczenia obrazów, które uwzględniają tło nocnego nieba, wyznaczone na podstawie procesu kalibracji, aby obniżyć próg energetyczny na poziomie analizy LST-1. Po drugie, przeprowadziłem szczegółowe badanie emisji z 9 kwazarów o płaskim widmie radiowym (ang. FSRQ – Flat Spectrum Radio Quasars) za pomocą teleskopów MAGIC.

Praca jest podzielona na następujące rozdziały:

Rozdział 1 przedstawiam w nim krótkie wprowadzenie do astronomii gamma oraz technik obserwacyjnych. Opisuję także procesy fizyczne, takie jak interakcja cząstek naładowanych i fotonów z materią, oraz formowanie się wielkich pęków atmosferycznych.

Rozdział 2 zawiera wprowadzenie do aktywnych jąder galaktyk, skupiając się na blazarach, a w szczególności na ich podtypie FSRQ. Omawiam aktualny stan wiedzy na temat tych obiektów, zwracając uwagę na wciąż otwarte pytania, takie jak lokalizacja regionu emisji, oraz metody wyznaczania parametrów fizycznych na podstawie obserwacji.

Rozdział 3 Prezentuję technikę detekcji promieniowania gamma oraz obecne teleskopy Czerenkowa, koncentrując się na eksperymentach MAGIC i LST-1, w których uczestniczę. Opisuję również metody analizy i odpowiadające im biblioteki używane do analizy danych w astronomii gamma. Przedstawiam typową analizę danych, począwszy od surowego elektronicznego sygnału , aż do fizycznych wyników w postaci widmowego rozkładu energii. Dodatkowo szczegółowo opisuję proces kalibracji niskiego poziomu, nad którym pracowałem dla LST-1.

Rozdział 4 W tym rozdziale opisuję moją analizę danych z LST-1, wykonaną dla źródła BL Lac, szczegółowo opisując wysokopoziomowe etapy przetwarzania danych w LST-1. Używam tego źródła jako przykładu, aby zbadać wydajność analizy teleskopu LST-1 oraz to, jak wydajność ta zależy od użytych symulacji Monte Carlo.

Rozdział 5 Rozdział ten opisuje obserwacje, analizę danych oraz wyniki dziewięciu FSRQ obserwowanych przez teleskopy MAGIC i *Fermi*-LAT od 2008 do 2020 roku. Zawiera szczegóły na temat badań, które doprowadziły do wyznaczenia górnych ograniczeń na emisję gamma . Następnie prezentuję prezentuje konstrukcję modelu emisji szerokopasmowej, który porównuję z górnymi limitami uzyskanymi z teleskopu MAGIC i danymi *Fermi*-LAT. W tym rozdziale omówione są również moje ulepszenia biblioteki `agnpy`, aby umożliwić mi przeprowadzenie bardziej wiarygodnego modelowania emisji, w tym użycie bardziej realistycznego modelu BLR (Broad Line Region – region szerokich linii).

Rozdział 6 Ten rozdział podsumowuje moją pracę doktorską i zawiera krótką dyskusję na temat przyszłości astronomii gamma oraz moich przyszłych planów.

Acknowledgements

Chciałem podziękować swojemu Promotorowi, bez jego pomocy ta praca by nie miała szans powstać.

Contents

List of Abbreviations

AGN Active Galactic Nuclei

BL Lac BL Lacertae

BLR Broad Line Region

CMB Cosmic Microwave Background

CORSIKA Cosmic Ray Simulations for KASCADE

CTA Cherenkov Telescope Array

CTAO Cherenkov Telescope Array Observatory

DAQ Data Acquisition

DL1 Data Level 1

DL2 Data Level 2

DL3 Data Level 3

DRS4 Domino Ring Sampler version 4

DT Dusty Torus

EAS Extensive Air Showers

EBL Extragalactic Background Light

EC External Compton

EHE Extreme-High-Energy

FSRQ Flat Spectrum Radio Quasars

GADF Gamma-Astro-Data-Formats

H.E.S.S. High Energy Stereoscopic System

HE High-Energy

HG High Gain

HSP High-Synchrotron-Peaked

IACT Imaging Atmospheric Cherenkov Telescope

IBL Intermediate-frequency-peaked BL Lac

ICRS International Celestial Reference System

IRF Instrument Response Functions

ISP Intermediate-Synchrotron-Peaked

LAT Large Area Telescope

LBL Low-frequency-peaked BL Lac

LC Light Curve

LE Low-Energy

LG Low Gain

LSP Low-Synchrotron-Peaked

LST Large-Sized Telescope

LST-1 Large Size Telescope-1

MAGIC Major Atmospheric Gamma Imaging Cherenkov

MARS MAGIC Analysis and Reconstruction Software

MC Monte Carlo

MWL Multi-Wavelength

NSB Night Sky Background

ORM Observatorio del Roque de los Muchachos

PMT Photomultiplier Tube

RF Random Forest

SED Spectral Energy Distribution

SSC Synchrotron Self-Compton

SUMT SUM Trigger

ToO Target of Opportunity

U.L. Upper Limit

UHE Ultra-High-Energy

UV Ultraviolet

VHE Very High Energy

VLBI Very Long Baseline Interferometry

ZD Zenith Distance

Chapter 1

High-energy astrophysics

1.1 Cosmic and gamma rays

The Earth is perpetually exposed to a bombardment of cosmic and gamma rays, spanning a vast spectrum of energies. Victor Hess discovered cosmic rays in 1912, and since then, cosmic rays have been explored using balloons, spaces, and ground-based and underground methods. This exploration has given rise to distinct branches, such as cosmic-ray astrophysics (centering on charged particles), Gamma-ray astrophysics and neutrino astrophysics [1].

Gaining knowledge about the production and transport of cosmic rays through the interstellar medium is a crucial issue that greatly affects our understanding of the structure and characteristics of the universe. Recent advancements in gamma-ray astronomy [2] and neutrino astronomy [3, 4, 5] have provided means to investigate various aspects of cosmic rays. The search for gamma rays or neutrinos primarily aims to identify cosmic ray sources and investigate the phenomena involved in their acceleration. This is because neutral particles like gamma rays and neutrinos are not affected by Galactic or extragalactic magnetic fields, which allows their directions to point to their production sites. Analyzing these particles' directions, flux, energy spectra, and variability can refine theoretical models about their sources and interactions during their journey to Earth. Because weak interactions have extremely small cross-sections, neutrinos can easily escape from compact sources, allowing researchers to obtain information about the interior or surrounding regions of supernovae, active galaxies, and other cosmic systems [6]. Although it is challenging to distinguish neutrino-induced muons from those produced by primary cosmic rays in the atmosphere, the issue is the extremely low cross-section, limiting the number of cases we observe. While the IceCube neutrino observatory has demonstrated that the neutrino energy spectrum must include components from cosmic sources [7], and there have been several 3-4 σ indications of possible sources and connections between flares and neutrinos [3, 8], to date, there has not been a definitive discovery of a neutrino source. Contrary to neutrinos, high energy photons have a limited cosmic horizon up to which can be observed as it is shown on Fig. 1.1 due to $\gamma\gamma$ absorption via e^+e^- pair production.

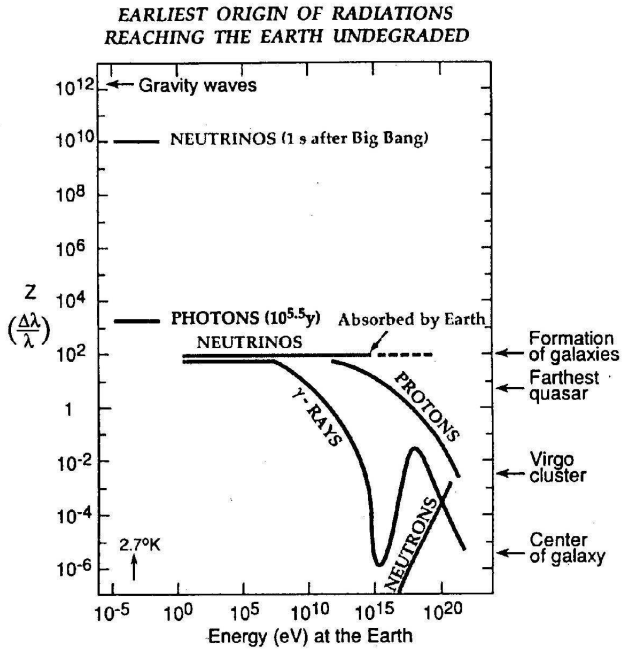

Figure 1.1: The redshift horizon, which varies with the energy of cosmic radiation as measured on Earth, provides insight into the maximum distance from which different types of cosmic radiation can reach us. Source: [6]

1.2 Gamma-ray astronomy

Gamma-ray astrophysics studies astronomical objects and phenomena that emit gamma rays, the most energetic form of electromagnetic radiation. This field of astronomy allows us to observe the most extreme environments in the universe, such as supernovae, vicinity regions of black holes, neutron stars, gamma-ray bursts, and active galactic nuclei [9]. Gamma-ray observations are made using satellites and ground-based detectors.

There are several distinct energy bands in gamma-ray astronomy. Each is typically studied with specific types of instruments [10]. The low-energy (LE) band, ranging from 100 keV to 30 MeV, is primarily studied by Compton telescopes (see Section 1.6.1), typically deployed on balloons or satellites. The high-energy (HE) band, spanning 30 MeV to 100 GeV, is typically observed using pair-creation instruments aboard satellites. Due to decreased flux with energy, observations at higher energies are generally conducted from the ground with large instruments. Within the very-high-energy (VHE) range of 100 GeV to 30 TeV, the detectors commonly used are atmospheric Cherenkov detectors. Water Cherenkov detectors are often employed for ultra-high-energy (UHE) observations between 30 TeV and 30 PeV. Finally, ground-based telescopes typically use the atmospheric fluorescence technique for the highest energy observations in the extreme-high-energy (EHE) range above 30 PeV. Notably, the sensitive range of different types of instruments often partially overlaps, allowing cross-calibration and studies of the same objects with ground-based and space-borne instruments.

Very high-energy (VHE) gamma-ray astronomy focuses on observing and analyzing the sources of these gamma rays. The observation of TeV gamma rays from numerous sources has provided compelling evidence for the presence of efficient acceleration mechanisms of charged cosmic particles [6]. Detecting VHE and UHE gamma rays for these sources gives us insights into how particles are accelerated to these extreme energies. Non-thermal spectra (meaning their emission does not align and is typically much broader than that of a blackbody at a given temperature) are commonly observed in these gamma-ray sources. Understanding such acceleration mechanisms is the primary driver of high-energy gamma-ray astronomy. Detecting TeV sources can improve our models of acceleration and radiation processes in extreme conditions [6].

1.3 From fundamental physics to astroparticle physics and back

From the 1950s to the 1990s, the majority of advancements in fundamental physics were driven by particle accelerators [11]. Despite this, major experiments investigating cosmic rays operated and contributed to their understanding. In astroparticle physics, cosmic rays have become increasingly significant over the past few decades. Numerous extensive projects are currently underway, each with various objectives, such as exploring the universe for dark matter and studying properties of the sources in the Galactic and Extragalactic Sky. Space-based gamma-ray telescopes, such as the *Fermi* Large Area Telescope (*Fermi*-LAT) [12] and AGILE (Astrorivelatore Gamma a Immagini LEggero) [13] have delivered groundbreaking findings. Eight decades after Rossi [14] and Auger's [15] discovery of air showers, the investigation of ultra-high-energy cosmic-ray showers is yielding essential information about the spectrum and origins of cosmic rays. The main focus of this research is to investigate the region surrounding the GZK cutoff [16], which is a theoretical boundary on the energy of cosmic rays originating from faraway sources. This limit predicts a distinct termination point in the spectrum of ultra-high-energy cosmic rays due to their interaction with the Cosmic Microwave Background radiation. The largest currently operating detector, the Pierre Auger Observatory [17], spans an area of approximately 3,000 square kilometers and is located in Argentina.

TeV instruments have uncovered potential associations between photon and cosmic ray accelerators within the Galaxy [18]. On the other hand, one of the most exciting capabilities of these instruments is their ability to examine the propagation of highly energetic photons over vast cosmological distances. By doing so, they can search for possible effects of Lorentz invariance violations at extreme energies and photon interactions with the quantum vacuum [19]. The development of a new detector, Cherenkov Telescope Array (CTA), is currently underway, and it is expected to surpass the capabilities of current detectors by at least an order of magnitude [20] [21].

1.4 Acceleration of charged particle

Cosmic rays, originating from various astrophysical sources, can be accelerated in areas with turbulent magnetic fields. Static magnetic fields are ineffective for particle acceleration. In contrast, fluctuating magnetic fields can create changing electric fields, which, through multiple cycles, can effectively accelerate particles [11].

I will first describe the Fermi mechanism in a unified and simplified manner, applicable to both first- and second-order versions. To achieve this, I introduce the average energy post-collision as $E = \beta E_0$, where E_0 is the pre-collision energy. After n collisions, the particle count is $N = N_0 P^n$ with energy levels $E = E_0 \beta^n$. Consequently, the energy distribution is expressed as [22]:

$$N(E)dE = \text{const.} \times E^{-1+\frac{\ln P}{\ln \beta}} dE \tag{1.1}$$

This formulation, demonstrating the anticipated power-law behavior, allows the parameters P, which denotes the likelihood of a particle staying within the acceleration zone post-collision, and β to be aligned with those identified in the Fermi second-order mechanism and adapted for the first-order mechanism.

1.4.1 Second-order Fermi acceleration

The initial formulation of the Fermi acceleration concept, subsequently known as second-order acceleration, was introduced by Enrico Fermi in 1949 [23]. This model accounts for the acceleration of relativistic particles through their interactions with interstellar clouds. These clouds, behaving akin to magnetic mirrors, randomly move and cause the particles to be reflected, as depicted in Fig. 1.2. Following [23, 24], it can be demonstrated that the mean energy increment per collision is given by

$$\left\langle \frac{\Delta E}{E} \right\rangle = \frac{8}{3} \left(\frac{v}{c} \right)^2 \tag{1.2}$$

where v and c represent the velocity of the cloud and the particle, respectively. The mean energy increment is directly proportional to $\left(\frac{v}{c}\right)^2$, indicating the process is termed as *second-order* acceleration

due to the power of the exponent. Calculating the mean interval between collisions allows for the derivation of an energy gain rate from the preceding equation:

$$\frac{dE}{dt} = \frac{4}{3}\left(\frac{v^2}{cL}\right)E = \alpha E \tag{1.3}$$

Here, L denotes the average free path between clouds along the magnetic field lines. By resolving a steady-state diffusion-loss equation and incorporating this energy gain rate, along with assuming τ_{esc} as the typical duration for a particle to stay within the acceleration zone, the energy spectrum $N(E)$ can be obtained:

$$N(E)dE = \text{const} \times E^{1+\frac{1}{\alpha\tau_{\text{esc}}}}dE \tag{1.4}$$

It's worth noting that while the second-order acceleration mechanism can generate a power-law spectrum, this approach has some limitations. One of the biggest challenges is the slow rate of energy gain due to the low density of observed clouds in a typical astrophysical scenario.

1.4.2 First-order Fermi acceleration

The scenario of the first-order acceleration mechanism is to achieve an energy increase proportional to (v/c), enhancing efficiency, particularly for higher v values. Such conditions arise during collisions with intense shock waves, for instance, those emanating from supernova blasts or active galactic nuclei, which can attain supersonic speeds (a thousandfold the velocity of an interstellar cloud).

Due to turbulence behind the shock and irregularities ahead of it, the particle velocity distribution appears isotropic in reference frames where the interstellar gas remains stationary on both shock sides. This symmetry ensures that, in the first-order (Fermi I) acceleration mechanism, particles experience "head-on" collisions on both sides of the shock, leading to a consistent energy gain, although not necessarily the same for every encounter, as depicted in Fig.1.2. In contrast, the second-order (Fermi II) acceleration involves a mix of *head-on* and *catch-up* collisions, resulting in variable outcomes where particles can either gain or lose energy depending on the nature of each collision.

During such crossings, particles are energized. It has been demonstrated [24] that the mean energy gain increment per round trip is

$$\left\langle \frac{\Delta E}{E} \right\rangle = \frac{4}{3}\left(\frac{v}{c}\right) \tag{1.5}$$

Another crucial factor is the escape probability P_{esc} (akin to $1-P$) from the shock. Kinetic theory yields

$$P_{\text{esc}} = \frac{4}{3}\left(\frac{v}{c}\right) \tag{1.6}$$

Incorporating these parameters into Equation 1.5, we obtain

$$N(E)dE = \text{const.} \times E^{-2}dE \tag{1.7}$$

Although the observed cosmic ray spectral index of approximately 2.7-2.8 [25] has not yet been fully matched by the first-order mechanism predictions, this approach remains highly promising as the most effective and likely scenario for cosmic ray acceleration. This discrepancy can typically be explained by the fact that sources emit cosmic rays into the galaxy with a harder spectrum (e.g., around -2). However, propagation and escape effects modify this spectrum; lower energy particles are more significantly influenced and trapped by magnetic fields, leading to a steeper observed spectrum, while higher energy particles, being less affected, can escape the galaxy more easily. This process results in the observed steepening of the spectrum. Unlike the second-order mechanism, this model presumes a spectral exponent of -2, under specific conditions: the shock must be strong but non-relativistic. The presented description of the Fermi process is based on [22].

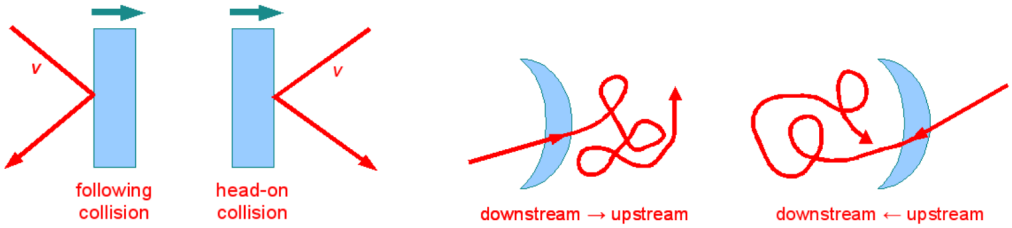

Figure 1.2: On the left is demonstrated the Second-order Fermi acceleration process; on the right is the First-order Fermi acceleration process. Source: [22].

1.4.3 Magnetic reconection

In plasma environments, magnetic reconnection is a crucial physical process. This process entails a transformation in the topology of magnetic field lines and their reconfiguration. As a result, the stored energy of the magnetic field is released and converted into the kinetic and thermal energy of the plasma particles [26]. The energy E stored in a magnetic field B is given by:

$$E = \frac{1}{2\mu_0} \int B^2 dV$$

,

where μ_0 denotes the permeability of free space, and the integral is taken over the volume V of the plasma where the magnetic field is present.

The importance of magnetic reconnection is amplified in the domain of high-energy astrophysics and gamma-ray astronomy. This mechanism was proposed to explain multiple many high-energy phenomena, including the powerful flares observed in blazars and gamma-ray bursts. When the magnetic field lines break apart and reconnect, magnetic energy is efficiently transformed into particle energy, creating non-thermal particles. Magnetic reconnection is considered crucial in forming relativistic jets observed in active galactic nuclei (AGNs) [27]. These jets, significant sources of gamma-ray emission, might be powered by the conversion of magnetic energy harnessed from the supermassive black holes situated at the centers of these galaxies.

1.5 Charged particles interaction with matter

In this section, I briefly describe the interactions of charged particles, in particular electrons, with matter and radiation fields, as this is the basis of physical processes that occur both in the Earth's atmosphere, forming particle cascades, and in cosmic sources.

Charged particles primarily interact with atoms through a variety of electromagnetic processes. These interactions can result in the expulsion of electrons (ionization), the elevation of electrons in atoms to higher energy states (excitation), or the emission of photons (bremsstrahlung, Cherenkov radiation, and transition radiation). In some cases, high-energy particles may also directly interact with atomic nuclei.

The radiation processes described here and cited formulas are based on [11].

1.5.1 Ionization Energy Loss

This is one of the most common processes in which a charged particle losses energy. As the particle travels through a homogeneous material with density ρ with speed v, the average specific energy loss (calculated per unit length) due to ionization and excitation is defined by the Bethe approximation. This formula maintains an accuracy of a few percent within the range of $0.1 < \beta\gamma < 1000$ (where $\beta = v/c$, c is the speed of light, and γ is Lorentz factor) for materials with intermediate atomic numbers (Z) and mass number (A):

$$-\frac{dE}{dx} \approx \rho D \left(\frac{Z}{A}\right) \frac{(z_p)^2}{\beta^2} \left[\frac{1}{2} \ln\left(\frac{2m_e c^2 \beta^2}{I}\right) - \beta^2 - \frac{\delta(\beta,\rho))}{2}\right] \tag{1.8}$$

where the material density is denoted by ρ. The particle's charge, represented by z_p, is measured in units of electron charge. A constant value of 0.307 MeV cm^2/g is denoted by D. The energy corresponding to the electron mass, around 0.511 MeV, is represented by $m_e c^2$. The mean excitation energy in the material can be approximated as $I \approx 16\mathrm{eV} \times Z^{0.9}$ for $Z > 1$. Lastly, a correction term (δ) becomes significant at high energies, accounting for the reduction in energy loss due to the density effect. As the incident particle's velocity increases, the medium becomes polarized, and its atoms can no longer be considered isolated.

In a first approximation, the energy loss due to ionization has the following characteristics:

- It is independent of the particle's mass;
- For high-energy particles it is typically small (about 2 MeV/cm in water) and can be roughly assumed to be proportional to the material's density;
- It is proportional to $1/\beta^2$ for $\beta\gamma \lesssim 3$, representing the minimum of ionization (referred to as a minimum ionizing particle);
- Essentially constant for $\beta > 0.96$, with a logarithmic increase after the minimum;
- Proportional to Z/A, where Z/A is approximately equal to 0.5 for most elements except hydrogen and the heaviest nuclei.

In practice, the mean energy loss rate of most of relativistic particles, such as cosmic-ray muons, are close to the minimum. These particles can be considered as minimum ionizing particles within a factor of less than two. The energy loss from a minimum ionizing particle can be effectively approximated by:

$$\frac{1}{\rho}\frac{dE}{dx} \approx -3.5 \left(\frac{Z}{A}\right) \mathrm{MeVcm}^2/\mathrm{g} \tag{1.9}$$

1.5.2 Cherenkov Radiation

Cherenkov radiation occurs when a charged particle travels through a medium faster than light's speed in that medium. Although the total energy loss from this process is minimal, Cherenkov radiation is notable for its application in detectors. The threshold velocity for this phenomenon is given as $\beta = 1/n$, where n is the refractive index of the medium. The light is emitted in a coherent cone at an angle as follows:

$$\theta_c = \arccos \frac{1}{n\beta} \tag{1.10}$$

from the direction of the emitting particle.

The number of photons generated per unit path length and per unit energy interval for the photons by a particle with charge z_pe at the maximum (limiting) angle can be expressed as:

$$\frac{d^2N}{dxdE} \approx \frac{\alpha z_p^2}{\hbar c} \sin^2\theta_c \approx 370 \sin^2\theta_c \mathrm{eV}^{-1}\mathrm{cm}^{-1} \tag{1.11}$$

The refractive index n typically depends on the photon energy E. Cherenkov radiation becomes relevant when $n > 1$ and the medium is transparent, which typically occurs in proximity to the visible light spectrum. The total energy radiated is small, roughly 10^{-4} times the energy lost by ionization. In the visible range (300-700 nm), the total number of emitted photons is about 40/m in air and approximately 500/cm in water. Due to the dependence on λ, it is important that Cherenkov detectors are sensitive close to the ultraviolet region.

1.5.3 Bremsstrahlung

According to classical electromagnetism, when a charged particle undergoes acceleration, it emits electromagnetic waves. The intensity of this radiation from a dipole is directly proportional to the square of the acceleration. This phenomenon also occurs in quantum physics and manifests as the emission of photons when particles are deflected by an electric field and is referred to as bremsstrahlung or breaking radiation. All the formulas in this section refer to bremsstrahlung in the electric field of atoms of the medium. In simple terms, the energy emitted, much like in the classical scenario, is inversely proportional to the particle's mass squared. Compared to the ionization energy loss mentioned in Equation 1.8, radiation effects become significant when $\beta\gamma$ is around or above 1000. This indicates an extremely high energy level for protons (approximately 1 TeV) and around 100 GeV for muons (as shown in Fig. 1.3). Bremsstrahlung is particularly noteworthy in the case of electrons and positrons. The Bethe approximation becomes less accurate for these particles at relatively lower energies. For a high-energy electron, the average fractional energy loss due to radiation is approximately constant, irrespective of the electron's energy, and can be expressed as follows:

$$\frac{1}{E}\frac{dE}{dx} \sim -\frac{1}{X_0} \tag{1.12}$$

X_0 is referred to as the radiation length, a property unique to each material. For air, the approximate value of X_0 is around 36.7 gcm^{-2} assuming standard temperature and pressure conditions [28].

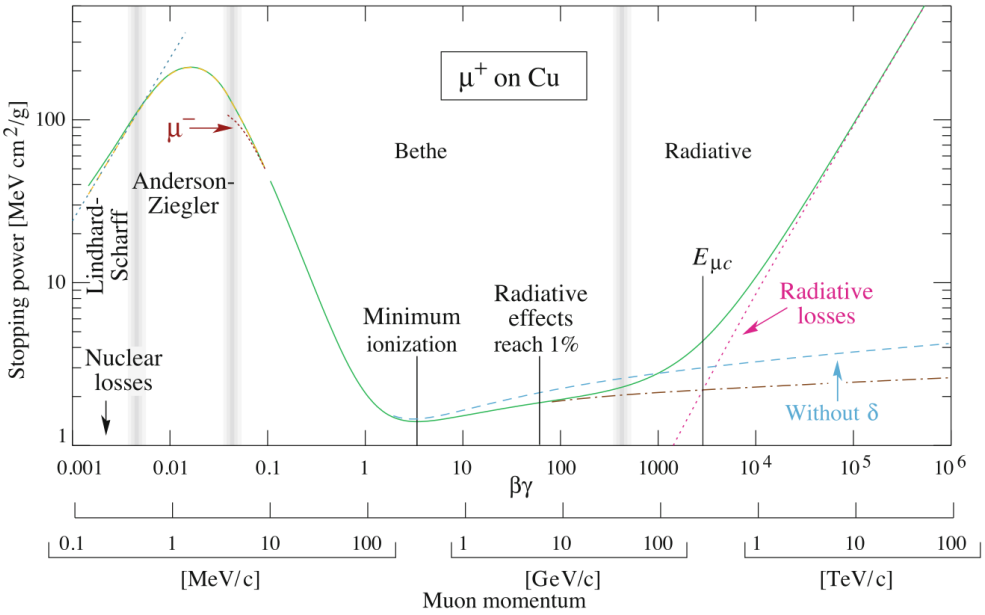

Figure 1.3: Energy loss per gramature, represented as $-\frac{dE}{dx}$, for positive muons moving through copper, is depicted as a function of $\beta\gamma = \frac{p}{Mc}$. Source: [29]

The bremsstrahlung spectrum is characterized by a significant amount of *soft bremsstrahlung* at lower energies, but it extends to energies comparable to the primary particle's energy. At lower energies, the spectrum is dominated by *soft bremsstrahlung*. This part of the spectrum arises when the deceleration of the electron is relatively mild, resulting in the emission of lower-energy photons. These photons are typically in the X-ray range and result from the electron losing only a small fraction of its kinetic energy. As we move to higher energies, the spectrum of bremsstrahlung radiation stretches to include much higher energy levels, potentially reaching energies comparable to those of the initial high-energy particle. In this high-energy regime, the bremsstrahlung process can produce VHE photons. This occurs when the electron decelerates significantly, losing much of its kinetic energy in a single

interaction. The energy of these photons can be quite substantial, sometimes approaching the initial energy of the electron.

Bremsstrahlung radiation is crucial in extensive atmospheric showers (EAS), which occur when high-energy cosmic rays interact with Earth's atmosphere; EAS will be described in more detail in 1.8.2.

1.6 Photon interactions

This section explains Compton Scattering and Pair Production, which are essential interactions between photons and matter. These processes are integral to understanding various physical phenomena.

1.6.1 Compton Scattering

Compton scattering involves a collision between a photon and an electron. Assuming the initial electron is free and stationary, let E represent the energy of the primary photon (which corresponds to a wavelength λ). After the collision, the photon is scattered at an angle θ, emerging with diminished energy E' and a corresponding wavelength λ'. The electron then gains energy equal to the difference $E - E'$. The conservation of energy and momentum laws lead to the relation known as the Compton formula:

$$\lambda' - \lambda = \lambda_c(1 - \cos\theta) \rightarrow E' = \frac{E}{1 + (E/m_e c^2)(1 - \cos\theta)}. \tag{1.13}$$

where θ is the scattering angle of the emitted photon; $\lambda_c = h/m_e c = 2.4$ pm is the Compton wavelength of the electron, where m_e is the electron rest mass.

When the target electron is not stationary, the scattered photon's energy can exceed that of the incoming one. This scenario is referred to as inverse Compton, which is highly significant in the emission of high-energy photons by astrophysical sources. Essentially, inverse Compton enables the "acceleration" of photons.

The concept of cross-section is fundamental to particle physics, as it helps to quantify the likelihood of a particle interaction such as scattering or absorption. The total cross-section, denoted by the symbol σ, is given by the following relation:

$$\sigma = \frac{1}{n \cdot \lambda}.$$

In this formula:

- λ represents the mean free path between collisions (the average distance a particle travels before colliding with another particle), measured in meters.
- n denotes the number density of target particles, expressed in units of particles per cubic meter (m^{-3}).

This expression describes how the effective cross-section for a two-particle collision, with units in square meters (m^2), inversely depends on the product of the particle's mean free path and the number density of the target particles. The resulting value of σ provides a measure of the probability of a particle interaction occurring. Another important concept in cross-section calculations is the differential cross-section, which can be denoted, e.g., as $\frac{d\sigma}{d\Omega}$. This function takes into account variables such as scattering angle or energy and provides a description of the probability of scattering in a specific direction. It is a critical tool in understanding the microscopic details of particle interactions and is often used in theoretical models that are then compared against experimental data to validate or refine these models.

Klein and Nishina computed the differential cross-section for Compton scattering [30]. In the Thomson limit, where the photon energy (measured in the electron rest frame) is much less than the electron's rest mass energy $m_e c^2$, the electrons are scattered non-relativistically, and the Thomson cross-section accurately represents the total cross-section:

$$\sigma_T = \frac{8\pi}{3}\left(\frac{e^2}{4\pi\varepsilon_0}\right)^2 \frac{1}{m_e^2 c^4} = \frac{8\pi r_e^2}{3} \tag{1.14}$$

where $r_e = (e^2/4\pi\varepsilon_0)/(m_e c^2) \approx 0.003$pm represents the classical electron radius, e is the electron charge, ε_0 is the vacuum permittivity, and c is the speed of light. When the photon energy is significantly greater than $m_e c^2$, it falls into the Klein-Nishina regime, where the total cross-section declines quickly as the energy increases.

$$\sigma_{KN} \approx \frac{3\sigma_T}{8}\frac{ln2E}{E} \tag{1.15}$$

1.6.2 Pair Production

Pair production is the predominant interaction process of photons with matter if their energies exceed a few tenths of MeV. In the vicinity of a nucleus, a high-energy photon can be converted into an electron and position. For a single photon, this process is kinematically prohibited unless an external field, no matter how small, is present. Energy conservation leads to the following relationship between the energy E of the primary photon and the total energies U and U' of the electron and positron: $E = U + U'$.

For energies between 100 MeV and 1 TeV, the fraction of energy $u = U/E$, taken by the secondary electron/positron, is approximately uniformly distributed between 0 and 1. As the energy increases beyond 1 PeV, this distribution becomes more peaked around the extremes. The cross-section rapidly increases from the kinematical threshold of approximately 1 MeV, reaching its asymptotic value around 100 MeV:

$$\sigma \approx \frac{7}{9}\frac{1}{n_a X_0} \tag{1.16}$$

Here, n_a denotes the density of atomic nuclei per unit volume, which determines the interaction length as $\lambda = 9/7X_0$. The emission angle for the particles in the pair is generally around $m_e c^2/E$.

1.7 Production of high-energy photons

1.7.1 Leptonic process

High-energy photons may arise from the interactions of high-energy charged particles (such as electrons, protons, and ions accelerated by shock waves from gravitational collapses) with nuclear targets like molecular clouds or radiation fields (such as magnetic or photon fields). Another possibility is the generation of high-energy photons through the decay of massive particles [11].

Various leptonic processes can create high energy photons: bremsstrahlung (described in section 1.5.3), synchrotron, and inverse Compton scattering. Let's consider a population of relativistic electrons in a magnetic field. They will produce synchrotron radiation. On their way out of the emission region, they will constitute a radiation field of soft photons. These synchrotron photons will have some probability of interacting again with the same populations of electrons by the Inverse Compton process. In a specific model called Synchrotron Self-Compton (SSC), electrons first make synchrotron radiation, then scatter towards higher energies. In this section, I will describe these processes in more detail, based on [11]

Synchrotron Emission: Magnetic fields in astrophysical environments considerably influence the dynamics of charged particles through the Lorentz force. Synchrotron photons are produced when relativistic electrons are accelerated due to giration in the magnetic field. The power associated with this emission, considering isotropic electron and magnetic field orientations, can be described by the rate of change of electron energy as:

$$\frac{dE}{dt} = -\frac{4}{3}\sigma_T c\gamma^2\frac{B^2}{8\pi}, \tag{1.17}$$

This formula applies under the assumption that the directions of the magnetic field and the electrons are random. where $\frac{dE}{dt}$ is the rate of change of energy, σ_T is the Thomson cross-section, c is the speed of light, γ is the Lorentz factor of the relativistic electrons, and B is the magnetic field strength. Given that the particle's acceleration is minimal in its rest frame, we can apply the nonrelativistic formula for the radiation rate.

Inverse Compton (IC) [31] scattering occurs when low-energy photons interact with high-energy electrons, as opposed to interactions with stationary electrons. This interaction results in an increase in the photon's energy, hence the term *inverse*. This mechanism, which effectively boosts photon energy, is particularly significant in regions with a high density of soft (low-energy) photons and energetic electrons.

Let's consider a population of relativistic electrons following a power law distribution with a differential spectral index q and a soft photon population following a blackbody distribution at a temperature T. We can determine the mean photon energies and energy distributions. This computation can be performed separately for electron energies within both the Thomson regime and the relativistic Klein-Nishina regime [11]:

$$\langle E_\gamma \rangle \approx \frac{4}{3}\gamma_e^2 \langle \eta \rangle \text{ for } \gamma_e \eta \ll m_e c^2 \text{ (Thomson limit)} \tag{1.18}$$

$$\langle E_\gamma \rangle \approx \frac{1}{2} \langle E_e \rangle \text{ for } \gamma_e \eta >> m_e c^2 \text{ (Klein-Nishina limit)} \tag{1.19}$$

$$\frac{dN_\gamma}{dE_\gamma} \propto E_\gamma^{-\frac{q+1}{2}} \text{ for } \gamma_e \eta << m_e c^2 \text{ (Thomson limit)} \tag{1.20}$$

$$\frac{dN_\gamma}{dE_\gamma} \propto E_\gamma^{-(q+1)} \ln(E_\gamma) \text{ for } \gamma_e \eta >> m_e c^2 \text{ (Klein-Nishina limit)} \tag{1.21}$$

The energy of the scattered photon is represented by E_γ, while E_e is the energy of the originating electron, and η is the energy of the seed photon. A handy approximation that connects the energy of the electron and the energy of the Compton-scattered photon in the Thomson regime can be expressed as follows:

$$E_\gamma \approx 6.5 \left(\frac{E_e}{\text{TeV}}\right)^2 \left(\frac{\eta}{\text{meV}}\right) \tag{1.22}$$

The Compton component commonly reaches energies in the GeV–TeV range in astrophysical sources.

A key feature of the SSC model is the established correlation between the product of synchrotron radiation and Inverse Compton scattering during a flare [32]. It would be challenging to integrate into the theory an "orphan flare," a flare in the Inverse Compton region unaccompanied by a flare in the synchrotron region. While the majority of flaring events are observed nearly simultaneously in TeV gamma-ray and X-ray fluxes, certain AGNs like 1ES 1959+650 have exhibited VHE gamma-ray flares without corresponding X-ray flares [33]. Flares that are observable in VHE gamma rays but lack significant activity in X-rays present a serious challenge to the standard SSC model despite the model's overall success in explaining the spectral energy distribution of blazars.

To model emission observed from Galactic and extra-galactic gamma-ray sources, we often use the *one-zone model*, which assumes that non-thermal radiation is produced in a single, homogeneous, and commonly spherical region in the jet. Certain parameters are necessary to characterize the emission region fully. These include the strength of the comoving magnetic field, the Doppler factor, and the comoving radius of the region [6]. Additionally, it is important to characterize the electron energy distribution; phenomenological functions are often used for it, assuming an equilibrium state.

The **SSC** mechanism [34, 35] is a basic purely leptonic process frequently observed in astrophysical entities that enable photon *acceleration*. In this method, ultrarelativistic electrons accelerated within a magnetic field, such as those found in AGN, generate synchrotron photons. Given the strength of the fields involved, these photons typically possess an energy spectrum that peaks in the infrared/X-ray range. These photons subsequently interact with their parent electron population through Compton scattering. Considering the ultrarelativistic nature of the electrons (with a Lorentz factor $\gamma_e \approx 10^{4-5}$ or even higher) [11], this interaction significantly enhances the energy of the upscattered photon.

1.7.2 Hadronic models

Alternative and supplementary models of VHE emission include multiple mechanisms: involves photons generated by cascades initiated by primary protons or nuclei accelerated within the system.

Additionally, proton synchrotron models suggest that VHE gamma rays can directly emanate from the synchrotron radiation of protons without the necessity for a cascade process. The key issue is that even while synchrotron radiation is less efficient in the case of protons, they are affected by much lesser energy losses than electrons and, hence, can be accelerated to extremely large energies. The accelerated hadrons collide with a target composed of nucleons (like a molecular cloud) or a radiation field in a process known as hadronic pion photoproduction. In both scenarios, according to the physics of hadronic cascades, the energy of the initial protons is needed to be one to two orders of magnitude higher than that of the gamma rays. This is because the predominant mechanism for photon production is the decay of the secondary π^0 mesons into $\gamma\gamma$ pairs at the termination of the hadronic cascade. Therefore, gamma-ray studies can contribute to a better understanding of the production of charged cosmic rays [36].

The energy of photons originating from the decay of π^0 is generally greater than that of photons produced by synchrotron radiation of electrons. In the rest of the frame of the neutral pion, the energy of both photons is about 70 MeV, and they have opposite momenta. When considering the energy boost from the movement of the π^0, and the angle of the emitted photons, the likelihood of emitting a photon with energy E_γ remains constant across the range of kinematically permissible energies.

Considering an energy spectrum of the accelerated protons at the source, which typically decreases as E^{-p} (where p is approximately 2), the decay spectrum viewed from a lab frame drops sharply below roughly 100-200 MeV due to the Lorentz boost, and its energy dependence mimics that of the parent protons at energies above 1 GeV. A distinctive peak corresponding to pion decay, which rises up to 70 MeV and then declines (potentially extending to GeV energies due to the Lorentz boost), is a clear identifier for gamma rays of hadronic origin.

1.8 Observation technique

The flux of gamma rays is very low, typically below a per mile of the one from the background of cosmic rays detected in a 1-degree angle around the direction of the source. Furthermore, the flux rapidly decreases as energy increases.

The emission spectra from cosmic sources in the high-energy range are generally steeply declining. They are typically modeled with a power-law differential spectrum, expressed as:

$$\frac{dN}{dE} \propto E^{-\gamma}, \tag{1.23}$$

where index γ often lies between 2 and 3. This indicates that photons of higher energy are less common, necessitating larger area detectors for their detection.

Small detectors onboard satellites typically allow observations of gamma rays with energies up to tens of GeV. To study the low flux at the highest energies, ground-based telescopes must be built to have big collection areas[6]. Ground-based detectors cannot directly observe gamma – rays as the Earth's atmosphere is opaque, with a total thickness of about 28 radiation lengths at sea level. The cosmic ray flux mainly consists of protons and heavier nuclei. Considering these restrictions, an observer on Earth must employ alternative methods to address the challenge of detecting gamma rays. There are two possible approaches to studying the cosmos in the gamma energy range: satellite experiments and ground-based telescopes. Below, I present a brief description of these two approaches.

1.8.1 GeV satellite

Using detectors mounted on satellites is a straightforward solution to circumvent the atmospheric limitations for detecting gamma rays. Satellites operate continuously and typically have a wide field of view, enabling extensive monitoring of cosmic phenomena. Satellite-based detectors typically include multiple converter layers where high-energy photons produce electron-positron pairs interlaced with a position detector. This tracking detector traces the path of the resulting particles to reconstruct the direction of the incident photon. Additionally, a total absorption calorimeter is used to estimate the photon's energy. A common approach to mitigate the effect of cosmic ray background is using a charged particle veto counter, which effectively filters out charged cosmic rays. Before being deployed

on satellites, detectors undergo calibration using accelerators, ensuring they have minimal systematic errors in energy determination. A major limitation of this technique is that the size of detectors is restricted by the weight limit that can be placed on satellites, which limits their collection area and also the performance at the highest energies, which might not be fully contained in the calorimeter. Given *Fermi*-LAT [12] collection area of approximately 1m^2, when observing the spectrum of the Crab Nebula, it captures one photon with an energy of about 100 GeV every two days, assuming constant observation in that direction; This frequency diminishes further due to the necessity of sky scanning. As a result, the collection area is not large enough to detect significant fluxes at high energies, which limits the maximum detectable energy to a level where the collection area is sufficient for statistical significance [6].

1.8.2 Ground-based detection

In the range of VHE gamma-ray observations, the low fluxes and steep spectral slopes of typical sources necessitate the use of very large detectors. This, in turn, requires that observations be carried out from the Earth's surface. As a result, ground-based telescopes employing the atmospheric Cherenkov technique have become the most successful tools for VHE gamma-ray astronomy in the last two decades. Ground-based detection of VHE photons is an indirect method where the nature, direction, and energy of the primary particle must be inferred from the observable properties of the secondary particles. This is done either through the use of shower arrays, which measure the properties of the secondary particles, or through the observation of the Cherenkov flash produced by the secondary particles in Cherenkov telescopes. The Earth's atmosphere is opaque to VHE photons, and only the secondary effects of atmospheric absorption can be observed.

The formation of Extensive Air Shower (EAS)

A gamma-ray is transformed into a pair of electron-positron particles after the initial interaction with a nucleus. Each particle in this pair subsequently generates photons via the bremsstrahlung process. This chain reaction is represented schematically in the top panel of Fig. 1.4. Notably, a similar, though more intricate, process occurs with protons and hadrons in general. The cosmic-ray particle showers are depicted in the bottom of Fig. 1.4. EAS are cascades of secondary particles that develop as the primary cosmic rays, mainly protons and atomic nuclei, collide with atmospheric nuclei and generate a multitude of secondary particles, such as electrons, positrons, and various mesons. In an EAS, bremsstrahlung radiation occurs when secondary electrons and positrons are decelerated or deflected by the electric field of the atmospheric nuclei. As they lose kinetic energy, these charged particles emit photons as bremsstrahlung radiation. These emitted photons can then interact with the surrounding matter, producing more electrons and positrons, emitting additional bremsstrahlung radiation. This process leads to a self-sustaining (until stopped by ionization energy losses), the amplifying cascade of particles and radiation that constitutes the EAS. This description of EAS is based on the review [10].

Heitler proposed in 1944 a valuable toy model for understanding the formation of electromagnetic showers [37]. With the simplifications that (1) the interaction cross-section does not depend on the energy or type of the particle, and (2) the impact of ionization and excitation are ignored, considering only brehmsstrahlung, we can write the following equation:

$$E(X) = E_0 e^{-X/X_0}, \tag{1.24}$$

In this equation, E_0 represents the energy of the primary particle initiating the shower, while E stands for its residual energy. The variable X denotes the total atmospheric depth traveled by the particle, expressed in g/cm^2. It is computed as the product of the atmospheric density ρ (which changes with altitude) and the path traveled in centimeters. For Earth's atmosphere, we approximate $X_0 \sim 37$ g/cm^2. According to this model, the average length of each step in the cascade is $d = \log_2 \cdot \text{X}_0$. The shower reaches a peak at a certain point, and then ionization losses of electrons become comparable to their bremsstrahlung energy losses. This peak is reached when the particles cascade down to an average energy known as the critical energy ($E_c \approx 86$ MeV).

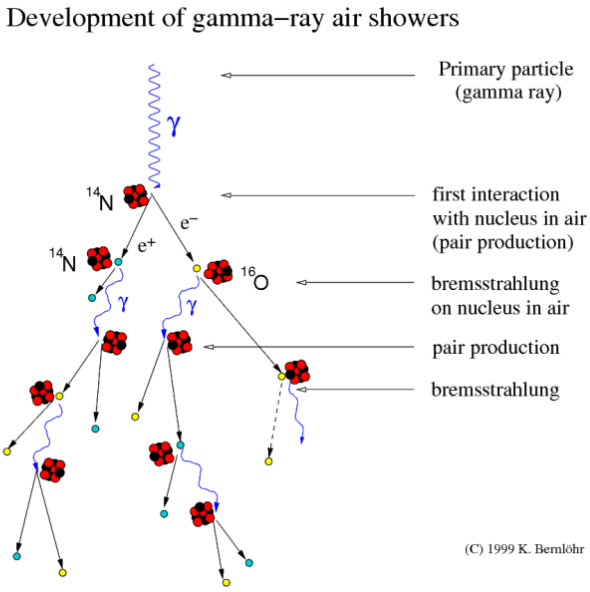

(a) Electromagnetic shower.

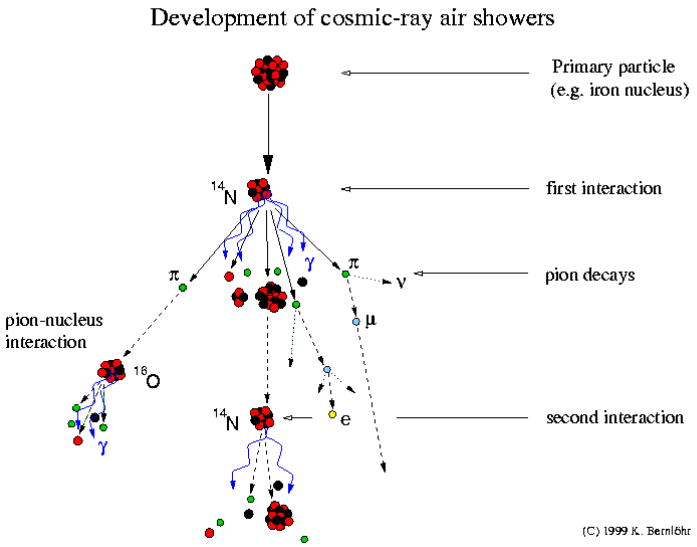

(b) Hadronic shower.

Figure 1.4: This schematic illustration shows the stages of development of an air shower initiated by a gamma photon or hadron. The cascade starts with the interaction of the primary particle with the atmosphere, leading to the production of secondary particles. As they travel through the air, these particles continue to interact and produce more secondary particles, resulting in a cascade of particles that eventually reach the ground. Credit:K. Bernlohr

The number of particles reaches $N = 2^n$ at step n. This count peaks at $N_{max} = 2^k \approx E_0/E_c$. This quantity is often designated as the *size* of the shower.

Owing to their relativistic energies, all particles involved in an air shower are notably directed within a narrow cone along the path of incidence. Multiple scattering primarily accounts for the lateral expansion of the shower [38], with a secondary contribution from the Earth's magnetic field's deflection. It is also crucial to consider that electrons and positrons can initiate electromagnetic showers exhibiting similar characteristics to those started by gamma rays. As such, these particles form an irreducible background for ground-based gamma-ray detection systems when no anticoincidence system can be used against the primary charged particles.

In the mid-1940s, Rossi and Greisen suggested refined analytical models describing these showers' development [14]. These models were conceived within the so-called "B approximation," which focuses on pair production and energy loss via Bremsstrahlung, neglecting other processes.

The analytical solution for N_e, which represents the total number of electrons and positrons above the critical energy, is expressed as:

$$N_e(t, E_0) = \frac{0.31}{\sqrt{\ln(E_0/E_c)}} \cdot e^{t \cdot (1 - 1.5 \ln s)}, \tag{1.25}$$

In this equation, t stands for the atmospheric depth, while s represents the *age parameter*, indicating the shower's stage of development. This parameter ranges from 0 at the initial interaction point to 1 at the shower's peak and eventually reaches 2 when the shower fades away. The pattern of N_e changing with t is often referred to as the shower's *longitudinal development*.

Detecting a gamma-ray shower directly requires a shower size of at least 100, which makes the energy threshold of an EAS detector heavily dependent on the altitude of the observatory, which is also known as a surface detector. Ideally, a ground array detector should be positioned at an altitude of 4 to 5 km to achieve maximum efficiency at an energy of a few TeV [39]. With standard analysis techniques, the energy threshold of an EAS detector is around 1 TeV, which is the threshold of the current generation of EAS detectors such as HAWC [40]. However, an alternative approach called the Imaging Atmospheric Cherenkov Technique (IACT) has been developed to achieve a lower threshold, which is the main topic of my thesis.

This description of EAS is based on the review [10].

Chapter 2

Astrophysics of blazars

2.1 Active Galactic Nuclei

Active Galactic Nuclei (AGN) are among the most luminous objects in the universe. In the unified scheme present in [41], AGN is a system consisting of a supermassive ($M_{bh} \sim 10^{6-10}\mathrm{M}_{\odot}$) black hole in the center, surrounded by an accretion disk. The central black hole is growing by being intensively fed with accreting material. The gravitational energy released from such matter falling into a black hole can eventually be converted into radiation and the kinetic energy of the outflow. These outflows can manifest as narrow, well-collimated plasma jets, moving at nearly light speed and bearing a significant amount of the energy originally released during the accretion process. This energy is finally emitted as radiation that we can detect across a broad spectrum of photon energies, spanning from radio waves to gamma rays [42]. A strong relation exists between the broadband spectral energy distribution (SED) of blazars and the properties of their central engine, such as the mass of the black hole (M_{bh}) and the luminosity of the accretion disk (L_{disk}) [43, 44].

To explain the observational features of AGN objects, their standard model involves a few components commonly present in them (however, in not all the source sub-classes, they are equally important), which are also shown in Fig. 2.1 [45], including:

- milli-pc accretion flow dominated by rotation, commonly known as an accretion disk. The disk can be optically thick and either geometrically thin (called a *thin* accretion disk [46]) or thick (referred to as a *slim* or *thick* accretion disk [47]).
- Broad Line Region (BLR) - dense gas clouds, largely devoid of dust, orbiting at velocities close to Keplerian motion at a luminosity-dependent distance of 0.01-1 pc from the BH.
- Dust Torus – A dusty, axisymmetric structure, typically believed to be present in the equatorial region of the AGN with size dependent on luminosity, typically between 0.1 and 10 pc. The dusty torus can obscure the central engine depending on the observation angle.
- Narrow Line Region (NLR) – Lower density ionized gas, which extends from just outside the torus to distances of hundreds or thousands of parsecs in the direction of the opening in the torus (*ionization cones*). This gas has lower velocities than the broad line region and typically contains dust, except for a small region close to the AGN known as the *coronal line region*.
- A pair of radio jets originating from the center. They are the emission place of broadband, non-thermal radiation that can extend up to gamma-ray energies.

2.1.1 SED

AGN emits electromagnetic radiation across a wide range of photon energies, from radio waves and microwaves through infrared, visible light, and X-ray to gamma rays. Gamma rays are detected as

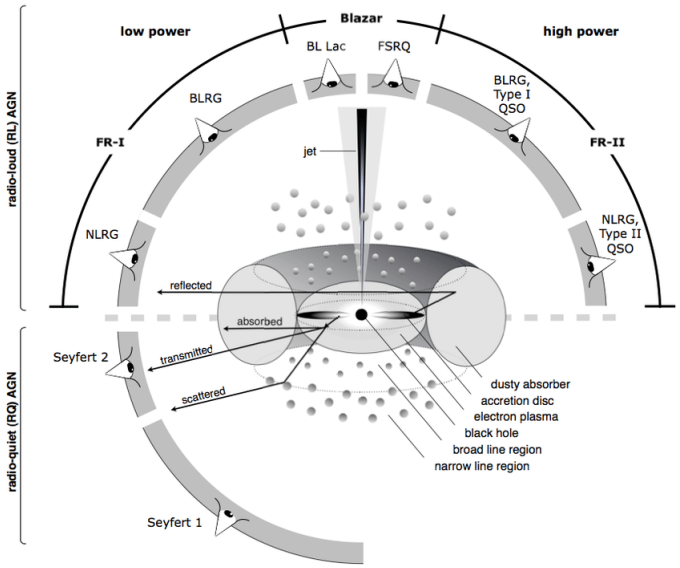

Figure 2.1: The unified model of AGNs. In the image, different components of AGN are present. Source: [48].

individual photons at the highest energies, and their energy can be estimated. Representing the energy emitted by a source across the electromagnetic spectrum in a unified way is important. This is where multiwavelength astrophysics comes in, which involves gathering and interpreting astronomical data collected by various instruments and detectors across different frequencies. The *spectral flux density* $F(\nu)$, typically expressed in units erg cm^{-2} s^{-1} Hz^{-1}, is a quantity that describes the amount of energy transferred by electromagnetic radiation through a real or virtual surface, per unit surface area, and at a given frequency ν. The frequency ν corresponds to the energy of the radiation, once multiplied by the Planck constant h [28]. However, it is important to distinguish between $F(\nu)$ and the SED, which is defined as $\nu F(\nu)$ and typically expressed in units of erg cm^{-2} s^{-1}. This formulation allows for a representation where the amount of energy is distributed not within a linear but within a logarithmic interval of energy, highlighting the distribution's characteristics across different energy scales.

SEDs have been the primary tool for studying AGN since the early stages of their research. Currently, a vast collection of SEDs is publicly available in the Space Science Data Center (*SSDC*[1]).

The radiation from AGN is usually attributed to a combination of:

- **Thermal radiation** ranges mainly in the IR - UV. This process occurs when falling matter is strongly heated in the inner parts of an accretion disk close to the central black hole. It is also assumed that the DT exhibits a rough thermal spectrum.

- **Non-thermal radiation** spans 20 orders of magnitude of the electromagnetic spectrum, from the radio to gamma-rays. The radiation is produced by high-energy particles accelerated in the magnetic field of a jet of material ejected from the nucleus at relativistic velocity.

The example SED is shown in Fig. 2.2.

2.1.2 Relativistically beamed AGN objects - blazars

Blazars are AGN characterized by their relativistic jets pointing nearly toward the observer [50]. Due to this small viewing angle, all emission from a region moving with Lorentz factor $\Gamma = (1-\beta_\Gamma^2)^{-1/2}$, where β_Γc is the jet speed, along the jet, at angle $\theta_{\rm obs}$ with respect to observer line of sight, will be Doppler boosted in frequency by a factor $\delta = (\Gamma[1 - \beta_\Gamma \cos\theta_{\rm obs}])^{-1}$ and in bolometric luminosity by a factor

[1] https://tools.ssdc.asi.it/

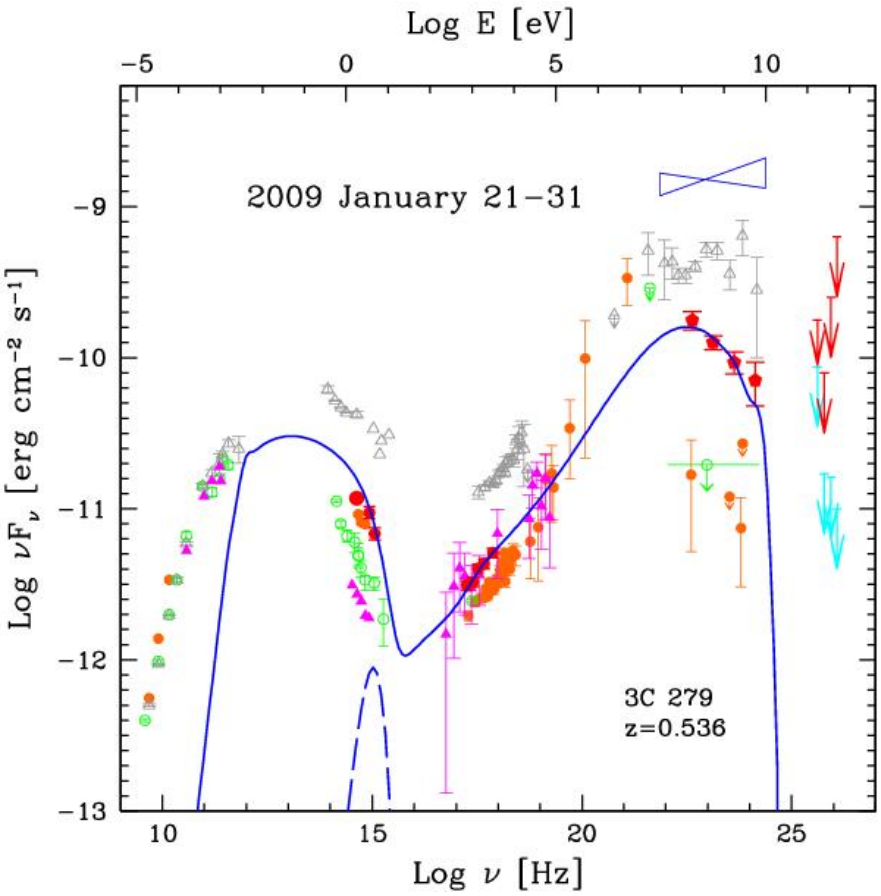

Figure 2.2: This is an example of the SED for 3C 279 recorded in January of 2009. The data was collected using MAGIC (between January 21st and 31st, with deabsorbed red arrows and observed cyan arrows), *Fermi*-LAT (averaged over the same period, represented by red pentagons), XRT and UVOT (represented by red squares collected on February 1st, 2009), and KVA (represented by a red filled circle collected on January 25th, 2009). The SED model assumes that the emission region is within the BLR. The black dashed line represents blackbody radiation from the IR torus, with red indicating its color. Source: [49].

δ^4 with respect to quantities measured in the co-moving frame of the emission zone. Any variability time scale measured in the co-moving frame will appear to the external observer to be reduced by a factor δ^{-1} [51]. These phenomena cause blazars to be the most luminous gamma-ray AGN observed in the extragalactic sky, showing variations, in some cases, occurring in time intervals as short as a few minutes [52, 53]. Historically, the categorization of beamed AGN relies on the broad emission lines present in their optical spectra. Blazars that exhibit strong and broad emission lines (with a rest-frame equivalent width (EW) $\geq$ 5 Å) are classified as Flat Spectrum Radio Quasars (FSRQs). The optical spectra of FSRQs indicate the presence of broad emission lines, which suggests that fast-moving gas clouds are located near the central engine (within 0.1 to 1 parsec). In contrast, the spectra of BL Lacs exhibit either weak or no emission lines. Broad emission lines identifiable in the spectra of AGN are created in BLR, which is considered photoionized by thermal radiation from the accretion disc [54]. On the other hand, the category of BL Lacertae or BL Lac sources includes objects with quasi-featureless spectra (EW $\leq$ 5 Å) [55]. It has been theorized that the absence of broad emission lines in the optical spectra of BL Lac sources may be attributed to Doppler boosting, which could overpower any spectral lines. However, absorption features from the host galaxy are observed in many nearby BL Lac sources with redshifts less than 1, indicating that the emission lines are intrinsically weak despite the presence of Doppler boosting [56]. To further complicate the matter, broad emission lines have been observed in several BL Lac objects' low jet activity states (see, e.g., [50]). Conversely, in the case of FSRQ B1420 [57], an increase in jet activity was associated with a decrease in emission line strength, with the EW dropping below 5 Å) during high activity states. Thus, a classification scheme for blazars based solely on the EW of their spectra is not sufficient to describe the physical differences in different types of blazars [43]. The SEDs of both subclasses of blazars exhibit two main peaks, with the first peak typically attributed to synchrotron emission. The inverse Compton scattering process (see Section 1.7.1) typically explains the SED's higher energy peak. Seed photons utilized for inverse Compton scattering originate from synchrotron emission (Synchrotron Self Compton, SSC, model) [35] or can arise from the dense radiation field generated by the direct and reprocessed accretion disk emission [58, 59] or molecular torus [60]. Alternative mechanisms for producing the second peak, based on hadronic processes, have also been proposed [61, 62], and have gained in popularity since the putative coincidence of neutrino with TXS 0506+056 [63]. In general, it is preferred to use SSC models for BL Lac objects, while external Compton (EC) models are favored for FSRQs [27].

Blazars could also be divided into low-, intermediate-, and high-synchrotron-peaked sources (LSP, ISP, and HSP, respectively) based on the peak frequency of the synchrotron component in their SEDs. LSP have peak frequency [Hz] $\log_{10}(\upsilon_{peak}) < 14$, ISP have $14 < \log_{10}(\upsilon_{peak}) < 15$ while HSP have $\log_{10}(\upsilon_{peak}) > 15$ [64]. This is a more physical distinction between different blazar classes. However, a number of sources have shown transitions between different classifications during their states of high activity (see, e.g., [65]). For FSRQs, the synchrotron peak in the SED is commonly observed in the infrared regime, which classifies them as LSPs. On the other hand, for BL Lacs, the location of the synchrotron peak can vary between infrared and hard X-rays, classifying them as LSPs, ISPs, or HSPs [27].

FSRQ

As FSRQ objects are the main topics of my doctoral thesis, I will describe them here in more detail. I will focus on the description of FSRQs in the HE and VHE energy ranges, which were investigated thoroughly in the last decade by the *Fermi*-LAT telescope and Cherenkov telescopes.

The study of FSRQs in the VHE range is essential for understanding the extreme physical processes occurring in these objects. The VHE gamma rays produced in FSRQs result from the interaction between the relativistic jets and the surrounding environment or the internal processes within the jets themselves. Detecting VHE gamma rays from FSRQs is challenging for various reasons, including that their gamma-ray emission is often significantly absorbed by interactions with the EBL during its travel toward Earth. This absorption effect is stronger at higher energies and larger distances, making detecting VHE gamma rays from more distant FSRQs challenging.

A groundbreaking discovery in the study of FSRQs was the first-ever detection of an FSRQ in the VHE range. This milestone was achieved by the MAGIC telescope during a flare in early 2006,

observing 3C 279 [66], a well-studied at lower energies FSRQ located at a significant redshift of $z = 0.536$ [67]. Before this breakthrough, observing such distant sources in the VHE range was considered unattainable due to the steep energy spectrum and the strong gamma-ray attenuation by the EBL photon field. This pioneering discovery has far-reaching implications for our understanding of the EBL and VHE gamma-ray emission mechanisms, which will be further explored and discussed in the context of FSRQs throughout my thesis.

FSRQs are highly variable (see, e.g., [68]). The VHE gamma-ray flux has been observed to fluctuate even by two orders of magnitude [69]. Due to this, the most successful approach for studying the FSRQs in the VHE gamma rays is to follow up alerts of enhanced activity at lower energies. Observations of FSRQs in the VHE band may hint at their nature and radiation processes.

The current list *TeVCat* (last access: March 13, 2024) of detected blazars at VHE consists of ~ 70 BL Lac and only 10 FSRQ. The distinction between FSRQ and BL Lac could be unclear, as discussed at the beginning of this section. The list of FSRQ objects detected in the VHE energy band is as follows: 3C 279 [66], PKS 1510-089 [70], 4C +21.35 [71], S3 0218+35 [72], PKS 1441+25 [73], PKS 0736+017 [74], TON 0599 [75], B2 1420+32 [57] and the most recent PKS 0346-27 [76] and OP 313 [77].

Observations of FSRQs in the VHE band may hint at its nature and radiation processes. PKS 1510-089 is unique as it has been detected in a low state by MAGIC [78] and H.E.S.S. [79], indicating different emission conditions. B0218+357 is noted for being the only gravitationally lensed FSRQ seen in the VHE band, offering insights into gravitational effects on VHE emissions.

The first catalog reporting upper limits (U.L.) from FSRQs in the TeV energy range was carried out by the Whipple group [80]. The catalog of U.L. for AGNs, including FSRQs sources, was also published by the H.E.S.S [81, 82]. Nowadays, the VERITAS collaboration performs a systematic and unbiased search for the TeV emission from a set of FSRQs [83]. Despite the studies mentioned above, there is still a need of systematic FSRQ investigations in VHE.

Observations of FSRQs in the VHE band may hint at its nature and radiation processes. The longstanding question pertains to the location of the gamma-ray emitting region within FSRQs. Recent evidence suggests that this region is likely located beyond the BLR, at least during the epoch of VHE gamma-ray emission. FSRQs experience variability in VHE gamma-rays with timescales of tens of minutes (see [71, 84]). It has been long argued that such variability would more naturally occur closer to the black hole however, as it has become evident that jets have substructures and that the emission region does not have to fill the full jet diameter (see, e.g., [27] for a recent review), this line of argumentation has become less popular. Nevertheless, the understanding of VHE emission of FSRQs still needs to be completed.

Broad Line Region (BLR) in FSRQs

In this section of the Ph.D. thesis, I discuss the apparent lack of interaction between BLR photons and jet electrons in jets of FSRQs, which challenges the external Compton (EC) mechanism on UV photons from the BLR.

The External Compton (EC) mechanism has been widely used to model the SED of gamma-ray detected FSRQs [85, 86]. According to this mechanism, the interaction of jet electrons in FSRQs with BLR photons is involved in the EC scattering process. However, the expected in this case strong cut-off in the gamma-ray spectrum is not solely due to EC itself. While EC can result in a spectral break associated with the Klein-Nishina effect, the ultimate high-energy cut-off is attributed to the absorption of gamma-ray photons through pair production in the same BLR radiation field, not directly by the EC process, which is primarily influenced by the maximal energy of electrons. Recent studies have found no evidence for this expected BLR cut-off in gamma-ray spectra, even in sources with large disk luminosities and BLR sizes [87]. When the emission region is located within the BLR, a sharp break in the gamma-ray spectrum is foreseen to occur due to the strong attenuation of the HE and VHE photons through their interaction with the optical and infrared photons. The optical depth for the interaction of HE photons could be very large, preventing their escape from the zone [88]. Therefore, if we can attribute the cause of the break/cut-off to the absorption, we can constrain the location of the gamma-ray emitting zone [89].

To keep a low optical depth within the BLR and handle the lack of interaction between BLR photons and jet electrons, two alternatives have been proposed: increasing the size of the BLR (if we assume that the radius from reverberation mapping is underestimated) or shifting the gamma-gamma threshold to higher energies [90]. However, neither scenario maintains the EC mechanism as a viable option for gamma-ray emission in FSRQs. Increasing the size of the BLR would lower the energy density for the BLR photons, rendering them negligible compared to other available energy densities. Shifting the gamma-gamma threshold to higher energies would require a specific geometry that would place the emitting region outside the BLR radius, making the EC mechanism unlikely. The lack of absorption of BLR photons by jet electrons in FSRQs suggests that the EC process is less efficient, as previously mentioned, rather than implying that BLR photons do not suppress VHE gamma rays. However, this result still indicates that most FSRQs can be emitters of VHE gamma rays under the right conditions and could be in the reach of Cherenkov telescopes [87]. Notably, such emission might not be detectable due to strong EBL absorption of farther FSRQ objects.

The lack of interaction between jet electrons and BLR photons in FSRQs suggests that the BLR acts as a proxy for accretion properties but does not directly affect jet emission through cooling [87].

2.1.3 Gamma ray properties of AGN objects

Observations in the gamma-ray spectrum allow for the study of the most energetic charged particles in AGNs, shedding light on high-energy processes in these astronomical objects. In the GeV range, sky-scanning satellites provide invaluable information, enhancing our understanding of the universe's extreme phenomena such as AGN. The *Fermi* Large Area Telescope (LAT) collaboration has released several catalogs containing lists of sources detected by the LAT, which have been progressively updated with accumulated data sets and improved analysis procedures. Among these are both general and class-specific catalogs. The 4th *Fermi* Large Area Telescope catalog (4FGL) of gamma-ray sources is based on data collected by the LAT during its first eight years of operation, covering an energy range from 50 MeV to 1 TeV [91]. In 4FGL, The AGN category is the largest source population in 4FGL, consisting of 3137 blazars, 42 radio galaxies, and 28 other AGNs. Among the blazar sample are 694 FSRQs, 1131 BLLs, and 1312 Blazar candidates of uncertain type. The 4FGL-DR3, spanning 12 years of data [92] containing over 6500 gamma-ray sources. More than 3000 of the identified or associated sources are blazars, with over 2/3 of the sources having counterparts at other wavelengths [93].

The *Fermi*-LAT gamma-ray satellite has significantly contributed to blazar studies by detecting over 1500 blazars in the gamma-ray band alone. This remarkable accomplishment was emphasized in the 3LAC study [94]. In the 4FGL catalog, three function forms are commonly used to fit the spectra of the sources: *Power–law*, *Log–parabola*, and *Cutoff*. The *Cutoff* form (a power–law with a super–exponential cutoff) is used in the 4FGL to fit the spectra of only one blazar 3C 454.3 [91].

The most common function used is *Fermi* catalog is the Power–Law function with index γ:

$$\frac{dN}{dE} = N_0 \left(\frac{E}{E_0}\right)^{-\gamma} \tag{2.1}$$

and the *log–parabola* function:

$$\frac{dN}{dE} = N_0 \left(\frac{E}{E_0}\right)^{-\alpha+\beta \ln(E/E_0)} \tag{2.2}$$

where $\frac{dN}{dE}$ is the differential flux as function of energy E. N_0, α, and β are the flux at the normalization energy E_0, the spectral index, and the curvature parameter of the spectrum at E_0.

PLSuperExpCutOff model is defined as:

$$\frac{dN}{dE} = N_0 E^{-\gamma_1} \exp(-(E)^b) \tag{2.3}$$

On average, sources that exhibit high gamma-ray luminosity, primarily FSRQs, are observed to have softer spectra compared to those with lower gamma-ray luminosity, primarily BL Lacs. However,

a few exceptions exist, such as high-synchrotron-peaked FSRQs and high-luminosity high-synchrotron-peaked BL Lacs. Another notable finding is a strong anti-correlation between the synchrotron peak position (ν_{peak}) and the spectral index (Γ) observed for both FSRQs and BL Lacs [95].

In figure 2.3, I present the dependence of the power-law spectrum index from the 4FGL-DR3 catalog on the acceleration disk luminosity L, with a division into BL Lac and FSRQ objects. Most of the sources in the figure are FSRQs since L was taken from a study on blazars, which includes broad emission-line systems and blazars whose optical spectra lack emission lines but are dominated by absorption features [43].

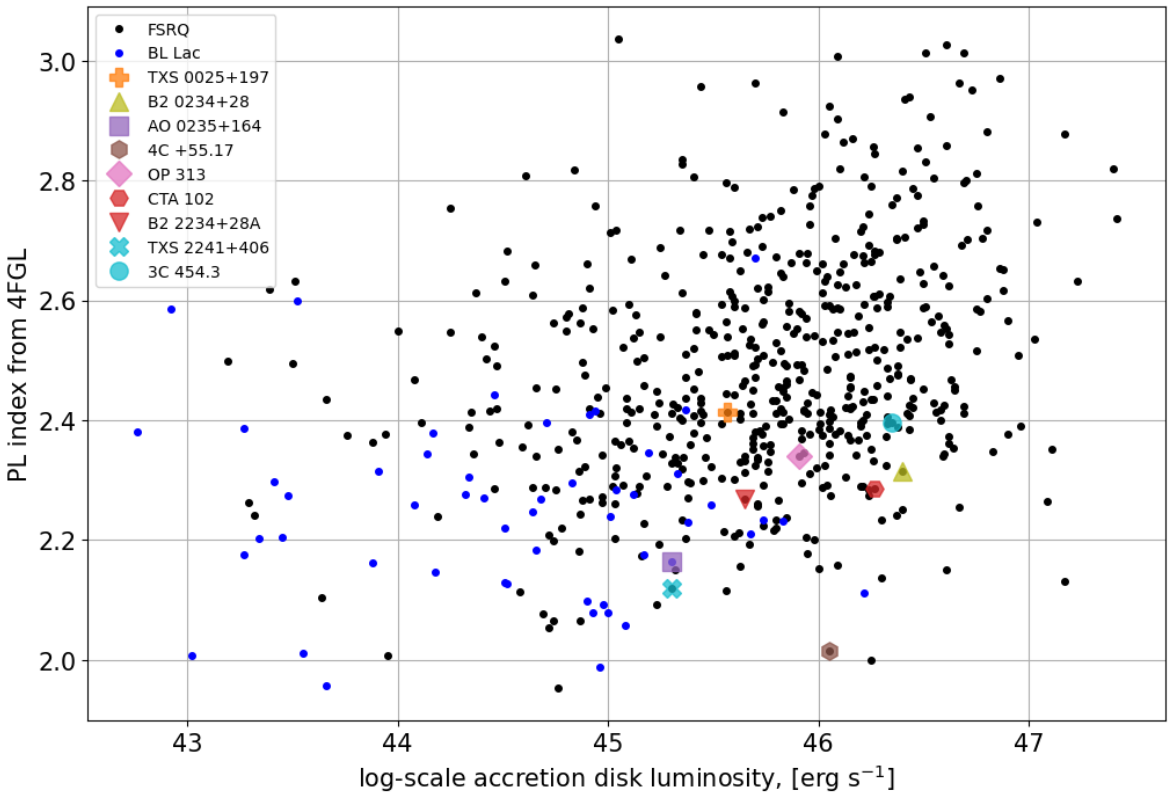

Figure 2.3: This diagram illustrates the power-law spectrum index from the 4FGL-DR3 catalog as a function of the acceleration disk luminosity for Fermi blazars studied in the *The Central Engines of Fermi Blazars* paper [43]. The sources being studied in the chapter 5 have been marked.

Multiwavelength observations and variability of blazars

Coordinated multiwavelength observations have played a critical role in advancing our understanding of blazars, which are known for their brightness and variability across a broad spectrum of electromagnetic radiation, from radio waves to high-energy gamma-rays, including the VHE range. The multiwavelength approach to observational studies was not widely available until the 1990s. Previously, gamma-ray observations were notably conducted by COMPTEL and EGRET, both instruments aboard the Compton Gamma-ray Observatory (CGRO) [96], complemented by studies from X-ray satellites [97]. The 1990s marked a period of advancement in blazar research, propelled by the operational capabilities of CGRO alongside the Rossi X-ray Timing Explorer These advancements enabled the organization of the first coordinated observational campaigns, which incorporated X-ray and gamma-ray observations alongside data collected from other wavelengths such as radio, near-IR, and optical. These campaigns were typically designed to ensure quasi-simultaneous measurements across the various electromagnetic spectra. Multiwavelength campaigns focused on blazars were usually conducted over several weeks to

months. Through these efforts, researchers gathered valuable data revealing that in numerous sources, the gamma-ray band played a dominant role in the total energy studied via SED observed from blazars. In other words, these observations revealed that many sources were strongly Compton-dominated [98]. Due to the limited sensitivity of the EGRET instrument, observational campaigns targeting blazars were restricted to a select group of the brightest sources, amounting to only 66 blazars identified within the EGRET catalog [99]. Furthermore, in only a few cases it was possible to study the variability of the gamma-ray band in connection with variability in other electromagnetic spectra due to the instrument's limitations. The advent of the *Fermi*-LAT gamma-ray satellite has significantly transformed blazar studies. The *Fermi*-LAT gamma-ray satellite has significantly contributed to blazar studies by detecting thousands of blazars (see Section 2.1.3).

When ground-based Cherenkov telescopes were developed, the high-energy window was expanded to include the VHE domain (see [100] for a review). The discovery of the first VHE gamma-ray emitting blazar, Mrk 421 [101], dates back to 1991. Since then, significant progress has been made in obtaining multiwavelength observations, resulting in a wealth of data for blazar studies. By 2000, only six blazars emitting VHE gamma rays had been detected. In the last two decades third-generation ground-based Cherenkov telescopes (H.E.S.S. [102], MAGIC [103], VERITAS [104]), have had a transformative impact on our understanding of the gamma-ray universe, revolutionizing our view and knowledge of this field. Quasi-simultaneous and well-sampled data sets are now available for many sources, including VHE gamma-ray data. With the current generation of Imaging Air Cherenkov Telescopes (IACTs), such as H.E.S.S., MAGIC, and VERITAS, the number of VHE gamma-ray emitting blazars has increased to ~ 90 (*TeVCat*[2]) [105].

Blazars are known for their significant variability across the entire electromagnetic spectrum, exhibiting changes on time scales ranging from years to minutes [28]. However, the lack of consistent correlation in the variability patterns between different wavelength bands presents a significant challenge in comprehending the optical through gamma-ray emission. Additionally, the very short time scales of variability pose significant difficulties for our understanding of blazars [51]. In recent years, the fast variability of blazars in VHE gamma rays has attracted increasing attention. This phenomenon was initially observed in the brightest VHE blazars, including Mrk 421 [106], PKS 2155-304 [52], Mrk 501 [53], as well as in different types of sources such as the FSRQ PKS 1222+21 [71], the BL Lac source [107], which can be classified as borderline ISP/LSP, and the radio galaxy IC 310 [108]. The observed variability time scales in VHE gamma-rays are on the order of minutes, representing the shortest variability time scales detected from blazars. Such fast variability has been detected from only one blazar, 3C 279 [109], in the *Fermi*-LAT band due to its much smaller collecting area compared to IACTs [27].

Absorption in the Extragalactic Background Light

Detection of very distant blazars emitting gamma rays with a large redshift is challenging due to absorption. In this subsection, I will describe how the Universe is opaque to gamma rays when the energy-dependent mean free path of the photon is comparable to or smaller than the source distance. The dominant process for absorption on the way to the observer of VHE photons with energy E produced by astrophysical sources is the pair production on low-energy extragalactic background photons of energy ϵ in the energy range from Cosmic Microwave Background (CMB) to the near-ultraviolet (UV) wavelengths. This process can be described by the following equation:

$$\gamma_E + \gamma_\epsilon \rightarrow e^+ e^- \tag{2.4}$$

This UV/optical/infrared background radiation is known as *extragalactic background light* (EBL). The EBL is the sum of light emitted by stars, galaxies, and AGN over the entire history of the Universe. Most EBL is due to direct starlight or subdominant contributions from AGN in the UV, optical, and near-infrared. From mid-infrared to submillimeter wavelengths, EBL consists of re-emitted light from dust particles, including continuous thermal radiation and line emission from particles The current photon background consists of light emitted at all epochs, modified by the redshift due to the expansion of the Universe. Therefore, in principle, the EBL contains information about the evolution of galaxies' baryonic matters and the Universe's structure [110].

[2] http://tevcat.uchicago.edu/

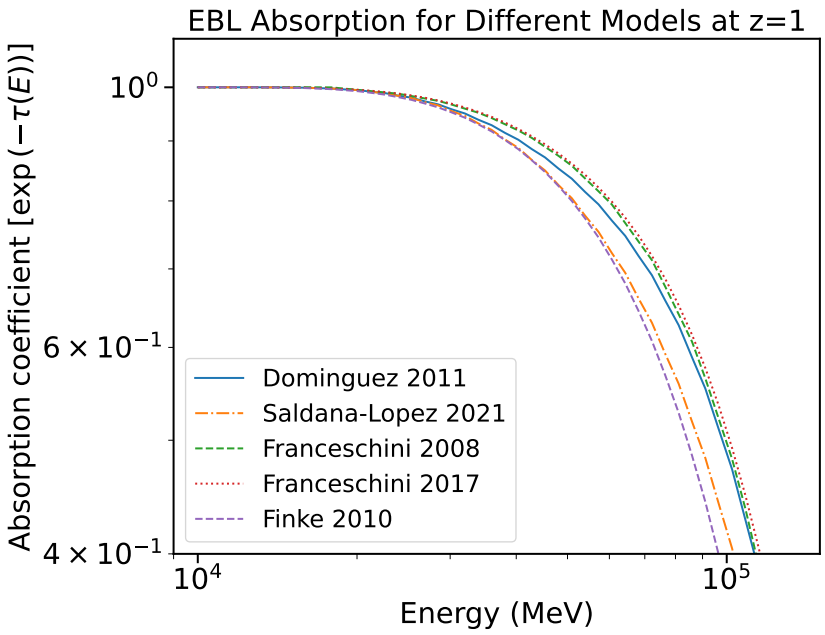

Figure 2.4: The $\gamma\gamma$ absorption for a source at redshift z=1 following the EBL models of Franceschini [111] [112], Finke [113], Domínguez [114], Saldana-Lopez [115].

Measuring EBL directly is problematic due to contamination from close objects and galactic light. Because of various modeling approaches and uncertainties in the underlying model parameters, the intensity and shape of the EBL spectrum are still disputed. Many EBL models have been developed: Franceschini [111] [112], Finke [113], Domínguez [114], Saldana-Lopez [115]. Fig. 2.4 created with `gammapy` v1.1 shows absorption for the four mentioned models.

Optical depth and spectrum attenuation

Optical depth (τ) quantifies the attenuation of radiation as it travels through a medium, taking into account the absorption and scattering of photons. In VHE gamma-ray astronomy, optical depth is particularly useful for describing the absorption of gamma-ray flux due to interactions with the Extragalactic Background Light (EBL). The optical depth dimensionless quantity $\tau_{\gamma\gamma}$ (E, z) can be calculated for a photon with the observed energy E that is emitted from a source at redshift z using the EBL energy density from a particular model. This calculation allows us to estimate the flux of a gamma ray with energy E, which is absorbed during its journey from the source at the redshift z to the observer. The attenuation coefficient for the radiation flux is typically taken into account while expressing the flux of a gamma ray:

$$I(E, z) = I_0(E)e^{-\tau_{\gamma\gamma}(E,z)} \tag{2.5}$$

where I_0 is the flux at the source (corrected for cosmological effects).

The energy dependence of $\tau_{\gamma\gamma}$ results in significant modifications to the observed spectrum of the source with respect to the spectrum at the source due to the exponential dependence in 2.5. With increasing energy (up to PeV range), $\tau_{\gamma\gamma}$ also increases, causing the observed flux to be more attenuated at higher energies. This reduces the effective mean free path of photons propagating in the Universe, $\lambda_\gamma(E)$. Fig. 2.5 illustrates how photons' mean free path (in Mpc) varies depending on the photon energy in the local universe. At energies around 100 TeV, Galactic sources of photons begin to be attenuated by the presence of background photons. Similarly, photons from the nearby Universe (within a few tens of Mpc) are also affected, with attenuation occurring above around 10 TeV due to the presence of the CMB, becoming important around 100 TeV. Observationally speaking,

the absorption of gamma rays poses a challenge to the field of gamma-ray astronomy. However, the detection of absorption features in the spectra of GeV-TeV gamma-rays offers a unique opportunity to obtain valuable information about the poorly understood EBL [116], and with it on the star formation history. To accomplish this, precise measurements of the gamma-ray flux from various extragalactic objects located at different redshifts are required, along with a good understanding of the intrinsic gamma-ray spectra at the sources, i.e., the quantity I_0 in 2.5 [28].

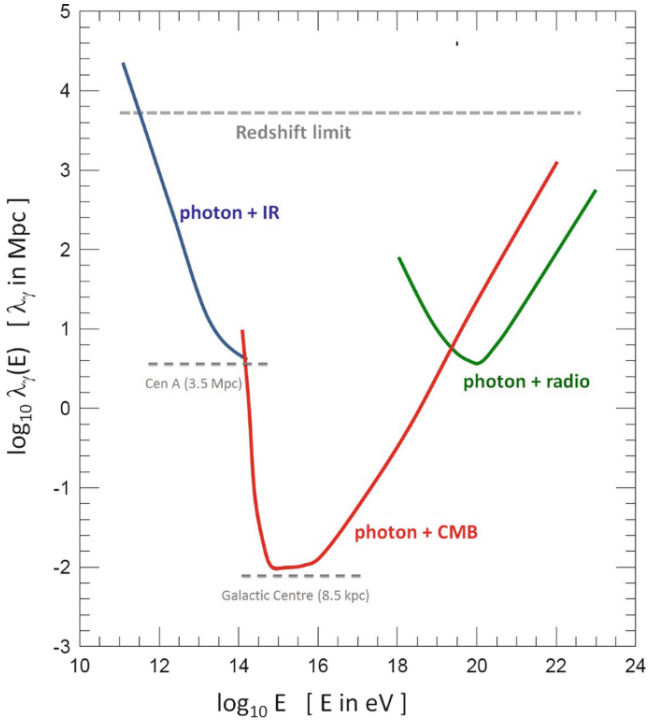

Figure 2.5: The mean free path of photons (in Mpc) as a function of photon energy, considering the contributions of scattering on background photons from the IR, CMB, and radio separately. The Galactic center's positions and the closest AGN are also shown in the figure. Source [28]

To compute the optical depth $\tau(E, z)$ as a function of observed energy E and redshift z, one must account for the energy scaling with redshift as $(1 + z)$. The optical depth is then calculated by convolving the photon number density of the background photon field with the cross-section between the incident gamma-ray and the background target photons and integrating the result over distance (redshift), scattering angle, and energy of the redshifted background photon:

$$\tau(E, z) = \int_0^z dz' \int_0^\infty dE' \int_{-1}^1 d\cos\theta n(E', z')\sigma(E, E', \theta)(1 + z')^3/H(z') \tag{2.6}$$

where: $n(E', z')$ is the photon number density of the background photon field, $\sigma(E, E', \theta)$ is the cross-section between the incident gamma-ray and the background target photons, θ is the scattering angle, $H(z')$ is the Hubble parameter at redshift z', E' is the energy of the (redshifted) background photon, z' is an integration variable for the redshift. The integrals account for the distance (redshift), energy and scattering angle of the redshifted background photon.

Location of blazar emission zone and the source of the seed photons for high-energy emission

The longstanding question pertains to the location of the gamma-ray emission region within FSRQs. This issue is closely related to the source of seed photons for inverse Compton scattering since their distance from the central engine influences their availability, as shown in Fig, 2.6. In FSRQs, the central

engine is expected to be surrounded by BLR clouds that re-scatter emissions from the accretion disk. Beyond this, a dusty torus envelops the BLR.

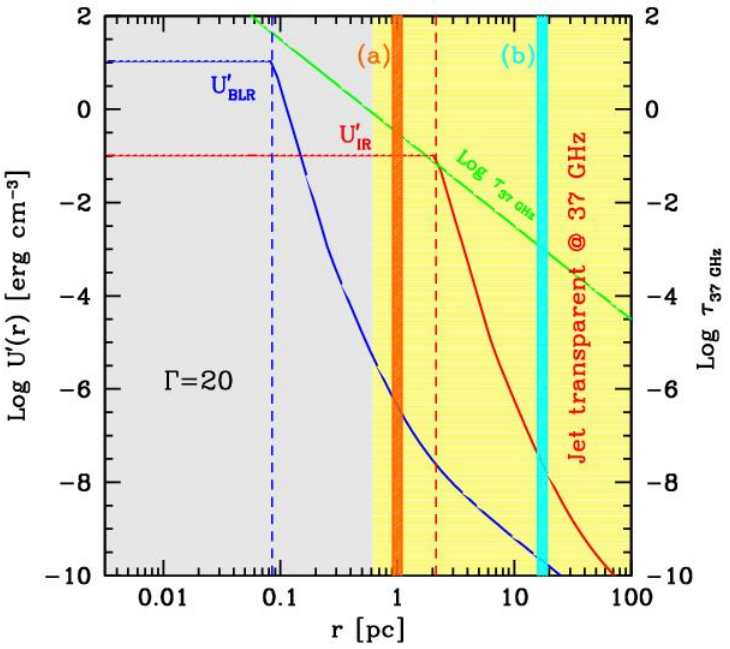

Figure 2.6: The energy density of the photon field for PKS 1510-089 as it relates to distance from the central engine. The blue lines represent the BLR, while the red lines represent an infrared torus. The green line shows the τ_{37} GHz (optical depth at 37 GHz, which was calculated using the magnetic field derived for case a model; as outlined in [117]), and the yellow zone indicates where the jet is transparent at 37 GHz. The dashed lines denote the assumed size of the BLR (blue) and dust torus (orange). The thick red and cyan vertical lines indicate the areas that were selected for SED modeling in [117]. Source:[117].

Recent evidence suggests that the emission region is likely located beyond the BLR, at least during the epoch of VHE gamma-ray emission. Such evidence stems both from the absence of absorption in the *Fermi*-LAT observations of FSRQs - where 2/3 of the selected FSRQs in one study (refer to [87]) displayed no signs of absorption within the >100 GeV range - as well as from the detection of VHE gamma-ray emissions from FSRQs. FSRQs experience variability in VHE gamma rays with timescales of tens of minutes; see [71, 84]. It has been long argued that such variability would more naturally occur closer to the black hole. Additionally, if the emission region is significantly smaller than previously thought, it implies that only a fraction of the jet's energy can be utilized for the observed emissions. Causality arguments in these cases indicate the presence of extremely compact emission regions, which can arise from magnetic reconnection events, recollimation shocks, or magnetoluminescence [118, 119]. As mentioned earlier, blazars display variability over a range of timescales, from as brief as the signal-to-noise ratio allows to as extended as the observational period. In the case of FSRQs, flux doubling times as brief as a few minutes have been detected at gamma-ray energies by ground-based Cherenkov telescopes and the *Fermi*-LAT. For FSRQs, the detection of gamma rays above 10 GeV suggests that these compact energy dissipation sites are situated at least hundreds of Schwarzschild radii away from the central supermassive black hole. If not, the gamma-ray emission would experience significant attenuation due to pair production on UV and optical photons emitted by the accretion disk and broad emission line clouds and subsequently scattered by the intercloud medium. Satisfying these constraints poses a challenge for conventional emission models, necessitating considering extreme relativistic bulk motion within the plasma [120, 121, 122].

VHE gamma rays are a powerful tool for determining the location of the emission region. For them to be produced, there must be a dense field of target photons forced during a low activity state [78].

In all instances, detecting VHE gamma rays, even at low levels, places the emission region outside the BLR. Fast variability has also been observed in FSRQs, with variability timescales of about 10-20 minutes [71], but the photon field cannot be too dense, or the gamma rays would be absorbed. If the blazar zone is situated within the BLR, VHE gamma rays would be absorbed [123, 124]. Despite this, several FSRQs have been detected emitting VHE gamma rays, starting with 3C 279. Most detections occurred during flares in other bands, but PKS 1510-089 was also detected in the VHE gamma-ray band during a low state [125]. This suggests that the emission region must be both small and located outside the BLR, providing direct observational evidence for the presence of substructures within the jet. Consequently, small emission regions can dominate the entire emission under certain conditions, and a small emission region does not necessarily mean that it must be near the central engine. A further argument to support the positioning of the blazar zone near the central engine is the observed rapid, sub-hour variability in gamma-rays (see, e.g. [126, 127]). For instance, in 3C 279, the variability time scale was as short as five minutes [122] in the GeV energy band, for PKS 1510-089 time scale was 20 minutes [125] in the VHE energy band. This rapid variability, as mentioned before, necessitates the emission region to be small, suggesting its nearness to the black hole. However, this inference is contingent on the assumption that the emission region occupies the entire diameter of the jet.

On the other hand, observational data from the Fermi-LAT telescope has supported the idea that gamma-ray emission zones in blazars are located quite far from the black hole [128, 129]. This conclusion is based on the combination of Very Long Baseline Interferometry (VLBI) observations and *Fermi*-LAT gamma-ray light curves, which revealed that gamma-ray flare timings align closely with activity seen in the 43 GHz VLBI core, suggesting that they occur in the same spatial region. This aligns with earlier findings from the EGRET era [130, 131], where timings of bright gamma-ray flares were compared with radio band flares. Given that the 43 GHz VLBI core is located significantly beyond the BLR radius, for instance, the BLR radius in PKS 1510-089 is around 0.1 pc while the 43 GHz VLBI core is situated at 6.4 pc [132], it seems likely that the BLR is not the source of seed photons for Compton scattering. This idea is further substantiated by the lack of observed BLR absorption in the broad sample of Fermi-LAT FSRQs [87]. However, some observations suggest this might be an oversimplified conclusion. For example, [133] observed a significant variation in the MgII emission line flux coincident with a superluminal jet component passing through the radio core in 3C 454.3. Other sources have observed similar behavior, too [134]. In addition to Very Long Baseline Interferometry (VLBI) and VHE gamma-ray observations, the location of the emission region within the jet can also be inferred using correlated variability. For instance, it's common to observe a correlation between the GeV gamma-ray and optical bands in FSRQs (see, [135]), although simultaneous flares in X-rays and gamma-rays are less frequently observed. However, it's important to note that observing simultaneous flares in two bands does not necessarily determine the exact location of the emission region. Instead, it merely indicates that at least a part of the emissions in these bands originate from the same region.

Assuming that the primary blazar zone in FSRQs is indeed situated near the 43 GHz VLBI core - a region located several parsecs from the central black hole, it is plausible that the dusty torus could supply the seed photons for Compton scattering [136]. However, this becomes complex when we consider sources like PKS 1510-089. In this case, the radius of the dusty torus is estimated to be around 3.2 parsecs [137], while the 43 GHz VLBA core is located at a distance of 6.4 parsecs. On the contrary, the SED of PKS 1510-089 - from near-infrared (IR) to VHE gamma-rays - is well described by an external Compton model where the dusty torus is considered as the primary source of seed photons [138, 139]. This presents a complex scenario for understanding the exact role of the dusty torus.

Suppose the main blazar zone occasionally situates itself beyond the BLR and the dusty torus. In that case, the seed photons required for Compton scattering might likely originate from a slower outer layer, or sheath, surrounding the jet, as suggested by [140]. Additionally, observed from the reference frame of the faster inner jet, this slower outer layer would appear to be moving toward the inner jet. Thus, its radiation would be enhanced by a similar Doppler effect that amplifies the resultant radiation we observe. Some observational evidence suggests that such a structure might exist in FSRQs [141, 142, 143]. For instance, [132] modeled such a scenario for PKS 1510-089 and found it provided a comparably good description of the observed SED. However, this model required the magnetic field strength in the emission region to be extremely low. A more detailed blob-sheath model was presented

by [142], where a localized enhancement within the jet sheath (a shocked segment/ring) provides seed photons for Compton scattering.

As previously discussed, BL Lacs with low and intermediate synchrotron peaks share some attributes with FSRQs and HSPs. Their SEDs do not exhibit substantial Compton dominance as seen in FSRQs; instead, their two SED peaks are similar to HSPs. Some LSP sources display faint emission lines, signifying the presence of a BLR, a feature absent in HSP sources. For instance, faint broad emission lines have been detected in BL Lac itself [144, 145]. Moreover, many LSP/ISP sources show standing shock features within the jets. There is growing observational evidence that, in some instances, the gamma-ray emission region lies tens of parsecs away from the central engine [146, 147]. Under such circumstances, the only available seed photons would be either the synchrotron photons themselves or those emanating from a surrounding jet sheath. In HSP sources and those teetering between ISP/HSP categorizations, pinpointing the emission regions poses a significant challenge. Typically, jets observed in radio with Very Long Baseline Interferometry (VLBI) in these sources exhibit subluminal motion [148], and no distinct components seem to emerge from the VLBI core. Conversely, these sources frequently emit bright VHE gamma rays, and the observed flux and variability necessitate high Doppler factors, suggesting that the VHE gamma-ray emission region is not the one we observe with VLBI. As a result, we have limited constraints for its location. We do know that VHE gamma-ray emission occurs concurrently with the X-ray emission, as most sources demonstrate correlations between X-rays and VHE gamma-rays with minor or no time lag (see, [149, 150]). The optical emission originates from the combined VHE gamma-ray/X-ray region and partially from the VLBI core [151]. The emission region in AGN jets is traditionally assumed to be closer to the black hole than the VLBI core because SED modeling usually requires higher Doppler factors than those seen in radio observations. This suggests that the jet decelerates as it moves from near the black hole This interpretation aligns with findings such as those reported by [152]. Another possibility involves a spine-sheath structure [140], wherein the spine emits the VHE gamma rays and X-rays, while the sheath is observable in the radio band.

In summary, the last decade has greatly expanded our understanding of the location of the blazar zone, establishing the existence of multiple zones. In FSRQs and LSP/ISP sources, the principal site often aligns closely with the 43 GHz VLBI core. However, this paradigm is challenged by observations of gamma-ray flares that occur independently of activity in the 43 GHz VLBI core (see, e.g. [153]), suggesting a more complex relationship between the emission regions. This discrepancy underscores the difficulties in universally positioning the emission region far from the black hole, also in the context of models used further in this thesis, where the emission region from FSRQ is located closer to the black hole. For HSP sources, the spatial relationship between the two (or possibly more) emission components, as observed in variability and SEDs, remains a subject of ongoing investigation.

2.2 Modeling

The aim of modeling the spectrum is to unveil the physical processes responsible for producing observed radiation. This approach allows for investigating various scenarios occurring at the source and testing which model is accurate. Moreover, it enables the imposition of certain constraints on the physical parameters describing the source.

In many cases, blazar emission is explained by a one-zone leptonic model by a relativistic electron population that is accelerated and radiates inside a spherical region [154]. This approach has been applied widely in modeling the blazar SED [155, 156]. In this approach, the low-frequency part is related to synchrotron radiation, while the higher energy part is connected to inverse Compton scattering. As models diverge from the one-zone approach, the number of free parameters needed to replicate the observed SED escalates. Hence, it becomes even more vital for these models to constrain some of the parameters directly from observational data. This section is based on a review paper [27].

2.2.1 Key blazar emission region parameters

Emission region

The emission region, for simplicity, is commonly conceptualized as a spherical blob populated with electrons whose energy distribution follows a smoothed broken power law in the simplest blazar emission model. This model describes the equilibrium spectrum, which emerges due to a combination of acceleration and energy losses. Consequently, there is a 'cooling break' in the spectrum, distinguishing between energies that cool at faster and slower rates:

$$N(\gamma) = K\gamma^{-n_1}\left(1+\frac{\gamma}{\gamma_{\rm b}}\right)^{n_1-n_2}, \gamma_{min} < \gamma < \gamma_{max}. \tag{2.7}$$

The distribution has a normalization K, slopes n_1 and n_2 below and above the break ($\gamma_{\rm b}$), and parameters such as magnetic field B, size R, and Doppler factor δ. If an external photon field is present, its luminosity also enters the calculation. There is some parameter degeneracy, as both a larger emission region and an increasing K result in higher luminosities for both SED peaks. The parameter degeneracy is present, as enlarging the emission region without altering the total normalization keeps the synchrotron photon emission unchanged, albeit with a reduced density, leading to a decrease in SSC efficiency. Conversely, an increase in K linearly boosts the synchrotron peak, while the SSC IC peak scales quadratically with K. Constraining these parameters from observations is essential, [157] described how γ_b, B, and δ can be solved from the frequencies and luminosities of the synchrotron and Compton peaks.

Variability time scale

The variability time scale of a source, t_{var}, constrains the size of the emitting region, $R \leq ct_{var}\delta(z+1)^{-1}$, where δ is the Doppler factor. The observed variability time scale is often the shortest in the gamma-ray band and longer at lower energies. To simplify SED modeling, the shortest time scale is usually used. VLBI observations can estimate the size of the radio-emitting region, which can then be used as the size of a larger emission region in two-zone SED models.

Doppler factors

Doppler factors, δ, can be calculated using radio observations [158, 159]. By comparing the observed brightness temperature ($T_{\rm b,obs}$) to the intrinsic brightness temperature ($T_{\rm b,int}$), often assumed to be the equipartition temperature $T_{\rm eq} \sim 10^{11}$ K [160], the Doppler factor can be estimated.

Studies focusing on FSRQs and radio-selected BL Lacs (mostly LSPs) found average Doppler factors of 14.6 for FSRQs and 6.3 for BL Lac objects [159]. Another study with a larger sample of sources observed by the Owens Valley Radio Observatory 40-m Telescope at 15 GHz found a median Doppler factor of approximately 11 for blazars [161]. However, tension exists between the observed Doppler factors and those used in SED modeling, particularly in the case of fast VHE gamma-ray flares. This discrepancy, known as the Doppler factor crisis, is especially prominent for HSP sources. SEDs cannot be modeled with Doppler factors as low as those derived from radio observations. Several solutions have been suggested, such as non-steady magnetized flows [162], decelerating jets [152], and spine-sheath models [140].

The fast flares imply Doppler factors greater than 50 ($\delta > 50$) because otherwise (at the assumption of the emission region filling the whole jet cross-section), the emission region would not be optically thin to $\gamma-\gamma$ absorption. For example, in the case of PKS 1222+216, fast variability requires $\delta = 75-80$ [121, 163], while VLBI observations suggest $\delta \sim 10$ for the jet [164]. The selection of appropriate values of δ is crucial due to the strong dependence of spectrum on δ; even a small change significantly impacts the resulting spectrum.

Magnetic field strength

The magnetic field strength B in blazar jets can be estimated using various methods, such as VLBI core shift measurements, which assume the equipartition of energy between particles and magnetic fields.

In a study [165], the median magnetic field strength for a sample of 18 BL Lac objects was found to be $0.4^{+0.3}_{-0.1}$G, and for a sample of 84 FSRQs, $0.9^{+0.2}_{-0.1}$G. These estimates were derived for a distance of 1 pc from the central black hole. However, the equipartition assumption has been questioned, particularly for BL Lac objects. Another more robust method to derive magnetic field strength directly from VLBI observations, without assuming equipartition, is possible by measuring individual components' spectra, size, and Doppler factors. This approach was used by [166] in their study of 3C 273, which resulted in an estimated magnetic field strength in the core of about 1 G. Nevertheless, performing such direct measurements can be challenging, and they have not yet been carried out for other blazars.

Low-energy cutoff

The low-energy cutoff of the electron spectrum, denoted as γ_{min}, can be constrained through circular polarization observations. If the circular polarization results from Faraday conversion, the amount of circular polarization can be used to estimate γ_{min} [167]. Modeling the full-polarization spectrum of 3C 279 allowed [168] to constrain the low-energy cutoff to $5 < \gamma_{min} < 35$. Values typically used in SED modeling range from 1 to 10^5 [120], a much wider range than derived from observations. High γ_{min} values ($\sim 10^4 - 10^5$) were initially suggested in [169] to explain the hard SSC spectra of extreme BL Lacs. Later, these values were used in an HBL source along with a soft spectral index above γ_b (n_2) to reproduce the narrow synchrotron peak and large separation between the two SED peaks [170]. A high γ_{min} ($10^3 - 10^4$) value has been supported by simulations of particle acceleration in relativistic shocks [171, 172]. However, due to the typically low fraction of circular polarization, it's challenging to study the circular polarization spectrum, hence observed constraints have not been widely used in SED modeling. Notably, the quiescent-jet model by [173] is an exception, suggesting the importance of accounting for the full jet emission in modeling attempts.

Energy density of the seed photon fields U_{BLR} and U_{DT}

FSRQs are unique among blazars in that they display strong emission lines in their observed spectra. These lines include Lyα, C IV, Mg II, Hγ, Hβ, Hα, C III, Fe II, and Fe III. Although not all of these lines are observed in every case, their typical line ratios are well-constrained, making it possible to calculate the BLR luminosity (L_{BLR}) from a few observed lines [174, 175]. Quasars usually have L_{BLR} values of 10^{43-46} erg/s, while BL Lacs have values of $10^{41.5-45}$ erg/s [174].

The luminosity and size of the BLR and DT must be known to determine the energy density of seed photon fields. The size of the BLR is typically estimated by scaling from the disk luminosity [176], which is generally estimated from UV data [177]. In contrast, the luminosity of the DT is challenging to determine directly due to the dominance of the non-thermal component in the IR SEDs of blazars. However, the presence of a hot dust component has been inferred in quasars such as 3C273 [178, 179], PKS1222+216, and CTA 102 [180].

The size of the DT can be constrained from theoretical considerations of the dust sublimation radius [181] and from reverberation measurements [182, 183]. These findings indicate that the inner radius of the dust-emitting regions of AGN is two to three times smaller than the theoretical value. The size of the dusty torus is typically estimated to be $1 - 5$ pc and scales with disk luminosity.

2.2.2 Modeling emission from AGN with agnpy

`agnpy` is an open-source Python package to model the jetted AGN's radiative processes [184]. The package is built entirely in the `numpy`, `scipy`, and `astropy` ecosystem, making it compatible with other data-analysis tools like `gammapy`. The package aims to extend the effort of modeling and interpreting the emission of extragalactic sources to a broader audience of astrophysicists. The software is developed to be accessible to the community, making reproducing or verifying results easier. This is particularly important as the next generation of gamma-ray instruments, CTAO, will provide valuable VHE gamma-ray information to broadband SEDs of various objects.

Rather than solving the differential equation regulating the development of the electron energy distribution (EED), `agnpy` assigns its maximum and break Lorentz factors using a simple parametrization of the acceleration, escape, and radiation processes. Throughout all the physical processes described

in the package, the angle of the jet axis to the observer line of sight, θ_s, is always considered among the model parameters, such that the use of `agnpy` is not restricted to the blazar case ($\theta_s \to 0$) but can also be extended to radio galaxies.

The `agnpy` allows the modeling of thermal and non-thermal radiation emission from various components of AGN. The `agnpy.emission_regions` module describes the emission regions responsible for non-thermal radiative processes. These regions contain the EED expressed as the distribution of Lorentz factors, γ, of the electron-positron pairs accelerated in the source. Recently, the proton synchrotron process has been added [185]. The `agnpy.targets` module describes line and thermal emitters that provide the photon fields targeted for inverse Compton scattering or $\gamma\gamma$ absorption. Various sources, including the AGN line, thermal emitters, or CMB, can produce these photon fields.

Non-thermal processes responsible for the broad-band emission observed in active galactic nuclei are described by synchrotron radiation and inverse Compton scattering mechanisms. The module `agnpy.synchrotron` computes synchrotron spectra (with the possibility of correcting it for the synchrotron-self-absorption), following [186]. The electron distribution is assumed to be immersed in a large-scale random magnetic field. The module `agnpy.compton` is used to calculate the inverse Compton (IC) scattering of photons. It considers two scenarios:

1. **Synchrotron Self-Compton (SSC)**: IC scattering of synchrotron photons produced by the same accelerated electrons. The SSC spectra are computed based on [186], and the target synchrotron radiation is assumed to be uniform in the blob, following [187].

2. **External Compton (EC)**: IC scattering of soft photon fields produced by an accretion disk, broad line region, dust torus, external to the jet, or by the Cosmic Microwave Background (CMB). The EC spectra are computed according to [188] and [189].

The full Compton cross-section, including the Klein-Nishina regime, is considered in both cases. The electron distribution is transformed to a frame comoving with the target photon field (in the case of EC) and then convolved with the energy distribution of the latter and the Compton cross-section. The head-on approximation is used, as in [58] and [190].

Using `agnpy`, it is possible to calculate the absorption caused by $\gamma\gamma$ pair production on the soft photon fields of various AGN components. This facilitates the evaluation of the model's internal consistency, explicitly examining whether the radiation field used for obtaining inverse Compton emission could absorb this emission. Additionally, `agnpy` offers the ability to calculate the absorption due to the EBL, which is particularly useful for studying distant sources. By incorporating these features, `agnpy` provides a comprehensive suite of tools for investigating AGN and the radiation they emit.

The interrelationships between `agnpy` modules and the computations they perform are presented in Fig. 2.7, providing a comprehensive overview of the underlying processes involved.

Computing the SED for a radiative process and fitting

To provide the integration of `agnpy` with other high-level data-analysis packages, `agnpy` has implemented, for each radiative process, a function that computes the SED. This function depends on the frequency and all the model parameters simultaneously (i.e., $\nu F_\nu(\nu;\theta)$, where θ is a vector of the model parameters that one aims to determine through some statistical procedure. Any fitting routine can easily wrap such functions, allowing the user to create an optimal fit model from any arbitrary combination of emission regions and radiative processes. Once the model is defined, users can choose which parameters have to be fixed and which ones are left free, depending on the completeness of their data set and information already available on the source. As an example, `agnpy` incorporates `sherpa` [191] and `gammapy` (see section 3.4.4) wrappers to fit broad-band emission from AGN. These wrappers take into account various radiative processes to form a `model` object, which can be utilized by the fitting routine of both packages [3].

[3] https://agnpy.readthedocs.io/en/latest/fit.html

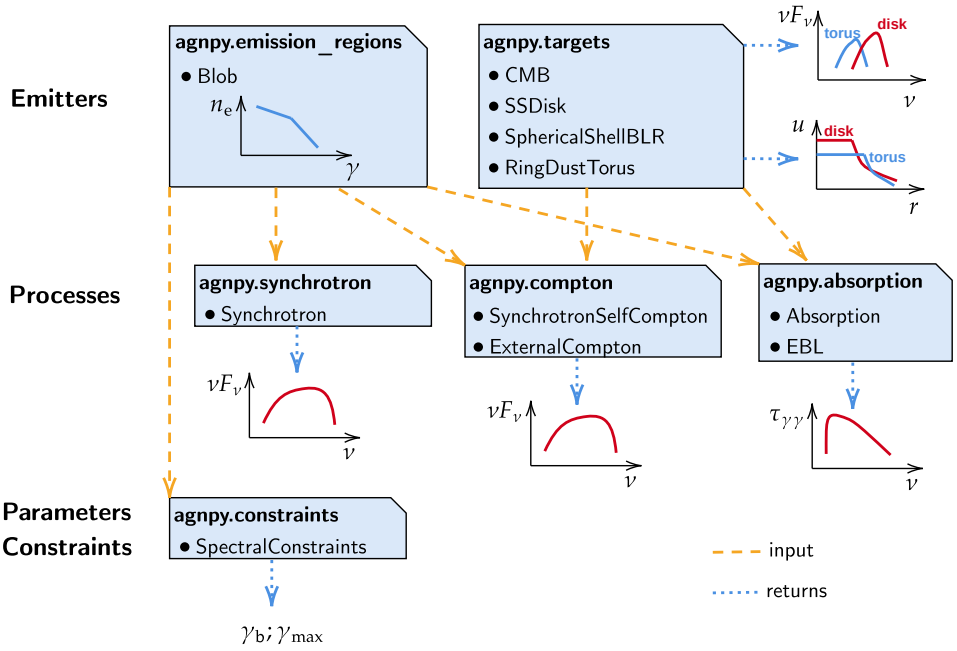

Figure 2.7: Components of `agnpy` and their functionalities. `emission_regions` describes the volume responsible for generating non-thermal emissions, including the (EED) and in the absorption module, to evaluate $\gamma\gamma$ absorption effects on synchrotron photons. This module serves as the foundation for various classes that simulate radiative processes and calculate their SEDs, such as `synchrotron` and `compton`. Additionally, `targets` comprise thermal and line emitters, which play a crucial role in external Compton modules and $\gamma\gamma$ absorption calculations within `absorption`. The class `targets` also enables the calculation of the targets' thermal SEDs and their energy densities (μ). Furthermore, the emission region is utilized in the self-consistent modeling class `constraints`. Source: [184]

Absorption

Two types of high-energy photon absorption can occur: internal and external. Firstly, photons can be absorbed via $\gamma\gamma$ pair production by the same soft photon fields that constitute the target for Compton scattering. Secondly, photons may be absorbed by the EBL on their path to Earth (see Section 2.1.3). To estimate the optical depth, $\tau_{\gamma\gamma}$, due to the former absorption mechanism, `agnpy` takes into account the soft photon fields of synchrotron radiation, the BLR and the DT, as well as a monochromatic point source behind the jet (this is mainly for test). As a result of photon absorption, the flux is attenuated by a factor $\exp(-\tau_{\gamma\gamma})$.

Absorption calculation on line and thermal emitters

The $\gamma\gamma$ absorption for a photon field with specific energy density $u(\epsilon, \mu, \phi; l)$ is given by [188]:

$$\tau_{\gamma\gamma}(\nu) = \int_r^{\infty} \mathrm{d}l \int_0^{2\pi} \mathrm{d}\phi \int_0^1 \mathrm{d}\mu \, (1 - \cos\psi) \int_0^{\infty} \mathrm{d}\epsilon \, \frac{u(\epsilon, \mu, \phi; l)}{\epsilon m_e c^2} \, \sigma_{\gamma\gamma}(s), \tag{2.8}$$

Where:

- $u(\epsilon, \mu, \phi; l)$ is the energy density of the target photon field with ϵ dimensionless energy, (μ, ϕ) angles, l distance of the photon;
- $\cos\psi = \mu\mu_s + \sqrt{1-\mu^2}\sqrt{1-\mu_s^2}\cos\phi$ is the cosine of the angle between the hitting and the absorbing photon;
- $\sigma_{\gamma\gamma}(s)$ is the pair-production cross section, with $s = \epsilon_1 \epsilon \, (1 - \cos\psi) \, / \, 2$ and $\epsilon_1 = h\nu \, / \, (m_e c^2)$ the dimensionless energy of the hitting photon.

While it's possible to consider arbitrary viewing angles in the calculation of optical depths using `agnpy`, it's worth noting that the notation used in the code is optimized for the case where photons travel parallel to the jet axis ($\mu_s \to 1$), as presented in [189]. This simplifies the integration by decoupling the cross-section and the $(1 - \cos\psi)$ term from the integral in ϕ. However, it's important to remember that the optical depths obtained using this method are valid for any jetted AGN.

A strong absorption in the radiation field can lead to a cutoff in the gamma-ray spectrum. The cutoff energy of the gamma rays depends on the distance r from the emission region to the black hole and the density of surrounding photons. `agnpy` computes gamma absorption in the electron-positron pair production process across multiple photon fields, including the external (CMB, EBL) and internal::

- **PointSourceBehindJet** models a monochromatic point source behind a jet, mainly to confirm that energy densities and external Compton SEDs of more complex scenarios reduce to this simplified case at large distances, following research from [192] and [190].
- **SSDisk** represents a Shakura-Sunyaev type accretion disk, which is geometrically thin and optically thick [46].
- **SphericalShellBLR** models the BLR as an infinitesimally thin spherical shell, based on [189].
- **RingDustTorus** depicts the dust torus as an infinitesimally thin ring, also based on [189].

Fig. 2.8 displays the example energy densities (as a function of the distance from the black hole) of several photons computed using `agnpy`.

BLR multi-layer model

In modeling, the BLR is frequently simplified to be characterized by a single dominant emission line, specifically Lyα. This approach is valid for inner regions of the BLR. However, this assumption falters at the BLR's outer edges, where the physical separation of emission lines is the most important, altering the overall emission characteristics [189]. If the emission region lies outside the BLR, the difference in absorption between the single-line and 26-line models, as demonstrated in Fig. 2.9, becomes significant.

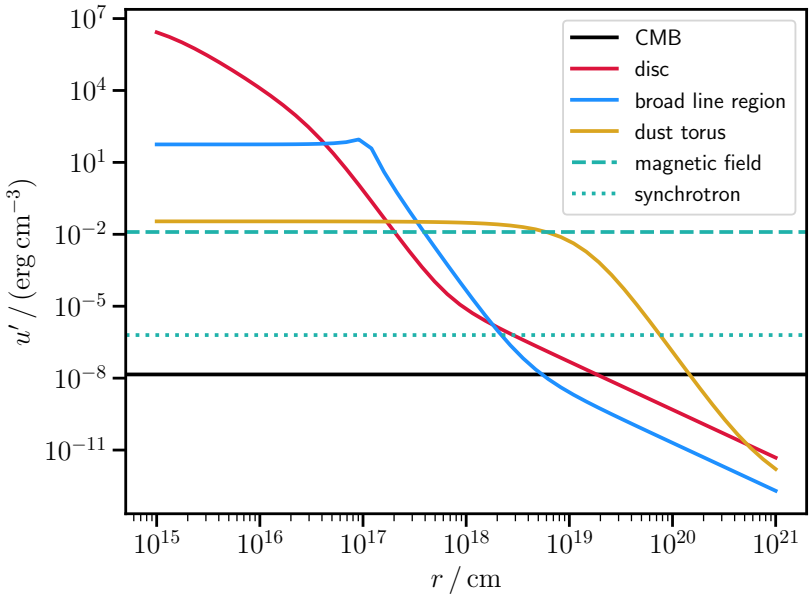

Figure 2.8: The example energy densities of different photon fields, computed with `agnpy` as a function of their distance from the central black hole, are presented. This includes the energy density of the accretion disk, depicted with a red solid line, the BLR in blue, the DT in yellow, and the CMB, shown with a black solid line. Additionally, for comparative purposes, the energy density of synchrotron radiation is shown with a green dotted line, and that of the magnetic field is shown with a green dashed line. The specific parameters used for these calculations are listed in Table B.1 (parameters for BT and BLR) and B.2 (parameters for blob and EED) in [184]. A BLR emitting the $Ly\alpha$ line has been considered in this context. Source: [184]

This has important implications for modeling the emission from FSRQs, which is the focus of my thesis research. As shown in Fig. 2.10, it is crucial to consider this to model the emission accurately. The absorption is similar when we are deep in the BLR, but as we move towards the edge, we start to see differences, especially at the low-energy part. If the emission region is beyond the BLR, we observe a big difference in τ.

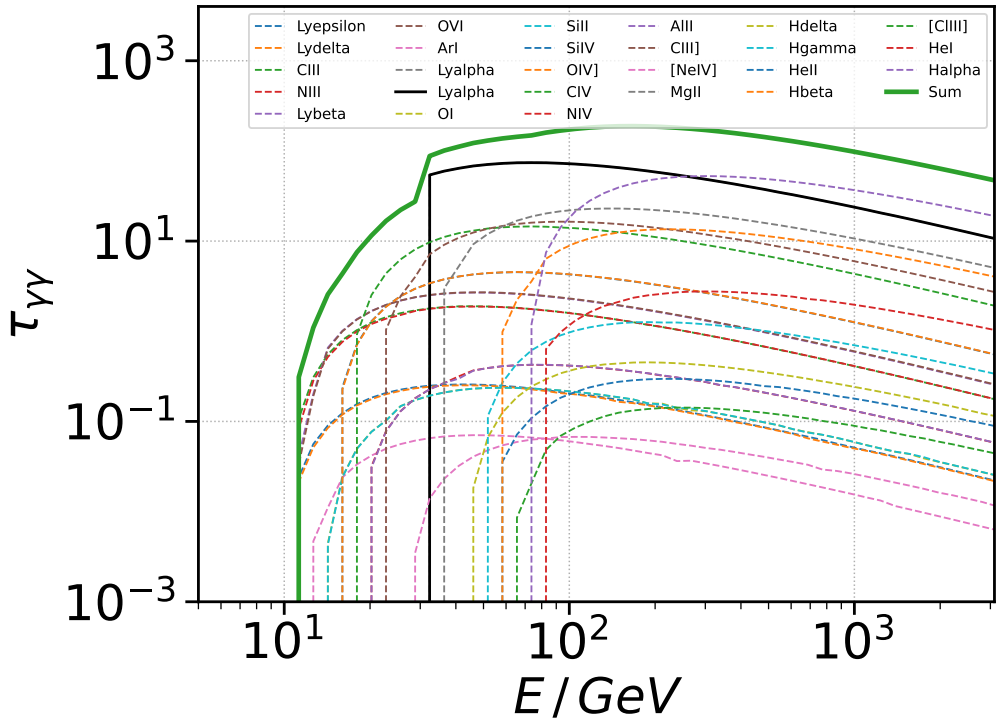

Figure 2.9: Optical depth $\tau_{\gamma\gamma}$ as a function of energy produced by the BLR calculated for $r = 0.75 \cdot R_\alpha$ based on the data for CTA 102 study further in the thesis (see chapter 5). The plot shows the contribution from the 26 individual lines; the strongest line, L_α, is represented by a solid black line. The sum of $\tau_{\gamma\gamma}$ of all the lines is shown as a solid green line.

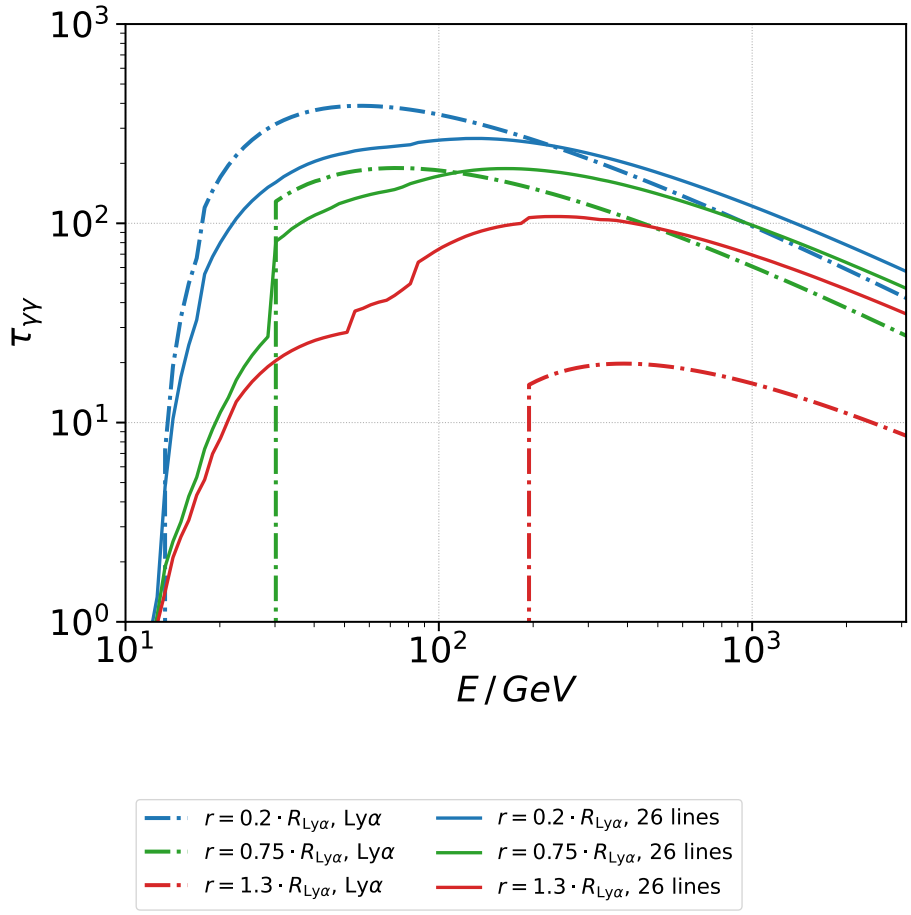

Figure 2.10: The change of the optical depth $\tau_{\gamma\gamma}$ with energy for different distances between the emission region and the black hole. The distances are normalized to the radius of the $\mathrm{R}_{Ly\alpha}$ line from the BLR. The dash-dotted line represents the optical depth calculated for a single line, while the solid line shows the result for a model consisting of 26 lines. As an example, this is shown for the CTA 102 study further in the thesis (see chapter 5).

Chapter 3

Imaging Atmospheric Cherenkov Technique

3.1 Cherenkov radiation and technique

The Earth's atmosphere, being opaque to gamma-ray photons, blocks their direct observation by ground-based telescopes. Atmospheric Cherenkov gamma-ray telescopes are designed to overcome this limitation by detecting Cherenkov radiation from air showers, which can be used in identifying the nature (gamma-ray or cosmic ray), arrival direction, and energy of the incoming particle. History of the last 35 years of development of the Chrenkov telescope can be found in [100].

This indirect detection method is pivotal for studying VHE radiation. A primary gamma-ray photon, upon interacting with an atmospheric nucleus, creates an electron-positron pair (e^+e^-) (see Section 1.6.2), which then emits additional gamma rays through Bremsstrahlung (see Section 1.5.3). When gamma rays with energy of the order of TeV hit the earth's atmosphere, it triggers an electromagnetic cascade and an EAS characterized by thousands of relativistic particles. These particles, when moving faster than the local speed of light in the atmosphere ($v > c/n_{\text{air}}$, where n_{air} is the refractive index), emit Cherenkov light. This light, which lasts for mere nanoseconds, has a distinctive UV-optical spectrum. Several factors, including the Night Sky Background (NSB), lunar illumination, and the Earth's magnetic [193] field—which can alter the paths of lower-energy particles—significantly influence the detection of the Cherenkov light.

Cherenkov light is emitted during the entire shower development, with peak emission coinciding roughly with the maximum particle count within the cascade. This typically occurs at an altitude of approximately 10 km for primary gamma-ray energies ranging from 100 GeV to 1 TeV [194]. Each particle generates Cherenkov light at a fixed angle θ_c to the direction of motion, given by equation 1.10. At sea level, the Cherenkov angle is approximately 1.3 degrees. The particles in the electromagnetic cascade also experience multiple Coulomb scattering, which slightly disperses their trajectories and contributes to the shower's lateral spread. Consequently, this creates a *pool* of Cherenkov light on the ground, where the photon density is about 100 photons per square meter for a 500 GeV gamma-ray primary as is shown in Fig. 3.1. The radial spread of this pool peaks around 130 meters, as shown in Fig. 3.1. This peak arises from a focusing effect caused by the varying Cherenkov emission angle at different atmospheric depths. The yield of Cherenkov photons scales with $\frac{dN}{d\lambda} \sim \frac{1}{\lambda^2}$, where λ represents the wavelength. Consequently, the spectrum is primarily characterized by blue/UV emissions, peaking near 340 nm. Emissions of shorter wavelengths are diminished by atmospheric absorption, especially by ozone, and only reach the ground if generated deep within the atmosphere, as with penetrating muons. The Cherenkov light from each air shower manifests in a short pulse lasting just a few nanoseconds. Though the time-averaged photon yield from all air showers is only 10^{-4}th of the ambient NSB [194], the illumination from a single shower can momentarily outshine the luminosity of the night's brightest celestial objects.

The Imaging Atmospheric Cherenkov Telescope (IACT) represents a sophisticated approach for

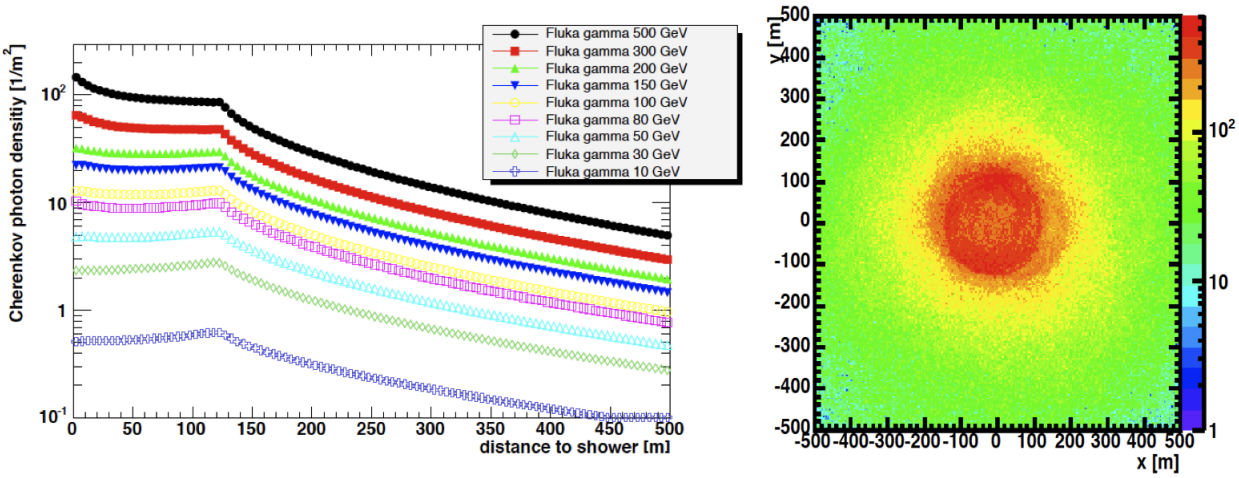

Figure 3.1: Monte Carlo modeling illustrating the distribution of Cherenkov photons on the ground due to gamma-ray-triggered air showers. The left graph depicts the density of Cherenkov photons relative to the radial distance from the shower's core across various primary energies. The right panel visualizes the number of photons per two-dimensional bin on the ground for an air shower initiated by a 300 GeV primary energy. Image attributed to G. Maier, source: [194, 195].

capturing VHE gamma rays. By recording the Cherenkov light from TeV particle cascades, IACTs provide invaluable insights into cosmic events. An optimally positioned telescope within this light pool can effectively capture the emitted Cherenkov light. As a result, even though the physical dimensions of current-generation IACT telescopes cover only a few hundred square meters, they can achieve an effective collection area for TeV gamma rays on the order of 100,000 m^2.

The IACT system is composed of five main components that work together to detect Cherenkov photons and convert them into an image of the particle cascade. These components include the mirror dish, the camera, the trigger, the drive, and the data acquisition system. The mirror dish collects the Cherenkov photons, and its size determines the energy threshold for the IACT's detection capabilities. By compiling these elements, the IACT can determine features of the particle cascade. The relationship between the zenith distance angle (ZD), effective area, and the energy threshold E_{thr} is characterized by the distribution and density of photons in the light pool produced. At low ZD values, the light pool's size shrinks, but the photon density increases for a given energy, thereby reducing the E-threshold. Conversely, when the ZD is high, the light pool expands due to the greater distance of the shower, causing a reduction in photon density for a specific energy. This results in a larger effective area at higher energies, particularly when observed with a single IACT or a small-sized array. Observations conducted at low ZD offer benefits for detecting low-energy photons due to the reduced absorption of the Cherenkov light with smaller atmospheric column density. As the ZD increases, the cascade initiated by the primary particle cascade occurs at higher altitudes, leading to more significant absorption of Cherenkov light and diminishing the detectability of such events.

One of the most important features of IACT (compared to the first generation of non-imaging Cherenkov telescopes) is the ability to construct images of EAS with telescopes' cameras. The light gathered by the telescope is focused on an optical plane composed of the order of 1000 photosensors (most commonly photomultipliers, PMT). The images of the shower captured by the camera allow one to construct the two-dimensional angular distribution of the observed light. Such images can be parametrized as ellipses, which facilitate the reconstruction of the properties of the primary particle [196], which will be described in more detail in 3.3.2. Due to the changing atmospheric refractive index with the height a.s.l., the long axis of the ellipse follows the longitudinal evolution of the shower and, the short axis is related to the latitudinal distribution [39].

Gamma-ray discrimination from isotropic cosmic ray background and event reconstruction is even more challenging than their detection by a telescope. The most successful approach used by most of

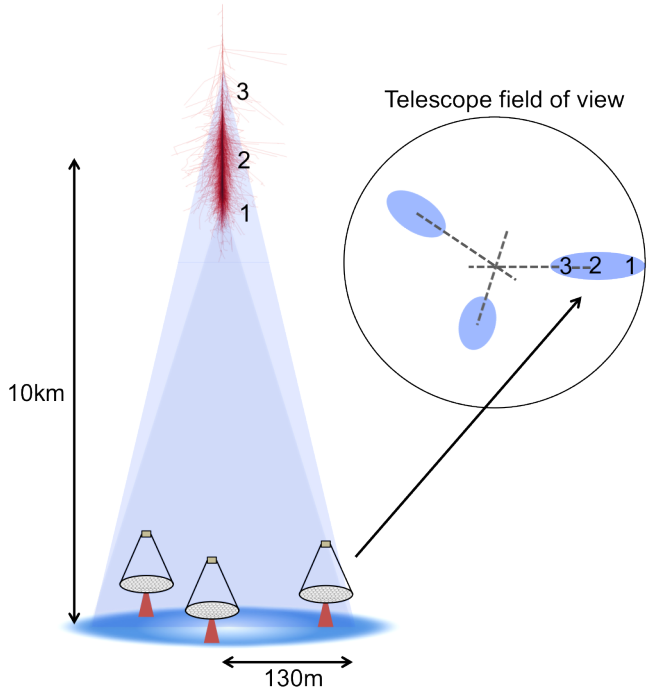

Figure 3.2: The stereoscopic imaging method. When a gamma ray initiates an electromagnetic cascade within the Earth's atmosphere, it produces Cherenkov radiation that forms a light pool on the ground. Telescopes positioned within this light pool capture an image of the shower, enabling the determination of the incoming primary photon's direction of arrival by crossing the main axes of all the images (see the inset panel). Source: [194]

the major facilities in operation today is the stereoscopic imaging technique; the main idea is to take two (or more) pictures of the same shower in Cherenkov light. Combining images of the same event seen by multiple nearby telescopes makes it possible to reconstruct the three-dimensional geometry of the event [197]. Additionally, a stereoscopic trigger is an efficient way of removing a background of single muon events both at hardware level [104] and during the analysis [198]. The principle of this is illustrated in Fig. 3.2

Since the first gamma-ray source detection of the Crab Nebula reported by the Whipple telescope in 1989 [199], IACTs have become by far the most successful instruments in ground-based gamma-ray astronomy[1]. The three major, currently operating stereoscopic IACT systems are H.E.S.S [200], MAGIC [103], and VERITAS [104]. The current generation of IACT arrays are characterized by an energy threshold of $\sim$ 25 to 100 GeV, a point-source integral flux sensitivity of 0.5 to 1.0% of the Crab Nebula flux in 50 hours (which is more than 100 times more sensitive than Fermi-LAT in 1 year at energies above 200 GeV), an angular resolution of less than 0.1 degrees, and an energy resolution of approximately 15% [201].

The description of Cherenkov methods for gamma-ray detection is presented in this chapter following mostly review articles: [194] and [201].

3.2 Cherenkov telescopes

In this part of the paper, I briefly describe the IACT experiments. I focus on MAGIC and LST-1 instruments since I participate in the collaborations that exploit them, and I report results from these telescopes in the next chapters of this thesis.

[1] In recent years, ground arrays such as HAWC or LHAASO have also begun detecting numerous sources, primarily galactic, in the energy range of tens of TeV [39].

The MAGIC telescopes [103], together with H.E.S.S. [200] and VERITAS [104], form the third generation of Cherenkov telescopes. This generation of instruments was the driving force in advancing Cherenkov astronomy at the beginning of the millennium, evolving from a developing field with only a dozen discovered sources to approximately 300 known sources to date [105]. LST-1 [202] represents the first instrument of the next generation of Cherenkov telescopes,

3.2.1 H.E.S.S

The High Energy Stereoscopic System (H.E.S.S.) has been operational since 2003 and is located in Namibia. The first phase of H.E.S.S. includes four telescopes, each with a 12m diameter reflector based on the Davies-Cotton design. These telescopes, standing at an altitude of 1800 meters, have been instrumental in advancing gamma-ray astronomy, particularly with their capability to detect gamma-ray fluxes as low as 1% of the Crab Nebula within 25 hours of observation[203]. The most essential aspect of the H.E.S.S. telescope is its location in the Southern Hemisphere. This provides an excellent view of our galaxy and, with its larger field of view, enables efficient sky scanning. H.E.S.S. has significantly contributed to the field by conducting the first detailed TeV gamma-ray survey of the Milky Way, discovering over a hundred different cosmic sources [204], measuring the energy spectrum of cosmic electrons beyond 600 GeV[205] and measuring the gamma-ray spectrum of the core of Centaurus A [206]. In its second phase from 2012, H.E.S.S. expanded its array with a 28m diameter telescope, the largest atmospheric Cherenkov telescope worldwide, enhancing the detection capabilities into the sub-20 GeV range.

3.2.2 VERITAS

The Very Energetic Radiation Imaging Telescope Array System (VERITAS), located at the Fred Lawrence Whipple Observatory in Arizona, consists of four 12m diameter telescopes designed for gamma-ray detection from 100 GeV to tens of TeV [207]. These telescopes feature alt-azimuth positioning, Davies-Cotton optics with 350 hexagonal mirrors, and high-precision pointing accuracy ($\pm 0.01^{\circ}$). The focal plane hosts a camera with 499 PMTs, achieving a field of view of 3.5°. VERITAS uses a three-level trigger system for enhanced background event filtering, achieving an angular resolution of 0.08° at 1 TeV. Notably, VERITAS has identified the starburst galaxy M82 and several active galactic nuclei as VHE gamma-ray emitters, showcasing its significant contributions to gamma-ray astronomy[208, 209, 210, 211].

3.2.3 MAGIC

MAGIC is a stereoscopic system with two 17 m diameter IACTs located at Observatorio del Roque de los Muchachos (ORM) on the Canary Island of La Palma [103]. The two telescopes were constructed in 2003 and 2009, respectively, with different cameras, triggers, and readout systems. In 2011-2012, the MAGIC collaboration undertook a major upgrade to make the stereoscopic system uniform, improving its overall performance and easing its maintenance [103].

The telescopes are designed to detect Cherenkov light from air showers initiated by gamma rays in the energy regime from around 50 GeV at low zenith angles [212] to more than 50 TeV. Due to such low energy threshold, they are well-suited for studies of high-redshift blazars.

The data can be taken with a standard trigger and with a special low-energy analog trigger called SUM-Trigger II (SUMT), designed to improve the performance of the telescopes in the sub-100 GeV energy range [213]. SUMT in a stereoscopic system allows the combination of the low energy trigger threshold with excellent background rejection. Usage of SUMT results in about twice the larger number of background counts (and thus also the volume of data). It also requires special analysis procedures to fully exploit its gain in the effective area. Therefore, it is used only with selected low-energy sources, particularly those located at high redshift values.

MAGIC telescopes, during 20 years of their operations, were used to discover the VHE gamma-ray emission of 52 out of 275 currently known sources (`http://tevcat.uchicago.edu/`, [105]). For example, in the last few years, the data obtained with the MAGIC telescopes have been used to report for the first time VHE gamma-ray emission from a GRB 190114C [9], showing the most significant

Figure 3.3: LST-1 during sunset.

case of association of gamma-ray emission with a neutrino [3], prove the hadronic emission of the gamma-ray emission in the nova RS Oph [214].

3.2.4 Cherenkov Telescope Array Observatory (CTAO) and LST-1

The Cherenkov Telescope Array Observatory (CTAO) is the next-generation ground-based observatory for VHE gamma-ray astronomy [215], designed to observe gamma rays within the 20 GeV - 300 TeV energy range. The LSTs are dedicated to observing the lowest part of the CTA energy range. Currently under construction, CTAO aims to surpass the sensitivity of existing imaging atmospheric Cherenkov telescopes by a factor of five to ten. CTA will consist of two separate arrays of IACTs of various sizes located at two sites: the ORM in La Palma, Canary Islands, in the Northern Hemisphere, and the Atacama Desert in Chile, in the Southern Hemisphere.

The largest telescopes within the CTA are the Large-Sized Telescopes [216], four of which will be part of the CTA-North array [217]. These LSTs will be equipped with 23-meter diameter mirror dishes, enabling them to detect faint Cherenkov flashes from air showers initiated by gamma rays down to approximately 20 GeV. The lightweight structure of the LSTs are designed for rapid slewing, making follow-up observations of transient events more accessible. LST-1, the prototype of the LST, was inaugurated at the ORM in October 2018 and has been taking sky data since November 2019 [218].

3.3 Observation and data analysis

The analysis of TeV data from IACT instruments can be divided into the following steps:

- low-level analysis: deals with calibration - reconstructed signal intensity and its timing of signals seen in individual photomultipliers.

- medium-level analysis: Determination of basic parameters of a single event detected by telescopes such as event type (gamma-ray or hadronic events), its energy, and arrival direction.

- high-level analysis: the individual events parameters are used to derive physical information about the source, such as the energy spectrum, morphology of the emission, or time variability.

The raw signal collected by Cherenkov telescopes consists of a digital record of the signal waveform in each camera photomultiplier. The first step in data processing is signal correction, the most basic being subtracting the pedestal value (the baseline signal value when the camera is closed) or more advanced correction depending on the readout system. A typical image produced by an EAS also includes electronic noise and NSB noise. Therefore, the next step is identifying those pixels in the camera that contain a significant (w.r.t. NSB) signal from the atmospheric shower. This is done by selecting pixels with signals above a set of thresholds and conditions. The cleaned image is then parameterized using the so-called Hillas parameters, which will be described in detail in the section 3.3.2.

3.3.1 Image cleaning

IACT images from particle showers always contain the background noise induced by photons of the night sky. An image-cleaning procedure is needed to reduce the participation of those noise photons in further analysis steps [219]. Only a tiny fraction of pixels carry the information from a gamma-ray shower. To achieve a low energy threshold and good low-energy performance, it is essential to determine which parts of an image are dominated by the signal from a cosmic shower rather than by noise. The brightest pixels in the image (above a given threshold) establish the core of the image. An additional condition is used to accept lower brightness pixels if they are neighboring one of the core pixels [220]; the remaining pixels are removed. Exploiting the signal timing significantly improves the reconstruction of low-energy showers [221] as it allows a decrease of the charge threshold with the same rate of surviving empty events.

The two most common types of image cleaning are tailcuts cleaning and SUM cleaning [222].

Tailcuts Cleaning, also known as Two-level Cleaning, is used for image cleaning when processing data in IACTs. It involves the following steps:

1. **Core Pixels Selection:** Initially, pixels with signals surpassing a higher threshold are selected. These pixels are considered the core of the shower image, indicating the strongest signal areas.

2. **Neighbor Pixels Addition:** Subsequently, pixels adjacent to the core pixels that exhibit signals above a lower threshold are incorporated into the image. This process is iteratively repeated, allowing the addition of neighbors of newly included pixels, provided they exceed the lower threshold.

3. **Isolation Removal:** Pixels not connected to the core region, such as isolated pixels or groups of pixels only above the lower threshold but not adjacent to any core pixel, are eliminated from the image.

This method effectively reduces noise by retaining only the relevant portions of the shower image, thereby enhancing the signal-to-noise ratio and improving the accuracy of shower reconstruction. The cleaning can be significantly enhanced if, in addition to the charge information also, the timing of the reconstructed signals in individual pixels is used [221].

SUM Cleaning is a technique that emphasizes the total signal within a group of neighboring pixels, applying a collective threshold rather than individual thresholds for each pixel. The method comprises the following steps:

1. **Signal Summation:** For each pixel, the sum of its signal and its immediate neighbors' signals is calculated. In order to avoid the sum being dominated by a single pixel with high charge (that could appear, e.g., due to afterpulsing), an additional clipping of the signals to a maximum value before the summation can be applied.

2. **Threshold Application:** A threshold is then applied to these sums. Pixels for which the summed signal exceeds this threshold are retained in the cleaned image.

3. **Noise Reduction:** This method effectively reduces noise by considering the sum of signals. It leverages that signals from Cherenkov showers are typically localized and exhibit correlated signals among adjacent pixels, distinguishing genuine shower signals from uncorrelated noise.

SUM Cleaning is particularly beneficial in scenarios with low signal-to-noise ratios, aiding in the preservation of weak shower images that might otherwise be lost by applying only individual pixel thresholds.

3.3.2 Hillas parametrization

Michael Hillas suggested the use of image parametrization based on their first and second moments, the approach that became known as the *Hillas parameters* to reduce the background [196] - a key milestone in the history of IACT [6]. One idea was to define parameters to quantify the observation that gamma-ray showers are more compact, concentrated, and aligned toward the source. This can be seen in Fig.3.4, which shows the Cherenkov footprint of a shower induced by gamma rays on the focal plane of a Cherenkov telescope. Certain inputs must be considered when analyzing an image from a Cherenkov telescope. These inputs include a list of cleaned pixels, the signal strength in each pixel, and the pulse time associated with each pixel. Parameterizing the image in this way simplifies the analysis and interpretation of the collected data, resulting in two sets of parameters: image quality parameters and Hillas parameters. Image quality parameters, including the number of islands and leakage, assess the overall health and integrity of the captured image. On the other hand, significant leakage suggests signal loss outside the intended region, which would likely worsen the reconstruction of the event. Hillas parameters describe the geometric characteristics of the signal distribution within the image, including width and length, typically extracted by fitting an ellipse to the signal region. These parameters are essential for distinguishing different types of events and characterizing their properties. Additional Hillas parameters include concentration and asymmetry, as well as source-dependent parameters such as Dist and *ALPHA*. Time parameters like time gradient and time RMS, as well as stereo parameters, notably the height of the shower maximum and impact point, are also commonly used in the analysis.

The Hillas ellipse is defined by several parameters, including the

- *size* (also referred to as *intensity*), which represents the total signal in all the pixels associated to the image.
- *centroid* is the coordinate of the center of gravity, represented by the x and y coordinates.
- The *main axis* is determined by the angle δ, which minimizes the signal-weighted sum of squared pixel distances and corresponds to the direction of the largest eigenvalue of the 2nd moment matrix diagonalization.
- The *length* represents the signal standard deviation (σ) along the main axis, calculated as the square root of the second central moment.
- The *width* represents the signal σ perpendicular to the main axis, calculated as the square root of the second central moment in that direction.

Several image quality parameters are also used to analyze Cherenkov telescope images. The *number of islands* represents the number of separate groups of pixels. A high number of islands might indicate the presence of noise or artifacts and is also typical of hadronic showers with multiple electromagnetic and muonic components. This parameter can also be used to characterize the quality of the cleaning process. *Leakage* is the fraction of signal in the last pixel ring of the camera and can characterize how the image leaks outside of the camera.

When performing single telescope analysis, several source-dependent parameters are commonly used, including:

- $ALPHA$: Angle between the main axis and the centroid-source line.

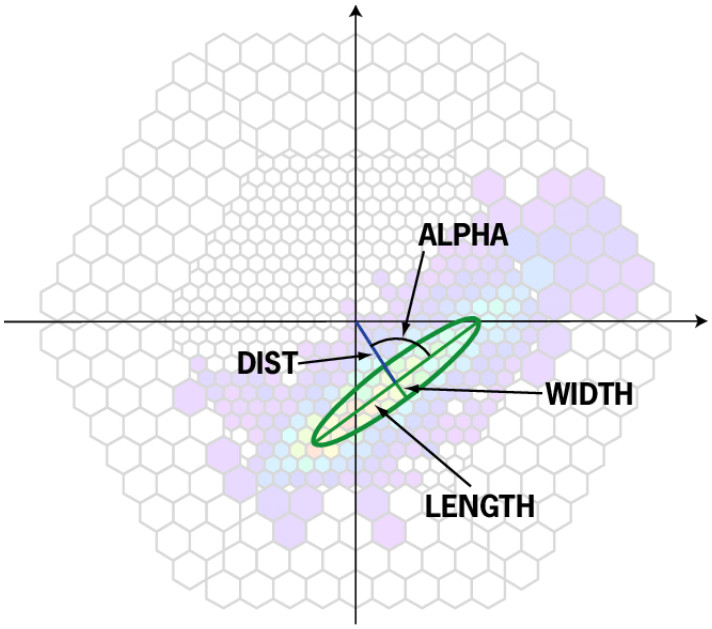

Figure 3.4: Quantifying an Air Shower Image Using Hillas Parameters. Source: [223].

- $DIST$: Distance between the centroid and source position.
- $MISS$: Distance between the main axis and the source position.

Gamma-ray astronomy uses Hillas parameters because they provide a robust and efficient method for discriminating between gamma-ray and cosmic-ray events, essential for reducing background noise and improving the sensitivity of ground-based gamma-ray observatories.

3.3.3 Random Forest

The Random Forest (RF) method can be used for energy estimation, reconstruction of arrival direction, as well as gamma-hadron separation. The RF method is a machine-learning algorithm that employs multiple decision trees to form a collective decision-making model (see, e.g., [224] for the application of RF in MAGIC). Other Cherenkov telescopes, including LST-1, also use the RF algorithm [202]. For each event observed by the telescope, data are characterized by a vector of parameters, including the well-known Hillas parameters. Additionally, observation-related parameters (e.g., zenith distance angle) are taken into account.

For the gamma-hadron separation, the two corresponding training samples are treated as a single labeled set, where each event is assigned a label, referred to as 'hadronness', indicating whether it belongs to the gamma class (hadronness = 0) or to the hadron class (hadronness = 1) [2]. Using these labeled samples, RF builds a binary decision tree that subdivides the parameter space, initially splitting it into two based on one of the parameters and then continuing this splitting process recursively. This approach helps efficiently classify the events by traversing down the decision trees based on the measured parameters of each event. The classification is average over multiple trees (of the order of 100) assigning hadroness value in between 0–1 for each event.

Apart from classification, the RF regressor allows the estimation of continuous quantities, such as the particles' energy, from the measured image parameters.

[2]Hadroness is used for the MAGIC analysis, while CTA is using gammaness = 1-hadroness

3.3.4 Identification of the gamma photons

Even for strong gamma-ray sources, cosmic ray showers are several orders of magnitude more numerous; even for a bright source, the factor can be as large as (10^3). Therefore, in IACT, effective separation of showers caused by cosmic radiation and those produced by gamma photons from the studied cosmic source is necessary. Images caused by gamma photons are typically narrower and shorter than cosmic ray images with a similar Cherenkov intensity and impact parameter. In the case of a single telescope, a simple selection of images with a small width and length forms the basis for distinguishing between different types of cosmic events. [225]. When multiple telescopes observe the same shower, the efficiency of this approach significantly increases. In this scenario, the location of the shower core, and consequently the impact distance from each telescope, can be determined with an accuracy of approximately 10 meters [194].

When the core location has been identified, the observed image width can be compared to the predicted width or length, referred to as width_{MC} or length_{MC} for images exhibiting identical Cherenkov intensity and impact parameter values. This comparison and the associated variability, σ_{mc}, emanate from detailed Monte Carlo simulations designed to investigate both the dynamics of the air shower and the telescope's detection capabilities. These predicted responses are systematically organized in look-up tables. Separate tables are constructed to reflect different observational scenarios, including variations in zenith angle and night sky luminosity. Additionally, these tables require updates whenever there is a change in the fundamental performance metrics of the telescope (such as changes in optical reflectivity or the point spread function) due to time-related degradation or maintenance activities.

Determining the arrival direction of the shower primary serves two main purposes: it allows for differentiation between gamma-ray photons originating from the source and the isotropic charged cosmic ray background; also, it aids in our understanding and representation of the gamma-ray emission. Pinpointing the direction of the gamma-ray emission is often important for identifying gamma-ray sources.

Within the telescope's field of view, the primary axes of the image ellipses converge at a point indicative of the primary particle's arrival direction, as shown in Fig. 3.2. This observation aids in estimating the arrival direction, typically using a weighting scheme that prioritizes the axes of the most luminous images [197]. The angular resolution achieved by this method varies based on energy. Typically 68% of the gamma rays from a point source are pinpointed to within $\sim 0.1^\circ$ of the source's location at energies near 1 TeV. However, fluctuations in the shower's development and a low number of Cherenkov photon data can diminish the resolution at lower energies.

3.3.5 Residual background estimation

After determining the arrival directions, any location within the field of view can be examined for potential gamma-ray emissions. This is done by choosing events that reside within a predetermined radius surrounding the test location. However, this task is made more intricate due to gamma-ray emissions from various points overlapping with mislabeled cosmic ray events in the background. To gauge the excess of gamma rays and determine the statistical significance of this excess, an independent assessment of the remaining background at each point becomes necessary. The background rate is determined by observing parts of the sky where minimal or no gamma-ray emission is present. This *OFF-source* areas can be identified in several manners: by dedicated studies of neighboring fields of view or, more frequently, by choosing zones within the same field of view positioned away from the test spot. Especially in the latter scenario, it's necessary to consider the differential detection efficiency across the field of view.

In the standard observations of IACT, the so-called *wobble-mode* is used [226]. In this method, telescopes are intentionally pointed slightly away from the source position, allowing for simultaneous observations of the source (the so-called ON) and background control (the so-called OFF) regions (see Fig. 3.5). This allows for the control of systematics associated with background determination and a more effective use of observation time. The choice of this offset is optimized based on two effects: a too-small offset may result in overlap between the ON and OFF regions, degrading background estimation; a too-large offset may significantly affect the source detection efficiency due to worse collection area at higher offsets from the camera center.

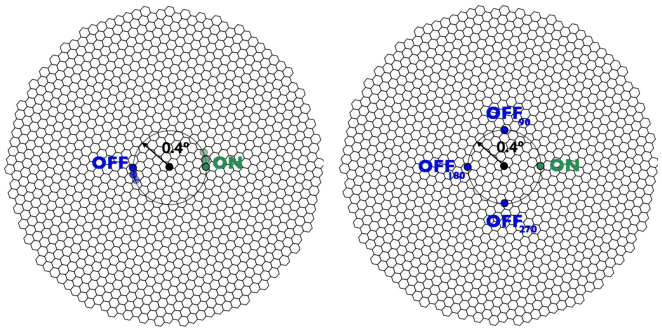

Figure 3.5: An illustrative representation of wobble mode observation: the telescope is pointed with a slight offset from the source and the background region, enabling simultaneous estimation of the background region—either singular (on the left) or multiple (on the right)—during ON-source observations. Image adapted with authorization from Dr. Ruben Lopez Coto's dissertation.

Multiple OFF regions can be selected depending on the source region's extension. The opposite position relative to the camera center is chosen for a single OFF position. Multiple OFF positions help in more precise (in terms of statistical uncertainty) background estimation. These positions are selected symmetrically around the source position to minimize inhomogeneity in the camera's field of view.

With the background established, it becomes possible to evaluate the gamma-ray excess at any given location and determine its significance. To estimate signals - the excess gamma-ray events from the assumed source and to calculate their significance, the squared angular distance between the nominal source position in the camera and the reconstructed source position is used. This quantity, referred to as θ^2, is then plotted. The background is estimated by plotting the θ^2 distribution in the OFF-regions, as illustrated in Fig. 3.6. The number of excess events is calculated after appropriate normalization in the region where no signal or excess is expected. The difference between the number of ON events and the number of OFF events determines this. The significance of the excess is typically calculated using the Li and Ma method Eq. 17 of [227].

3.3.6 Gamma-Ray photons: Energy, Flux, and Spectrum

The estimation of the energy of an incoming gamma-ray is based on the principle that the number of particles in the shower, and hence the Cherenkov photon yield, correlates directly with the primary energy. By assessing the intensity of the Cherenkov emission and taking into account the distance to the shower, one can derive an approximation of the gamma-ray energy [228]. The accuracy of this energy estimate is significantly enhanced with the use of multiple telescopes. They offer several observations of the shower's light output, along with a more precise determination of the shower's core location [229]. The energy estimation can be done using reference tables that indicate the expected gamma-ray energy based on impact parameters and Cherenkov intensity or RF method (described above). These tables are generated from Monte Carlo simulations, taking into account both the evolution of the shower and the telescope's responsiveness. Multiple tables are produced to account for varied observing conditions, such as zenith angle, background night-sky luminosity, and source offset within the field of view. Energy estimation, as well as gamma-hadron separation, can also be done with the random forest method

To convert the observed energy distribution of gamma rays from a source into a flux estimate or energy spectrum, one must evaluate the effective area of the detector. For IACTs, the effective area is defined by the extent of the Cherenkov light pool. This effective area typically exceeds $10^5\,\mathrm{m}^2$ at energies sufficiently higher than the telescope threshold energy. At lower energies, the trigger efficiency, and consequently the effective area, declines. To determine the energy-dependent effective area, one simulates gamma-ray showers spanning a full range of impact parameters, aligning with an energy distribution reminiscent of a typical source (for instance, a power law having an index of -2.0).

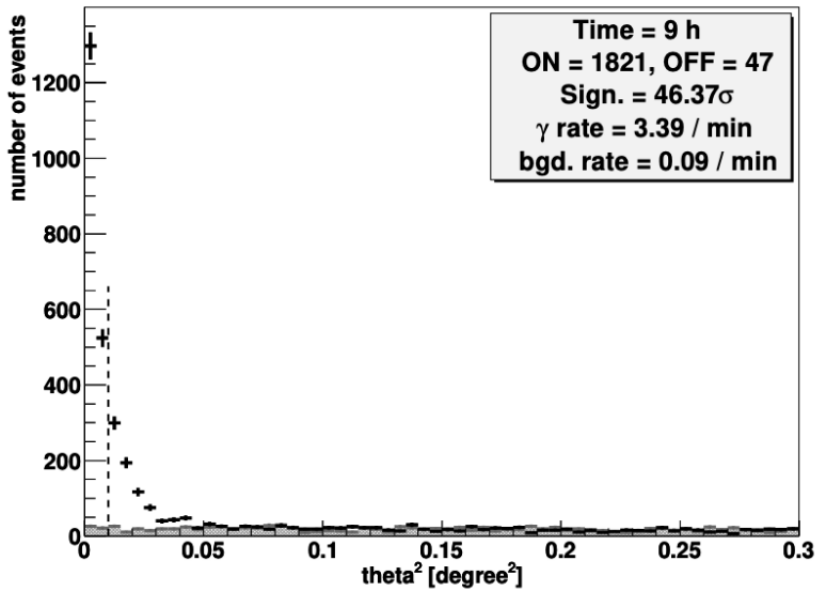

Figure 3.6: A characteristic θ^2 distribution oriented towards the Crab Nebula is presented, illustrating signal events (in black) and background events (in grey) exceeding an estimated energy of 300 GeV. The vertical dashed line indicates the θ^2 cut employed to assess the significance of the signal. This figure has been taken from [198].

The ratio of the count of triggered events to the simulated events, when multiplied by the area over which these events were generated, yields the (trigger level) effective area. A multitude of operating conditions, such as zenith angle and sky brightness, influences the effective area. Additionally, analysis parameters, including gamma-ray selection criteria and the specific analysis technique, further lower the effective collection area compared to the one evaluated at the trigger level.

An upper limit to the excess events can be set in scenarios without clear detection. An *upper limit* denotes the maximum value for gamma-ray flux allowed at a given confidence level consistent with the observed event statistics in the ON and OFF regions. It can be interpreted as the particular source is highly unlikely to produce gamma rays beyond this computed limit; otherwise, our equipment would have registered it. Such limits are customarily noted with a 95% C.L. (Confidence Level), suggesting that, hypothetically, in 95 out of 100 instances, the gamma-ray emission from the source would remain beneath this demarcated limit. To translate the excess (or the upper limit) into a measurement of the photon flux originating from the source (expressed in photons cm^{-2} s^{-1} or photons cm^{-2} GeV^{-1}), the energy-dependent effective area and energy migration matrix are required.

The energy distribution of reconstructed gamma-ray events from a source can be normalized by the energy-dependent effective area, allowing us to deduce the true energy spectrum of the source. Gamma-ray source spectra are smooth continua, typically well-fit by straight or curved power laws or by a power-law with an exponential cutoff. The spectra can be most straightforwardly parameterized by fitting a chosen function to the gamma-ray flux points. A more sophisticated approach is to perform a maximum-likelihood estimation of the spectral parameters, incorporating both the effective area and the energy-resolution function of the detector [230].

The ability of VHE gamma-ray tools to detect signals is measured by the lowest level of gamma rays they can pick up from an assumed origin, achieving a 5 σ level of statistical significance over an observation period of 50 hours. Fig. 3.7 illustrates the energy-dependent sensitivity differences (expressed in energy bins) between the "Alpha Configuration" of CTA arrays and the existing IACT generation. In addition, this figure includes sensitivity comparisons with orbital detectors (e.g., *Fermi-*

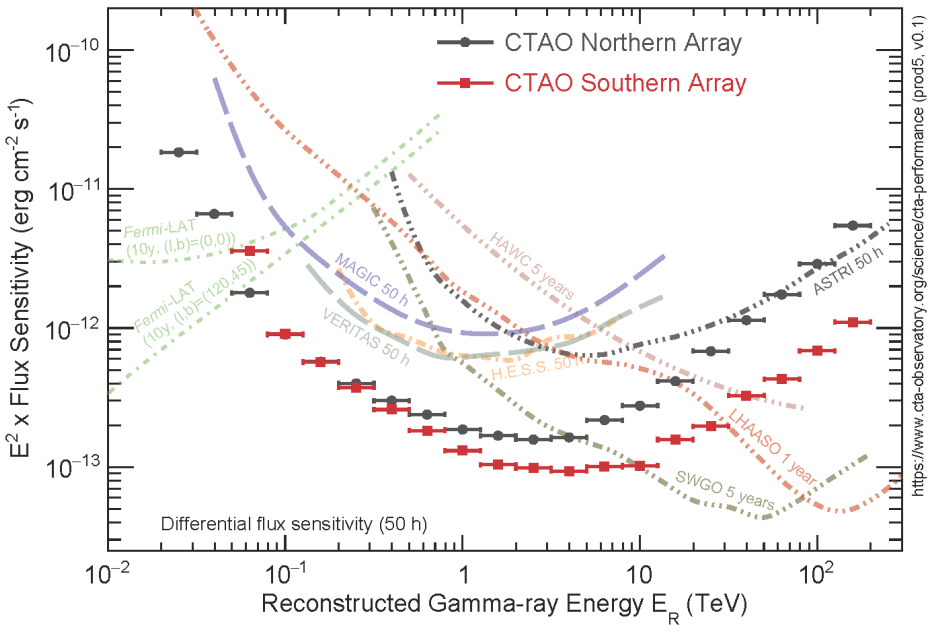

Figure 3.7: Differential flux sensitivity for various VHE gamma-ray instruments (see the legend in the plot). Source CTAO webpage.

LAT) and terrestrial particle shower array systems (e.g., HAWC) over various durations. Generally, detectors in space suffer from reduced efficiency in collecting gamma rays due to their smaller size, necessitating extended periods of data accumulation to observe a significant quantity of high-energy photons. Consequently, this results in diminished detection capabilities of orbital instruments for energies exceeding several GeV [201]. The performance of IACTs in terms of sensitivity begins to decline at energies approximately in the range of tens of GeV, a deterioration attributed to the inefficiency of gamma-hadron separation at these energy levels. A similar decline is observed at energies surpassing a few tens of TeV, where the sensitivity is constrained by the statistical number of photons emanating from the source.

3.4 Software for IACT data analysis

Data processing from raw waveforms (signal) in DAQ to physical results in the form of SED and LC, taking into account Monte Carlo simulations, requires specialized libraries.

3.4.1 ctapipe

The `ctapipe` is an open-source python framework for the processing of gamma-ray observatory data [231]. Designed to facilitate raw data calibration, image extraction, parametrization, and event reconstruction, it serves as a core package in the data processing pipeline for gamma-ray observatories. The software's primary objective is to transform pre-calibrated raw data into science-ready datasets, analyzing the intricate patterns of Cherenkov light emissions. A distinguishing feature of `ctapipe` is its integration of machine learning techniques, which play a pivotal role in event reconstruction, particularly in estimating the energy and type of primary particles. The framework uses a systematic approach, breaking down the analysis into sequential steps, from image extraction to the detailed reconstruction of primary particle properties. Its adaptability is showcased through a flexible configuration system, allowing for tailored analyses based on specific requirements.

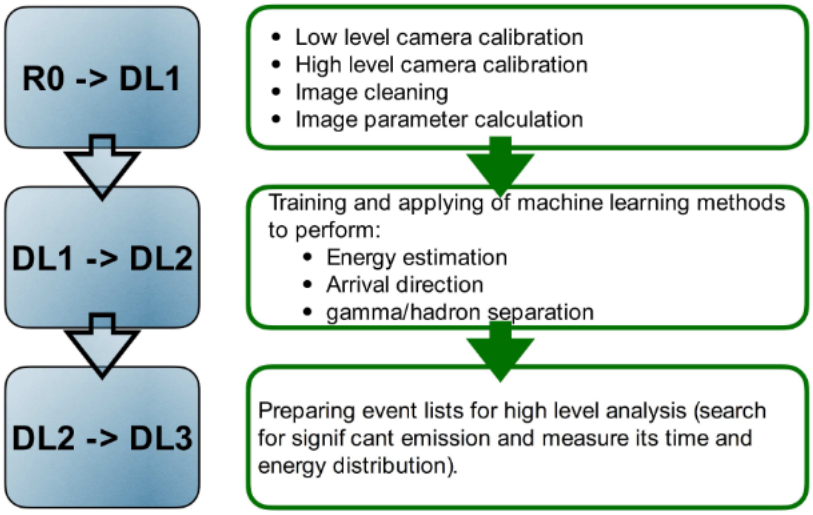

Figure 3.8: The analysis workflow for LST-1 data using `lstchain` involves processing the raw inputs through various stages to ultimately compile a list of gamma-ray candidates. Subsequent data analysis can be conducted using the existing suite of high-level gamma-ray analysis tools. Source: [232]

3.4.2 lstchain

The `lstchain` [232] is the dedicated pipeline software designed for data reconstruction from the LSTs. Drawing heavily from `ctapipe`, this software serves as a crucial foundation for devising low-level data processing techniques for the CTA. A visual representation of `lstchain` workflow is shown in Fig. 3.8. It commences with raw data (R0), progresses to pulse integration (after the low-level calibration), and subsequently calibrates these pulses into observed photoelectrons. A subsequent image-cleaning step filters out pixels, selecting those affected primarily by the shower rather than the ambient night skylight. The software then computes various image parameters, notably capturing moments up to the 3rd order related to the light distribution, resulting in the Data Level 1 (DL1). Employing Random Forest models—trained on Monte Carlo simulations—the software estimates primary energy, determines arrival direction, and discerns between gamma-ray candidates and hadron-produced images. When these models are used to process data, the aforementioned image parameters are merged with the reconstructed energy, directions, and gamma-ray likelihood, leading to Data Level 2 (DL2). Concluding the pipeline, an event selection phase filters for gamma-ray candidates, resulting in Data Level 3 (DL3).

The `lstosa` library [233], dedicated to automating the data processing sequence for LST-1 via the `lstchain`, significantly streamlines the on-site data reduction process. This automation allows the analysis to start with DL1 files.

3.4.3 MAGIC Analysis and Reconstruction Software (MARS)

The MAGIC Analysis and Reconstruction Software (MARS) [234] is a comprehensive software package developed by the MAGIC collaboration for analyzing and reconstructing data from the MAGIC telescopes. The software is developed in C++ and based on the ROOT framework[3], designed to process the data collected by the MAGIC telescopes. MARS includes algorithms for the reconstruction of

[3] https://root.cern/

shower images from raw telescope data, event stereoscopic reconstruction, background estimation, and extraction of physical information(light curve, SED, sky-maps).

The analysis process in MARS is carried out in several steps. First, the raw data is converted into ROOT format, and the signals from each pixel are calibrated. This involves correcting for baseline offsets and applying flat fielding and absolute calibration to convert the signal into photo-electrons (p.e.). Next, relevant pixels in the images are identified (image cleaning). The images are then parameterized using Hillas parameters to describe their orientation, shape, and timing properties. The stereoscopic shower reconstruction combines data from both telescopes to estimate the height of the shower maximum, impact parameters, and arrival directions of the primary particle. Background discrimination is used to distinguish between gamma-ray-induced showers and background cosmic-ray showers based on the Hillas, timing, and stereoscopic parameters using the RF method. The energy can also be estimated using the RF regressor or with look-up tables. The estimation of the shower direction is improved using a revised disp-method, which calculates the distance between the image center of gravity and the actual shower direction. Gamma-ray sources are identified by comparing the count of gamma-ray events to the estimated background. Finally, MARS estimates the differential energy spectrum of detected gamma rays and constructs light curves to study their temporal behavior. It also generates two-dimensional maps of the sky, indicating the arrival directions of gamma-ray events after processing and background subtraction.

3.4.4 Gammapy

`Gammapy` is an open-source Python package designed to analyze astronomical gamma-ray data [235]. It provides a method for processing and modeling data from various gamma-ray instruments, such as Cherenkov telescopes or *Fermi*-LAT space telescope. Built on the modern Python scientific ecosystem, it complies with established data conventions in high-energy astrophysics. Key features of `gammapy` include data reduction starting from event lists and instrument response functions, binning these data in energy and sky coordinates, and implementing several background estimation techniques to address residual hadronic background in gamma-ray instruments. After binning, it allows for estimating the flux and morphology of one or more gamma-ray sources using Poisson maximum likelihood fitting with various spectral, temporal, and spatial models. It also supports estimating flux points, likelihood profiles, and light curves.

Gamma-Astro-Data-Formats (GADF) is an initiative in gamma-ray astronomy aimed at standardizing the data format across various gamma-ray telescopes and instruments [236] [237]. After calibrating the data, gamma-ray data analysis software reconstructs shower events and separates gamma rays from cosmic rays. This results in lists of gamma-ray-like events, which, after considering instrument-specific response functions (IRFs), makes the derivation of scientific outcomes like spectra, sky maps, and light curves possible. Once the data is reduced to event lists with reconstructed properties of the primary particle, it achieves independence from the specific data reduction process and the detection technique employed. This level of universality facilitates the representation of high-level data from diverse telescopes, including IACTs, within a unified data model. The GADF initiative enforces a prototype specification for producing files in the Flexible Image Transport System (FITS) format [238], encapsulating gamma-ray-like events and associated IRFs. Python has gained immense popularity in scientific programming and data sciences in recent years. Its simple syntax, ability to integrate different programming languages, and a rich ecosystem of packages have particularly influenced computational astronomy. Projects like `astropy` and `gammapy` have emerged, with `gammapy` being a key tool in gamma-ray data analysis. `Gammapy` aligns with the GADF initiative, enabling various gamma-ray instruments to export data into a standard format for combined analysis. The public availability of GADF specifications and the `gammapy` package has led to the release of limited gamma-ray data sets by several collaborations, like H.E.S.S., MAGIC, HAWC, FACT, VERITAS, and Fermi-LAT. These releases facilitate validating and testing analysis tools like `gammapy`, marking a significant stride in collaborative and standardized gamma-ray data analysis. Such initiatives as GADF, complemented by software like `gammapy`, demonstrate the evolving landscape of gamma-ray astronomy, where data sharing, standardization, and collaborative tool development are increasingly central to advancing scientific discovery.

High-level gamma-rays data analysis with `gammapy`

The process of analyzing data in gamma-ray astronomy involves two stages. The first one, sometimes called low-level analysis, deals with the data processing from detector measurement, calibration, event reconstruction, and selection to yield a list of reconstructed gamma-ray event candidates, as described in the previous chapter. The next stage, high-level analysis, involves extracting physical quantities related to gamma-ray sources and producing high-level science products such as spectra and light curves. The core of the analysis consists of predicting the result of an observation by modeling the flux distribution of an astrophysical object and passing it through an instrument model.

The high-level analysis begins with DL3 files, where gamma-rays are expressed in the form of lists containing events and their corresponding IRFs, which are required to characterize how the instrument responds to gamma-ray of different energies. The DL3 data is usually structured into individual observations, each considered as a stable data acquisition period. In the case of IACTs, which are the focus of the GADF data model and `gammapy` software, these periods typically last between 15 to 30 minutes, and an LST-1 run takes a maximum of 20 minutes. Within DL3, the event list is a simple table where each row represents an individual event, and columns contain the measured properties of these events, such as reconstructed incident direction and energy, arrival time, and reconstruction quality. Once the DL3 data is collected, high-level analysis processes it further into DL5/6 to derive physically relevant quantities such as fluxes, spectra, and light curves of sources. The initial phase of high-level gamma-ray data analysis involves choosing and extracting a specific set of observations, a process guided by their metadata. This metadata encompasses details like the direction of the telescope pointing and the observation time. After the initial selection, the analysis process moves to data reduction. In this stage, events from observations and responses from the instrument are integrated into or mapped onto a standardized physical coordinate system, which is outlined by a specific map geometry. This geometry usually includes a spectral aspect characterized by an energy axis with defined bins and spatial elements. These spatial dimensions are responsible for translating celestial coordinates into a pixelized image space through a spherical projection or for defining a singular region in the sky. In the form of maps, the counts data and the processed IRFs are compiled into datasets, constituting the DL4.

The usual approach involves modeling the datasets through binned Poisson maximum likelihood fitting. By assuming that each bin follows Poisson statistics, the log-likelihood for an observation is calculated using the Cash statistics [239]

$$\mathcal{C} = 2 \sum_{i=0}^{K} N_{\mathrm{Pred,i}} - N_{\mathrm{Obs,i}} \ln N_{\mathrm{Pred,i}} \tag{3.1}$$

The expected number of events in the observation is determined by applying a source model through the IRF in a process known as forward folding:

$$\begin{aligned} N_{\mathrm{Pred}}(p, E; \hat{\theta})\ \mathrm{d}p\ \mathrm{d}E = & E_{\mathrm{disp}} \circledast \left[PSF \circledast \left(A_{\mathrm{eff}} \cdot t_{\mathrm{obs}} \cdot \Phi(\hat{\theta}) \right) \right] \\ & + Bkg(p, E) \cdot t_{\mathrm{obs}} \end{aligned} . \tag{3.2}$$

This formula integrates the IRF elements previously discussed and an analytical model of the assumed source emission. The model depicts the radiation intensity from gamma-ray sources, which varies according to the true energy E_{true}.

3.5 Monte Carlo simulation

The development of an atmospheric shower and the emission and propagation of Cherenkov light are usually simulated using CORSIKA [240, 241]. The atmosphere plays a pivotal role in the detection processes of IACT, yet its exhaustive characterization under controlled conditions remains inaccessible. Moreover, the evolution of atmospheric showers also presents significant challenges in accurately describing them through analytical models. In addition to these, issues related to signal reconstruction in individual pixels further complicate the scenario, making Monte Carlo simulations the most straightforward approach for evaluating the response of the telescope from cascades initiated by cosmic events with known attributes of primary particles. The telescope simulation contains the reflection of Cherenkov light on the mirror dish, transmission through the camera entrance window, and detection on the focal plane, which is equipped with light concentrators and photo-multiplier tubes (PMTs).

IACT image analysis is used to reconstruct the properties of the primary shower, such as particle type, energy, and direction. This analysis heavily depends on detailed MC simulations of the shower development and the telescope. The simulation enables training event reconstruction algorithms using events with known primary attributes, which are then applied to real data. An independent MC test sample is also used to derive Instrument Response Functions (IRFs). The simulation also factors in the laboratory-measured performance of telescope components, often including their dependence on photon wavelength and incident direction. Furthermore, the camera trigger system, electronic signal processing chain, and analog signal digitization are simulated to create digital waveforms, mirroring those in real LST-1 data post-correction for data acquisition electronics' low-level features. Although this method allows for applying the same analysis pipeline to both simulated and observed data, it is important to remember that Monte Carlo simulations do not replicate all the details of real data. Furthermore, the calibration process differs in `lstchain` pipeline: real data use the excess noise factor method, while simulated data employ a simplified approach based on assumed pulse parameters. However, in MARS (software used by the MAGIC telescopes), the excess noise factor method is utilized for both Monte Carlo simulations and real data [242].

3.5.1 Gamma-Ray and protons generation for LST-1

MC simulation data are organized into distinct sets: for the `lstchain`, simulations of two primary particle types, gamma rays, and protons, are used to train the event reconstruction algorithms of the LST-1 telescope. In contrast, simulations cover various zenith angles for all azimuths for the MAGIC analysis, reflecting a different approach to data handling and analysis.

To evaluate the telescope's response, while simulations include both gamma rays and protons, the IRFs are derived solely from the gamma-ray simulations. Gamma rays, the sample used for the training, were simulated by LST-1 collaboration with a differential energy spectrum adhering to $dN/dE \propto E^{-2}$. For vertical incidence showers, LST-1, an energy spectrum ranging from 5 GeV to 50 TeV, was used. The gamma rays' directions were isotropically distributed around the telescope's pointing, limited to an offset angle of 2.5°. In the test samples, the gamma rays were generated with a fixed angular offset of 0.4 deg from the telescope pointing direction, following simulation parameter settings that indirectly influenced the maximum impact distance, effectively capping it at 700 m for vertical incidence [202]. This approach was not only efficient but also ensured that the fraction of events not reproduced in the simulations remained negligible.

The LST-1 generated protons alongside gamma rays for the training sample. The energy spectrum for vertical incidence was restricted between 10 GeV and 100 TeV, considering that protons exhibit a lower Cherenkov light yield than gamma rays of the same energy. For vertical showers, the maximum impact parameter is 1500 m. The telescope pointing had an isotropic spread of directions within an 8° radius, also for vertical observations. LST-1's simulations of gamma rays and protons spanned a diverse range of telescope-pointing directions, extending to an approximate zenith distance of 70°. However, it is important to note that this range varies depending on the specific declination line, and for some lines, zenith distances greater than 70° were also simulated.

LST-1 used a methodology of pointings that were aligned with *declination lines*. These pointings were specifically designed to follow the trajectory in horizontal (Alt-Az) coordinates and trace all

sources at a specific declination, as observed from the LST-1 site. The primary objective behind this grid design was to train the algorithms efficiently, ensuring that they encompass all directions along the selected declination line. On the other hand, the test MC was structured in a grid combining zenith and azimuth values. For an individual IACT, the performance is predominantly influenced by the air mass and the orthogonal component of the geomagnetic field to the shower axis. This grid is used for LST-1 in calculating the IRFs for each node, subsequently interpolating them to derive the IRFs for any arbitrary telescope orientation.

3.5.2 Instrument Response Functions (IRFs)

IRF is a function describing how a telescope responds to the signal it collects [231]. In practice, IRFs are used to characterize and model the performance and behavior of instruments. The instrument's response to the gamma-ray signal is needed for Cherenkov telescopes to estimate the spectrum of a source emitting gamma rays. The description of a gamma-ray telescope's instrumental response is dependent on various factors, such as the instrument itself, the specific analysis being conducted, and the surrounding environmental conditions. An integral equation is typically used to transform the true properties of the gamma rays into observable quantities [231]:

$$\begin{aligned} R(p, E|p_{\text{true}}, E_{\text{true}}) = & A_{\text{eff}}(p_{\text{true}}, E_{\text{true}}) \\ & \times \text{PSF}(p|p_{\text{true}}, E_{\text{true}}) \\ & \times E_{\text{disp}}(E|p_{\text{true}}, E_{\text{true}}) \end{aligned} \tag{3.3}$$

where the components are defined as:

- $A_{\text{eff}}(p_{\text{true}}, E_{\text{true}})$, the effective collection area of the detector, is computed as the product of the detector's collection area and its detection efficiency at the true energy E_{true} and position p_{true}.
- $\text{PSF}(p|p_{\text{true}}, E_{\text{true}})$, the point spread function, provides the probability density of measuring a direction p given the true direction p_{true} and true energy E_{true}. For gamma-ray instruments, the radial symmetry of the PSF is a common assumption, which means that the probability density $\text{PSF}(\Delta p|p_{\text{true}}, E_{\text{true}})$ depends only on the angular separation $\Delta p = p_{\text{true}} - p$.
- $E_{\text{disp}}(E|p_{\text{true}}, E_{\text{true}})$, the energy dispersion, denotes the probability of reconstructing the photon at energy E when the true energy is E_{true} and the position is p_{true}. gamma-ray instruments often consider $E_{\text{disp}}(\mu|p_{\text{true}}, E_{\text{true}})$, representing the probability density of event migration, where $\mu = \frac{E}{E_{\text{true}}}$.

Additionally, the instrumental background, resulting from hadronic events misclassified as gamma-ray events, forms a uniform background against gamma-ray events. For instruments like *Fermi*-LAT, this residual hadronic background is negligible (less than 1%) due to the veto layer and is often overlooked. However, for IACTs and WCDs, this background can represent a significant portion (over 95%) of the events, requiring careful consideration in analyses. `Gammapy` typically relies on the background models supplied with the DL3 data, which generally only depend on the reconstructed event position and energy, $Bkg(p, E)$. Nevertheless, it is important to note that all IRFs can be influenced by the geometric parameters of the detector, such as the event's location in the Field of View (FoV) or the elevation angle of the incoming event direction. As such, IRFs might also be parameterized as functions of these detector-specific coordinates.

The LST-1 pipeline utilizes the `pyirf` [243] Python library for generating IRFs.

3.6 LST-1 low-level data analysis

The following section describes how the first stages of the analysis are applied to real cosmic data from the LST-1 telescope. As part of my doctoral thesis, I focused on developing methods for processing raw data, especially low-level calibration.

After the Data acquisition (DAQ) registers a signal from the cosmic shower, the data analysis pipeline of LST-1 `lstchain` takes in pre-calibrated raw data as time series data (waveform) for each

pixel for every event. It performs low-level calibration, such as baseline correction, delta time correction, and time arrival correction. Then, image extraction, cleaning, and parametrization are conducted.

3.6.1 Low-level waveform calibration

The LST-1 uses the Dragon readout system, developed at the Institute of Cosmic Ray Research (ICRR) of the University of Tokyo, which utilizes the Domino Ring Sampler version 4 (DRS4) chip [244, 245]. The LST-1's extensive mirror area captures NSB photons at rates up to several hundred megahertz (MHz) per pixel [216]. The Dragon system effectively samples incoming signals at around 1 gigahertz (GHz) [216], significantly enhancing the signal-to-noise ratio. The high sampling rate and sophisticated analysis methods are crucial in reducing the impact of noise from night sky background (NSB) and electronics, thereby improving the quality of data gathered by the telescope.

The LST-1 camera is composed of 265 modules, each containing 7 photomultiplier tubes (PMTs), resulting in a total of 1855 pixels. Each module contains 8 DRS4 chips for the signal reading, seven photomultipliers, a preamplifier, and a power supply. Signal readout from each pixel uses four channels of the DRS4 chip to provide the readout depth of 4 μs. For each pixel, the signal from the preamplifier is split into high-gain (HG), low-gain (LG), and a trigger line, with each both HG and LG signals. Upon triggering, an external analog-to-digital converter (ADC) digitizes the signal waveform (both HG and LG) [246]. Following an event trigger, only a fraction of the capacitors is read out, with each capacitor corresponding to 1 ns, typically saving 40-time slices (and excluding the first three and the last one capacitor because they are noisier due to the internal construction of the chip).

The LST-1's readout data system, based on the DRS4 chip, requires a series of software corrections to maintain low electronic noise. I developed these corrections at the beginning of my involvement with LST-1 in 2019. Over time, the data acquisition and analysis chain evolved, and the corrections are now integrated into the Data Acquisition (DAQ) system, occurring in real-time during data collection. During my doctoral research, I played a significant role in assessing the effectiveness of this online implementation. Additionally, I was responsible for integrating the time arrival correction for pulses into the `lst-chain`.

Baseline correction

Each capacitor in each DRS4 channel has its baseline value. This means that for the whole camera, $1855 \times 2 \times 4096 = 1.5 \times 10^7$ pedestal values are required. The differences in the mean value of the baseline value caused by the physical nature of the storage capacitor are much bigger than the standard deviation of the baseline of the individual capacitors. Therefore, they need to be taken into account to avoid a significant increase in the noise of the readout. Due to the internal construction of the DRS4 chip, there is a relatively big step in the baseline at capacitor 512 (in the middle of the readout DRS4 ring). The average pedestal value of each capacitor is used to correct the offset of individual capacitors. An example baseline of capacitors and waveform before and after applied correction is shown in Figure 3.9. These values are obtained from a dedicated pedestal run conducted every night, which is crucial for calibrating data collected during that night.

Each capacitor must be calibrated to achieve low electronic noise of the readout. The pedestal values are sensitive to the temperature of the readout. A dedicated pedestal run is taken to find individual capacitor pedestal values. For each capacitor, an average from all the values of the events that cover it is calculated. This mean baseline value can then be subtracted from the signal in a given capacitor. This correction is now performed online during the data acquisition process.

Δt correction

The pedestal value additionally depends on the last time this particular capacitor was read. Even after baseline correction, the signal in the waveform is not fully stable for randomly arriving triggers. Since each event is triggered at a different location in the DRS4 ring and only selected parts of the capacitor are read out, it can happen that the slice of the capacitor of the timely readout part has been read out later than the others. When it happens, the signal *jump* appears in the waveform shown in Fig. 3.10. The dependence of the pedestal shift as a function of the last reading time can be fit with power law;

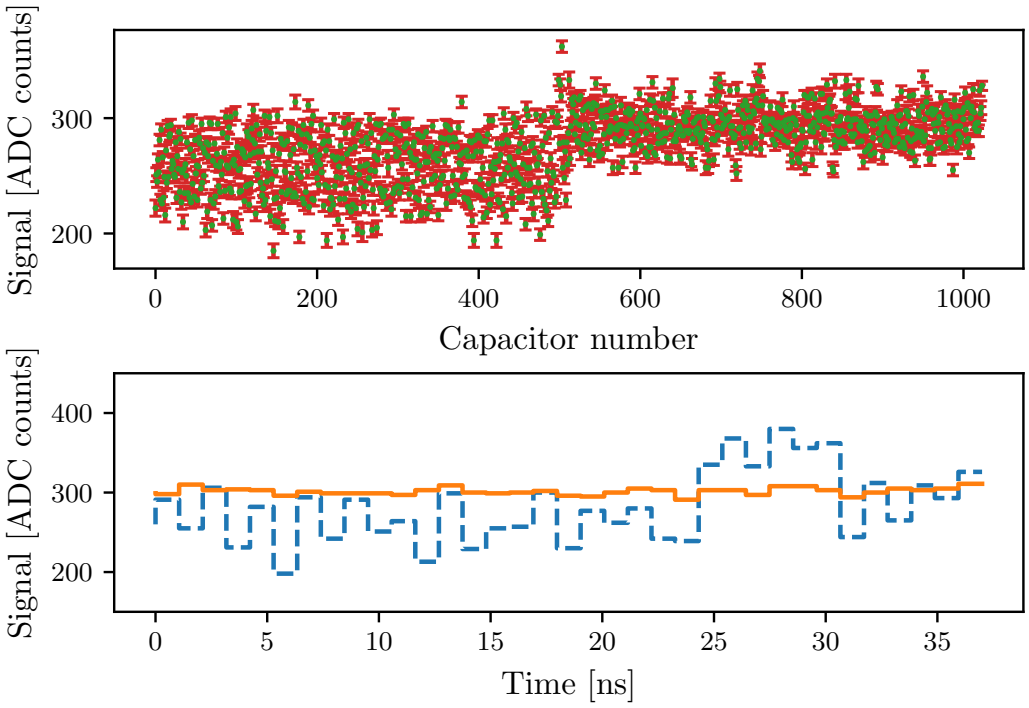

Figure 3.9: Top: Pedestal values of individual capacitors, with error bars calculated as standard deviation, for a single DRS4 channel (out of 4) for a particular pixel. Bottom: The electronic signal in the form of a waveform. The blue dashed line represents the raw signal from DAQ, while the solid orange line represents the signal after pedestal subtraction.

it depends only mildly on the capacitor/pixel, and there is additional dependence on the temperature. A power-law dependence is used for the correction as shown in Fig. 3.11. The pedestal subtraction takes the difference in the current and the last time reading of this capacitor and subtracts the value given by the power-law function. If the time difference is large, $> 10\,\text{ms}$, no correction is performed; the curve is very flat in this range, and the correction would be overestimated.

Non gaussian noise correction

In the signal readout, a signal spike (shown in the bottom signal waveform in the 3.10) is also associated with the DRS4 chip construction, which can be predicted and interpolated, or a predefined value of a typical spike can be subtracted. This correction is important because such spikes can mimic the signal from low-energy gamma rays.

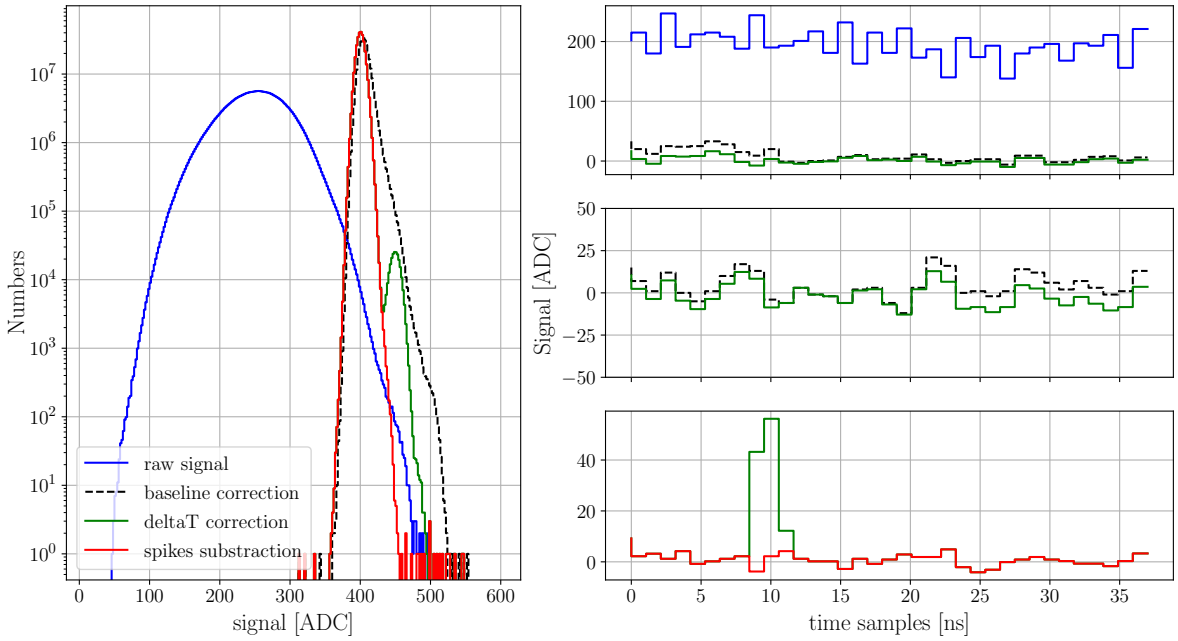

Figure 3.10: The left panel shows the distribution of electronic noise before and after applying signal corrections. The histogram shows the signal distribution after applying each correction. The right panel displays a few signal waveforms containing an example signal before and after correction. The top and middle waveform examples show baseline jumps due to time dependencies of read-out capacitors. The spikes in the waveform examples are predictable signal jumps due to the internal construction of the DRS4 chip.

Residual electronic noise

A reduction in signal noise is observed after applying the standard corrections on the signal performed during LST-1 operation. Initially, the standard deviation of the raw signal across all camera pixels is 42.1 ADC. This value decreases to 8.4 ADC following baseline subtraction. Subsequently, the ΔT correction further reduces to 6.1 ADC. The removal of the non-Gaussian component brings it down to 5.9 ADC. The results that were obtained are consistent with those observed during daily calibration runs [216]. The histogram in Fig. 3.10 depicts the resulting distribution.

3.6.2 Flat-Field calibration

Flat-fielding is a calibration process in Cherenkov telescopes that ensures a uniform and constant response from each PMT. This process is vital for defining a uniform background. Without such

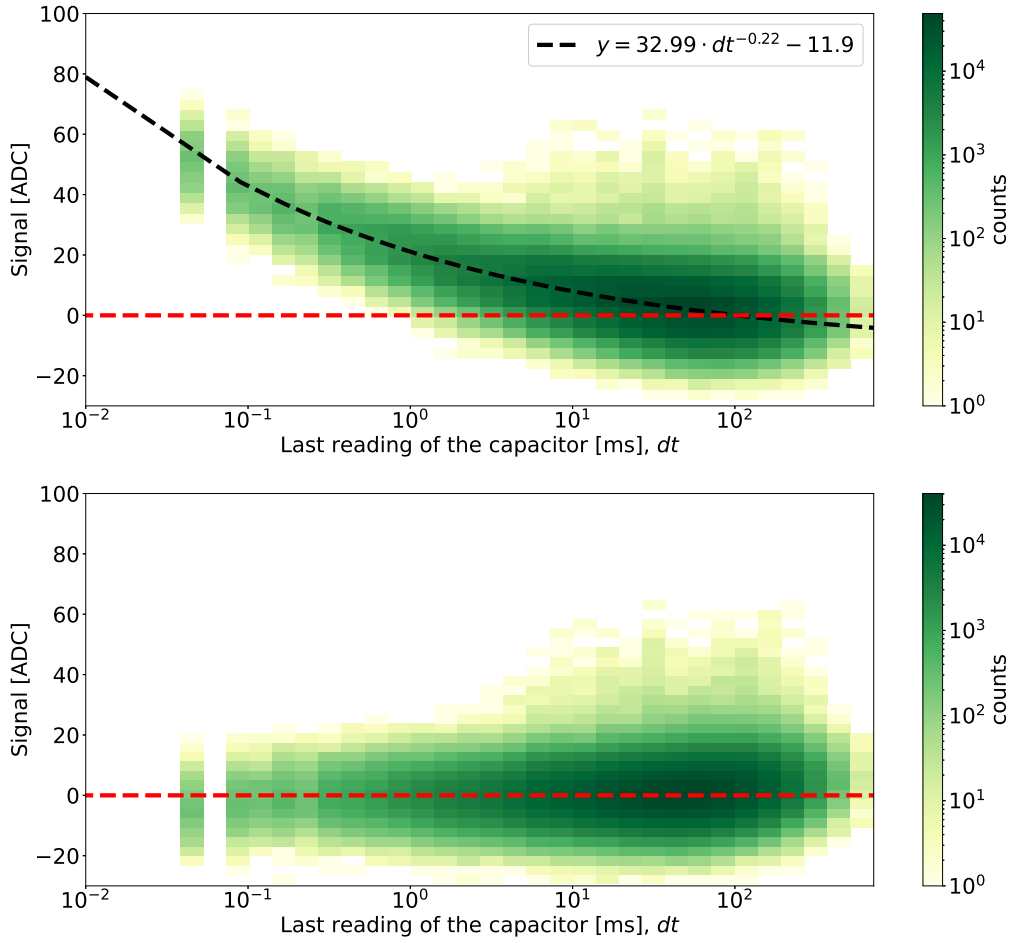

Figure 3.11: A 2D histogram depicting the relationship between signal intensity and the time lapse to the previous reading of this capacitor overlaid with a power-law curve representing the time corrections curve. The bottom part of the image shows the 2D histogram after these corrections have been applied.

relative calibration, the images would be less consistent and could be mistaken for hadrons. LST-1 cameras require consistent calibration over a broad dynamic range, accommodating up to 10^4 photo-electrons (p.e.) for each PMT [247].

The initial stage of the flat-fielding process involves exposing the entire detection surface of the camera to short pulses of uniformly distributed light source, which has been designed specifically for calibration purposes. Following this, each pixel's response to the uniform light is precisely measured for large (of the order of thousands) events. While it would be ideal for all sensors to produce identical outputs, variations are commonly observed in practice.

After measuring each pixel's response, calibration values are calculated to quantify how much each pixel's response deviates from the expected average. These values are use for adjusting the output from each pixel during telescope operation, which ensures that the data accurately represents the actual distribution of Cherenkov radiation across the field of view, without any bias.

The LST-1 camera calibration device, CaliBox, is equipped with a 355 nm UV pulsed laser and two filter wheels to guarantee adequate photon dynamic range for each PMT. The CaliBox produces light pulses that are 400 ps wide, with an adjustable rate between 1 Hz and 2000 Hz. A range of filters covers the dynamic range from 10 to 10^4 p.e. per PMT. The system also includes a trigger mechanism to coordinate with the camera at each laser shot [247].

3.6.3 Time calibration - correction of signal time sampling

Due to slightly uneven sampling of the DRS4, an additional time shift of typically 1 ns up to 4 ns occurs depending on the position in the DRS4 ring. Calibration pulses are used to calibrate differences in arrival time. Specific calibration measurements are carried out by introducing pulses from a laser to achieve time calibration. The average arrival time of the pulse is calculated as a function of the pulse position in the domino ring, which varies for different channels in the DRS4 chip. To obtain correction functions (coefficients) for each channel, a Fourier series expansion is utilized

$$y(FC) = B_0 + \sum_{i=1}^{N} \left(A_i \sin\left(\frac{i \cdot (FC \bmod 1024)}{1024} \right) + B_i \cos\left(\frac{i \cdot (FC \bmod 1024)}{1024} \right) \right) \tag{3.4}$$

where A_i and B_i are coefficients of the function's Fourier series expansion; N is the number of harmonics, and FC is the first capacitor position in the readout ring.

As seen in the figure 3.12, the curves for the pulse arrival time dependency on the position of the first capacitor in the DRS4 ring are unique for each pixel and vary depending on the DRS4 chip.

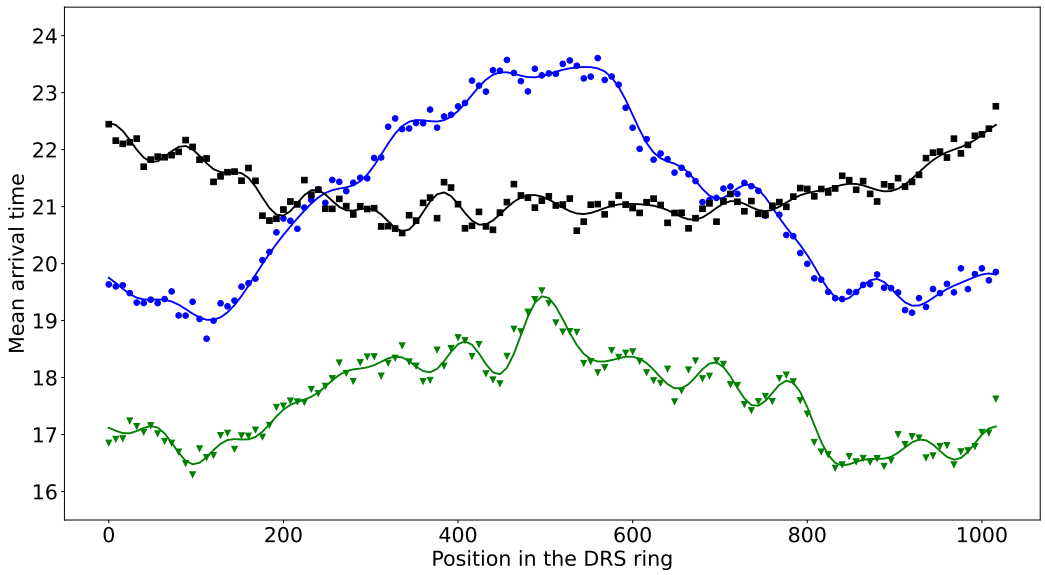

Figure 3.12: The relationship between the average pulse arrival time and its position in the DRS4 ring across 1024 capacitors, with a function curve fitted using a Fourier series expansion incorporating 16 harmonics for three different pixels.

Given that a single pixel in the Dragon signal readout system is processed by four channels from the same DRS4 chip, all channels exhibit identical delay curves. This consistency allows for the implementation of corrections based on the absolute position, calculated as modulo 1024 with respect to the first capacitor's read position in the DRS4 ring. To further enhance statistical accuracy, data from eight capacitors are aggregated, treating them as a single point in the analysis. This approach not only streamlines the correction process but also significantly improves the precision of statistical measurements.

Accurately determining the temporal evolution of the shower development is vital for analyzing the signal from the cosmic shower. Time calibration plays a significant role in determining the signal's arrival time, one of the key parameters used in the image-cleaning process. Furthermore, calculating the gradient of the pulse arrival time along the main line of the image helps determine the direction of the incoming primary particle and distinguish gamma photons from the background [221].

As part of my doctoral research, I implemented the functionality for calculating calibration coefficients and saving them in a binary file in the *cta-lstchain* code. Additionally, I wrote code that applies this correction in the LST-1 pipeline during data processing.

Pulse arrival time correction

In the readout system of LST-1, three types of time corrections can be distinguished:

- **pixel time** subtracted mean arrival time (from numerous events) in a given pixel. This achieves a time-flat fielding of different pixels of the camera.
- **curve time** involving subtracting the time from the given delay curve for a given pixel from the determined pulse arrival time. This improves the time resolution at the level of a single pixel. This is used in processing data.
- **trigger jitter** subtracted the mean arrival time in each pixel based on the mean pulse time from a given event.

Pixel time and curve time correction are used to process LST-1 data. In the DRS4 system, every pixel has a unique average pulse arrival time that is further influenced by its position within the ring. To

address this, I incorporate a delay curve in my calibration process to account for the positional effect. Having determined the delay curves based on the position of the first read capacitor, I apply curve correction to improve the temporal resolution of the pulse arrival time. To adjust for the mean arrival time of numerous events in a specific pixel, I subtract the mean arrival time base of many events for each pulse. Correcting both of these effects during calibration is crucial to ensure that all pixels have the same arrival time. Additionally, the trigger itself experiences a delay, resulting in a consistent shift forward or backward for all the pixels during readout. To address this, I subtract each pixel's mean time of particular events. This correction is not used in the data as the global time shifts do not influence shower image analysis but are utilized to verify the performance of the arrival time resolution after all the corrections.

Figure 3.13 displays a pulse arrival time histogram for two pixels, both before and after corrections. Figure 3.14 contains the same information for all pixels. These plots demonstrate that the time and curve correction of pixel time significantly improves time resolution, reducing the standard deviation from 1.78 ns to 0.91 ns. With additional jitter correction, the readout system's time resolution is approximately 0.4 ns.

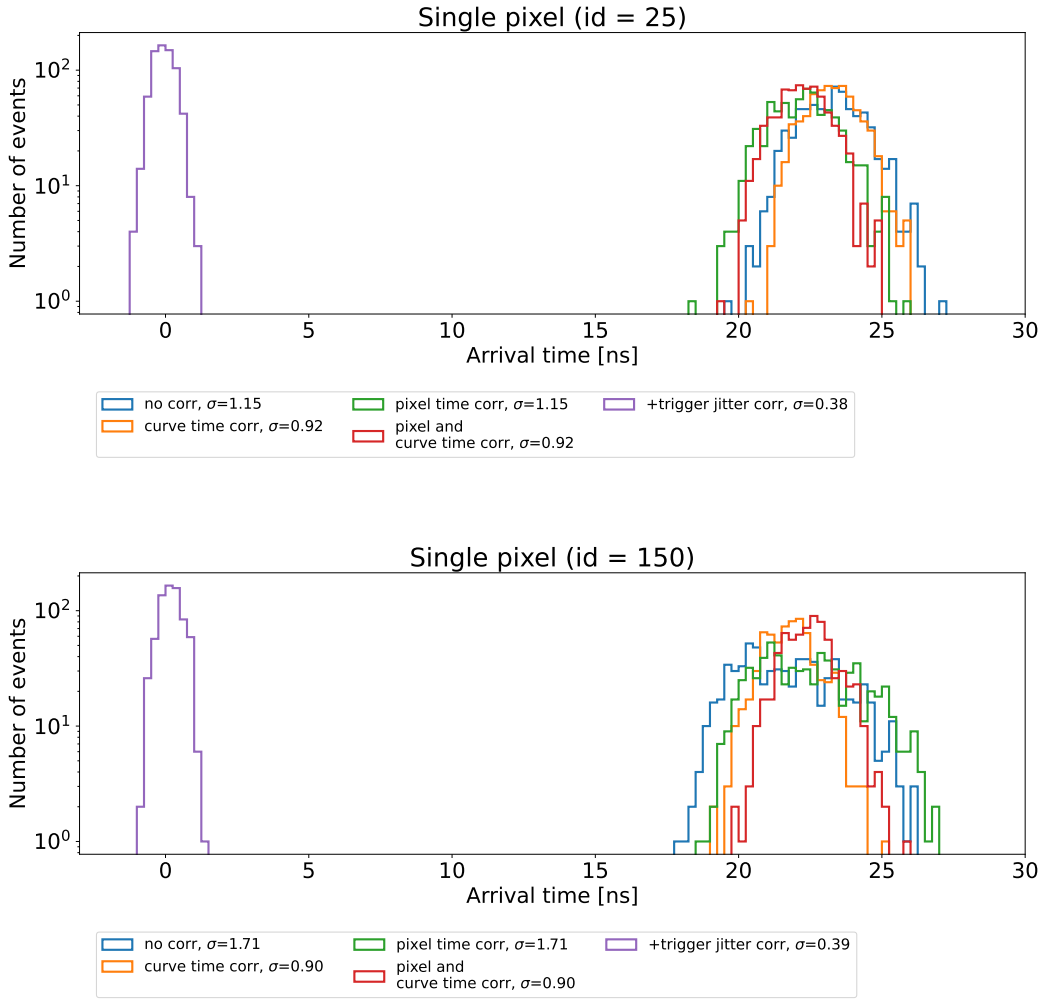

Figure 3.13: Histogram of arrival time for two pixels before correction and after correction, σ specifies the standard deviation of the distribution.

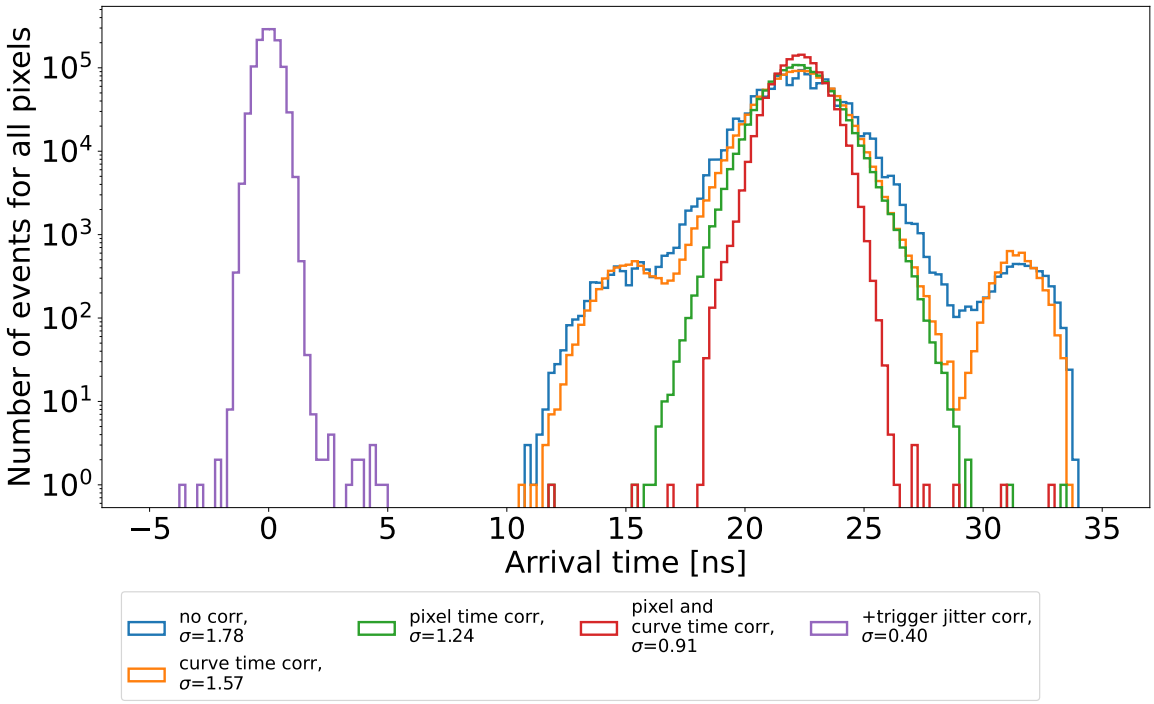

Figure 3.14: Histogram of arrival time for all camera pixels after different time correction stages.

3.6.4 Pixel-wise charge integration and image cleaning

The conversion from a charge in each waveform to its equivalent in units of a single photoelectron signal occurs using factors derived from calibration runs, utilizing the F-factor (also referred to as the excess noise factor) method [216]. In addition to the integrated charge, a signal arrival time for each pixel is computed using a basic charge-weighted average of the sample times, adding an essential temporal dimension to the data analysis. The signal processing in the form of waveforms involves an integration step, executed within a specific 8-sample window (equivalent to approximately eight ns), using the LocalPeakWindowSum algorithm from `ctapipe`. This window is dynamically selected based on the sample (s_{max}) with the peak value in the calibrated waveform, ranging from [s_{max} - 3, s_{max} + 4] [202].

After the preliminary calibration of the raw signal and converting ADC counts into photoelectron and charge integration, the subsequent phase involves image cleaning. This step is important as the majority of pixel signals are dominated by noise from the NSB, while only a limited subset of pixels contain signals pertinent to atmospheric showers. The cleaning process uses both the signal intensity and temporal information from each pixel to effectively distinguish and isolate relevant shower signals from the prevalent background noise. The image-cleaning process involves two approaches: one based solely on the signal strength and another that also incorporates the timing of the signals.

The function `tailcuts_clean`[4] is used to clean an image using a two-threshold tail-cuts procedure. The `tailcuts_clean` function is governed by several parameters. This method selects pixels based on picture core and boundary thresholds determined by the sky background (e.g., for moon time observations, higher thresholds are used). Essentially, pixels are retained if they meet two criteria: their signal exceeds the picture and boundary threshold, and they satisfy the specific time condition related to the neighboring pixels. The `picture_thresh` parameter sets the threshold above which all pixels are automatically retained. The `boundary_thresh` parameter determines which neighboring pixels are retained

[4] https://ctapipe.readthedocs.io/en/latest/api/ctapipe.image.cleaning.tailcuts_clean.html#ctapipe.image.cleaning.tailcuts_clean

based on their proximity to those above the picture threshold. The `keep_isolated_pixels` parameter dictates whether pixels above the picture threshold should always be included (`True`) or only if they have neighboring pixels in the picture or boundary (`False`). Lastly, `min_number_picture_neighbors` is an integer that specifies the minimum number of picture neighbors a pixel must have to be retained, though this is only relevant if `keep_isolated_pixels` is set to `False`.

The function `apply_time_delta_cleaning` [5] is also vital in refining image processing by focusing on the temporal aspect of pixel data. It operates on a pre-selected group of pixels, identifying those with fewer than a specified number of neighbors with arrival times within a certain timeframe. This function enhances the cleaning process by considering both the pixel arrival times and their spatial relationships. The `time_limit` parameter defines the allowable time window within which the arrival times of neighboring pixels must fall. This parameter helps identify selected pixels that have fewer than N neighbors arriving within this specified timeframe. This time delta cleaning is typically employed after the initial tailcuts cleaning. It provides an additional layer of refinement by considering the temporal relationships between pixels, further enhancing the quality of the image analysis.

Image cleaning and parametrization in LST-1

Pedestal cleaning is a process that enhances the cleaning efficiency by incorporating an additional condition that allows for dynamic computation of the threshold for each pixel. I have implemented and optimized this process within `lstchain`, and it is now an integral part of the standard analysis pipeline.. The process works as follows:

1. The picture threshold is dynamically adjusted to reduce noise in pixels with elevated background noise levels. This is achieved by substituting the default value with a pixel-dependent new threshold calculated as
$$\langle Q_{ped} \rangle + 2.5 \cdot \sigma_{Q_{ped}}, \tag{3.5}$$
provided this value surpasses the standard threshold of 8 p.e. Here, $< Q_{ped} >$ and $\sigma_{Q_{ped}}$ represent the mean and standard deviation of the reconstructed charge for the specific pixel, determined using interleaved pedestal events.

2. The next processing steps follow the standard `tailcuts_clean` method.

The final selection of pixels for inclusion in the image is made by applying additional criteria: a pixel must have at least two neighbors (from the initially pre-selected pixel set) whose signal arrival time differs by no more than two nanoseconds from its own.

I developed this new technique to enhance the image-cleaning process for the LST-1. To make use of the *pedestal cleaning* methods, it is necessary to have estimates of the threshold for each pixel. The *interleaved pedestal events* are events that contain only noise from the sky and electronics, which are collected at a frequency of 50 Hz. I calculate the pedestal value in each pixel from calibration events by:

- Retrieve the pedestal's mean value and standard deviation for the DL1 file.
- Check if there is a problem with the standard deviation values for pedestal events using monitoring data from data taking. If so, it uses the standard deviation values from the calibration run.
- Calculates the cleaning threshold based on the mean pedestal value and standard deviation.
- Searches for unusable pixels, likely due to dead pixels caused by stars in interleaved pedestal events; such pixels are removed from the analysis.

In Fig. 3.15, I show a map of the distribution of the threshold values for cleaning, calculated based on the average charge and standard deviation of the signal from the *interleaved pedestal events*. As the signal distribution map of the camera shows, images during observations of Galactic sources are

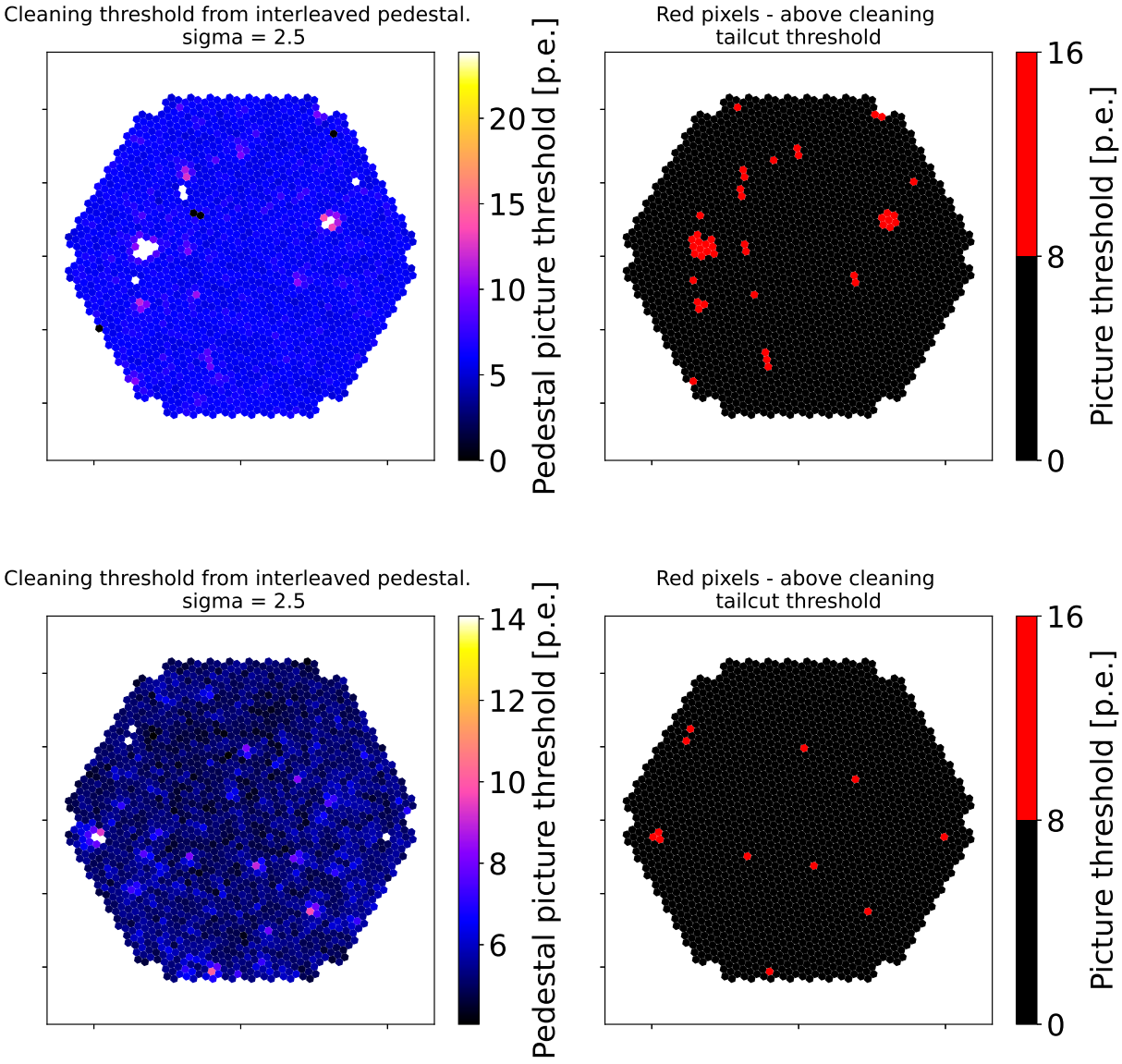

Figure 3.15: Example map of the distribution of the threshold values for cleaning. This image shows data for the Galactic (Crab Nebula, top image) and Extragalactic source (BL Lac, down image). In the field of view of the Crab, a strong star is a source of high noise. On the left side is the derived threshold value for each pixel in the camera. On the right side is a binary map showing which pixels have a higher value than the standard picture threshold cleaning value. Only for these pixels will the higher cleaning threshold be used.

more noisy compared to those of Extragalactic sources. This is expected both due to a higher level of diffuse NSB as well as the presence of individual bright stars.

A practical method for evaluating the performance of the image-cleaning algorithm is to analyze the probability of a pedestal event successfully passing through the procedure, which means it has at least three surviving pixels. This same probability can be used to identify any spurious noise events that survive the cleaning process and potentially interfere with the reconstruction of the shower image. By implementing the above conditions, it is possible to achieve a fraction of cleaning-surviving pedestal events that are less than $O(10^{-3})$, specifically in dark conditions using LST-1.

In Figure 3.17, I present several cosmic images processed using standard and *pedestal cleaning*. This comparison illustrates the significance of pedestal cleaning in effectively removing unwanted noise from the images, thereby demonstrating its importance in data analysis.

Assuming you have n images and the probability of each image surviving is p, the number of images that will survive follows a binomial distribution with parameters n and p.

The mean (expected value) of the number of images that will survive is:

$$\mu = np$$

The standard deviation for the binomial distribution is:

$$\sigma = \sqrt{np(1-p)}$$

The measurement error for the number of survived images is typically expressed in terms of the standard error, leading to the final expression for the percentage of surviving cases being $p \pm \sigma$.

To evaluate the effectiveness of image cleaning methods and determine the optimal parameters, I examine how many images containing only night sky noise and electronic noise were not completely cleaned. I aim to minimize this number, indicating effective noise reduction. However, overly aggressive cleaning could result in the removal of pixels from cosmic ray hits, which is undesirable. Balancing these two aspects is crucial for optimizing image-cleaning processes in LST-1 data analysis.

The plots in Fig. 3.16 display multiple curves, illustrating various aspects of pedestal event cleaning. These include the dependency of cleaning effectiveness on the chosen parameters, the utilization of temporal information, and comparisons between Galactic and Extragalactic sources. The parameters tested were picture thresholds of 6 and 8 and boundary thresholds of 3 and 4. I also implemented extra conditions for the picture threshold to eliminate the noisiest pixels. The incorporation of temporal information is shown to significantly improve the cleaning process efficiency. Additionally, the comparison demonstrates that Extragalactic sources, which exhibit significantly lower noise, allow for the use of less aggressive cleaning settings. For example, cleaning with a picture threshold of 8 and a boundary threshold of 4 proves similarly effective to a 6-3 setting with an additional sigma condition, particularly for these lower-noise sources.

I examined what pedestal cleaning approaches have an impact on image parameters. To illustrate the resulting variations, I presented various images processed with the standard tailcuts cleaning method and modified by information from pedestal events. In some instances, using the pedestal cleaning method leads to more effective noise removal, resulting in more accurate image parameter values, as demonstrated in Fig. 3.17.

Image cleaning in LST-1 summary

The standard cleaning settings currently utilized in LST-1 involve pedestal cleaning with a picture threshold of 8 and boundary of 4, along with a sigma value of 2.5 [218]. Additionally, delta time cleaning is used with a time limit of 2 seconds. According to a study conducted in this chapter on Galactic sources, the percentage of survived pedestal images from interleave calibration is less than 1%, while for Extragalactic sources, it is less than 0.1%. Therefore not only the fraction of noise-only events is very low, but also the shower images will very rarely be burdened by artificial islands.

[5] https://ctapipe.readthedocs.io/en/latest/api/ctapipe.image.cleaning.apply_time_delta_cleaning.html#ctapipe.image.cleaning.apply_time_delta_cleaning

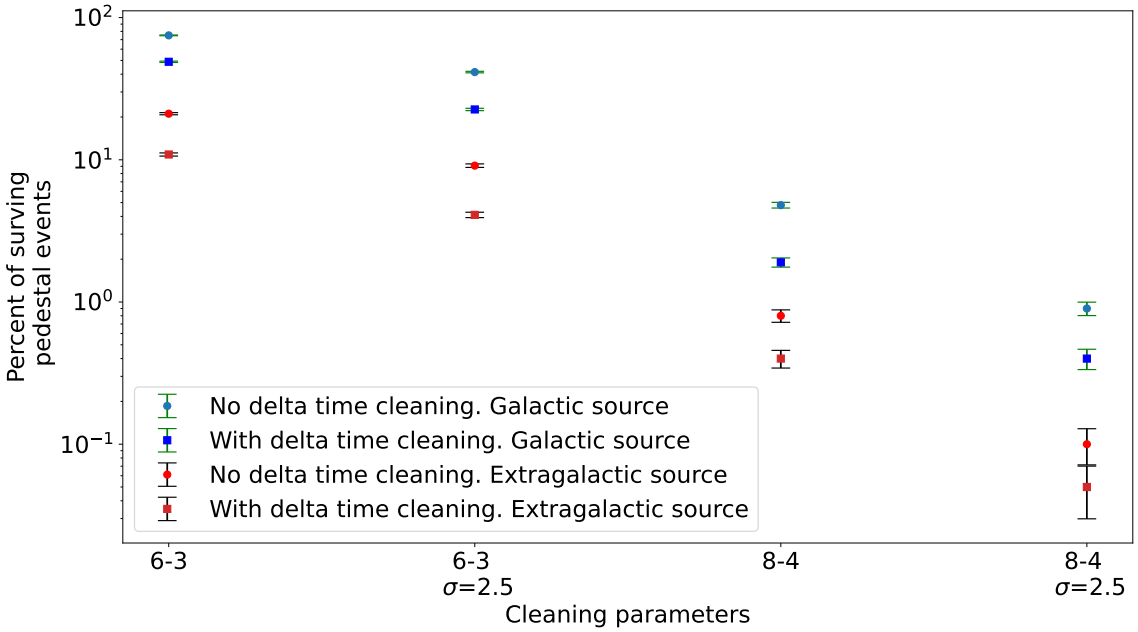

Figure 3.16: Efficiency of cleaning with various parameters for Galactic and Extragalactic sources with and without temporal cleaning (delta time = 2 ns).

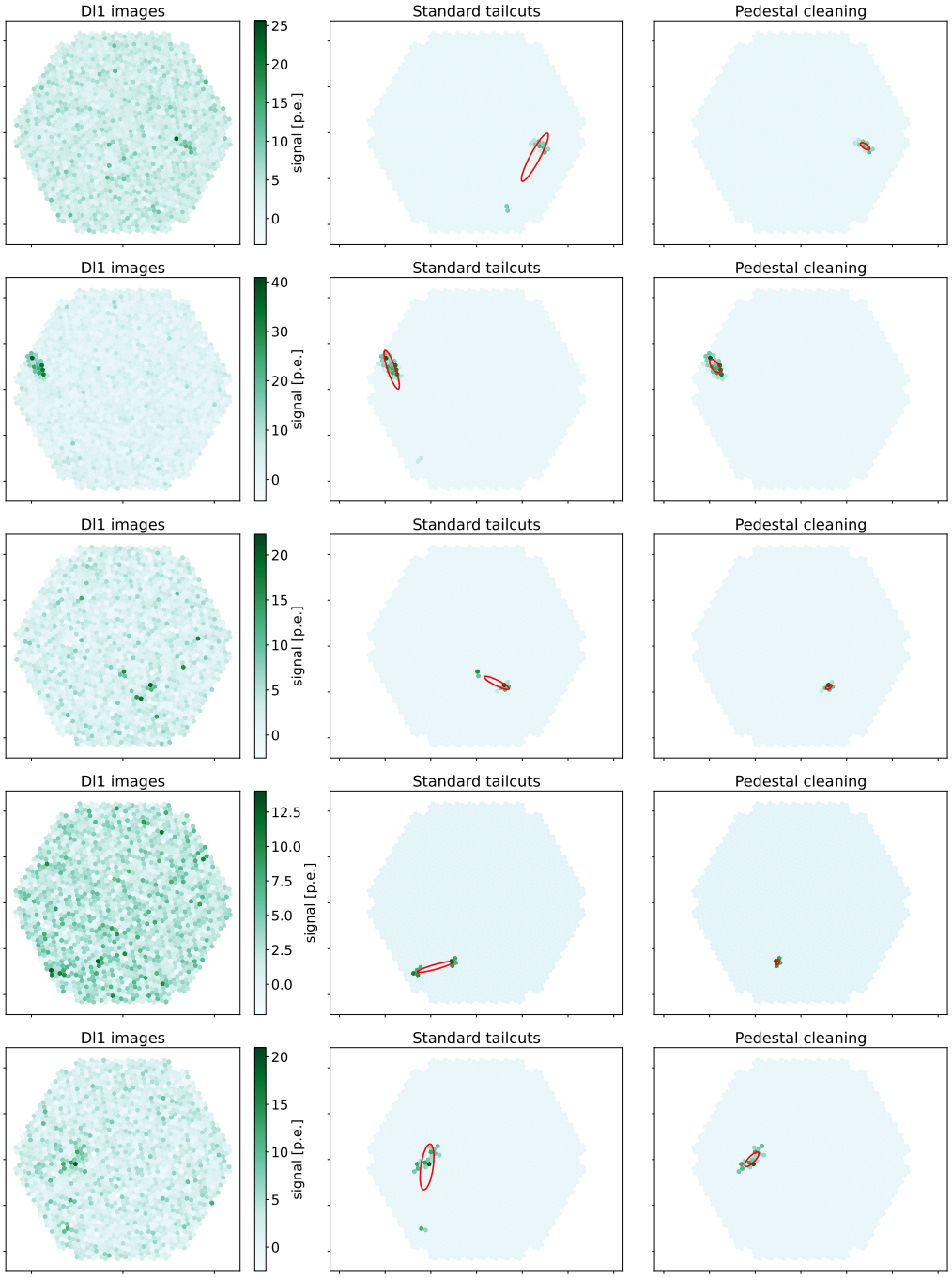

Figure 3.17: A series of images from real LST-1 data showing cosmic showers images and images after applying various cleaning methods. The first image on the left shows the original signal from the camera before any cleaning is used. The central image in each row illustrates the data after applying a standard procedure called *tailcuts* with delta time cleaning with threshold 2ns. After applying a special technique called *pedestal cleaning*, the picture on the right represents the result, which allows for more efficient noise removal.

Chapter 4

BL Lac analysis

In this chapter, I present my analysis of the LST-1 observations of the BL Lac source. By applying the data analysis pipeline explained in the previous chapter to real data, I illustrate the application of the LST-1 pipeline to scientific observations of a flaring source. In this chapter, I focus on the analysis steps applied to the DL2 (data level 2) data within the LST-1 pipeline framework, detailed previously, leading to the derivation of physical results such as the Spectral Energy Distribution (SED) and light curve. I gained expertise in handling the LST pipeline during my seven-month research stay at the Institut de Fisica d'Altes Energies in Barcelona. I focused on the issue of using a limited library of MC simulations for source analysis. As part of this task, I attempted to address this problem by comparing the results obtained from different MC samples available for analysis. I demonstrate this using the BL Lac source as an example to check the performance of the LST-1 telescope in flux reconstruction with various MC simulations.

4.1 Source

BL Lacertae (BL Lac), a blazar located at redshift 0.069 [248], is located according to International Celestial Reference System (ICRS) coordinates (epoch J2000) 22:02:43.29 in right ascension and +42:16:39.98 in declination, as observed in the optical observations. Typically classified as LBL (see [249]) but occasionally referred to as IBL (refer to [250]), is notable for its flux variability across different energy bands, as detailed in [251]. The entire class of BL Lac objects is named after it, although subsequent studies have shown a state in which it had emission lines that did not qualify it as a BL Lac-type object [50].

BL Lac detection in the VHE gamma-ray band has occurred exclusively during its flaring states until now. BL Lac was first claimed in the VHE gamma-ray band (over 1 TeV) in 1998 by Crimean Observatory [252]. Concurrently, HEGRA also observed the source during the same period and established upper limits on the emissions, which were not consistent with the findings from the Crimean Observatory [253]. The first unequivocal detection was later accomplished by MAGIC in 2005 [254]. Since then, MAGIC and VERITAS have detected multiple instances of the BL Lac flare, each displaying a range of flux levels. BL Lac has shown considerable activity in the gamma-ray band since 2019, with MAGIC detecting numerous VHE gamma-ray flares during this period [255, 256, 257]. The light curve from *Fermi*-LAT for BL Lac is shobardzo wysokich energiiwn in Fig 4.1. BL Lac was detected at the VHE energy range not only during flare events but also during lower states of emission [254].

BL Lac exhibited a period of enhanced activity from August 2020 to November 2022, with a peak in July-August 2021. During this time, BL Lac reached historic brightness maxima in various energy ranges, which were observed by several observatories, including the Crimean Astrophysical Observatory [258], the Ferson telescope [259], the MAGIC telescopes [257] and Kanata telescope [260]. LST-1 observatories also detected this increased activity. On July 11, 2021 (MJD 59406), LST-1 observed a differential flux of $(1.3 \pm 0.2) \times 10^{-9}$ cm^{-2} s^{-1} TeV^{-1}, corresponding to 25% of the Crab Nebula flux, at 100 GeV with 8 sigma significance [261]. In 2021, LST-1 observed a BL Lac outburst [262], detecting high-energy gamma-ray emissions consistently across the campaign. Particularly on August

9, the observations yielded a significant detection at 43.4σ, showcasing notable intra-night variability with peak flux levels between 3 and 4 Crab Units. On August 2, 2021 (MJD 59428.9), MAGIC detected a flux corresponding to about 1.3 C.U. at E>100 GeV, roughly an order of magnitude higher than typical non-flaring flux values [263].

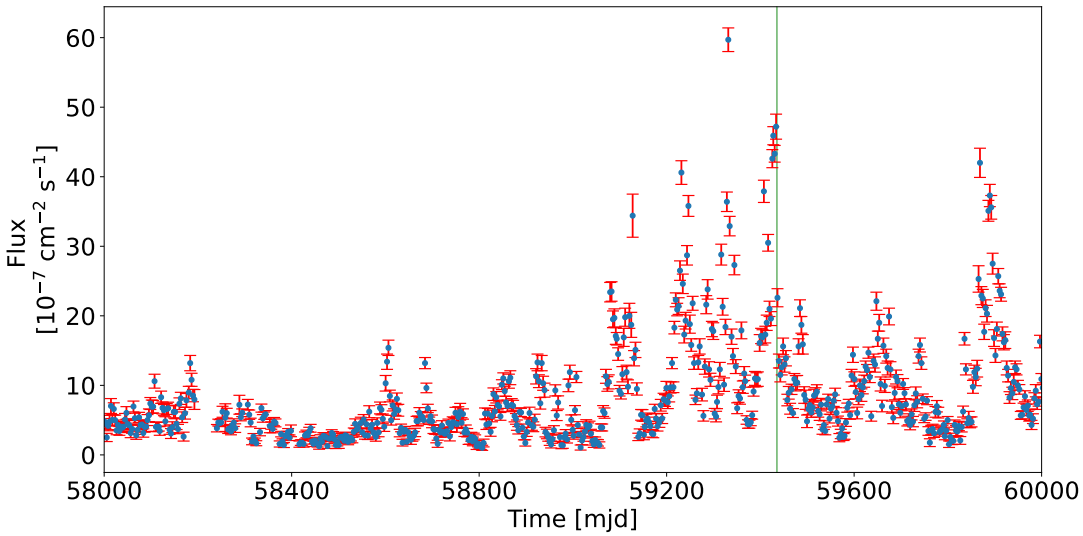

Figure 4.1: *Fermi*-LAT light curve for energy 0.1-100 GeV with the green line indicating the August 8, 2021 data used for my analysis. Source: [264].

4.1.1 Monte Carlo for analysis

As discussed in the previous chapter, MC simulations play a crucial role in IACT data analysis. For the analysis of a very strong flare, such as the one from BL Lac, one expects small statistical errors. Therefore the analysis is more prone to systematic effects. I aim to study the relationship between the analysis outputs, namely θ^2, SED, LC, and the set of IRFs employed. I have generated two sets of IRFs for this goal, each processed with a separate training output based on different MC samples. These IRFs have to be applied to corresponding DL2 data files (of BL Lac observations) and processed with the same training outputs. In summary, I am checking how the selection of a specific declination line of generated MC simulations for training purposes affects the analysis results.

The MC training is conducted by simulating pointings along lines of declination, meaning it tracks the path in horizontal coordinates (Altitude-Azimuth) that all objects at a specific declination take, as seen from the LST-1 location. In LST-1, MC simulations involve fifteen distinct declination lines, ranging from -29 degrees to +67 degrees, distributed in steps determined by the cosine of the minimum zenith angle ($\cos(ZD_{\rm min})$), where $ZD_{\rm min}$ represents the zenith angle at culmination. Fig. 4.2 displays the telescope's pointing at the sky in azimuth and zenith coordinates with marked declination lines for which LST-1 has MC simulation data available. For my work, I have conducted data analysis for two MC lines that are the closest to the BL Lac nominal declination and compared the results I obtained. The declination line of 48.22° is closer to BL Lac (5.9 degrees vs. 7.5 degrees) than 34.76°. However, it does not cover the entire range of zenith angles. This analysis is aimed to provide valuable insights into how the analysis chain functions in LST-1, as it investigates whether using different MC data sets leads to significant differences in the analysis and would contribute to the systematic errors associated with the current data analysis scheme in LST-1.

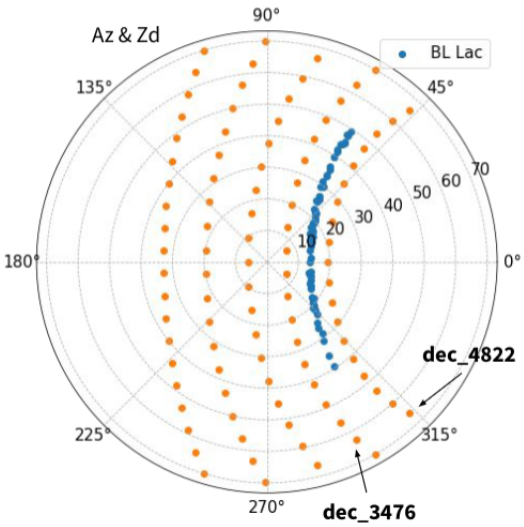

Figure 4.2: This plot presents the pointing of the telescope sky in Azimuth and Zenith coordinates with marked declination lines. The closest nodes to the BL Lac path, corresponding to declinations 34.76° and 48.22°, are visible. Credit: Dr. Seiya Nozaki.

4.1.2 LST-1 observations and data processing

The observations of BL Lac by the LST-1, detailed in this chapter, were conducted during the moonless night of August 8th to 9th, 2021. These observations were restricted to periods when the source was less than 50 degrees from the zenith.

I selected the data from the night of August 8/9 because the weather conditions were good, and the source exhibited the highest activity observed by LST-1 during this period. The total duration of the observations was 1.83 hours after data selection, with each observation run lasting 20 minutes. To ensure data quality, I selected only those datasets where the camera-averaged rate of pixel pulses with a charge above 50 photoelectrons (p.e.) met quality criteria: Specifically, the datasets with a camera-averaged rate of pixel pulses exceeding 30 p.e. more than 4.5 s^{-1} and runs where the rate of shower images with an intensity between 80 and 120 photoelectrons (p.e.) exceeded 800 Hz. These thresholds, aimed primarily at outlier removal, were calculated based on run-averaged values, although the exact cut-off points are somewhat arbitrary, as detailed in [202]. This rate indicates the atmospheric conditions during the observation, serving as a reliable metric for assessing the quality of the data collected. For the event selection process, I select gamma-ray candidates by using energy-dependent gammaness and angular cuts that preserve a certain percentage of the point-like MC gamma-ray events in each reconstructed energy bin. The corresponding efficiency was set 80% for the gamma/hadron separation cut. Additionally, we set the maximum values to 0.95 for the gammaness cut and 0.2 degrees for the θ cut. I processed the data from DL1 to DL2 using the `lstchain` developer version (corresponding to `lstchain` version v0.9.7). I used a development version of the software because, at the time, the latest stable version that was available was outdated and unable to perform the required task for my work on BL Lac analysis. So, instead of using the stable version, I opted to work with the development version that had the necessary features and capabilities to meet my needs. Then, I performed a high-level analysis of DL3, DL4, and DL5 (including spectra and light curve) using `gammapy` v.0.19 [265]. This analysis was carried out on the LST-1 computing cluster, which was chosen due to its direct access to the necessary datasets and its substantial computational power and RAM availability, facilitating a more efficient processing environment.

Comparison of background and signal rates

To assess the influence of the selected MC along a specific declination line, I conduct a comparative analysis of the significance of detection, the number of gamma photons within the ON and OFF regions,

and the corresponding rates of gamma rays and background radiation. The resulting plots are shown in the fig. 4.3

To begin the analysis, I compare the angular distribution of the events for BL Lac. Fig. 4.3 displays the θ^2 parameter distributions, which measure the squared angular distance between the reconstructed event directions and the source. For the background, the distribution is approximately uniform, while the signal should reveal itself as a peak at low values of θ. The parameter is divided into six energy ranges. Upon analyzing the plots, it is evident that there are significant differences in the number of ON and OFF events for the energy range of 0.01-0.03 TeV. Specifically, the data processing with declination line 48.22° shows around 20% more events than the other data processing method for the same energy range. Moreover, the significance of the results obtained from this processing method remained higher by 1.3 σ[1]. More events were also observed for data processing with declination line 48.22° for the energy range of 0.03-0.3 TeV. In addition, a slightly higher significance was noticed for the data processing with declination line 34.76° in the energy range of 0.1-0.3 TeV. However, for energies above 0.3 TeV, the results in the theta plots were similar. These observations indicate that processing data for the declination of BL Lac using MC samples for declination line 48.22° is potentially slightly more sensitive for lower VHE energies (10 to 300 GeV), though the overall differences are not significant. However, it's important to note that the lowest energy ranges may exhibit an energy bias effect, which can vary depending on the training applied. In the figure labeled as Fig. 4.4 and 4.5, I have included a comparison of the significance (σ) and the rate of gamma and background events per minute in 5 estimated energy ranges (ranging from 0.01 to 10 TeV). From the analysis of these plots, we can observe that the significance in the energy range of 10 to 100 GeV is slightly higher for the analysis with declination line 48.22°. On the other hand, for the energy range of 100 to 300 GeV, the significance is higher for the analysis with declination 34.76°. The results for the other energy ranges are quite similar. Additionally, the rate of gamma and background events is slightly higher in each energy range for the analysis based on MC with declination line 48.22°.

Light curve and SED comparison

Studying SED and light curves during a strong flare is important to search for analysis-related systematic errors. I used `gammapy` v0.19 for this part of the data analysis for BL Lac as described in section 3.4.4. I used `gammapy.modeling` for parametric models and the related fitting functionalities. Additionally, I utilized `gammapy.estimators` to compute light curves and differential flux points expressed in the form of SED.

After conducting an analysis, I found significant differences in the energy range below 50 GeV in the case of SED. In the analysis using MC simulations based on the declination line of 48.22°, the data points were higher compared to others within the same energy range. However, this discrepancy was reduced for energy levels above 100 GeV, where the SED point near 50 GeV was observed to be three times higher than SED points for analysis with a declination line of 34.76°. This finding should be considered in light of the LST-1 performance paper [218], which indicates that at these lower energies, significant systematic errors related to background estimation can occur. These errors could potentially impact the comparison between the two analyses presented here, particularly in the context of systematic differences at lower energies.

I determined that a logarithmic function accurately describes the spectrum in the him/VHE range. This model is called the LogParabolaSpectralModel and can be expressed as:

$$F(E) = F_0 \times \left(\frac{E}{E_0}\right)^{-\alpha-\beta\log_{10}\left(\frac{E}{E_0}\right)} \tag{4.1}$$

The data was fitted to this model, and the result of the fit is presented in Table 4.1. The LogParabolaSpectralModel is characterized by amplitude, reference energy, α, and β parameters. These

[1]If no signal is present, the significance is estimated with an accuracy of approximately $\pm$ 1 σ. In contrast, for a very strong signal, it can be determined numerically that the statistical accuracy improves to about $\pm$ 0.5 σ. Since the two analyses compared are not independent, the observed difference of 1.3 sigma is of the same order as these accuracies. Therefore, although a certain effect is observed, it is not pronounced, which is advantageous as it indicates that the effects of different Monte Carlo simulations are moderate.

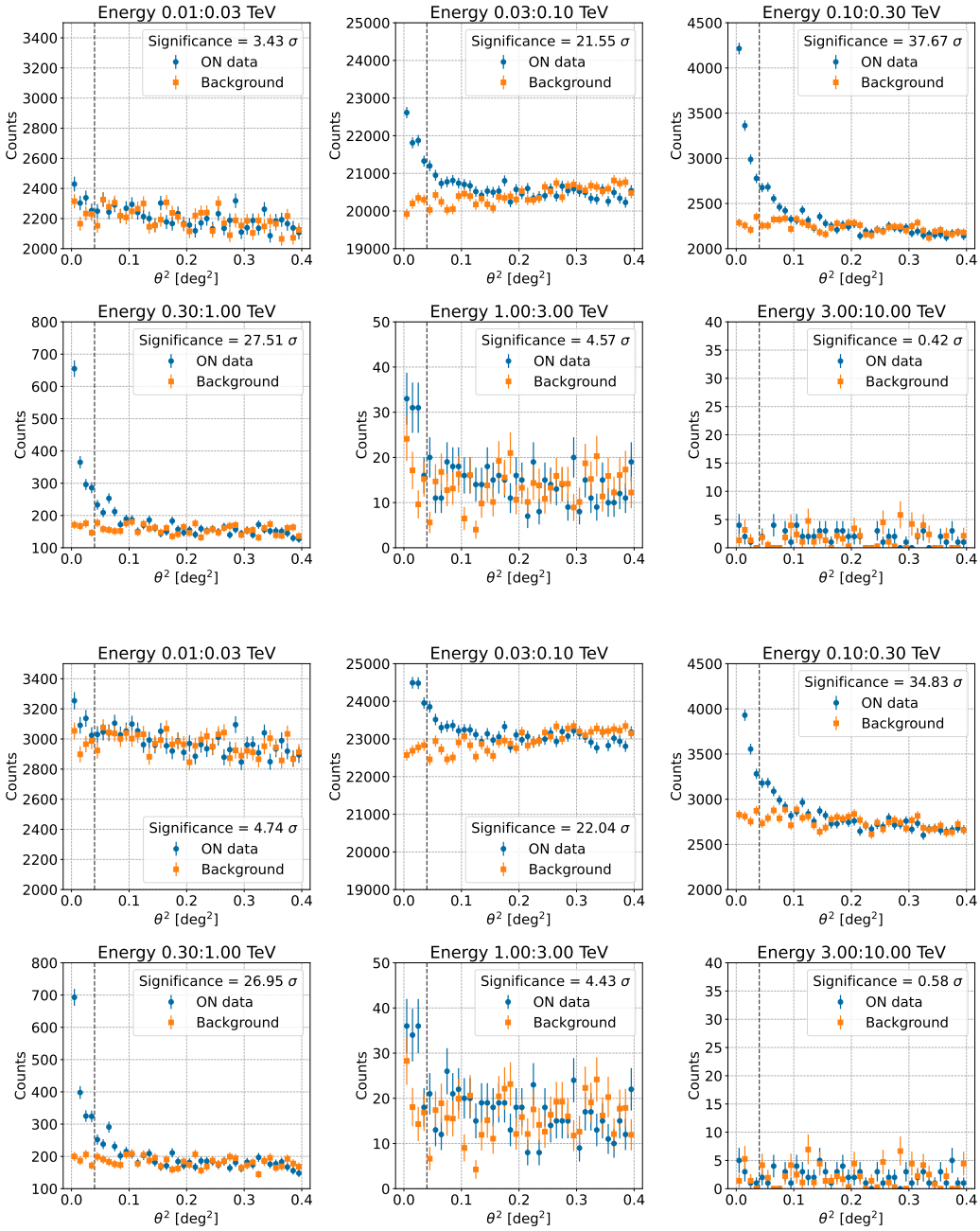

Figure 4.3: The θ^2 plots for observations of BL Lac on August 8, 2021, across six different energy ranges. The results were obtained through data processing using MC simulation produced along two declination lines, 34.76° (top six panels) and 48.22° (bottom six panels).

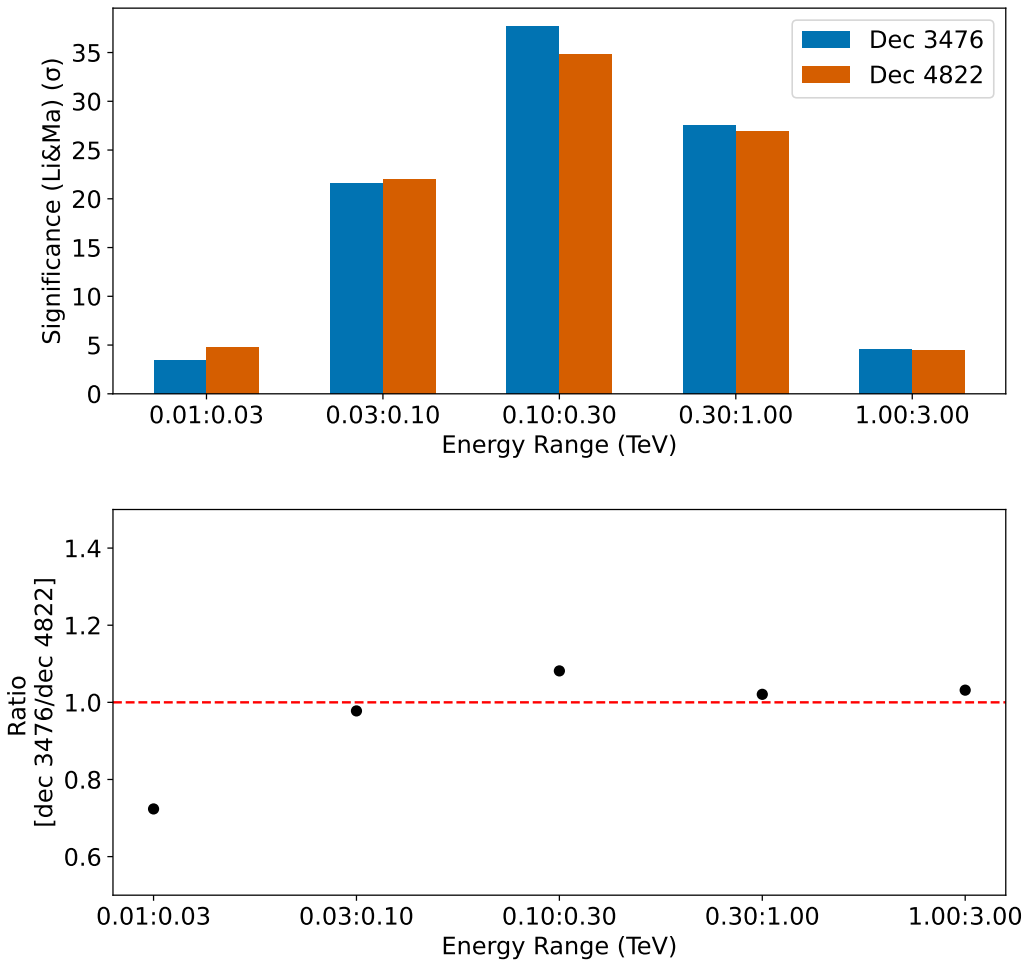

Figure 4.4: The bar plots show the DL3 parameters for observations of BL Lac on August 8, 2021. The significance across five energy ranges with ratio is compared. The results were obtained through data processing using MC simulation produced along two declination lines, 34.76° and 48.22°.

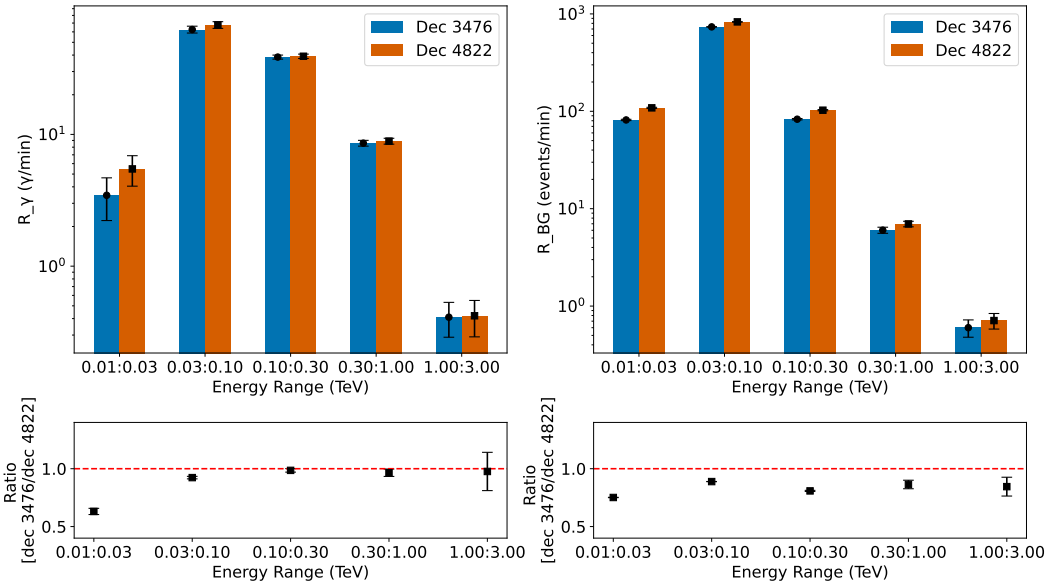

Figure 4.5: The bar plots show the DL3 parameters for observations of BL Lac on August 8, 2021. The comparison includes the rate of gamma and background events across five energy ranges. The results were obtained through data processing using MC simulation produced along two declination lines, 34.76° and 48.22°.

parameters were estimated for both observations and are summarized in Table 4.1. Fig. 4.6 displays data points with a fitted spectrum for two different analyses, each with a different declination line. The upper limit point at around 30 GeV in the analysis with declination line 34.76° is notably lower than the corresponding point with a different declination line. Additionally, the flux point with energy around 50 GeV is slightly lower in the analysis with declination line 34.76° than in the study with declination line 48.22°. These discrepancies lead to a more curved fit function for the data obtained with the declination line 34.76°. There are also differences in normalization and the spectral index. While these differences are not large, they still exceed the stated statistical uncertainties. The normalization for dec 34.76° was $(8.99 \pm 0.30) \cdot 10^{-9}\,\mathrm{cm}^{-2}\,\mathrm{s}^{-1}\,\mathrm{TeV}^{-1}$ compared to $(7.99 \pm 0.27) \cdot 10^{-9}\,\mathrm{cm}^{-2}\,\mathrm{s}^{-1}\,\mathrm{TeV}^{-1}$ for dec 48.22°. The spectral index was also 2.79±0.04 for dec 34.76° and 2.96±0.03 for dec 48.22°. The observed discrepancies could be attributed to the systematic errors in the lower part of the HE/VHE SED, as highlighted in [202], which says that below 100 GeV, the energy of mono analysis worsens fast.

Fig. 4.7 displays the light curve data, which shows a consistent trend. It was observed that the flux was consistently lower for 48.22° than for 34.76°. This trend was consistent throughout the observation period, which also aligns with the fact that in Table4.1, there is a 10% difference in normalization between these two analyses.

Parameter	dec 34.76°	dec 48.22°
Amplitude $(10^{-9}\,\mathrm{cm}^{-2}\,\mathrm{s}^{-1}\,\mathrm{TeV}^{-1})$	8.99 ± 0.30	7.99 ± 0.27
Reference Energy (TeV)	0.13 (frozen)	0.13 (frozen)
α	2.79 ± 0.04	2.96 ± 0.03
β	0.31 ± 0.04	0.19 ± 0.03

Table 4.1: Parameters from fitting procedures.

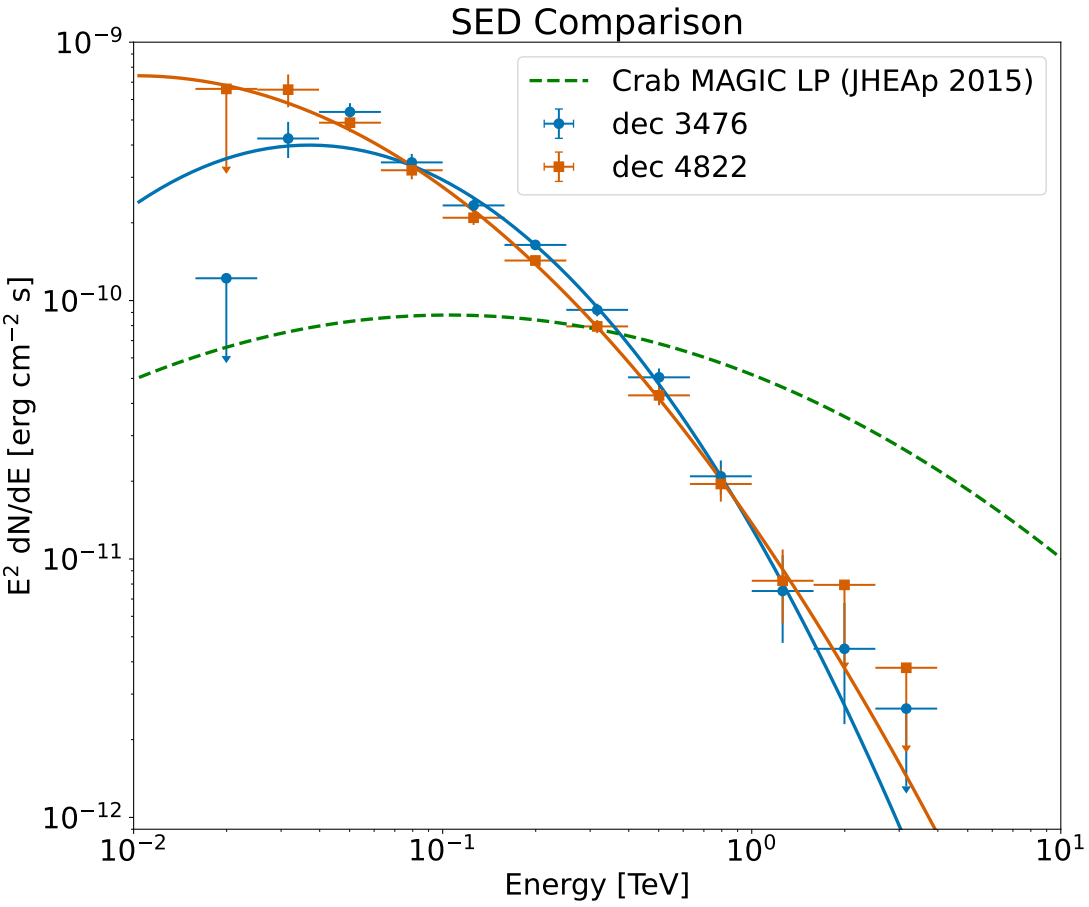

Figure 4.6: Comparison of SED and LC for two data sets obtained using different declination lines in MC simulation. To provide context, the Crab Nebula spectrum is also displayed following [266].

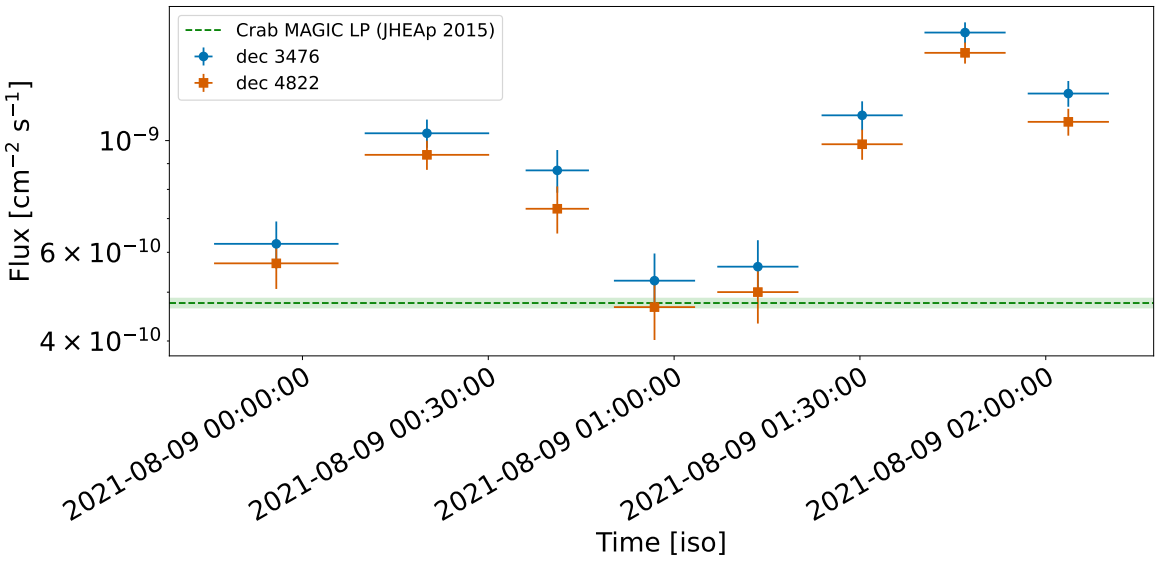

Figure 4.7: Light curve for two analyses with different MC simulations shown for SED (for $E > 100$ GeV and $E < 10$ TeV). The Crab Nebula integral flux [266] is also displayed to provide context.

4.1.3 Summary

In the analysis of BL Lac objects, the study revealed that using different MC simulations along specific declination lines affects the detection of gamma rays, particularly in lower energy ranges. Specifically, data processed with declination line 48.22° showed about 20% more events (on and background) than based on the MC sample with dec 34.76° in the 0.01-0.03 TeV range. The significance was slightly higher for declination line 48.22° in the 10 to 100 GeV range, while for 100 to 300 GeV, it was higher for declination line 34.76°. Additionally, the gamma and background events rate was marginally higher across all energy ranges for analysis based on MC with declination line 48.22°. However, the results converged for energies above 0.3 TeV, suggesting that the influence of selecting a specific declination line in MC simulations is more significant at lower energy ranges. This observation should again be contextualized with respect to typical systematic uncertainties. At the lowest energies, variations in background estimation remain the most critical factor and also affect the presented here comparison as both analyses are based on different training and hence are burdened by partially independent backgrounds. Unfortunately, for higher energies, the LST-1 performance paper [202] does not provide systematic uncertainty values.

Chapter 5

Constraints on VHE gamma-ray emission of FSRQs with the MAGIC telescopes

This chapter describes studies of nine FSRQs observed by the MAGIC telescopes and *Fermi*-LAT between 2008 and 2020. The findings presented in this chapter are based on the publication entitled *Constraints on VHE gamma-ray emission of Flat Spectrum Radio Quasars with the MAGIC telescopes* about to submitted to MNRAS [267], which I had the privilege to prepare as the corresponding author in the MAGIC collaboration. I present the VHE gamma-ray observations, data analysis, and results of: TXS 0025+197, B2 0234+28, AO 0235+16, 4C 55.17, OP 313, CTA 102, B2 2234+28 A, TXS 2241+406, 3C 454.3. The data used in this study were gathered by the MAGIC telescopes together with the optical data from the Kungliga Vetenskapsakademien (KVA) along with X-ray and UV data from *Swift*-XRT and *Swift*-UVOT, respectively. The paper also had dedicated *Fermi*-LAT analysis contemporaneous to the MAGIC observations and averaged over 12 years of Fermi-LAT operations. No statistically significant ($\geq 5\ \sigma$) signal was found for any of the studied sources. Thus, I present a MAGIC catalog of upper limits (U.L.) on these sources' gamma-ray emission. Next, I construct a theoretical model using the *Fermi*-LAT data and the MAGIC U.L. exploiting the absorption in BLR and, finally, derive a broadband emission model based on the EC scenario. I also present the improvements necessary in `agnpy` to enable emissions modeling considering the BLR.

5.1 Instruments, observation and data analysis

5.1.1 Fermi-LAT telescope

The *Fermi* Gamma-ray Space Telescope is a space-based observatory designed to study the Universe in gamma-ray energies. The Fermi Gamma-ray Space Telescope, also known as *Fermi*, was sent into space on June 11th, 2008, from the Cape Canaveral Kennedy Space Center in Florida. It began conducting scientific experiments in August of that same year, and to this day, after more than a decade of observations, it remains active in a low-Earth orbit. The satellite's current altitude is approximately 565 kilometers, with an inclination of 25.6 degrees relative to the Equator. It orbits the Earth with a period of about 90 minutes [93].

The *Fermi* telescope has on-board two instruments: Gamma-ray Burst Monitor (GBM) dedicated to detecting transient events in energy range ~ 8 keV to 40 MeV and the Large Area Telescope (LAT) [12] designed to monitor high-energy gamma-ray sources in the energy range from 20 MeV to 300 GeV in an all-sky survey. The Fermi-LAT measures high-energy gamma-ray photons energy, arrival time, and direction. It comprises a high-resolution converter tracker (for measurement of the direction of the incident gamma rays), a CsI(Tl) crystal calorimeter (for energy measurement), and an anti-coincidence detector to efficiently identify and veto the background of charged particles. Incident gamma photons,

interacting with the converter tracker, produce electron-position pairs. The silicon strip detector then tracks the path of these charged particles through the detector. A CsI(Tl) crystal calorimeter measures the energy deposition of the electromagnetic cascade. The anti-coincidence detector is the outermost detector, surrounding the tracker, and rejects charged-particle background, such as the cosmic-ray background.

Fermi-LAT data analysis

Dedicated analysis [268] of *Fermi*-LAT data spanning 12 years, from August 4, 2008, to August 4, 2020, for FSRQ paper was performed by Giacomo Principe.

The analysis adopted rigorous criteria to mitigate the impact of background noise and ensure the precision of photon event selection, particularly emphasizing the exclusion of events with large uncertainties in their arrival directions. For this analysis, P8R3 SOURCE class events [269] were selected within the energy range of 100 MeV to 1 TeV. The analysis considered a 15° radius region of interest (ROI) centered on each FSRQ, utilizing the `Fermipy` software [270] for data analysis, which included tasks such as model optimization, source localization, and the examination of the spectrum and variability of gamma-ray emissions. A similar analysis technique has also been applied in [268].

To study the gamma-ray emission variability of each FSRQ, the *Fermi*-LAT data were divided into two-month time intervals. In the light curve analysis, the photon index was fixed to the value obtained for 12 years, and only the normalization was left free to vary. The 95% upper limit was reported in each time interval with Test Statistics (TS) [271] < 10. In addition to the study of the whole 12 years of *Fermi*-LAT data, a cumulative analysis was performed to counteract the source variability and provide contemporaneous measurement to the one obtained with the MAGIC telescopes. Select dedicated periods based on MAGIC observations. In this procedure, all the individual days were stacked together as a single time window. The previously described analysis procedure was then used to investigate the LAT emission in the selected periods.

5.1.2 *Swift*

The Neil Gehrels *Swift* Observatory [272] is a satellite launched in 2004 by the National Aeronautics and Space Administration. It is equipped with three telescopes, namely the Ultraviolet and Optical Telescope UVOT [273] is capable of performing optical and ultraviolet photometry, the Burst Alert Telescope *BAT* [274] is dedicated to detecting gamma-ray bursts and provide fast alerts to other, due to multiple instruments and rapid alert response, the *Swift* observatory is ideal for gathering simultaneous data in MWL campaigns. The board allows us to monitor the gamma-ray bursts and their afterglow phase and, eventually, to collect data in optical, UV, and X-rays from any source. Furthermore, due to multiple instruments and rapid alert response, the *Swift* observatory is ideal for gathering simultaneous data in MWL campaigns.

The spectral analysis was performed simultaneously with the MAGIC observations and derived the long-term LCs for two sources, CTA 102 and B2 2234+28A. This analysis was done for the FSRQ paper by N. Żywucka. Both sources were monitored in U (345 nm), B (439 nm), and V (544 nm) optical bands, UVW2 (188 nm), UVM2 (217 nm), and UVW1 (251 nm) UV regime, as well as in X-ray energies between 0.2 and 10 keV. The comprehensive analysis was performed in the ISIS environment with HEASOFT [275] version 6.30.

The *Swift*-UVOT instrumental magnitudes were calculated within a circular region centered at the source coordinates with a radius of 5″, using the UVOTSOURCE task. An annulus region centered at the same coordinates with the radii of (26″and 40″) were used for the background determination. The choice was made to prevent signal contamination from other sources in the closest vicinity of the studied blazars. The fluxes are derived taking into account the Galactic extinction A_V correction based on the hydrogen absorption column density N_H in the direction of the object and using the color excess E(B-V), calculated as $E(B-V) = N_H/(1.79 \cdot 10^{21} A_V)$ [276].

5.1.3 KVA

The data used in this chapter are also reported in [267] and were obtained through observations in the optical spectrum using a 35 cm Celestron telescope, which was coupled with the KVA telescope as part of the Tuorla Blazar Monitoring Program [277]. The program was initiated in 2002, primarily focusing on TeV candidate BL Lac objects identified in [278], but the monitoring sample has since expanded over the years. Observations were typically conducted twice per week, with the Cousins R-filter being used[1].

Data analysis was done by the Tuorla group using a semi-automatic differential photometry pipeline developed specifically for this study [249]. For AO 0235+164, the comparison and control star magnitudes were sourced from [279]. The comparison stars were calibrated for other sources using observations of sources with known comparison star magnitudes from the same night.

Given the high redshift and bright optical nucleus of the sources, the contribution of the host galaxy to the optical flux was found to be negligible and, therefore, not corrected. Magnitudes were corrected for galactic extinction using the galactic extinction model of [280].

5.2 Source sample

The MAGIC Collaboration's interest in observing FSRQs stems from the theoretical challenges posed by their emissions. Despite the high redshift and absorption in the BLR, these objects exhibit VHE emission, which has been observed from 10 such objects (see Section 2.1.2). This emission is often highly variable, suggesting that the area is small and close to a black hole, i.e., in BLR. However, the problem of where the emission region is located remains one of the main issues when considering FSRQs (see Section 2.1.3). My research is devoted to analyzing the observations made using the MAGIC telescopes that have yet to result in any significant detection. Through my work, I aim to determine whether absorption in EBL from FSRQ objects can explain the lack of detection or if there is a need to explain observed U.L. with an additional absorption in BLR.

Between 2008 and 2020, MAGIC attempted to observe specific FSRQs when the high activity of the sources triggered MAGIC observations on multiple occasions. Most of these sources have been observed by MAGIC as a target of opportunity (ToO): OP 313, AO 0235+16, 3C 454.3, TXS 0025+197, B2 2234+28A, B2 0234+28 following alerts by the MWL partners, mainly *Fermi*-LAT. Moreover, 4C+55.17 and TXS 2241+406 were observed within the deep-exposure monitoring program based on their average GeV emission in the preceding years. The sources included in my study are listed in Table 5.1 and Table 5.2. Table 5.1 contains information about the studied sources based on the information in the 4FGL catalog [91], namely their positions, variability index, the integrated flux from the catalog, as well as the values obtained from the dedicated analysis for the periods when the MAGIC telescopes observed the sources. Table 5.2 provides Information about the data collected from those sources by the MAGIC telescopes, such as observation time (exposure), zenith angle at which the source was observed, date of observations in MJD, the excess signal calculated using the [227] formula, and integral U.L..

The MAGIC data selection was based on the atmospheric transmission measured mainly with Light Detection and Ranging (LIDAR) system [281, 282] and rates of background events. The data were analyzed using the MAGIC Analysis Reconstruction Software (MARS) framework [234, 212].

In agreement with the preferred spectral model reported in the 4FGL catalog, most of the sources (except for 3C 454.3) studied in this paper are well described with the log parabola (LP) spectral model $\frac{dN}{dE} \propto E^{-\alpha+\beta \ln(E/E_b)}$ in the GeV range, the fit parameters are reported in Table 5.3 and model are taken from *Source Model Definitions for gtlike* [2]. For 3C 454.3, the spectrum is fitted with the PLSuperExpCutOff model (see Section 2.1.3).

All sources are classified as FSRQs in the *Fermi*-LAT 10-year Source Catalog (4FGL-DR2), as well as in the latest 4FGL-DR4 (which is based on 14 years of LAT data), except for AO 0235+16 (4FGL J0238.6+1637) which is classified as BL Lac in both data releases(see details below).

[1] R-band points on the light curve were measured by KVA

[2] https://fermi.gsfc.nasa.gov/ssc/data/analysis/scitools/source_models.html

These sources were continuously observed by *Fermi*-LAT (see 12 years LCs at Fig. 5.10) and KVA from 2008 to 2020. I investigated the MWL behavior of these nine FSRQs contemporaneously with the MAGIC observations. The integrated flux ranging from 0.1 to 1000 GeV from the *Fermi*-LAT telescope over 12 years of observations of each of the sources (denoted as $\overline{\phi}_{\mathrm{HE,12}}$) is presented in the fifth column in Table 5.1, and the last column, the integral flux during MAGIC observations. The state of the source is determined by dividing the flux during MAGIC observations by the flux over the first 12 years of Fermi-LAT operations.

CTA 102 (z=1.037, [283]) is one of the most studied FSRQs in the MWL context, but still poorly investigated in the VHE band. High activity in gamma rays was detected for the first time by the Energetic Gamma Ray Experiment Telescope (EGRET) on board the Compton Gamma-Ray Observatory ([284]). CTA 102 is one of the brightest FSRQs observed by *Fermi*-LAT. Strong gamma-ray outbursts have been observed from CTA 102 several times [285]. From late 2016 to early 2017, CTA 102 exhibited a hugely bright 4-month-long outburst, with the fluxes in all bands steadily increasing during the early stage of the high state. As a result, CTA 102 became one of the brightest gamma-ray sources in the sky at that moment [286, 287, 288, 289]. The MAGIC telescopes followed up CTA 102 during the very high state at the end of 2016 (flux from *Fermi*-LAT was 20 – 30 times stronger than the average $\overline{\phi}_{\mathrm{HE,12}}$) and also during increasing activity in HE range at the end of 2017 (flux from *Fermi*-LAT was 10 times stronger than $\overline{\phi}_{\mathrm{HE,12}}$) for a total of $\sim$ 3.5 hours. The optical, UV, and X-ray LCs, demonstrating the source's heightened activity during the period of observation by the MAGIC telescopes, are displayed in Fig.5.1. It also includes the LCs from MAGIC and *Fermi*-LAT.

3C 454.3 (z=0.859, [290]) is another well studied, highly variable FSRQ. The source was first detected in the GeV range by EGRET [291]. 3C 454.3 reached a high flux phase in 2000 and was extremely active in 2005 when it peaked at one of the highest optical brightness recorded from an AGN [292, 293]. *Fermi*-LAT has reported strong and variable gamma-ray emission from this FSRQ in 2008 [293]. In 2010, during the unusual bright gamma-ray flare, *Fermi*-LAT measured flux at $E >$ 100 MeV to be $(66 \pm 2) \cdot 10^{-6}$ photons cm^{-2} s^{-1}. This emission was three times higher than its previous maximum flux recorded in December 2009 [294]. At that time, 3C 454.3 was one of the brightest gamma-ray sources in the sky. The MAGIC-I telescope observed the source for the first time during the high states of July/August and November/December 2007. The observation was carried out in mono mode. No significant emission was found, and the flux U.L. was derived [295]. The obtained data were consistent with the model based on the IC scattering of the ambient photons from BLR by relativistic electrons, which predicted a sharp cut-off above 20-30 GeV due to the absorption of gamma-rays internally and the reduced effectiveness of the IC emission [296]. Observations were carried out at different times when the state of the source varied considerably. In November 2010, observations occurred when the source was most potent, and the flux was 20 times greater than $\overline{\phi}_{\mathrm{HE,12}}$. In September, October, and November 2013, the source had an average flux comparable to or smaller than $\overline{\phi}_{\mathrm{HE,12}}$. By June and July 2014, the flux had risen to be 2 to 4 times higher than $\overline{\phi}_{\mathrm{HE,12}}$. Furthermore, by August 2015, high emission levels were reemerging. However, MAGIC observations resulted in no significant detection.

These observations, triggered by alerts from multi-wavelength partners such as KVA and *Fermi*-LAT, marking the time of the MAGIC observations, are depicted in Fig. 5.2. Following data selection, the total effective time of these observations amounted to 32 hours.

OP 313 (z = 0.99, [297]): In 2014, this blazar exhibited an upsurge in its activity in the GeV energy range, which led to its inclusion in the LAT Monitored Sources catalog [298]. From 2019 onwards, an increase in the source's activity was observed once again, evident in both the optical [299] and the gamma-ray bands [300]. MWL LCs, focusing on the time of the MAGIC observations, are shown in Fig. 5.3. During these periods of high activity, the MAGIC telescopes gathered 12.3 hours of high-quality data. Specifically, in 2014, the flux was documented as 11 times higher than the reference flux, $\overline{\phi}_{\mathrm{HE,12}}$. In 2019, the flux increased to 5 and 10 times that of $\overline{\phi}_{\mathrm{HE,12}}$. Despite these high activity periods, no detections were made by the MAGIC telescopes.

In December 2023, LST-1 detected high-energy gamma-ray emissions from OP 313 exhibiting a significant flux level of over 5 σ, corresponding to 15% of the Crab Nebula's flux above 100 GeV [77].

TXS 0025+197 (z = 1.552, [301]) is the FSRQ with the highest redshift among the analyzed sources. The *Fermi*-LAT has observed an increased gamma-ray flux on 14 August 2019. Preliminary

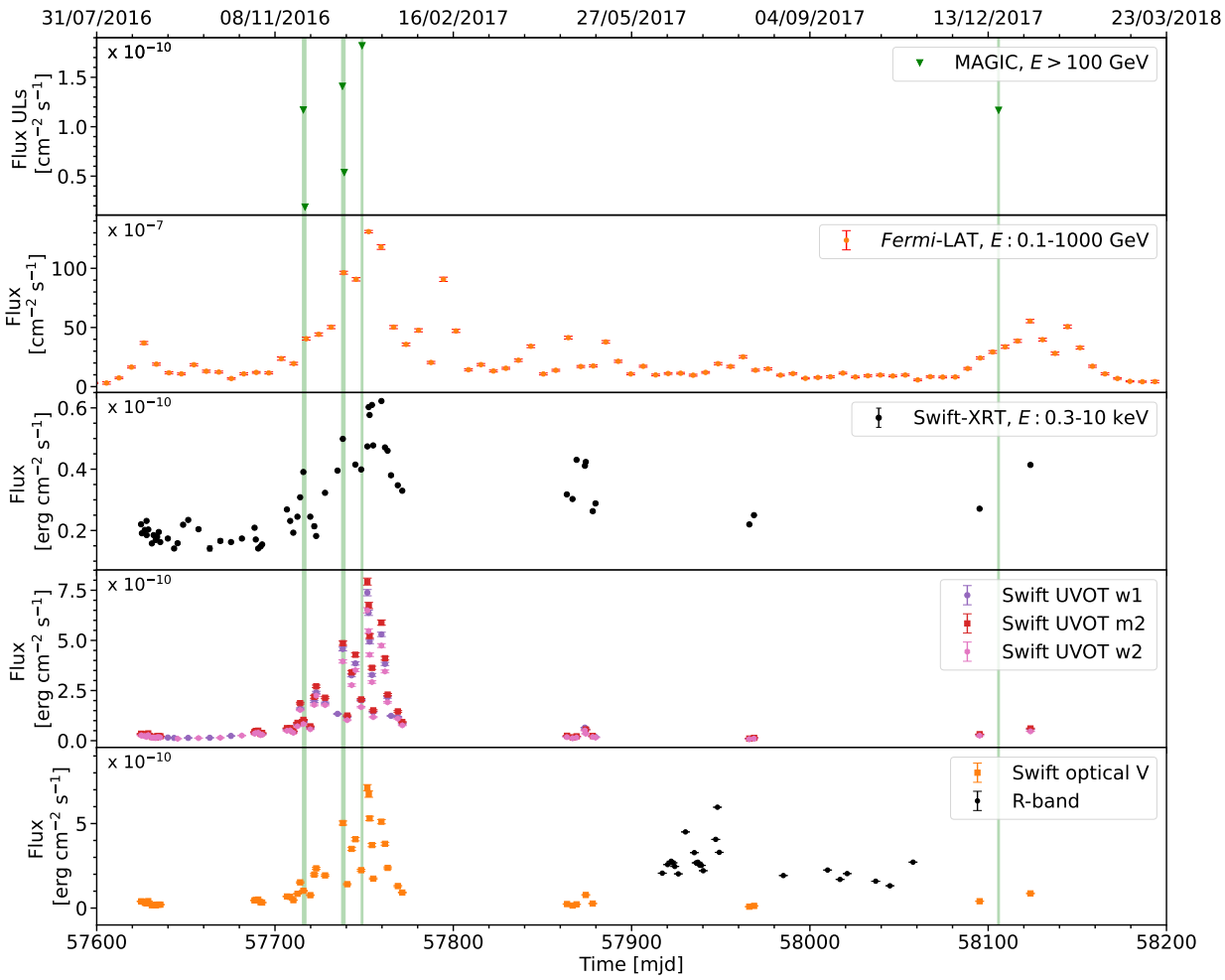

Figure 5.1: Light curve of CTA 102. The green vertical areas indicate the days during which MAGIC observations were carried out. For *Fermi*-LAT light curve, only points that met two criteria: a minimum TS value of 9 and a signal-to-noise ratio greater than 2 were selected. The KVA telescope measured R-band points.

analysis indicates that the source reached a peak daily flux ($E > 100$ MeV) of (1.0 ± 0.2) x 10^{-6} photons cm^{-2} s^{-1} [302]. MAGIC observed TXS 0025+197 in September and November-December 2019, during an increased activity observed by *Fermi*-LAT in the gamma-ray band (with a flux 50 – 60 times higher than $\overline{\phi}_{\mathrm{HE},12}$) and collected 5 hours of good quality data. *Fermi*-LAT LC, focusing the time of the MAGIC observation is shown in Fig 5.4. Unfortunately, simultaneous optical KVA data were not available.

B2 2234+28A ($z = 0.790$, [303]): The Guillermo Haro Observatory recorded notable activity from the source during the past decade [304]. Especially they detected a considerable increase in the source's luminosity in the near-infrared (NIR) band. On November 26, 2010, the luminosity of the source in the NIR band increased approximately by a factor of 11 on a day timescale [304]. Later 2016, the same observation revealed a sixfold increase [305]. MAGIC observed B2 2234+28A during its increased activity in the optical and GeV energy bands observed by KVA and *Fermi*-LAT (flux ∼ 1.3 – 2 times higher than $\overline{\phi}_{\mathrm{HE},12}$), respectively, in September 2018 and June/July 2019 and collected 6.7 hours of good-quality data. Fig. 5.5 illustrates the UVOT and XRT light curves, demonstrating that the source was undergoing a phase of amplified activity during the period of MAGIC observation.

B2 0234+28 ($z = 1.206$, [303]): In October 2018, the Special Astrophysical Observatory of the

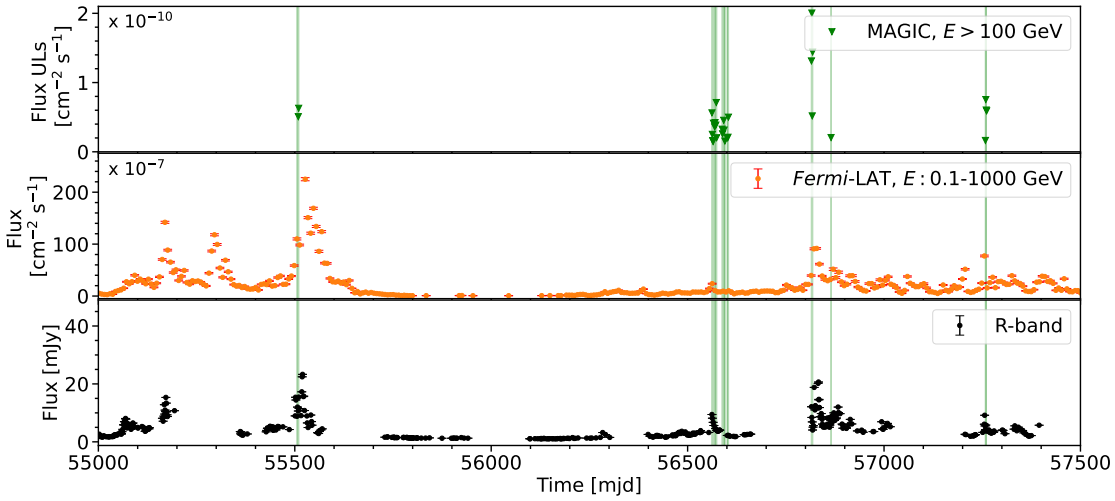

Figure 5.2: Light curve of 3C 454.3.

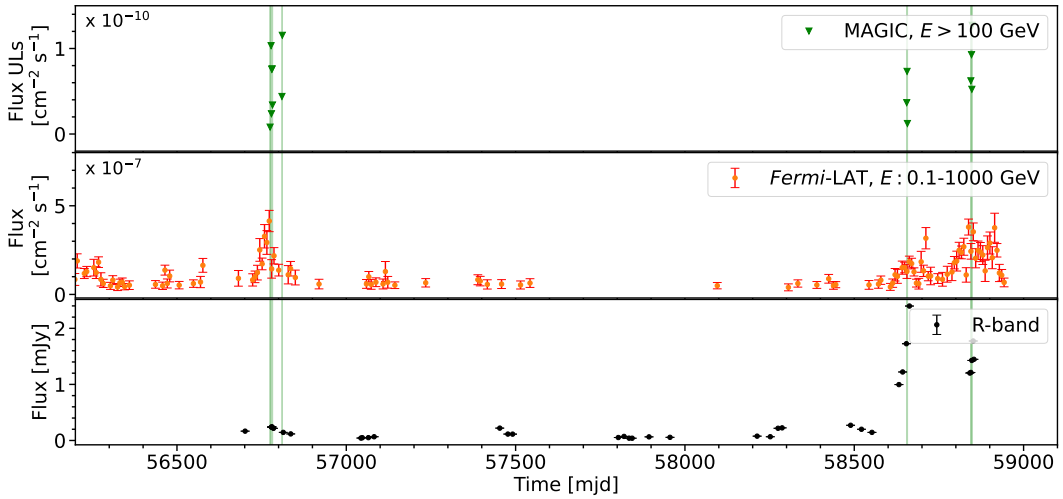

Figure 5.3: Light curve of OP 313.

Russian Academy of Sciences (SAO RAS) reported a new active phase of the source, which increased its flux in the R band by a magnitude of 3 with respect to its quiet state [306]. The Guillermo Haro Observatory observed a flare in NIR on 5 January 2019. They reported that the source had increased its flux by 50% [307]. The increase in the flux level happened on a day-timescale. MAGIC observed the source in 2018 and 2019 during its increased activity in the optical band. The source reached the highest flux in October 2018, which was 6–10 times higher than the average flux $\overline{\phi}_{\mathrm{HE},12}$. KVA and *Fermi*-LAT LCs are shown in Fig. 5.6, covering the time of MAGIC observation. MAGIC telescopes followed this source at that time and collected 25.6 h of data.

AO 0235+16 ($z = 0.94$, [308]): The classification of AO 0235+16 is not certain [279]. It was one of the first objects classified as a BL Lac object [309] and is still often classified as such. However, it has some characteristics of FSRQs, namely, strong emission lines have been detected in the spectra of A0 0235+16 during faint optical states [310, 311]. The source is also strongly Compton-dominated

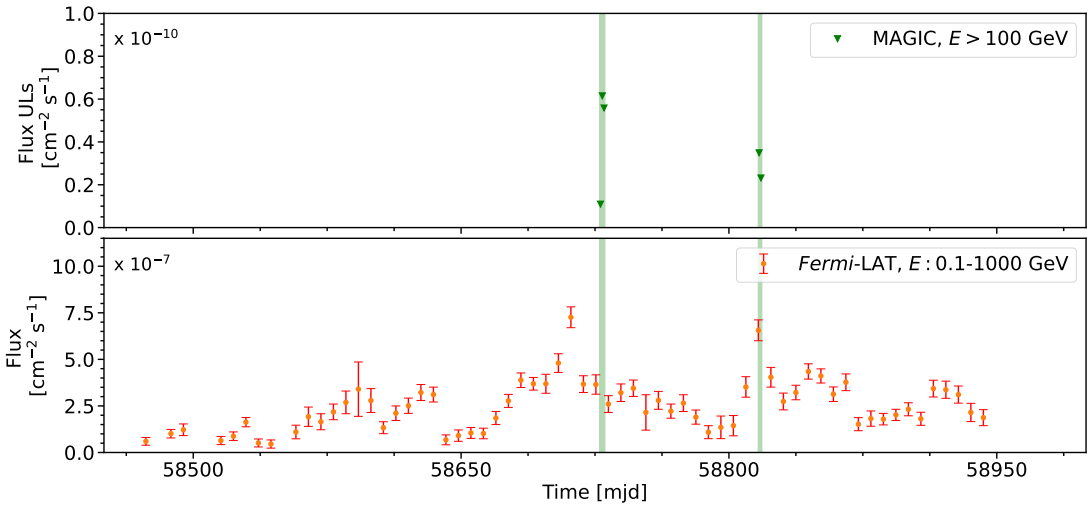

Figure 5.4: Light curve of TXS 0025+197.

during the flares, indicating that external seed photons must exist for the Compton scattering [312]. At the end of 2014 and the beginning of 2015, the source showed unusually powerful optical and radio flares [313, 314]. AO 0235+16 showed increased activity in the optical band at the end of 2015 and the beginning of 2016, triggering the MAGIC observations (see LC in Fig. 5.7). MAGIC collected a total of 6.1 hours of good-quality data from the direction of this source.

4C 55.17 ($z = 0.902$, [301]) is a bright *Fermi*-LAT FSRQ, which made the source a promising VHE emission candidate, due to high brightness and lack of strong variability (a low variability index is reported in all data releases of the 4FGL catalogs). MAGIC monitored this source in the VHE band (during the low state, flux below average $\overline{\phi}_{\mathrm{HE},12}$) from November 2010 to January 2011 for 28 hours of good-quality data. No significant VHE gamma-ray signal above 100 GeV was detected. Integral and differential U.L. of gamma-ray flux were derived [315]. The VERITAS telescope also observed the source for 45 hours between May 2010 and March 2012. These observations showed no significant VHE gamma-ray signal as well [316]. The source state was stable between 2008 and 2020, as shown in Fig. 5.8). To carry out the analysis for this work, I combined archival old ∼30 h data from [315] with the ∼50 h MAGIC observations taken after 2011.

TXS 2241+406 ($z = 1.171$, [303]): While being a promising candidate to emit VHE gamma rays, it also showed exceptional variability in the past time. For the first time in February 2015, *Fermi*-LAT observed a gamma-ray outburst from this source on a daily timescale [317]. TXS 2241+406 was also monitored with KVA, showing optical variability spanning over 2.5 mag. As can be seen in the MWL LC (Fig. 5.9 and Fig. 5.10), the number of flares has drastically increased since 2015 compared to the previous six years of *Fermi*-LAT observations, encouraging monitoring with the MAGIC telescopes. In August 2017, MAGIC followed this source for the first time and subsequently conducted a 27-hour observational campaign from July to December 2019. Unfortunately, during this period, the activity of the source was low, and it was either not detected by *Fermi*-LAT or the flux was below the average *Fermi*-LAT flux $\overline{\phi}_{\mathrm{HE},12}$.

5.3 Gamma-ray emission

I modeled the SED by employing data from *Fermi*-LAT telescope observations and accounting for redshift-dependent absorption by the EBL. Subsequently, I calculated the differential U.L. using data from the MAGIC telescopes, providing insights into the emission properties and the possible additional absorption in the radiation field surrounding BLR. The U.L. were calculated using the method pre-

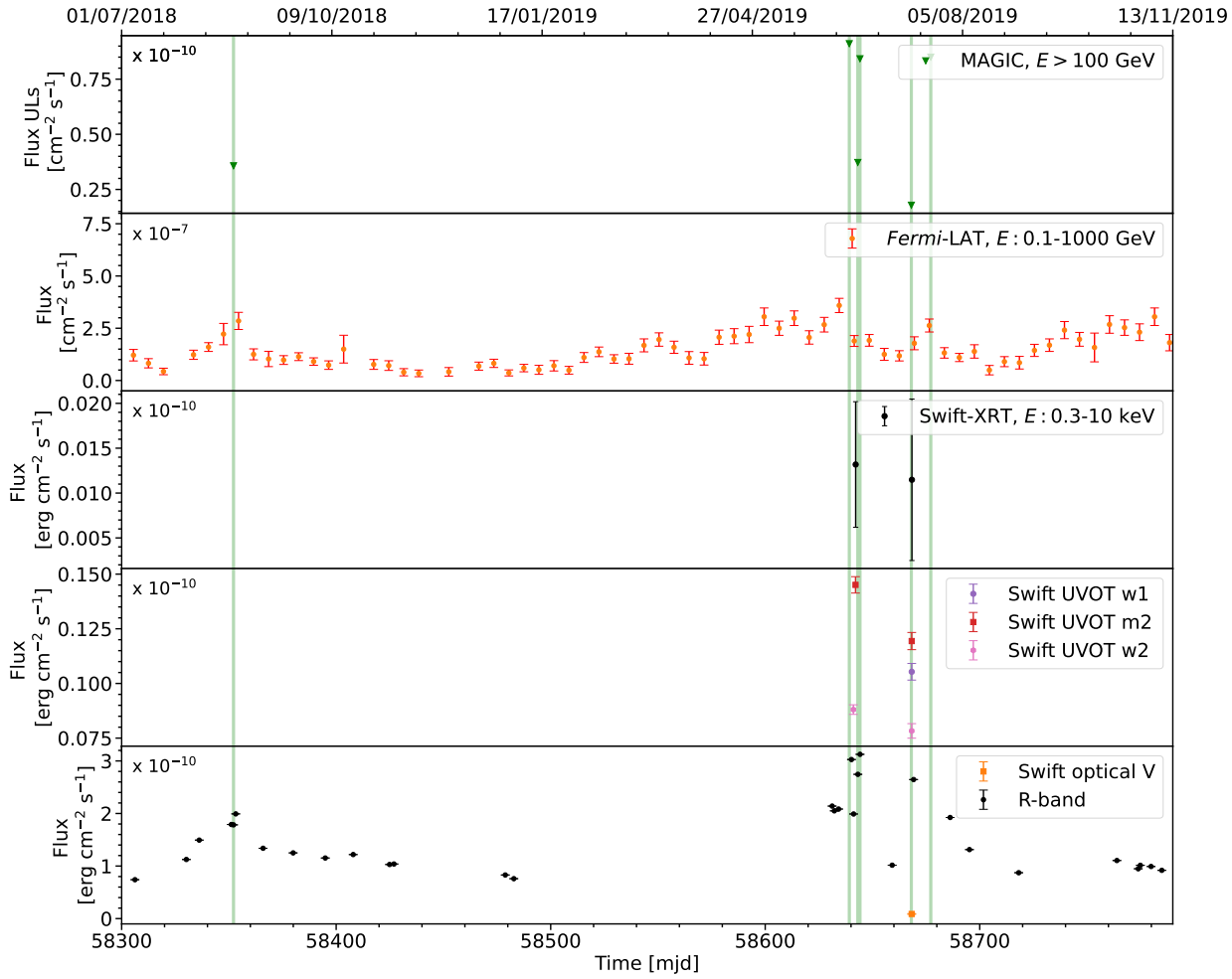

Figure 5.5: Light curve of B2 2234+28A. The green vertical areas indicate the days during which MAGIC observations were carried out. The KVA telescope measured R-band points.

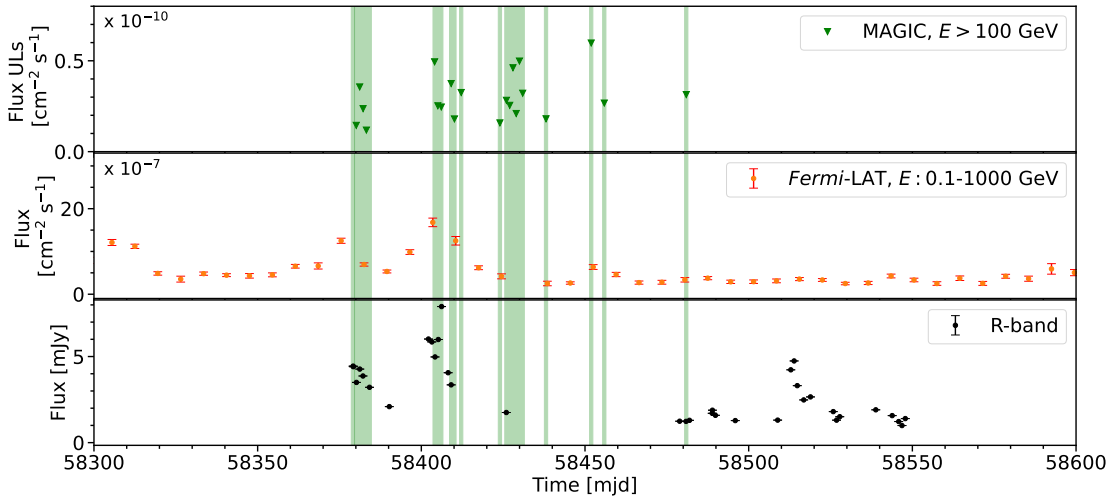

Figure 5.6: Light curve of B2 0234+28.

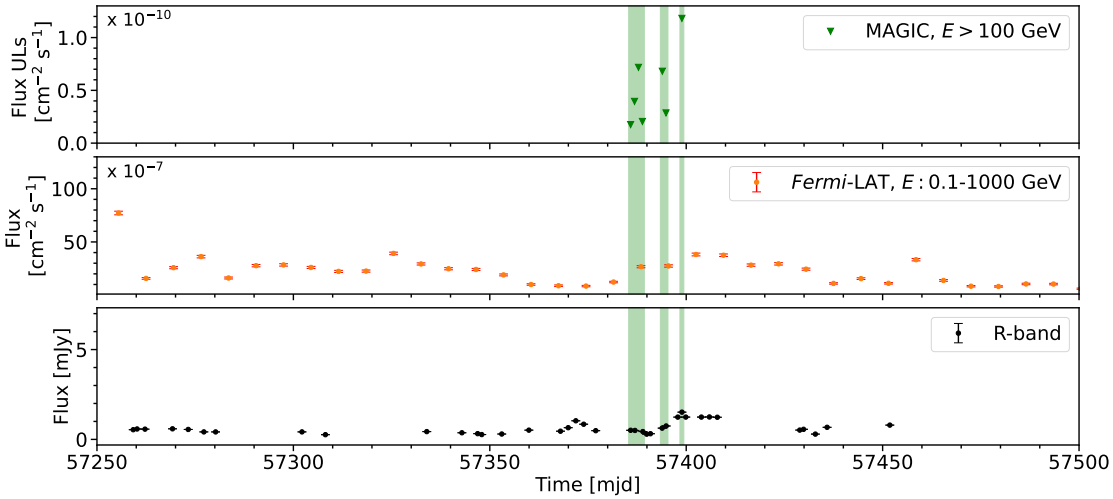

Figure 5.7: Light curve of AO 0235+16.

Table 5.1: GeV emission properties of the FSRQ sample, obtained from 4GFL catalog [91], as well as integral flux measured by *Fermi*-LAT,Φ_{cont} - integral flux for observation in time period contemporaneous to MAGIC observation (0.1-1000 GeV).

Name	R.A. [°]	Decl. [°]	Integral flux (0.1-1000 GeV) 10^{-8} cm^{-2} s^{-1}	Variability index	Φ_{cont} 10^{-8} cm^{-2} s^{-1}
TXS 0025+197	7.12	20.03	1.2 ± 0.2	28	63.4 ± 7.8
J0028.4+2001					
B2 0234+28	39.46	28.80	16.7 ± 0.4	3220	80.3 ± 4.2
J0237.8+2848					
AO 0235+16	39.67	16.62	13.1 ± 0.5	65	20.1 ± 5.1
J0238.6+1637					
4C +55.17	149.42	55.38	8.5 ± 0.3	33	7.3 ± 1.0
J0957.6+5523					
OP 313	197.65	32.35	3.7 ± 0.6	170	9.0 ± 5.1
J1310.5+3221					
CTA 102	338.10	11.73	41.6 ± 0.6	14315	1030.0 ± 20.0
J2232.6+1143					
B2 2234+28A	339.08	28.45	6.6 ± 0.3	388	16.9 ± 4.8
J2236.3+2828					
TXS 2241+406	341.06	40.95	6.3 ± 0.4	3930	1.9 ± 1.7
J2244.2+4057					
3C 454.3	343.49	16.15	215.0 ± 1.0	50905	261.0 ± 8.0
J2253.9+1609					

Table 5.2: Information on data collection by the MAGIC telescopes.

Association name	Exposure [h]	Zenith distance [°]	Significance of excess [σ]	U.L. $E > 100$ GeV 10^{-12} cm^{-2} s^{-1}
TXS 0025+197	5.0	9-35	0.2	13.0
B2 0234+28	25.6	0-36	1.6	4.4
AO 0235+16	6.1	11-26	0.7	20.9
4C +55.17	50.0	26-42	1.5	6.5
OP 313	13.6	4-39	-0.5	9.2
CTA 102	3.2	17-42	1.7	62.4
B2 2234+28A	6.7	1-47	0.5	17.2
TXS 2241+406	29.5	22-35	0.2	2.0
3C 454.3	34.6	12-48	0.6	4.0

Table 5.3: *Fermi*-LAT FSRQ fit model in catalog 4FGL and results of the fit LP model (except 3C 454.3, see text for details) to the *Fermi*-LAT data simultaneous to the MAGIC observations. The index b in the LAT analysis of 3C454.3 during MAGIC observations has been fixed for fit convergence.

Association name	Model	*Fermi*-LAT fit 4FGL		*Fermi*-LAT fit during MAGIC obs	
		α	β	α	β
TXS 0025+197	LP	2.092 ± 0.026	0.108 ± 0.015	2.53 ± 0.24	0.41 ± 0.19
B2 0234+28	LP	2.27 ± 0.02	0.0898 ± 0.0091	2.07 ± 0.06	0.10 ± 0.04
AO 0235+16	LP	2.080 ± 0.018	0.0954 ± 0.0095	1.67 ± 0.17	0.21 ± 0.09
4C +55.17	LP	1.901 ± 0.013	0.0767 ± 0.0067	1.93 ± 0.09	0.03 ± 0.04
OP 313	LP	2.282 ± 0.044	0.104 ± 0.0024	1.98 ± 0.23	0.26 ± 0.01
CTA 102	LP	2.261 ± 0.009	0.1007 ± 0.0060	1.95 ± 0.03	0.05 ± 0.01
B2 2234+28A	LP	2.273 ± 0.018	0.0898 ± 0.0091	1.72 ± 0.23	0.06 ± 0.07
TXS 2241+406	LP	2.088 ± 0.025	0.090 ± 0.013	2.13 ± 0.60	0.65 ± 0.56
3C 454.3	SuperExpPL	$-\gamma_1 = 2.014 \pm 0.010$	$b = 0.5183 \pm 0.0066$	$-\gamma_1$ =0.69 ± 0.05	$b = 0.5183$

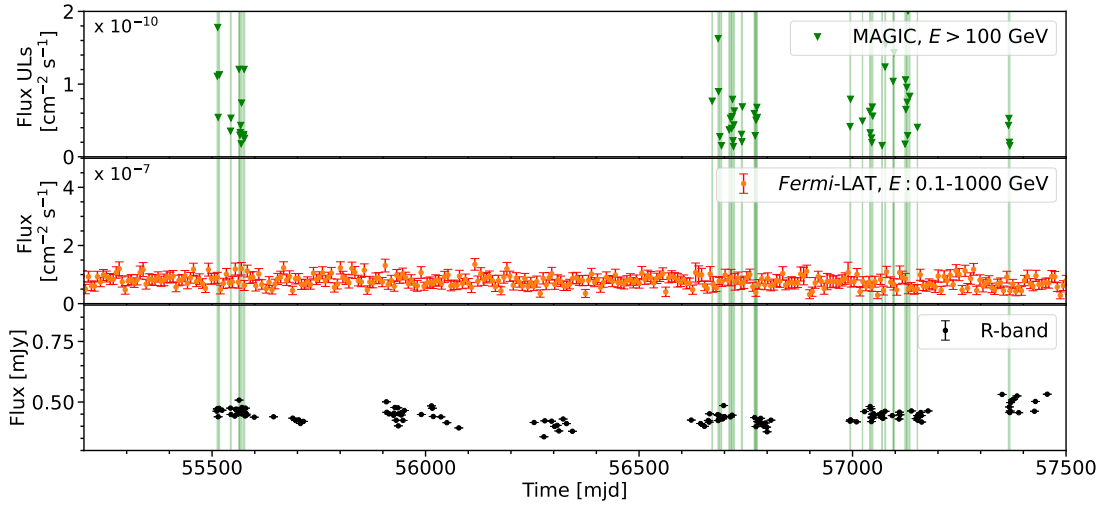

Figure 5.8: Light curve of 4C 55.17.

sented in [318], with a 95% Confidence Level (C.L.). This approach assumes a systematic (Gaussian) uncertainty in the detector efficiency, i.e., the effective area, with a standard deviation of 30%.

Table 5.2 reports the MAGIC observation results for each of the nine FSRQs. No statistically significant signal ($> 5\sigma$ excess) was found for any sources in the VHE energy band. The significance was determined using the Li & Ma formula number 17, as described in [227]. Simultaneous *Fermi*-LAT SEDs analysis was performed following the MAGIC observations. Using MAGIC data, I calculated differential U.L. in 5 energy bins in the energy range from 50 GeV to 500 GeV. The assumed intrinsic spectral index of the gamma-ray photon distribution is α=2.2 for all sources.

Next, I extrapolate the flux for each FSRQ into the VHE range from the *Fermi*-LAT data, considering the absorption of gamma-rays in the EBL following [114] model. This extrapolation operates under the assumption that there are no breaks or cutoffs in the photon spectra between HE and VHE due to particle distribution cooling. Following this, the extrapolated model is compared to the MAGIC U.L. . If the MAGIC upper limits are more constraining than such an extrapolation, it could suggest an absorption-induced cut-off in the VHE range. The combined results of the *Fermi*-LAT analysis and the U.L. from the MAGIC data analysis, along with the HE/VHE SED of all the investigated sources incorporating an EBL attenuation emission model, are presented in Fig. 5.11.

The calculated differential U.L. for seven sources are consistent with the LP model extended from *Fermi*-LAT energy attenuated by EBL. This shows how difficult is to detect with Cherenkov telescope emissions from distant FSRQs due to their rapid variability and EBL absorption. Notably, some of the non-detected sources were in highly elevated flux (e.g., TXS 0025+197 was a factor of ∼50 above the average 4FGL flux). For four sources, the MAGIC U.L. lie above the *Fermi*-LAT extrapolated model, and for three of the sources, the U.L. are close to the *Fermi*-LAT extrapolated model.

Finally, the remaining two sources, B2 2234+28A and CTA 102, the MAGIC U.L. around 100 GeV, are below the *Fermi*-LAT EBL extrapolation model. Therefore, those two objects are plausible candidates for sources in which absorption in BLR could introduce an extra cut-off. I further investigate this possibility in the next section 5.4.

5.4 Modelling

As a result of my analyses, two sources, B2 2234+28A and especially CTA 102, showed a hint of cut-off in the HE/VHE SED that cannot be explained only by the EBL absorption. In the case of B2 2234+28A, if we also consider uncertainties with the EBL extrapolation, the EBL absorption might

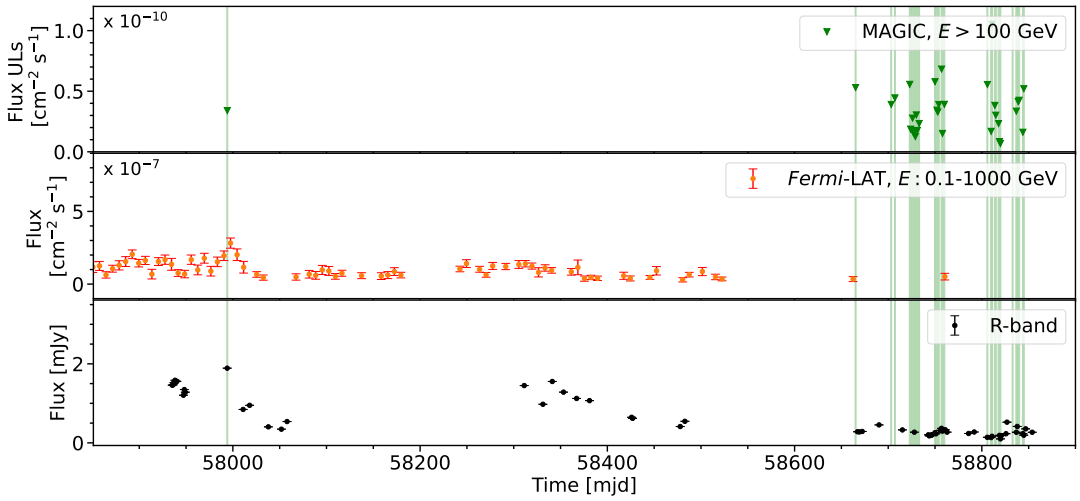

Figure 5.9: Light curve of TXS 2241+406.

explain the cut-off; in the case of CTA 102, the change of behavior from HE to VHE is more robust. Subsequently, I investigated the possibility of explaining this effect with additional absorption in the BLR for these two sources.

The methodology approach to constrain the distance between the black hole and the emission region (a blob) R_{blob_BH} and check its consistency using the broadband model involves two types of models. Firstly, modeling the shape of the SED in HE and VHE ranges (*Fermi*-LAT flux measurements and MAGIC U.L.) allows us to estimate R_{blob_BH} that could introduce the necessary level of absorption of VHE gamma rays. This is done using a phenomenological model that assumes extrapolation of intrinsic GeV emission into the VHE range. The absorption in the BLR radiation field is introduced, and the resulting spectrum is compared with the MAGIC U.L. on the flux. Secondly, I consider a broadband emission model, which tests the underlying blazar physics and parameters from the phenomenological study. This broadband emission model is used to check the consistency of the previous results obtained using the phenomenological model. However, improvement in `agnpy` was needed to perform modeling in a robust and efficient way.

5.4.1 Enhancing `agnpy` for effective modeling of FSRQ emission

During my research stay in Barcelona, I focused on enhancing and extending a computational module designed to calculate absorption phenomena in the BLR. This development was crucial to my work on modeling the absorption in FSRQ objects.

Calculating absorption in BLR, especially when we want to consider many lines, including in the BLR model, is a rather resource-demanding numerical task as it involves (energy-dependent) four-dimensional integral. Originally `agnpy` utilized a simple composite trapezoidal integration rule that was numerically inefficient. Moreover, the infinitesimal thickness of the BLR spheres occasionally resulted in large numerical errors (if one of the integration points was close to the location of one of the BLR spheres). To improve numerical stability, I implemented a new method in `agnpy` using the `CubePy`[3] package created by Alex Reustle. `CubePy` is a Python package that allows for efficient numerical integration of multi-dimensional vector functions using Genz-Malik adaptive cubature algorithm [319, 320]. The Adaptive Genz-Malik Cubature Scheme [319, 320] is an advanced numerical method for calculating multidimensional integrals. Developed by Alan Genz and Abid Malik, this scheme is a refined version of the cubature formula, specifically tailored for high-dimensional spaces

[3] https://github.com/Areustle/cubepy

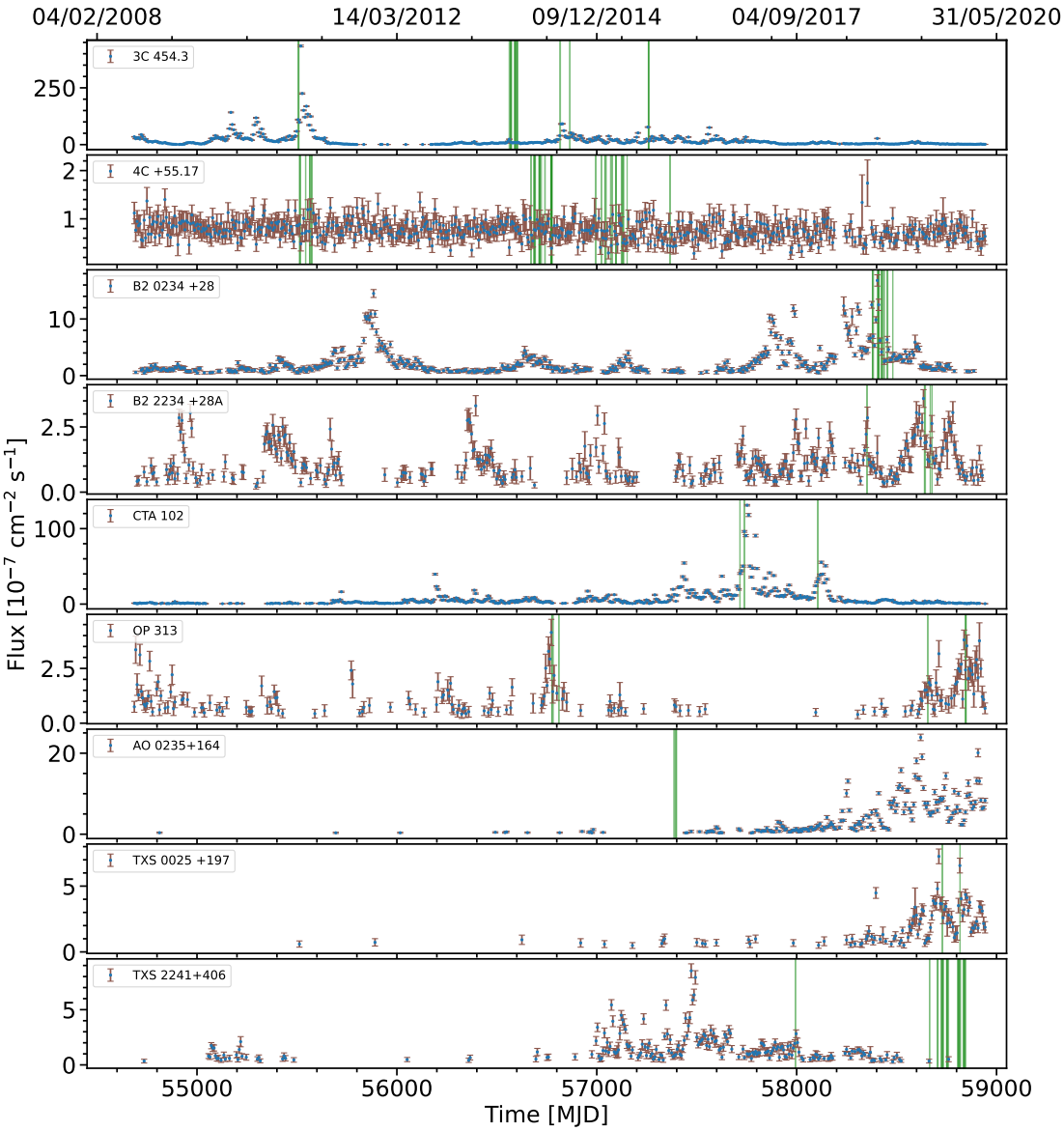

Figure 5.10: *Fermi*-LAT light curve representing data from 2008 to 2020. The green vertical areas on the graph indicate the specific days when MAGIC observations were carried out. This data is presented in weekly bins with an energy range of 0.1 - 1000 GeV.

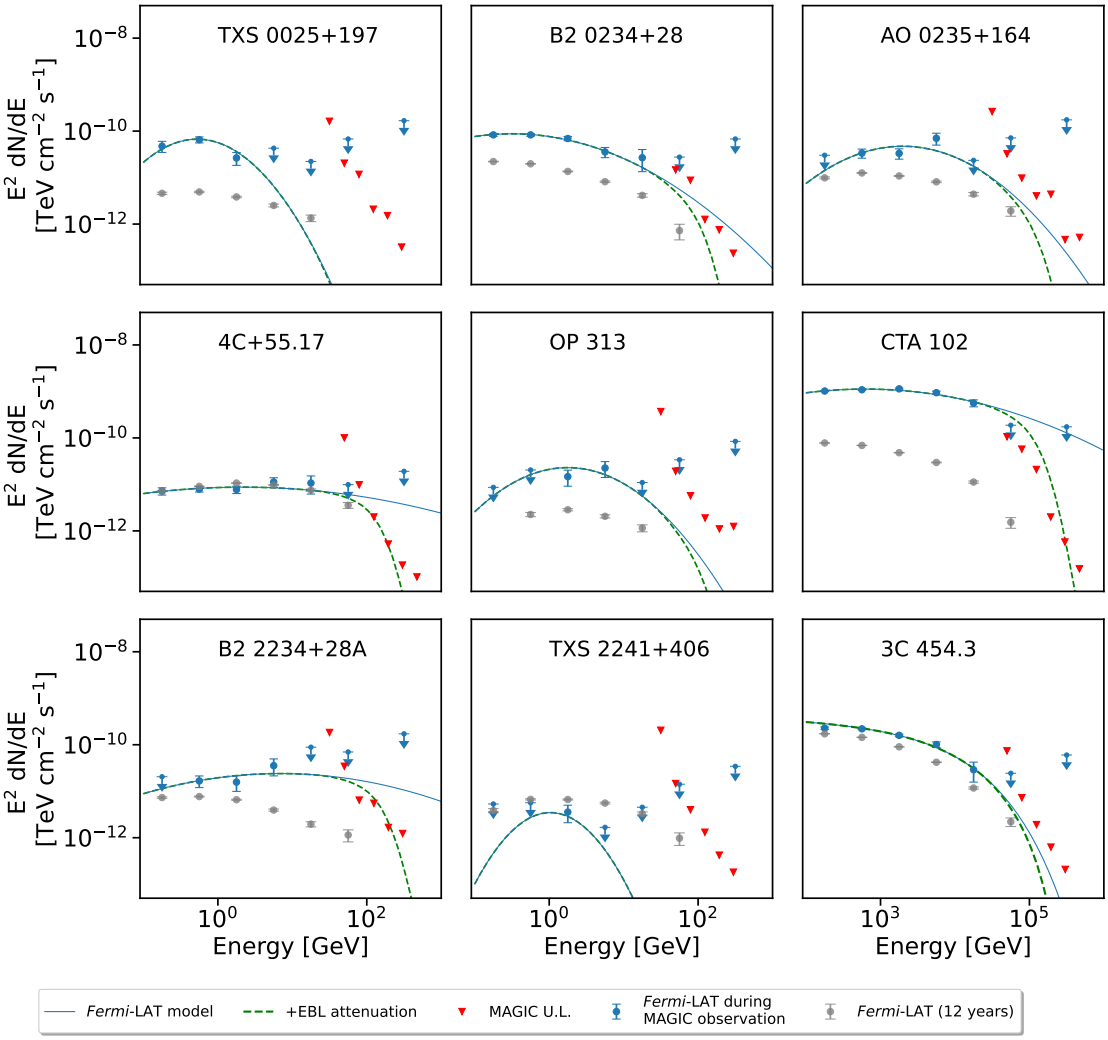

Figure 5.11: Comparisison of *Fermi*-LAT and MAGIC measurements of SED for all studied sources. The spectra simultaneous to MAGIC observations are shown with a blue solid line. The spectra extrapolated at VHE considering the EBL absorption are shown with a green dashed line. SED points (gray dots) from data collected by *Fermi*-LAT over a period of 12 years show the average state of each source.

where traditional methods like Monte Carlo simulations or quadrature are likely to be inefficient. One of the standout features of integrands is their adaptivity. Integrands adjust to the integrand's local characteristics, enabling more accurate and efficient calculations than non-adaptive methods. This adaptability is particularly beneficial when dealing with complex, variable functions. Another key aspect is its reliance on cubature formulas [321]. These formula functions are integrals using weighted sums of the function's values at specific points. In the Genz-Malik scheme, these points and weights are strategically selected to maximize accuracy and efficiency. This method highlights multidimensional problems often encountered in applied mathematics, physics, and engineering. The Genz-Malik scheme is optimized to reduce computational efforts while still maintaining a high level of precision.

The `CubePy` is fully vectorized, making it a powerful tool for scientific computing. I implemented methods to evaluate the $\gamma\gamma$ absorption produced by a spherical shell BLR for a general set of model parameters with `CubePy`'s integration method. Improving the algorithm's performance is crucial for using the absorption calculation in fitting procedures, which was necessary to create an emission and absorption model for the studied FSRQs.

secondly, I have expanded `agnpy`'s functionalities to incorporate fitting models for the multi-shell BLR, which was needed for accurately modeling FSRQ emissions and considering absorption in complex BLR structures.

Numerical instability

The problem I encountered when calculating absorption in the BLR was numerical instability, which manifests through significant changes in the absorption coefficient over a small change in the distance from the emission region of the black hole. This issue, resulting from the limitations of the default trapezoidal integration, I resolved using a more advanced integration method based on the adaptive Genz Malik Cubature scheme [319], approach from the *cubepy* library.

Figure 5.12 compares the optical depth plotted against the relative distance from the black hole. The calculations were done using the standard trapezoidal method and the `cubepy` approach for photons with 100 GeV energy. It is evident that the standard trapezoidal method resulted in instability at certain distances, in most cases leading to stronger absorption than what is expected from the model due to numerical instability.

5.4.2 Applied model of BLR

The empirical stratified BLR model from [189] is applied to study the emission from blazars surrounded by BLR. It relies on the reverberation mapping method of AGNs [322, 323]. It assumes that accretion disk radiation is absorbed by the BLR clouds surrounding the emission and re-emitted as monochromatic lines. Each line has individual intensity and distance from the accretion disk. A similar approach was used in a study of 3C 279 [324].

My BLR model comprises 26 concentric infinitesimally thin spherical shells containing gas, each producing a single emission line from Ly*epsilon* to H*alpha*. The radii and luminosities of individual lines of the BLR are required to calculate the gamma-ray production and absorption. I estimated the luminosity of the disk, $L_{\rm disk}$, and the luminosity and radius for each of the 26 concentric shells for both sources using the stratified BLR model. Instead of directly measuring the radius of individual lines in the BLR using the Hβ emission, which is relatively weak, I derived these values by scaling from a stronger line, specifically Mg II, using ratios reported by [189]. All other shell luminosities and radii were then scaled based on the one emitting the Mg II line. To achieve this scaling, I employed the following relation, which is based on the reverberation mapping of AGN objects:

$$R(\mathrm{H}\beta) = 10^{16.94\pm0.03}\left(\frac{L(5100\,\text{Å})}{10^{44}\text{erg s}^{-1}}\right)^{0.533\pm0.035}\ \text{cm},$$
$$\left(\frac{L(5100\,\text{Å})}{10^{44}\text{erg s}^{-1}}\right) = \left(\frac{L(\mathrm{H}\beta)}{(1.425\pm0.007)\times10^{42}\text{erg s}^{-1}}\right)^{0.8826\pm0.0039}$$

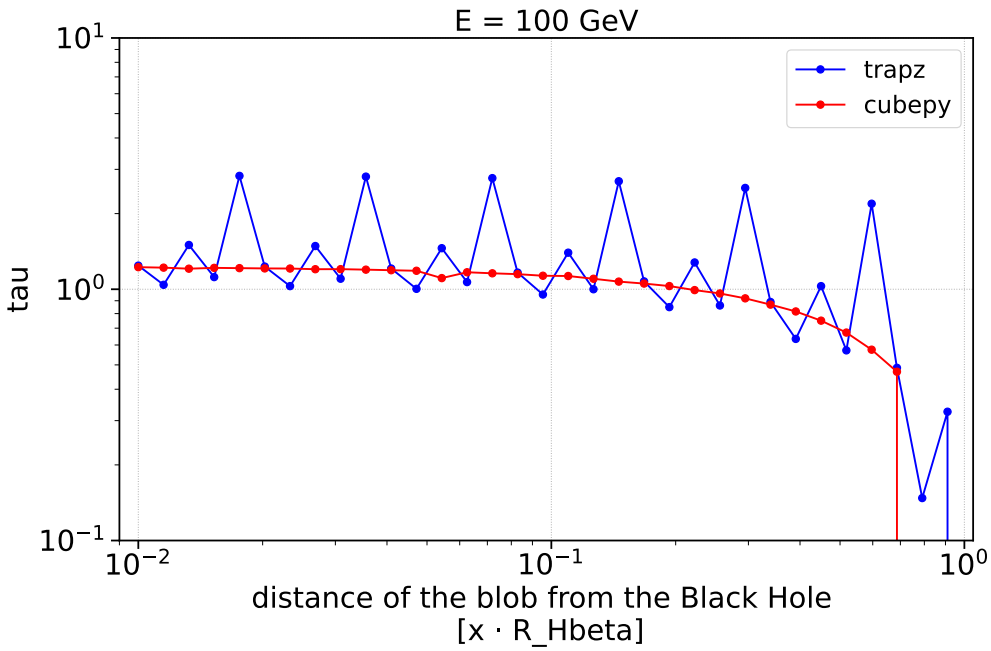

Figure 5.12: Comparison of optical depth (τ) as a function of the relative distance from the black hole calculated using the standard trapezoidal method (blue) and with `cubepy` (red). In this example, CTA 102 with the following parameters: Disk luminosity L = 8.93×10^{43} erg/s, $\xi_{line} = 0.1$, $R_{H\beta} = 5.13 \times 10^{17}$ cm.

as described in [325] and [323]. To derive the necessary values of the Hβ line from those of MgII, I used the relative line luminosities L(MgII) and L(Hβ) from [43] and converted these values using the broad emission line parameters from [189], namely $L(\text{MgII})/L(\text{H}\beta) = 1.7$. With the method described above, I derived the following luminosity $L_{H\beta}$ and radius $R_{H\beta}$ for line Hβ values for CTA 102: $L_{H\beta} = 6.7 \cdot 10^{43}$ erg s^{-1} and $R_{H\beta} = 5.13 \cdot 10^{17}$ cm, for B2 2234+28A: $L_{H\beta} = 1.62 \cdot 10^{43}$ erg s^{-1} and $R_{H\beta} = 2.67 \cdot 10^{17}$ cm. The distances and luminosities of the remaining lines are scaled following values from Table 5 in [189].

5.4.3 Phenomenological model

The contemporaneous observations of CTA 102 and B2 2234+28A by *Fermi*-LAT and MAGIC telescopes allowed for a combination of the *Fermi*-LAT spectral fit and the MAGIC U.L. to constrain the minimum distance of the emission regions to the black holes R_{blob_BH}. To constrain the distance of the emission region from the black hole, I used the *Fermi*-LAT fit model, considering both EBL and BLR absorption features in SED. I vary the BLR absorption level by varying the distance of the emission region from the black hole with steps of 0.1 $R_{H\beta}$. By comparing this fit model with EBL and BLR absorption with the measured U.L., I can put constraints on the location of the emission region from the black hole. In order to determine the BLR absorption, I utilized the complete set of lines from Table 5 in [189]. To ensure greater precision in the multi-dimensional integration process, I employed the `agnpy` modeling package [184], which also incorporated advanced numerical techniques from `cubepy`[4] (see section 5.4.1) that I personally implemented.

The *absorption* module and the *SphericalShellBLR* geometry from the *agnpy* package were used to construct the phenomenological model. Under the assumption that the steepening/cut-off of the gamma-ray emission in the VHE band is due to the absorption in the BLR, I place a constraint on the maximum distance between the black hole and the emission region R_{blob_BH}. For CTA 102 I obtain

[4] https://github.com/Areustle/cubepy

$R_{blob\_BH} < 1.5 \cdot R_{H\beta}$ and for B2 2234+28A I got a similar value of $R_{blob\_BH} < 1.6 \cdot R_{H\beta}$. Fig. 5.13 shows gamma-ray SEDs from CTA 102 and B2 2234+28A, the two sources for which an additional steepening caused by internal absorption can be invoked to make the extrapolation of GeV emission consistent with the VHE U.L. It is important to note that a cut-off in the gamma-ray spectrum at high energies does not always indicate absorption in the BLR.

The dependency of the integrated disk radiation reprocessed in all the shells located farther than a given distance of the emission region is shown in Fig. 5.14. The plot demonstrates that, according to the used method, it suffices that the emission region is located within the radiation field of a small fraction of the BLR (about 1/10 of the BLR, corresponding to approximately 1% of the disk brightness) to induce the required level of absorption. The distance is large enough that the emission region is within the outermost part of the BLR. However, even this location provides sufficient absorption to explain the *Fermi*-LAT and MAGIC data. Other factors, such as the cut-off in the emitting particle distribution, can also explain this phenomenon [87]. Therefore, in the next section. I performed broadband modeling to validate this hypothesis.

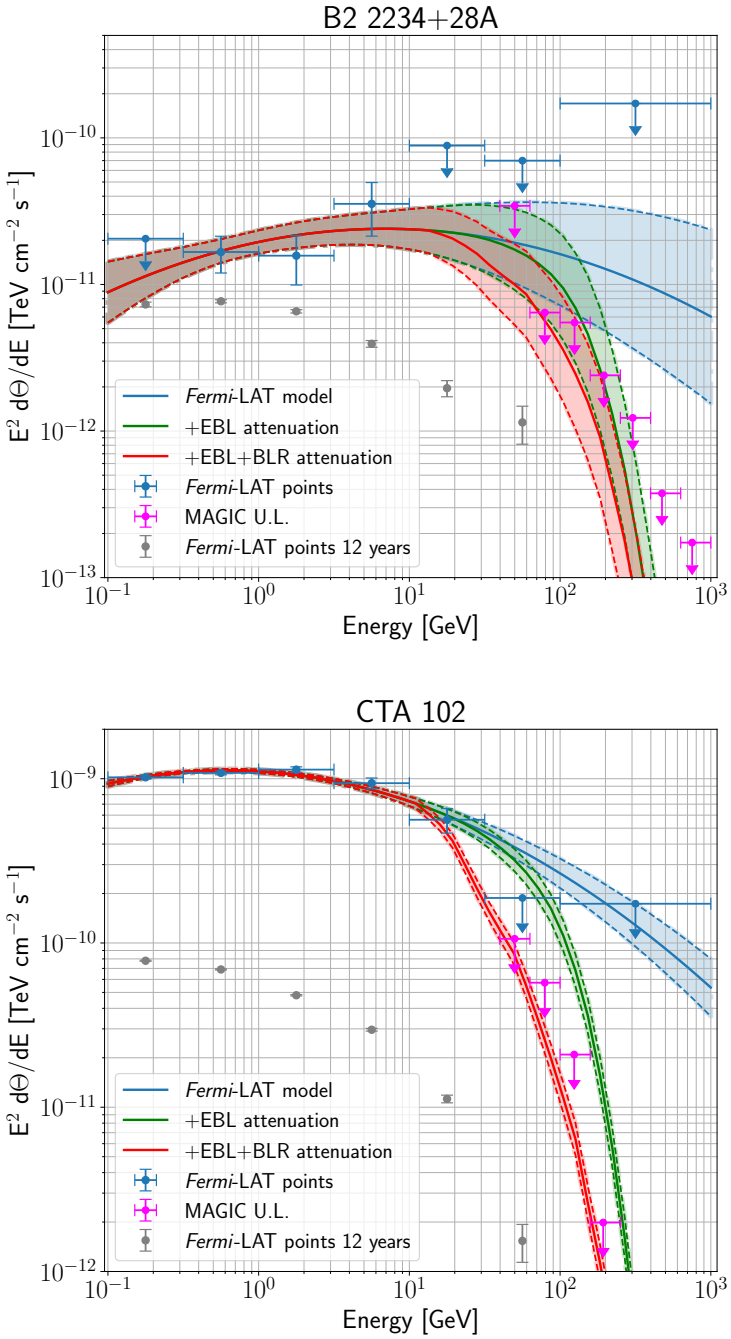

Figure 5.13: SED of CTA 102 (on the top) and B2 2234+28A (on the bottom) in HE and VHE range: derived VHE differential upper limits (95 % C.L.) on the flux by MAGIC (magenta markers) and *Fermi*-LAT (blue markers) spectrum obtained during the MAGIC observation period (blue points). A blue solid line depicts a spectral fit of *Fermi*-LAT emission with the LP model. The spectrum is shown taking into account the uncertainty of the parameters obtained when fitting the *Fermi*-LAT data (shaded region). The spectrum attenuated with EBL model [114] is shown with a green line. The red line shows the spectrum, taking into account the uncertainty of the parameters obtained when fitting the *Fermi*-LAT data (shaded region).the spectrum after considering additional absorption on multiple BLR lines. The spectra points of B2 2234+28A and CTA 102 obtained in 12 years of *Fermi*-LAT observations are also shown (gray dots).

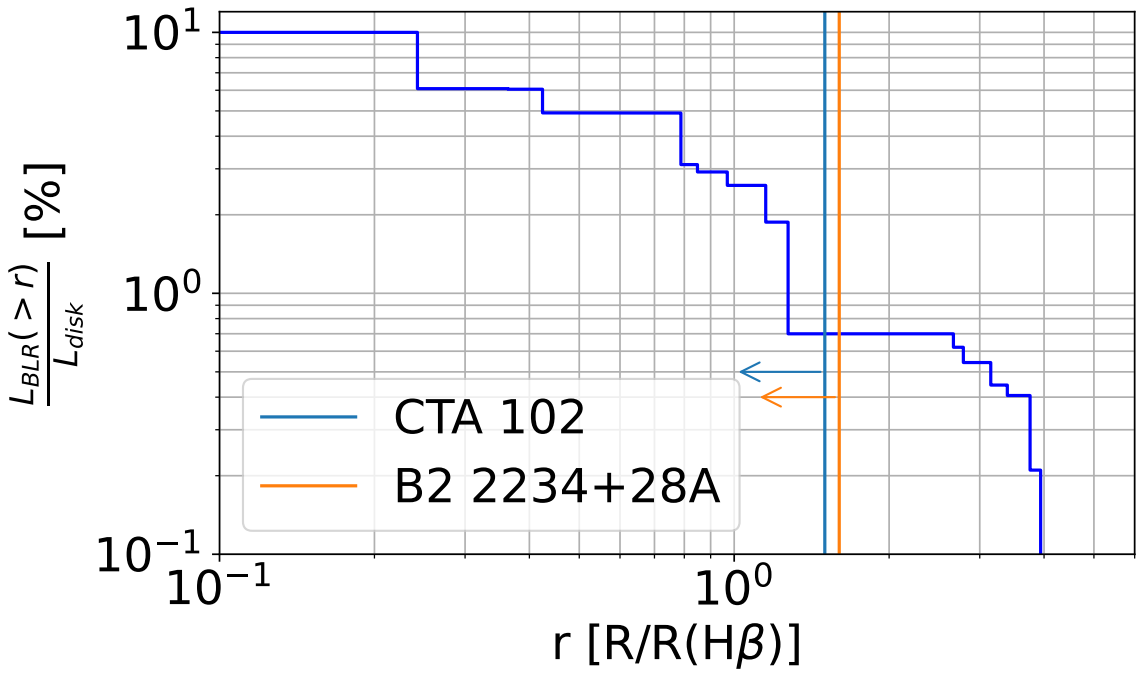

Figure 5.14: Percentage (in blue), $L_{BLR}(> r)/L_{disk}$, of the disk radiation reprocessed in shells located farther than the distance r from the black hole, according to the used BLR model. The distance from the emission region is normalized to the radius of the Hβ line. Vertical lines show the derived maximum distance from the black hole for the two studied sources to have sufficient BLR absorption to explain the lack of the observed VHE gamma-ray emission.

5.4.4 Broadband modeling for constraining physical conditions of the VHE gamma-ray emission of FSRQ

In the previous section, I determined the distance between the emission region and the black hole, denoted as R_{blob_BH}, in a phenomenological way based on observations made by the *Fermi*-LAT and MAGIC telescopes. I now compare these obtained values with a physical model that describes the broadband emission of the jet.

One-zone SSC models and EC models are typically utilized to model the gamma-ray emission from FSRQs [27]. Additionally, a DT surrounds the central engine on a pc scale. The radiation field of the accretion disk, reprocessed in the BLR and DT, provides additional targets for the IC process and gamma-ray pair production absorption. Given the studied sources do not exhibit significant VHE photon emission, the most straightforward target for the EC model would be the BLR radiation field, which strongly absorbs VHE gamma rays in the sub-TeV range. I assembled data from KVA, *Swift*-UVOT, *Swift*-XRT, *Fermi*-LAT and U.L. from the MAGIC telescopes to construct broadband SEDs of B2 2234+28A and CTA 102. Both sources are modeled in a framework of a simple one-zone leptonic model with *agnpy*, in which a spherical emission region with a radius R_{blob} is isotropically and homogeneously filled with a magnetic field B and electrons. The electron spectrum is described by a broken power-law electron energy distribution with spectral normalization k_e and spans from γ_{min} to γ_{max} with indices p_1 and p_2 below and above the break at γ_b, differential number density K_e at γ_b. The single emission region propagates along the jet with the bulk Lorentz factor Γ at an angle $\theta = 0°$ to the line of sight, which implies that the corresponding Doppler factor δ_D is assumed to equal 2Γ. I assume that the emission region is situated at a distance that explains the steepening of emission due to the absorption derived in the phenomenological study (see subsection 5.4.3).

In my model, the radiation field consists of multiple lines from the corresponding BLR shells and also the thermal IR radiation from the DT. The DT is assumed to be an infinitesimally thin ring with typical temperature $T_{dt} = 10^3$ K [189], and the radius of the ring representing the torus $R_{dt} = 3.5 \cdot 10^{18}(L_{\mathtt{disk}}/10^{45}\mathtt{erg\ s\text{-}1})^{1/2} \times (T_{\mathtt{dt}}/10^{3}\mathtt{K})^{-2.6}$ cm is estimated from [189]. The model also includes a synchrotron (taking into account the synchrotron self-absorption) and an SSC process, which are responsible for the emission in the radio and X-ray energy ranges, respectively. The procedure checks whether the DT emission does not surpass the synchrotron radiation. While the contribution of DT thermal emission to the SED of the MWL is typically considered for FSRQs, it is often hidden by the dominant synchrotron emission. To assess this, I use the single-temperature black-body radiation computed with *agnpy*. Therefore, to check the self-consistency of the modeling, I will determine if the DT emission is significantly lower in magnitude compared to the synchrotron emission.

My model assumes that the emission region is outside most of the shells in the BLR, as shown in Fig. 5.14. The radius of the emission region is established according to the formula $R_{blob} = R_{blob\_BH}/\Gamma$, i.e., assuming a conical jet with a half-opening angle of $\sim 1/\Gamma$. For CTA 102, I selected a Doppler factor δ_D of 40, comparable to the value of 34±4 obtained from VLBI radio measurements (that observe the source at larger scales) to explain HE emissions [326]. For B2 2234+28A, I used $\delta_D = 13$ as a weighted average Doppler factor value for the FSRQ from *VLBA-BUBLAZAR* study [164]. I will further discuss another value of the Doppler factor for B2 2234+28A in this chapter. The model parameters (K_e, p_1, γ_b, γ_{max}, B) have been estimated by fitting the SED with the open source package `gammapy` (see section 3.4.4) using a *Synchrotron, SynchrotronSelfComtpon, and ExternalCompton* classes from `agnpy`. I assume a classical cooling break setting $p_2 = p_1 + 1$. The fitting procedure was performed, taking into account a simplified systematic error on the flux points. I use a conservative estimation of the systematic errors, i.e., 10% for the HE and X-ray instruments and 5% for the optical telescopes. The result of the fitting is shown in Fig 5.15, while the parameters are given in Table 5.4. The absorption processes in both EBL and BLRs can affect the modeling and interpretation of the data. The modeling results are corrected by considering the absorption on those two radiation fields (red solid line). I test the constraint on the distance between the emission region and the black hole to be $< 1.5 \cdot R_{H\beta}$ for CTA 102, and $< 1.6 \cdot R_{H\beta}$ for B2 2234+28A from the previous section. Broadband modeling with the leptonic model performed in this section indicates that it is possible to reconstruct the observations with constraints from the phenomenological model.

Table 5.4: Parameters used for modeling sources with `agnpy`, utilizing an emission region represented as a blob, DT, and BLR. Parameters K_e, p_1, γ_b, γ_{max}, B were derived during the fitting process, p_2 was fixed to p_1+1. $R_{blob_BH}$was estimated using the phenomenological model. The remaining parameters were fixed according to the information gathered from the literature (see text). Electron, U_e, and magnetic field, U_B, energy density are derived from the fitting parameters. B2 2234+28A and B2 2234+28A* are different modelings of the same source for two different assumptions of Delta factor (average weighted values from BUBLAZAR study) and CTA 102-like valu

parameter	CTA 102	B2 2234+28A*	B2 2234+28A
Mass [10^8 $M_\odot$]	12.30	2.75	2.75
$R_{blob\_BH}[R_{H\beta}]$	1.5	1.6	1.6
emission regions			
$p1$	1.97 ± 0.02	2.34 ± 0.06	2.18 ± 0.08
$p2$	2.97	3.34	3.18
δ_D	40	40	13
R [10^{15} cm]	28.5	20.8	61.0
K_e [10^{-5} cm^{-3}]	546 ± 24	3.39 ± 0.04	4.47 ± 0.05
Γ	20.5	20.5	7
γ_b	850 ± 2	1482 ± 7	5929 ± 271
γ_{min}	1	1	1
γ_{max}	8616 ± 19	13 044 ± 60	16 292 ± 4021
B [Gauss]	1.12 ± 0.04	1.73 ± 0.31	0.52 ± 0.03
Dusty Torus			
ξ_{dt}	0.6	0.6	0.6
T_{dt} [K]	1000	1000	1000
R_{dt} 10^{17} [cm]	159	78	78
Broad-Line Region			
$R_{H\beta}$ [10^{17} cm]	5.13	2.67	2.67
$L_{H\beta}$ [10^{43} erg /s]	6.7	1.62	1.62
ξ	0.1	0.1	0.1
U_e [erg /cm^3]	0.022	0.0040	0.027
U_B [erg /cm^3]	0.047	0.1191	0.011

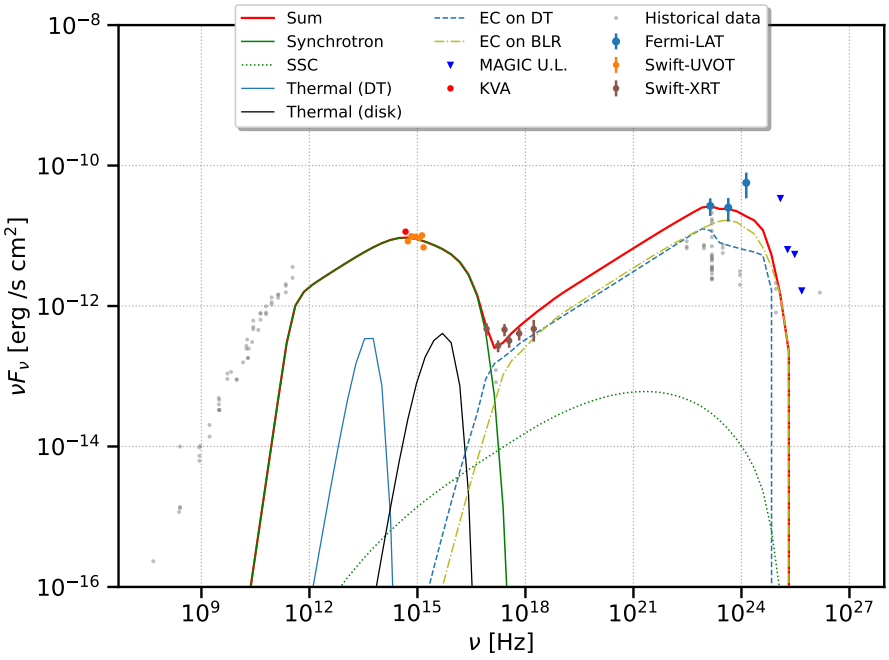

(a) B2 2234+28A

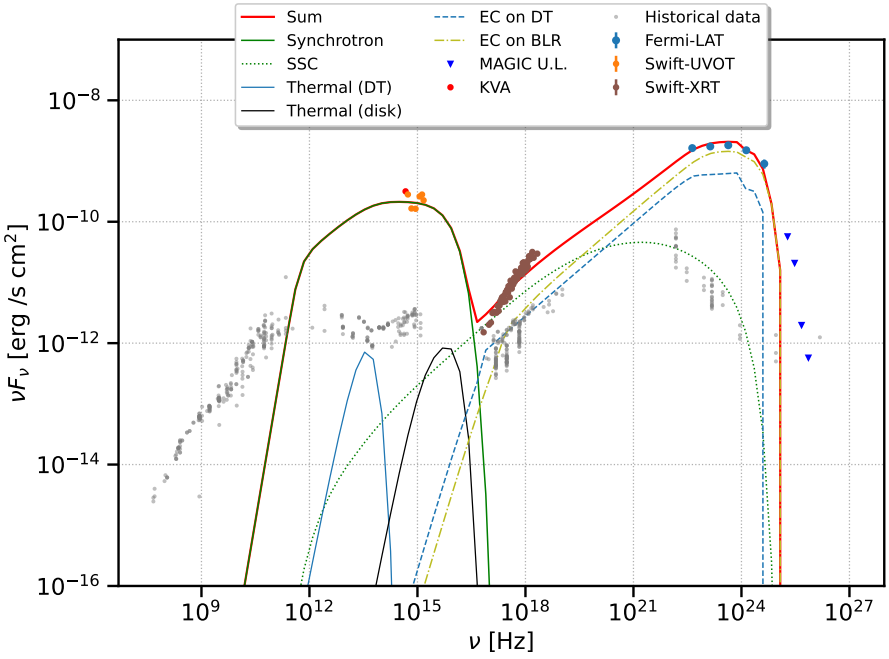

(b) CTA 102

Figure 5.15: Broadband modeling with agnpy of B2 2234+28A (top panel) and CTA 102 (bottom panel). The solid red line shows the overall emission modeled. The low-energy peak is dominated by synchrotron radiation (green solid line), and the high-energy peak is dominated by the emission produced in the external Compton mechanism using the seed photons from DT (blue dashed line) and BLR produced in 26 shells (yellow dash-dot line). Gray points – archival data from the Space Science Data Center - ASI [327].

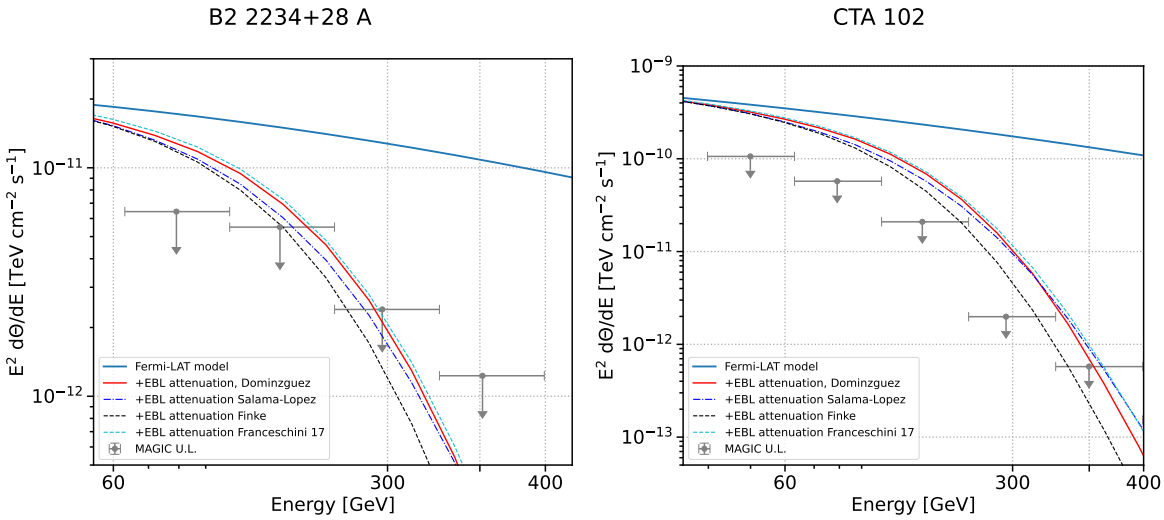

Figure 5.16: HE/VHW SED for B2 2234+28A and CTA 102. The lines show *Fermi*-LAT spectrum extrapolation with attenuation with the most popular EBL models: Franceschini [112], Finke [113], Domínguez [114], Saldana-Lopez [115]. The points show the derived upper limits from MAGIC measurements.

5.4.5 Influence of the EBL model discussion

I have analyzed nine sources and identified two that require further investigation due to potential BLR absorption. B2 2234+28A is one such source that shows U.L. consistent with the EBL-absorbed spectrum, albeit with a caveat—when accounting for the uncertainties associated with the *Fermi*-LAT data extrapolation. In the initial analysis, I applied the EBL model from [114] to all sources under investigation.

I conducted further testing on an alternative EBL model to determine if the selected model influenced the conclusion regarding the existence of a cut-off. Numerous EBL models have been developed to tackle absorption in EBL. I evaluated three alternative EBL models to analyze the HE/VHE SED for CTA 102 and B2 2234+28A. As depicted in Fig. 5.16, additional BLR absorption is required to account for the observed upper limit points, regardless of the particular model utilized.

5.4.6 Broadband modeling discussion

As there is no measurement available of the superluminal motion on B2 2234+28A, initially, I used the average FSRQ value (over blazar sample studied in radio frequency) Doppler factor δ_D=13 for this source. However, as a test, I also considered a higher Doppler factor of 40, corresponding to what was used for CTA 102 during a strong flare. This is to potentially observe enhanced emissions, as the high Doppler Factor in CTA 102 flare suggests increased activity.

Comparisons between models that use these two Doppler factors are shown in Fig. 5.17, with the model parameters explained in Table 5.4. As seen in the figure, setting δ_D to 13 enhances the importance of SSC. However, the dominant contribution to high-energy emission remains the same, which is a combination of EC on DT and BLR, even with δ_D=40.

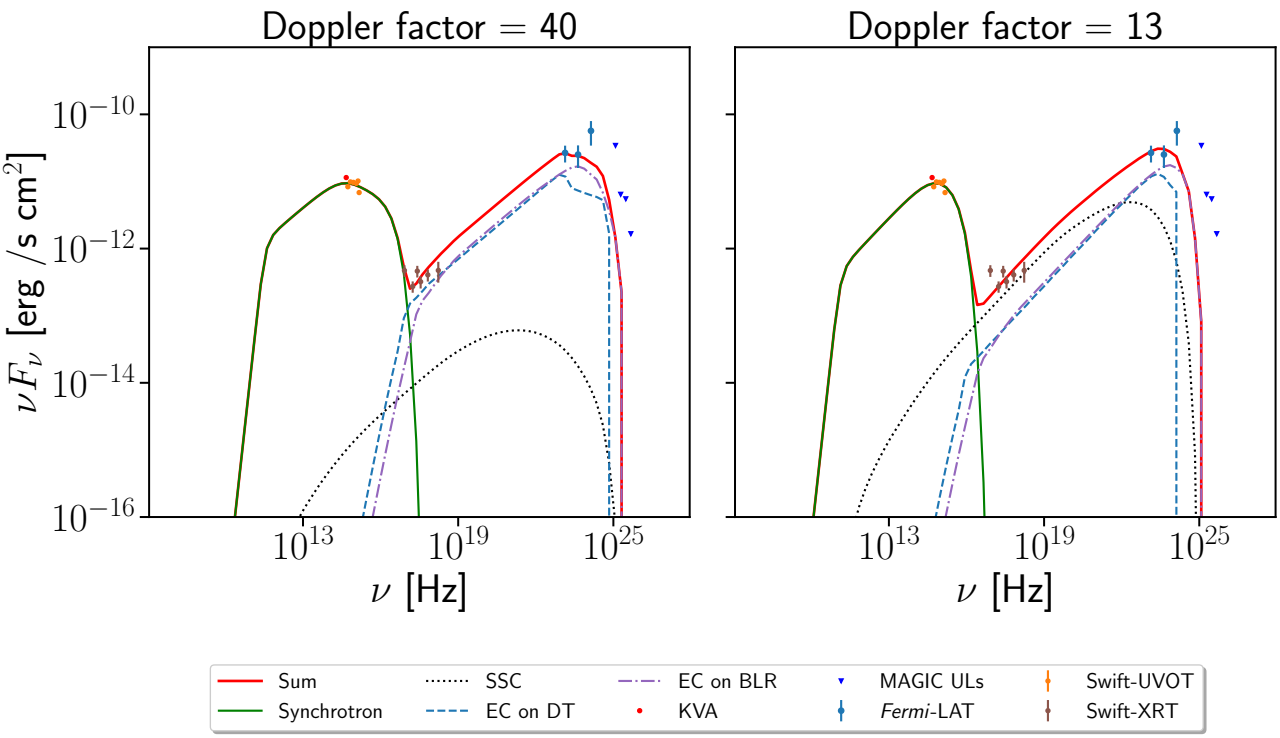

Figure 5.17: Two broadband fits for B2 2234+28A: Comparative modeling with different δ_D=13 and 40.

Points derivation from broadband fit

The plot in Fig 5.15 displays the fitting model for B2 2234+28A. The plot shows that most of the data points obtained from KVA, *Swift*, and two points from *Fermi*-LAT fit well with the model. However, there appears to be one *Fermi* point, which shows an apparent deviation from the line represented by the model. Upon closer inspection, it is found that the deviation has a value of 1.62 σ, which is still within an acceptable range of statistical fluctuations.

The analysis of the broadband fit spectrum for CTA 102 reveals an interesting observation. The *Swift*-XRT spectrum appears to deviate from the fit. This deviation is noteworthy as both the data and the model exhibit characteristics resembling a power-law distribution at this points, as shown in Fig. 5.18. The difference can be caused by a number of reasons: simplifications of the modeling (consideration of only one zone, homogeneity, and isotropy, usage of equilibrium EED, ...) and non-strict simultaneity of the data. To further investigate this deviation, I fit a power-law function to the data and model and compare the differences. The broadband model has a softer spectrum compared to the XRT data. However, the difference in the index is only 0.3.

Two approaches for modeling emission

In this section, I compare the consistency of the two methodologies used to determine the position of the emitting region. Specifically, I am curious about whether a log-parabola intrinsic spectrum is consistent with the later source modeling.

I utilized two partially independent approaches. Firstly, I conducted a naive extrapolation of the *Fermi*-LAT spectrum, using only the EBL absorption. From this approach, I discovered that the MAGIC limits fall below the extrapolation. At the assumption that the VHE flux is decreased due to absorption in the BLR, I calculated the maximum distance of the emission region using this methodology. However, different explanations are possible, such as those due to the cutoff in the electron maximum energy.

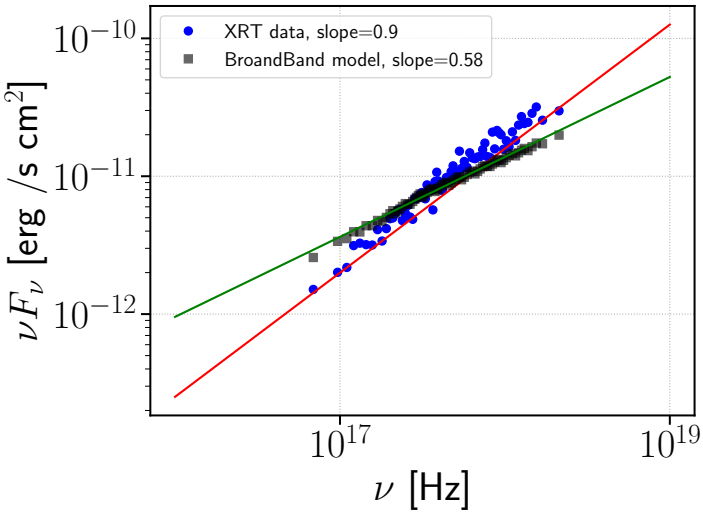

Figure 5.18: Part of CTA 102 spectrum in XRT energy range with derivation points.

Next, I applied the second method using the full MWL fit. I obtained a fit describing the data with a cutoff of the electron spectrum at relatively low energy.

Upon closer observation, I have noticed that the upper limits established by MAGIC's U.L. exceed the predictions generated by my broadband modeling. This observation has prompted me to reconsider the fundamental assumptions that underpin our current model. In particular, it has raised the question of whether a revised model that incorporates absorption effects might be necessary to reconcile my model with these upper limits. To investigate this, I examined the modeled spectrum without internal absorption and checked whether it overshoots the MAGIC U.L. This is shown in Fig. 5.19, and the obtained full-modeling solution does not require significant BLR absorption.

The results obtained from the two approaches to modeling the emission from FSRQs indicate a lack of consistency between them. This discrepancy suggests that absorption seems necessary according to the first method (phenomenological model). However, it might be missed through full modeling, underscoring the need for the second, more complex approach. However, it is important to note that this broadband modeling assumes a specific location of the emission region, which is associated with the absorption of this radiation. In other words, the emission area is placed on the edge of the BLR to ensure a sufficiently strong radiation field for EC emission, implying that the same radiation field will also absorb gamma photons.

5.5 Summary and Conclusions

The analysis conducted in this chapter led to the construction of a catalog with the upper limits of emission from nine FSRQs. These FSRQs were observed by the MAGIC telescopes over the past decade with a total of 174 hours of observation data. Most of the publications reporting observations of the Cherenkov telescope of FSRQs focus on detections of VHE emissions. This can produce a bias, suggesting that emission is typically produced beyond the BLR. Observations that do not lead to the detection in this range are rarely reported to the community. I investigated if such non-detections during high states of FSRQ change this paradigm. This study demonstrates that even these undetected sources can be explained within a model where the emission is produced in the outer parts of the BLR, resulting in little internal absorption.

I compared the limits on the VHE gamma-ray emission of these sources derived with the MAGIC telescopes with the extrapolation of the contemporaneous GeV emission seen by *Fermi*-LAT, taking into account the absorption in EBL. For four out of nine investigated sources (namely TXS 0025+197, AO

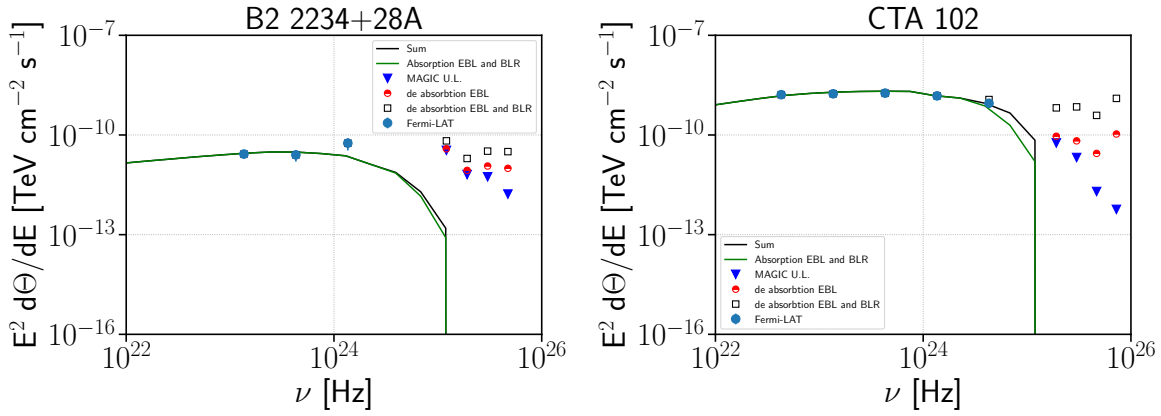

Figure 5.19: The solid black line represents the sum of emissions (without any absorption neither in BLR nor in EBL), and the solid green line is the sum of emissions after considering EBL and BLR absorption. The data points are shown in two variants: red points are deabsorbed only with the expected EBL, and black squares are deabsorbed for both EBL and BLR.

0235+164, OP 313, and TXS 2241+406), the MAGIC telescopes U.L. lie above the emission predicted by the model. For the other three sources (4C 55.17, 3C 454.3, and B2 0234+28), the spectra, after accounting for absorption in the EBL, are close to the U.L. obtained by MAGIC. The fact that for these seven sources, the MAGIC U.L. lies very close to or above the *Fermi*-LAT extrapolated model does not allow us to set any additional constraints on the absorption by the BLR. Their large redshift distances could explain these sources' lack of detection in the VHE range. It may also be because there is a certain delay between the emission enhancement triggering the ToO and the time when pointing instruments, such as the MAGIC telescopes, start their observations, which can also be additionally limited by atmospheric conditions or moonlight (nevertheless the GeV flux of those sources during MAGIC observations was 2 to 50 times higher than average).

Lastly, for two sources, B2 2234+28A and CTA 102, I obtained with the MAGIC telescopes upper limits on the flux below the emission predicted by the *Fermi*-LAT extrapolation model, which could suggest the presence of an additional absorption from the BLR. I investigated two approaches: a phenomenological description of gamma-ray band spectral shape and a fitting of a broadband radiative model. The first was limited to the HE and VHE gamma-ray range and was used to constrain the distance between the emission region and the black hole. As shown in Fig. 5.14, the required absorption in BLR to explain the constraints derived by the MAGIC telescopes for both sources is a weak radiation field of only 1% of the disk luminosity. In the applied multi-spherical BLR model, this places the distance between the emission region and the black hole corresponding to the edge of the BLR, namely $\lesssim 1.6 \cdot R_{H\beta}$. This agrees with findings for another FSRQ object in [328], which suggest that the gamma-ray emission located in 3C 279 most likely originates from the edge of the BLR. The second approach instead considers the emission over the whole spectrum, where the constraint from the phenomenological approach was tested in a leptonic emission model. Based on the SED shown in Fig. 5.15, it can be said that the major contribution to the HE emissions from the two sources, B2 2234+28A and CTA 102, studied in this work is the combination of the EC processes on the DT and the BLRs. The data fitting process yielded the values of parameters that describe the broad-band emission model. However, it is important to remember that such a simplified, homogeneous, one-zone leptonic model may only partially represent the complex conditions within the jet.

Regarding CTA102, the magnetic field's energy density (U_B) and the total energy density of electrons (U_e) seem approximately equal. Concerning B2 2234+28A, the magnetic field dominates when modeling is done with the assumption of the Doppler factor being 40. However, when I used a Doppler factor of 13, U_B and U_e were comparable as well.

It is important to note that the conclusion drawn is highly dependent on the used approach.

Based on our phenomenological model, my analysis of the observations made on CTA 102 and B2 2234+28A in the HE and VHE ranges leads us to conclude that weak absorption in the BLR is sufficient. Furthermore, the model's best-fit solution, which considers the full broadband spectrum, is consistent with the U.L. set by MAGIC. However, the lack of detectable VHE gamma-ray emission can mainly be attributed to the limited energy range of the electrons. Therefore, it can be inferred that the observed steepening at VHE energies is primarily due to the characteristics of the particle distribution, such as its maximum energy or distribution slope, rather than being significantly influenced by absorption effects. These observations are consistent with the study performed with the *Fermi*-LAT telescope, which found no evidence for the expected BLR absorption [87]. It is crucial to note that location constraints based on a naive extrapolation of the *Fermi*-LAT spectrum may not be robust. This is because the intrinsic spectrum cannot be assumed to behave straightforwardly, which should be considered in future studies, such as those with CTA [20] data. The lack of evidence for strong absorption of the VHE gamma-ray radiation in FSRQs is promising for future observations of FSRQ objects with the present and next generation of IACTs. On the other hand, the findings from the second approach point to cut off in the maximum energy of electrons are less promising for the detection of further sources. Further observations of FSRQ objects with the largest CTA telescopes, LST, will allow to probe the emission at few tens of GeV and possibly distinguish between the electron energy cut-off and absorption effects.

Chapter 6

Conclusion and future

6.1 Conclusion about PhD

During my thesis, one of my main focuses was on developing data analysis methods for LST-1, specifically low-level techniques such as signal correction and image cleaning. This was crucial in enhancing the telescope's performance, especially in the low energy range of VHE gamma-ray. I developed a code for low-level calibration, parts of which are now performed online, and I have tested if everything is working correctly. I also developed a special cleaning method currently being used in processing LST-1 data that lowers the influence of the additional noise from stars in the telescope's field of view on the Cherenkov images. I assisted in selecting the right parameters for the production of standardized data files after the first stages of data reduction and conducted a study on the efficiency of the cleaning methods.

Simultaneously to my work on the next generation of IACTs, I also exploited the current one for scientific investigations. Using MAGIC data collected over a span of 10 years, I investigated nine FSRQ objects. To do this, I developed tools in `agnpy`, allowing me to improve numerical calculations and consider absorption based on the multi-line BLR model. I analyzed 174 hours of data, which are reported in [267], which I am leading as a corresponding author. I did not find any statistically significant ($> 5\ \sigma$) signal for any of the studied sources, leading to upper limits on the emission in the VHE energy range. Based on the analysis of two sources, it was observed that the upper limits on the gamma-ray emission were constrained to be below the extrapolation from the emission model, taking into account the EBL. This could potentially indicate the presence of absorption in the BLR. My analysis focused on modeling the VHE emission of these sources, searching for absorption signatures within the BLR radiation field. I derived constraints on the distance between the emission region and the central black hole for these specific sources using a phenomenological model. These constraints were then tested using a framework based on a leptonic model.

Throughout my Ph.D. journey, I had the opportunity to present my research findings at various conferences and meetings. At the MAGIC and CTA/LST collaboration meetings, I discussed the results of my work. During the LST general meetings, I presented three topics, including my development of new pedestal cleaning methods, a cleaning study, and low-level corrections for LST-1. At the MAGIC collaboration meeting, I presented work on FSRQ publications. I also had the privilege of presenting a poster about the upper limits catalog FSRQ observations with MAGIC at the Particle Astrophysics conference held in Poland in 2023. Additionally, I presented updates on the development of `agnpy` at the TeVPA conference in Naples the same year.

During my PhD, I was honored to receive the NAWA fellowship, which allowed me to spend seven months at Instituto Fisica d'Altes Energies in Barcelona. I have also applied for a Preludium grant to develop a smart camera system that would enhance safety measures and enable remote operation of the MAGIC telescope.

6.2 Future of gamma-ray astronomy

The field of gamma-ray astronomy is currently undergoing a significant transformation that prioritizes inclusivity and openness. In the past, major observatories like H.E.S.S., MAGIC, and VERITAS have played a critical role in advancing our knowledge of the universe. However, access to these facilities and their data was largely limited to specific collaborations. This trend is shifting with the rise of open observatories, which will allow a broader range of scientists to submit observational proposals and engage in data analysis. This transition marks a major step towards democratizing the field, enabling more people to contribute to and benefit from gamma-ray astronomy. This move towards openness is part of a larger trend in science that emphasizes transparency and inclusivity, fostering greater innovation and collaboration in the field.

The CTA is set to become the first open VHE gamma-ray observatory [215]. It will comprise around 100 Cherenkov Telescopes of varying sizes, situated across two locations - La Palma, Spain (North) and Paranal, Chile (South). With an expected factor of a few improvements in sensitivity, CTA is additionally expected to significantly extend the observable energy range compared to current VHE experiments. For blazar observations, pushing the energy threshold towards $\sim$20 GeV is particularly important, as most blazars have soft spectra in the VHE gamma-ray range. Construction of the telescopes has already begun in La Palma.

I am most interested in blazars, which play a significant role in CTA's key science programs [329]. These programs consist of three different observational approaches: high-quality spectra, long-term monitoring, and target-of-opportunity observations of flares. The detailed gamma-ray spectral studies made possible by CTA's improved sensitivity will enable the detection of potential spectral features, such as those expected due to $\gamma\gamma$ absorption in the BLR or DT. In addition to studying blazar intrinsic spectral features, CTA's high-quality spectra will also be used to study EBL. As there are several possible origins for these spectral features, observing a large sample of blazars from different sub-classes and in different redshifts is crucial.

Although there is an observational bias towards VHE blazars detected during flares in lower energy bands, observing the flares is a mandatory part of VHE gamma-ray observations. With current IACTs, many sources can only be detected during flares. Extending the AGN population to fainter classes, such as narrow-line Seyfert-1 galaxies, is also within CTA's reach. The flares are essential for studying the mechanism of fast (time scale of < 10 minutes) variability [324]. Observing a large number of such flares is crucial, as it is impossible to identify the mechanism causing the fast variability from single flares from a single source. Blazars will also be targeted with proposal-based programs. According to simulations, the number of blazars detectable by CTA will be almost an order of magnitude larger than with the current generation of telescopes [330].

6.2.1 My plans for future

I am interested in enhancing the `agnpy` further by enabling users to calculate more advanced models of BLR while improving its speed. At present, the computation needed for the complex BLR model utilized in this work is quite slow. Additionally, it would be great to develop a widget that allows manipulation of starting parameters for fit.

In December 2023, LST-1 made an exciting announcement regarding detecting VHE emission from OP 313 [77], one of the sources I studied with the MAGIC telescopes. With the redshift of $z = 0.997$ [331]. it is currently nominally the farthest AGN for which VHE emission has been detected. It presents a unique opportunity to test the models developed in this thesis further. The preliminary offline analysis conducted on the data from 2023/12/11 to 2023/12/14 has revealed that OP 313 was detected with a significance greater than 5 σ and an integrated flux above 100 GeV, at 15% flux of the Crab Nebula. This detection of OP 313 opens up new avenues for research and provides an opportunity to study the properties of high-energy emissions from AGNs at extreme distances. I will also try to adapt this thesis's phenomenological and broadband approach to the LST-1 OP 313 data.

Another concept I propose addresses the challenge of managing a substantial volume of scholarly articles. It would be advantageous to have tools capable of reviewing numerous papers to locate specific sections relevant to the source I intend to study and to extract parameters necessary for modeling.

For this purpose, Natural Language Processing (NLP) tools could be employed to efficiently search for pertinent papers and identify essential parameters for model fitting.

Bibliography

[1] Michael A. DuVernois and Giuseppe Di Sciascio. "Detecting Gamma-Rays with Moderate Resolution and Large Field of View: Particle Detector Arrays and Water Cherenkov Technique". In: *Handbook of X-ray and Gamma-ray Astrophysics*. 2022, 21, p. 21. DOI: 10.1007/978-981-16-4544-0_64-1.

[2] D. Bose et al. "Galactic and extragalactic sources of very high energy gamma rays". In: *European Physical Journal Special Topics* 231.1 (Jan. 2022), pp. 27–66. DOI: 10.1140/epjs/s11734-022-00434-8. arXiv: 2201.06789 [astro-ph.HE].

[3] S. Ansoldi et al. "The Blazar TXS 0506+056 Associated with a High-energy Neutrino: Insights into Extragalactic Jets and Cosmic-Ray Acceleration". In: *The Astrophysical Journal Letters* 863.1, L10 (Aug. 2018), p. L10. DOI: 10.3847/2041-8213/aad083. arXiv: 1807.04300 [astro-ph.HE].

[4] R. Abbasi et al. "All-Sky Search for Transient Astrophysical Neutrino Emission with 10 Years of IceCube Cascade Events". In: *arXiv e-prints*, arXiv:2312.05362 (Dec. 2023), arXiv:2312.05362. arXiv: 2312.05362 [astro-ph.HE].

[5] Icecube Collaboration et al. "Observation of high-energy neutrinos from the Galactic plane". In: *Science* 380.6652 (June 2023), pp. 1338–1343. DOI: 10.1126/science.adc9818. arXiv: 2307.04427 [astro-ph.HE].

[6] Giuseppe Di Sciascio. "Ground-based Gamma-Ray Astronomy: an Introduction". In: *Journal of Physics Conference Series*. Vol. 1263. Journal of Physics Conference Series. June 2019, 012003, p. 012003. DOI: 10.1088/1742-6596/1263/1/012003. arXiv: 1904.06218 [astro-ph.IM].

[7] IceCube Collaboration. "Evidence for High-Energy Extraterrestrial Neutrinos at the IceCube Detector". In: *Science* 342.6161, 1242856 (Nov. 2013), p. 1242856. DOI: 10.1126/science.1242856. arXiv: 1311.5238 [astro-ph.HE].

[8] IceCube Collaboration et al. "Evidence for neutrino emission from the nearby active galaxy NGC 1068". In: *Science* 378.6619 (Nov. 2022), pp. 538–543. DOI: 10.1126/science.abg3395. arXiv: 2211.09972 [astro-ph.HE].

[9] MAGIC Collaboration et al. "Teraelectronvolt emission from the γ-ray burst GRB 190114C". In: *Nature* 575.7783 (Nov. 2019), pp. 455–458. DOI: 10.1038/s41586-019-1750-x. arXiv: 2006.07249 [astro-ph.HE].

[10] Elisa Prandini, Konstantinos Dialektopoulos, and Jelena Strišković. "Gamma rays: propagation and detection". In: *arXiv e-prints*, arXiv:2211.17021 (Nov. 2022), arXiv:2211.17021. DOI: 10.48550/arXiv.2211.17021. arXiv: 2211.17021 [astro-ph.HE].

[11] Alessandro De Angelis and Mário Pimenta. *Introduction to Particle and Astroparticle Physics*. 2018. DOI: 10.1007/978-3-319-78181-5.

[12] W. B. Atwood et al. "The Large Area Telescope on the Fermi Gamma-Ray Space Telescope Mission". In: *The Astrophysical Journal* 697.2 (June 2009), pp. 1071–1102. DOI: 10.1088/0004-637X/697/2/1071. arXiv: 0902.1089 [astro-ph.IM].

[13] A. Morselli et al. "The space gamma-ray observatory AGILE". In: *Nuclear Physics B Proceedings Supplements* 85.1-3 (May 2000), pp. 22–27. DOI: 10.1016/S0920-5632(00)00477-1.

[14] Bruno Rossi and Kenneth Greisen. "Cosmic-Ray Theory". In: *Reviews of Modern Physics* 13.4 (Oct. 1941), pp. 240–309. DOI: 10.1103/RevModPhys.13.240.

[15] P. Auger et al. "Extensive Cosmic-Ray Showers". In: *Reviews of Modern Physics* 11.3-4 (July 1939), pp. 288–291. DOI: 10.1103/RevModPhys.11.288.

[16] Kenneth Greisen. "End to the Cosmic-Ray Spectrum?" In: *Physical Review Letters* 16.17 (Apr. 1966), pp. 748–750. DOI: 10.1103/PhysRevLett.16.748.

[17] The Pierre Auger Collaboration. "The Pierre Auger Cosmic Ray Observatory". In: *arXiv e-prints*, arXiv:1502.01323 (Feb. 2015), arXiv:1502.01323. DOI: 10.48550/arXiv.1502.01323. arXiv: 1502.01323 [astro-ph.IM].

[18] H. E. S. S. Collaboration et al. "The H.E.S.S. Galactic plane survey". In: *Astronomy and Astrophysics* 612, A1 (Apr. 2018), A1. DOI: 10.1051/0004-6361/201732098. arXiv: 1804.02432 [astro-ph.HE].

[19] V. A. Acciari et al. "Bounds on Lorentz Invariance Violation from MAGIC Observation of GRB 190114C". In: *Physical Review Letters* 125.2, 021301 (July 2020), p. 021301. DOI: 10.1103/PhysRevLett.125.021301. arXiv: 2001.09728 [astro-ph.HE].

[20] B. S. Acharya et al. "Introducing the CTA concept". In: *Astroparticle Physics* 43 (Mar. 2013), pp. 3–18. DOI: 10.1016/j.astropartphys.2013.01.007.

[21] Cherenkov Telescope Array Consortium et al. *Science with the Cherenkov Telescope Array*. 2019. DOI: 10.1142/10986.

[22] M Bustamante et al. "High-energy cosmic-ray acceleration". In: (2010). DOI: 10.5170/CERN-2010-001.533. URL: https://cds.cern.ch/record/1249755.

[23] Enrico Fermi. "On the Origin of the Cosmic Radiation". In: *Physical Review* 75.8 (Apr. 1949), pp. 1169–1174. DOI: 10.1103/PhysRev.75.1169.

[24] Malcolm S. Longair. *High energy astrophysics. Vol.2: Stars, the galaxy and the interstellar medium*. Vol. 2. 1994.

[25] A. Aab et al. "Combined fit of spectrum and composition data as measured by the Pierre Auger Observatory". In: *Journal of Cosmology and Astroparticle Physics* 2017.4, 038 (Apr. 2017), p. 038. DOI: 10.1088/1475-7516/2017/04/038. arXiv: 1612.07155 [astro-ph.HE].

[26] Ellen G. Zweibel and Masaaki Yamada. "Magnetic Reconnection in Astrophysical and Laboratory Plasmas". In: *Annual Review of Astronomy and Astrophysics* 47.1 (Sept. 2009), pp. 291–332. DOI: 10.1146/annurev-astro-082708-101726.

[27] Talvikki Hovatta and Elina Lindfors. "Relativistic Jets of Blazars". In: *New Astronomy Reviews* 87, 101541 (Dec. 2019), p. 101541. DOI: 10.1016/j.newar.2020.101541. arXiv: 2003.06322 [astro-ph.HE].

[28] Maurizio Spurio. *Particles and Astrophysics. A Multi-Messenger Approach*. Astronomy and Astrophysics Library. Springer, 2015. ISBN: 978-3-319-08050-5.

[29] K. A. Olive et al. "Review of Particle Physics". In: *Chin. Phys. C* 38 (2014), p. 090001. DOI: 10.1088/1674-1137/38/9/090001.

[30] O. Klein and T. Nishina. "Über die Streuung von Strahlung durch freie Elektronen nach der neuen relativistischen Quantendynamik von Dirac". In: *Zeitschrift fur Physik* 52.11-12 (Nov. 1929), pp. 853–868. DOI: 10.1007/BF01366453.

[31] M. J. Rees. "Studies in radio source structure-III. Inverse Compton radiation from radio sources". In: *Monthly Notices of the Royal Astronomical Society* 137 (Jan. 1967), p. 429. DOI: 10.1093/mnras/137.4.429.

[32] E. J. Lindfors, E. Valtaoja, and M. Türler. "SSC mechanism in the gamma-ray blazar 3C 279". In: *Astronomy and Astrophysics* 440.3 (Sept. 2005), pp. 845–853. DOI: 10.1051/0004-6361:20040196.

[33] H. Krawczynski et al. "Multiwavelength Observations of Strong Flares from the TeV Blazar 1ES 1959+650". In: *The Astrophysical Journal* 601.1 (Jan. 2004), pp. 151–164. DOI: 10.1086/380393. arXiv: astro-ph/0310158 [astro-ph].

[34] M. J. Rees. "Studies in radio source structure-I. A relativistically expanding model for variable quasi-stellar radio sources". In: *Monthly Notices of the Royal Astronomical Society* 135 (Jan. 1967), p. 345. DOI: 10.1093/mnras/135.4.345.

[35] L. Maraschi, G. Ghisellini, and A. Celotti. "A Jet Model for the Gamma-Ray–emitting Blazar 3C 279". In: *The Astrophysical Journal Letters* 397 (Sept. 1992), p. L5. DOI: 10.1086/186531.

[36] Luigi Tibaldo, Daniele Gaggero, and Pierrick Martin. "Gamma Rays as Probes of Cosmic-Ray Propagation and Interactions in Galaxies". In: *Universe* 7.5, 141 (May 2021), p. 141. DOI: 10.3390/universe7050141. arXiv: 2103.16423 [astro-ph.HE].

[37] W. Heitler. *Quantum theory of radiation*. 1954.

[38] K. Kamata and J. Nishimura. "The Lateral and the Angular Structure Functions of Electron Showers". In: *Progress of Theoretical Physics Supplement* 6 (Jan. 1958), pp. 93–155. DOI: 10.1143/PTPS.6.93.

[39] Julian Sitarek. "TeV Instrumentation: Current and Future". In: *Galaxies* 10.1 (Jan. 2022), p. 21. DOI: 10.3390/galaxies10010021. arXiv: 2201.08611 [astro-ph.IM].

[40] A. U. Abeysekara et al. "Observation of the Crab Nebula with the HAWC Gamma-Ray Observatory". In: *The Astrophysical Journal* 843.1, 39 (July 2017), p. 39. DOI: 10.3847/1538-4357/aa7555. arXiv: 1701.01778 [astro-ph.HE].

[41] C. Megan Urry and Paolo Padovani. "Unified Schemes for Radio-Loud Active Galactic Nuclei". In: *Publications of the Astronomical Society of the Pacific* 107 (Sept. 1995), p. 803. DOI: 10.1086/133630. arXiv: astro-ph/9506063 [astro-ph].

[42] Grzegorz (Greg) Madejski and Marek Sikora. "Gamma-Ray Observations of Active Galactic Nuclei". In: *Annual Review of Astronomy and Astrophysics* 54 (Sept. 2016), pp. 725–760. DOI: 10.1146/annurev-astro-081913-040044.

[43] Vaidehi S. Paliya et al. "The Central Engines of Fermi Blazars". In: *The Astrophysical Journal Supplement Series* 253.2, 46 (Apr. 2021), p. 46. DOI: 10.3847/1538-4365/abe135. arXiv: 2101.10849 [astro-ph.HE].

[44] G. Ghisellini et al. "The power of relativistic jets is larger than the luminosity of their accretion disks". In: *Nature* 515.7527 (Nov. 2014), pp. 376–378. DOI: 10.1038/nature13856. arXiv: 1411.5368 [astro-ph.HE].

[45] Hagai Netzer. "Revisiting the Unified Model of Active Galactic Nuclei". In: *Annual Review of Astronomy and Astrophysics* 53 (Aug. 2015), pp. 365–408. DOI: 10.1146/annurev-astro-082214-122302. arXiv: 1505.00811 [astro-ph.GA].

[46] N. I. Shakura and R. A. Sunyaev. "Black holes in binary systems. Observational appearance." In: *Astronomy and Astrophysics* 24 (Jan. 1973), pp. 337–355.

[47] M. A. Abramowicz et al. "Slim Accretion Disks". In: *The Astrophysical Journal* 332 (Sept. 1988), p. 646. DOI: 10.1086/166683.

[48] Volker Beckmann and Chris R. Shrader. *Active Galactic Nuclei*. 2012.

[49] J. Aleksić et al. "MAGIC Observations and multiwavelength properties of the quasar 3C 279 in 2007 and 2009". In: *Astronomy and Astrophysics* 530, A4 (June 2011), A4. DOI: 10.1051/0004-6361/201116497. arXiv: 1101.2522 [astro-ph.CO].

[50] R. C. Vermeulen et al. "When Is BL Lac Not a BL Lac?" In: *The Astrophysical Journal Letters* 452 (Oct. 1995), p. L5. DOI: 10.1086/309716.

[51] Markus Böttcher. "Progress in Multi-wavelength and Multi-Messenger Observations of Blazars and Theoretical Challenges". In: *Galaxies* 7.1 (Jan. 2019), p. 20. DOI: 10.3390/galaxies7010020. arXiv: 1901.04178 [astro-ph.HE].

[52] F. Aharonian et al. "An Exceptional Very High Energy Gamma-Ray Flare of PKS 2155-304". In: *The Astrophysical Journal Letters* 664.2 (Aug. 2007), pp. L71–L74. DOI: 10.1086/520635. arXiv: 0706.0797 [astro-ph].

[53] J. Albert et al. "Variable Very High Energy γ-Ray Emission from Markarian 501". In: *The Astrophysical Journal* 669.2 (Nov. 2007), pp. 862–883. DOI: 10.1086/521382. arXiv: astro-ph/0702008 [astro-ph].

[54] Suvendu Rakshit. "Broad line region and black hole mass of PKS 1510-089 from spectroscopic reverberation mapping". In: *Astronomy and Astrophysics* 642, A59 (Oct. 2020), A59. DOI: 10.1051/0004-6361/202038324. arXiv: 2007.07672 [astro-ph.GA].

[55] M. Stickel et al. "The Complete Sample of 1 Jansky BL Lacertae Objects. I. Summary Properties". In: *The Astrophysical Journal* 374 (June 1991), p. 431. DOI: 10.1086/170133.

[56] R. M. Plotkin et al. "Dynamical black hole masses of BL Lac objects from the Sloan Digital Sky Survey". In: *Monthly Notices of the Royal Astronomical Society* 413.2 (May 2011), pp. 805–812. DOI: 10.1111/j.1365-2966.2010.18172.x. arXiv: 1012.1601 [astro-ph.CO].

[57] MAGIC Collaboration et al. "VHE gamma-ray detection of FSRQ QSO B1420+326 and modeling of its enhanced broadband state in 2020". In: *Astronomy and Astrophysics* 647, A163 (Mar. 2021), A163. DOI: 10.1051/0004-6361/202039687. arXiv: 2012.11380 [astro-ph.HE].

[58] Charles D. Dermer and Reinhard Schlickeiser. "Model for the High-Energy Emission from Blazars". In: *The Astrophysical Journal* 416 (Oct. 1993), p. 458. DOI: 10.1086/173251.

[59] Marek Sikora, Mitchell C. Begelman, and Martin J. Rees. "Comptonization of Diffuse Ambient Radiation by a Relativistic Jet: The Source of Gamma Rays from Blazars?" In: *The Astrophysical Journal* 421 (Jan. 1994), p. 153. DOI: 10.1086/173633.

[60] Marek Sikora, RafaŁ Moderski, and Greg M. Madejski. "3C 454.3 Reveals the Structure and Physics of Its "Blazar Zone"". In: *The Astrophysical Journal* 675.1 (Mar. 2008), pp. 71–78. DOI: 10.1086/526419. arXiv: 0711.3524 [astro-ph].

[61] K. Mannheim. "The proton blazar." In: *Astronomy and Astrophysics* 269 (Mar. 1993), pp. 67–76. DOI: 10.48550/arXiv.astro-ph/9302006. arXiv: astro-ph/9302006 [astro-ph].

[62] A. Mücke and R. J. Protheroe. "A proton synchrotron blazar model for flaring in Markarian 501". In: *Astroparticle Physics* 15.1 (Mar. 2001), pp. 121–136. DOI: 10.1016/S0927-6505(00)00141-9. arXiv: astro-ph/0004052 [astro-ph].

[63] M. Cerruti et al. "Leptohadronic single-zone models for the electromagnetic and neutrino emission of TXS 0506+056". In: *Monthly Notices of the Royal Astronomical Society* 483.1 (Feb. 2019), pp. L12–L16. DOI: 10.1093/mnrasl/sly210. arXiv: 1807.04335 [astro-ph.HE].

[64] A. A. Abdo et al. "The Spectral Energy Distribution of Fermi Bright Blazars". In: *The Astrophysical Journal* 716.1 (June 2010), pp. 30–70. DOI: 10.1088/0004-637X/716/1/30. arXiv: 0912.2040 [astro-ph.CO].

[65] Janeth Valverde et al. "A Decade of Multiwavelength Observations of the TeV Blazar 1ES 1215+303: Extreme Shift of the Synchrotron Peak Frequency and Long-term Optical-Gamma-Ray Flux Increase". In: *The Astrophysical Journal* 891.2, 170 (Mar. 2020), p. 170. DOI: 10.3847/1538-4357/ab765d. arXiv: 2002.04119 [astro-ph.HE].

[66] M. Errando et al. "Discovery of very high energy gamma-rays from the flat spectrum radio quasar 3C 279 with the MAGIC telescope". In: *American Institute of Physics Conference Series*. Ed. by Felix A. Aharonian, Werner Hofmann, and Frank Rieger. Vol. 1085. American Institute of Physics Conference Series. Dec. 2008, pp. 423–426. DOI: 10.1063/1.3076698. arXiv: 0901.3275 [astro-ph.HE].

[67] A. Hewitt and G. Burbidge. "A Revised and Updated Catalog of Quasi-stellar Objects". In: *The Astrophysical Journal Supplement Series* 87 (Aug. 1993), p. 451. DOI: 10.1086/191811.

[68] Manuel Meyer, Jeffrey D. Scargle, and Roger D. Blandford. "Characterizing the Gamma-Ray Variability of the Brightest Flat Spectrum Radio Quasars Observed with the Fermi LAT". In: *The Astrophysical Journal* 877.1, 39 (May 2019), p. 39. DOI: 10.3847/1538-4357/ab1651. arXiv: 1902.02291 [astro-ph.HE].

[69] Michael Zacharias et al. "The VHE γ-Ray View of the FSRQ PKS 1510-089". In: *Galaxies* 7.1 (Mar. 2019), p. 41. DOI: 10.3390/galaxies7010041. arXiv: 1903.08535 [astro-ph.HE].

[70] H. E. S. S. Collaboration et al. "H.E.S.S. discovery of VHE γ-rays from the quasar PKS 1510-089". In: *Astronomy and Astrophysics* 554, A107 (June 2013), A107. DOI: 10.1051/0004-6361/201321135. arXiv: 1304.8071 [astro-ph.HE].

[71] J. Aleksić et al. "MAGIC Discovery of Very High Energy Emission from the FSRQ PKS 1222+21". In: *The Astrophysical Journal Letters* 730.1, L8 (Mar. 2011), p. L8. DOI: 10.1088/2041-8205/730/1/L8. arXiv: 1101.4645 [astro-ph.HE].

[72] M. L. Ahnen et al. "Detection of very high energy gamma-ray emission from the gravitationally lensed blazar QSO B0218+357 with the MAGIC telescopes". In: *Astronomy and Astrophysics* 595, A98 (Nov. 2016), A98. DOI: 10.1051/0004-6361/201629461. arXiv: 1609.01095 [astro-ph.HE].

[73] M. L. Ahnen et al. "Very High Energy γ-Rays from the Universe's Middle Age: Detection of the z = 0.940 Blazar PKS 1441+25 with MAGIC". In: *The Astrophysical Journal Letters* 815.2, L23 (Dec. 2015), p. L23. DOI: 10.1088/2041-8205/815/2/L23. arXiv: 1512.04435 [astro-ph.GA].

[74] H. E. S. S. Collaboration et al. "H.E.S.S. detection of very high-energy γ-ray emission from the quasar PKS 0736+017". In: *Astronomy and Astrophysics* 633, A162 (Jan. 2020), A162. DOI: 10.1051/0004-6361/201935906. arXiv: 1911.04761 [astro-ph.HE].

[75] Razmik Mirzoyan. "Detection of very-high-energy gamma-ray emission from the FSRQ Ton 0599 with the MAGIC telescopes". In: *The Astronomer's Telegram* 11061 (Dec. 2017), p. 1.

[76] S. Wagner, B. Rani, and H. E. S. S. Collaboration. "Enhanced HE and VHE gamma-ray activity from the FSRQ PKS 0346-27". In: *The Astronomer's Telegram* 15020 (Nov. 2021), p. 1.

[77] Juan Cortina and CTAO LST Collaboration. "First detection of VHE gamma-ray emission from FSRQ OP 313 with LST-1". In: *The Astronomer's Telegram* 16381 (Dec. 2023), p. 1.

[78] MAGIC Collaboration et al. "Detection of persistent VHE gamma-ray emission from PKS 1510-089 by the MAGIC telescopes during low states between 2012 and 2017". In: *Astronomy and Astrophysics* 619, A159 (Nov. 2018), A159. DOI: 10.1051/0004-6361/201833618. arXiv: 1806.05367 [astro-ph.GA].

[79] F. Aharonian et al. "The Vanishing of the Primary Emission Region in PKS 1510-089". In: *The Astrophysical Journal Letters* 952.2, L38 (Aug. 2023), p. L38. DOI: 10.3847/2041-8213/ace3c0. arXiv: 2307.01692 [astro-ph.HE].

[80] A. D. Falcone et al. "A Search for TeV Gamma-Ray Emission from High-peaked Flat-Spectrum Radio Quasars Using the Whipple Air Cerenkov Telescope". In: *The Astrophysical Journal* 613.2 (Oct. 2004), pp. 710–715. DOI: 10.1086/423128. arXiv: astro-ph/0408365 [astro-ph].

[81] F. Aharonian et al. "Upper limits from HESS active galactic nuclei observations in 2005-2007". In: *Astronomy and Astrophysics* 478.2 (Feb. 2008), pp. 387–393. DOI: 10.1051/0004-6361:20078604. arXiv: 0711.3196 [astro-ph].

[82] H. E. S. S. Collaboration et al. "Flux upper limits for 47 AGN observed with H.E.S.S. in 2004-2011". In: *Astronomy and Astrophysics* 564, A9 (Mar. 2014), A9. DOI: 10.1051/0004-6361/201322897. arXiv: 1402.2332 [astro-ph.GA].

[83] S. R. Patel and VERITAS Collaboration. "TeV emission from FSRQs: The first systematic and unbiased survey". In: *37th International Cosmic Ray Conference*. Mar. 2022, 824, p. 824. DOI: 10.22323/1.395.0824. arXiv: 2108.06099 [astro-ph.HE].

[84] M. Zacharias et al. "The exceptional VHE gamma-ray outburst of PKS 1510-089 in May 2016". In: *35th International Cosmic Ray Conference (ICRC2017)*. Vol. 301. International Cosmic Ray Conference. July 2017, 655, p. 655. DOI: 10.22323/1.301.0655. arXiv: 1708.00653 [astro-ph.HE].

[85] G. Ghisellini et al. "A theoretical unifying scheme for gamma-ray bright blazars". In: *Monthly Notices of the Royal Astronomical Society* 301.2 (Dec. 1998), pp. 451–468. DOI: 10.1046/j.1365-8711.1998.02032.x. arXiv: astro-ph/9807317 [astro-ph].

[86] Justin D. Finke. "Compton Dominance and the Blazar Sequence". In: *The Astrophysical Journal* 763.2, 134 (Feb. 2013), p. 134. DOI: 10.1088/0004-637X/763/2/134. arXiv: 1212.0869 [astro-ph.HE].

[87] L. Costamante et al. "On the origin of gamma-rays in Fermi blazars: beyondthe broad-line region". In: *Monthly Notices of the Royal Astronomical Society* 477.4 (July 2018), pp. 4749–4767. DOI: 10.1093/mnras/sty887. arXiv: 1804.02408 [astro-ph.HE].

[88] H. T. Liu and J. M. Bai. "Absorption of 10-200 GeV Gamma Rays by Radiation from Broad-Line Regions in Blazars". In: *The Astrophysical Journal* 653.2 (Dec. 2006), pp. 1089–1097. DOI: 10.1086/509097. arXiv: 0807.3135 [astro-ph].

[89] N. Sahakyan. "Investigation of the γ-ray spectrum of CTA 102 during the exceptional flaring state in 2016-2017". In: *Astronomy and Astrophysics* 635, A25 (Mar. 2020), A25. DOI: 10.1051/0004-6361/201936715. arXiv: 1911.12087 [astro-ph.HE].

[90] L. Costamante. "Blazars - an updated review". In: *Multifrequency Behaviour of High Energy Cosmic Sources - XIII. 3-8 June 2019. Palermo*. Dec. 2020, 35, p. 35. DOI: 10.22323/1.362.0035.

[91] S. Abdollahi et al. "Fermi Large Area Telescope Fourth Source Catalog". In: *The Astrophysical Journal Supplement Series* 247.1, 33 (Mar. 2020), p. 33. DOI: 10.3847/1538-4365/ab6bcb. arXiv: 1902.10045 [astro-ph.HE].

[92] S. Abdollahi et al. "Incremental Fermi Large Area Telescope Fourth Source Catalog". In: *The Astrophysical Journal Supplement Series* 260.2, 53 (June 2022), p. 53. DOI: 10.3847/1538-4365/ac6751. arXiv: 2201.11184 [astro-ph.HE].

[93] Davide Serini. "Science with the Fermi Large Area Telescope". In: *Journal of Physics Conference Series*. Vol. 2429. Journal of Physics Conference Series. Feb. 2023, 012018, p. 012018. DOI: 10.1088/1742-6596/2429/1/012018.

[94] F. Acero et al. "Fermi Large Area Telescope Third Source Catalog". In: *The Astrophysical Journal Supplement Series* 218.2, 23 (June 2015), p. 23. DOI: 10.1088/0067-0049/218/2/23. arXiv: 1501.02003 [astro-ph.HE].

[95] Filippo D'Ammando. "Jet physics of accreting super-massive black holes in the era of the Fermi Gamma-ray Space Telescope". In: *Frontiers in Astronomy and Space Sciences* 4, 53 (Nov. 2017), p. 53. DOI: 10.3389/fspas.2017.00053. arXiv: 1711.06284 [astro-ph.HE].

[96] V. Schoenfelder et al. "Instrument Description and Performance of the Imaging Gamma-Ray Telescope COMPTEL aboard the Compton Gamma-Ray Observatory". In: *The Astrophysical Journal Supplement Series* 86 (June 1993), p. 657. DOI: 10.1086/191794.

[97] Riccardo Giacconi. "History of X-ray telescopes and astronomy". In: *Experimental Astronomy* 25.1-3 (Aug. 2009), pp. 143–156. DOI: 10.1007/s10686-009-9139-8.

[98] R. C. Hartman et al. "Detection of High-Energy Gamma Radiation from Quasar 3C 279 by the EGRET Telescope on the Compton Gamma Ray Observatory". In: *The Astrophysical Journal Letters* 385 (Jan. 1992), p. L1. DOI: 10.1086/186263.

[99] R. C. Hartman et al. "The Third EGRET Catalog of High-Energy Gamma-Ray Sources". In: *The Astrophysical Journal Supplement Series* 123.1 (July 1999), pp. 79–202. DOI: 10.1086/313231.

[100] Paula Chadwick. "35 Years of Ground-Based Gamma-ray Astronomy". In: *Universe* 7.11 (Nov. 2021), p. 432. DOI: 10.3390/universe7110432.

[101] M. Punch et al. "Detection of TeV photons from Markarian 421." In: *Compton Gamma-ray Observatory*. Ed. by M. Friedlander, N. Gehrels, and D. J. Macomb. Vol. 280. American Institute of Physics Conference Series. Jan. 1993, pp. 488–492. DOI: 10.1063/1.44272.

[102] K. Bernlöhr et al. "The optical system of the H.E.S.S. imaging atmospheric Cherenkov telescopes. Part I: layout and components of the system". In: *Astroparticle Physics* 20.2 (Nov. 2003), pp. 111–128. DOI: 10.1016/S0927-6505(03)00171-3. arXiv: astro-ph/0308246 [astro-ph].

[103] J. Aleksić et al. "The major upgrade of the MAGIC telescopes, Part I: The hardware improvements and the commissioning of the system". In: *Astroparticle Physics* 72 (Jan. 2016), pp. 61–75. DOI: 10.1016/j.astropartphys.2015.04.004. arXiv: 1409.6073 [astro-ph.IM].

[104] J. Holder et al. "The first VERITAS telescope". In: *Astroparticle Physics* 25.6 (July 2006), pp. 391–401. DOI: 10.1016/j.astropartphys.2006.04.002. arXiv: astro-ph/0604119 [astro-ph].

[105] S. P. Wakely and D. Horan. "TeVCat: An online catalog for Very High Energy Gamma-Ray Astronomy". In: *International Cosmic Ray Conference*. Vol. 3. International Cosmic Ray Conference. Jan. 2008, pp. 1341–1344.

[106] J. A. Gaidos et al. "Extremely rapid bursts of TeV photons from the active galaxy Markarian 421". In: *Nature* 383.6598 (Sept. 1996), pp. 319–320. DOI: 10.1038/383319a0.

[107] T. Arlen et al. "Rapid TeV Gamma-Ray Flaring of BL Lacertae". In: *The Astrophysical Journal* 762.2, 92 (Jan. 2013), p. 92. DOI: 10.1088/0004-637X/762/2/92. arXiv: 1211.3073 [astro-ph.HE].

[108] J. Aleksić et al. "Black hole lightning due to particle acceleration at subhorizon scales". In: *Science* 346.6213 (Nov. 2014), pp. 1080–1084. DOI: 10.1126/science.1256183. arXiv: 1412.4936 [astro-ph.HE].

[109] M. Ackermann et al. "Minute-timescale >100 MeV γ-Ray Variability during the Giant Outburst of Quasar 3C 279 Observed by Fermi-LAT in 2015 June". In: *The Astrophysical Journal Letters* 824.2, L20 (June 2016), p. L20. DOI: 10.3847/2041-8205/824/2/L20. arXiv: 1605.05324 [astro-ph.HE].

[110] Eli Dwek and Frank Krennrich. "The extragalactic background light and the gamma-ray opacity of the universe". In: *Astroparticle Physics* 43 (Mar. 2013), pp. 112–133. DOI: 10.1016/j.astropartphys.2012.09.003. arXiv: 1209.4661 [astro-ph.CO].

[111] A. Franceschini, G. Rodighiero, and M. Vaccari. "Extragalactic optical-infrared background radiation, its time evolution and the cosmic photon-photon opacity". In: *Astronomy and Astrophysics* 487.3 (Sept. 2008), pp. 837–852. DOI: 10.1051/0004-6361:200809691. arXiv: 0805.1841 [astro-ph].

[112] Alberto Franceschini and Giulia Rodighiero. "The extragalactic background light revisited and the cosmic photon-photon opacity". In: *Astronomy and Astrophysics* 603, A34 (July 2017), A34. DOI: 10.1051/0004-6361/201629684. arXiv: 1705.10256 [astro-ph.HE].

[113] Justin D. Finke, Soebur Razzaque, and Charles D. Dermer. "Modeling the Extragalactic Background Light from Stars and Dust". In: *The Astrophysical Journal* 712.1 (Mar. 2010), pp. 238–249. DOI: 10.1088/0004-637X/712/1/238. arXiv: 0905.1115 [astro-ph.HE].

[114] A. Domínguez et al. "Extragalactic background light inferred from AEGIS galaxy-SED-type fractions". In: *Monthly Notices of the Royal Astronomical Society* 410.4 (Feb. 2011), pp. 2556–2578. DOI: 10.1111/j.1365-2966.2010.17631.x. arXiv: 1007.1459 [astro-ph.CO].

[115] Alberto Saldana-Lopez et al. "An observational determination of the evolving extragalactic background light from the multiwavelength HST/CANDELS survey in the Fermi and CTA era". In: *Monthly Notices of the Royal Astronomical Society* 507.4 (Nov. 2021), pp. 5144–5160. DOI: 10.1093/mnras/stab2393. arXiv: 2012.03035 [astro-ph.CO].

[116] L. Foffano et al. "Absorption Features in Sub-TeV Gamma-Ray Spectra of BL Lac Objects". In: *The Astrophysical Journal* 926.1, 95 (Feb. 2022), p. 95. DOI: 10.3847/1538-4357/ac46fc. arXiv: 2201.02454 [astro-ph.HE].

[117] J. Aleksić et al. "MAGIC gamma-ray and multi-frequency observations of flat spectrum radio quasar PKS 1510-089 in early 2012". In: *Astronomy and Astrophysics* 569, A46 (Sept. 2014), A46. DOI: 10.1051/0004-6361/201423484. arXiv: 1401.5646 [astro-ph.HE].

[118] M. Petropoulou et al. "Photohadronic origin of γ -ray BL Lac emission: implications for IceCube neutrinos". In: *Monthly Notices of the Royal Astronomical Society* 448 (Apr. 2015), pp. 2412–2429. DOI: 10.1093/mnras/stv179. arXiv: 1501.07115 [astro-ph.HE].

[119] R. Blandford, D. Meier, and A. Readhead. "Relativistic Jets in Active Galactic Nuclei". In: *arXiv e-prints* (Dec. 2018). arXiv: 1812.06025 [astro-ph.HE].

[120] F. Tavecchio et al. "TeV BL Lac objects at the dawn of the Fermi era". In: *Monthly Notices of the Royal Astronomical Society* 401 (Jan. 2010), pp. 1570–1586. DOI: 10.1111/j.1365-2966.2009.15784.x. arXiv: 0909.0651 [astro-ph.HE].

[121] F. Tavecchio et al. "On the origin of the γ-ray emission from the flaring blazar PKS 1222+216". In: *Astronomy and Astrophysics* 534, A86 (Oct. 2011), A86. DOI: 10.1051/0004-6361/201117204. arXiv: 1104.0048 [astro-ph.HE].

[122] M. Ackermann et al. "Minute-timescale >100 MeV γ-Ray Variability during the Giant Outburst of Quasar 3C 279 Observed by Fermi-LAT in 2015 June". In: *The Astrophysical Journal Letters* 824, L20 (June 2016), p. L20. DOI: 10.3847/2041-8205/824/2/L20. arXiv: 1605.05324 [astro-ph.HE].

[123] Alina-C. Donea and R. J. Protheroe. "Radiation fields of disk, BLR and torus in quasars and blazars: implications for /γ-ray absorption". In: *Astroparticle Physics* 18.4 (Jan. 2003), pp. 377–393. DOI: 10.1016/S0927-6505(02)00155-X. arXiv: astro-ph/0202068 [astro-ph].

[124] Fabrizio Tavecchio and Daniel Mazin. "Intrinsic absorption in 3C 279 at GeV-TeV energies and consequences for estimates of the extragalactic background light". In: *Monthly Notices of the Royal Astronomical Society* 392.1 (Jan. 2009), pp. L40–L44. DOI: 10.1111/j.1745-3933.2008.00584.x. arXiv: 0809.2467 [astro-ph].

[125] H. E. S. S. Collaboration et al. "H.E.S.S. and MAGIC observations of a sudden cessation of a very-high-energy γ-ray flare in PKS 1510−089 in May 2016". In: *Astronomy and Astrophysics* 648, A23 (Apr. 2021), A23. DOI: 10.1051/0004-6361/202038949. arXiv: 2012.10254 [astro-ph.HE].

[126] S. Saito et al. "Very Rapid High-amplitude Gamma-Ray Variability in Luminous Blazar PKS 1510-089 Studied with Fermi-LAT". In: *The Astrophysical Journal Letters* 766, L11 (Mar. 2013), p. L11. DOI: 10.1088/2041-8205/766/1/L11. arXiv: 1302.0335 [astro-ph.HE].

[127] L. Foschini et al. "Fermi/LAT detection of extraordinary variability in the gamma-ray emission of the blazar PKS 1510-089". In: *Astronomy and Astrophysics* 555, A138 (July 2013), A138. DOI: 10.1051/0004-6361/201321675. arXiv: 1304.2878 [astro-ph.HE].

[128] A. P. Marscher et al. "Relation between Events in the Millimeter-wave Core and Gamma-ray Outbursts in Blazar Jets". In: *arXiv e-prints* (Apr. 2012). arXiv: 1204.6707 [astro-ph.HE].

[129] S. G. Jorstad et al. "A Tight Connection between Gamma-Ray Outbursts and Parsec-scale Jet Activity in the Quasar 3C 454.3". In: *The Astrophysical Journal* 773, 147 (Aug. 2013), p. 147. DOI: 10.1088/0004-637X/773/2/147. arXiv: 1307.2522 [astro-ph.HE].

[130] A. Lähteenmäki and E. Valtaoja. "Testing of Inverse Compton Models for Active Galactic Nuclei with Gamma-Ray and Radio Observations". In: *The Astrophysical Journal* 590 (June 2003), pp. 95–108. DOI: 10.1086/374883.

[131] E. J. Lindfors et al. "Synchrotron flaring in the jet of 3C 279". In: *Astronomy and Astrophysics* 456 (Sept. 2006), pp. 895–903. DOI: 10.1051/0004-6361:20053679. eprint: astro-ph/0606646.

[132] J. Aleksić et al. "MAGIC gamma-ray and multi-frequency observations of flat spectrum radio quasar PKS 1510-089 in early 2012". In: *Astronomy and Astrophysics* 569, A46 (Sept. 2014), A46. DOI: 10.1051/0004-6361/201423484. arXiv: 1401.5646 [astro-ph.HE].

[133] J. León-Tavares et al. "Flare-like Variability of the Mg II λ2800 Emission Line in the Γ-Ray Blazar 3C 454.3". In: *The Astrophysical Journal Letters* 763.2, L36 (Feb. 2013), p. L36. DOI: 10.1088/2041-8205/763/2/L36. arXiv: 1301.3064 [astro-ph.HE].

[134] Vahram Chavushyan et al. "Flare-like Variability of the Mg II λ2798 Emission Line and UV Fe II Band in the Blazar CTA 102". In: *The Astrophysical Journal* 891.1, 68 (Mar. 2020), p. 68. DOI: 10.3847/1538-4357/ab6ef6. arXiv: 2001.08296 [astro-ph.HE].

[135] M. Hayashida et al. "The Structure and Emission Model of the Relativistic Jet in the Quasar 3C 279 Inferred from Radio to High-energy γ-Ray Observations in 2008-2010". In: *The Astrophysical Journal* 754, 114 (Aug. 2012), p. 114. DOI: 10.1088/0004-637X/754/2/114. arXiv: 1206.0745 [astro-ph.HE].

[136] M. Sikora et al. "Constraining Emission Models of Luminous Blazar Sources". In: *The Astrophysical Journal* 704 (Oct. 2009), pp. 38–50. DOI: 10.1088/0004-637X/704/1/38. arXiv: 0904.1414 [astro-ph.CO].

[137] K. Nalewajko et al. "Herschel PACS and SPIRE Observations of Blazar PKS 1510-089: A Case for Two Blazar Zones". In: *The Astrophysical Journal* 760, 69 (Nov. 2012), p. 69. DOI: 10.1088/0004-637X/760/1/69. arXiv: 1210.4552 [astro-ph.HE].

[138] S. Saito et al. "Time-dependent Modeling of Gamma-Ray Flares in Blazar PKS1510–089". In: *The Astrophysical Journal* 809, 171 (Aug. 2015), p. 171. DOI: 10.1088/0004-637X/809/2/171. arXiv: 1507.02442 [astro-ph.HE].

[139] M. L. Ahnen et al. "Multiwavelength observations of a VHE gamma-ray flare from PKS 1510-089 in 2015". In: *Astronomy and Astrophysics* 603, A29 (July 2017), A29. DOI: 10.1051/0004-6361/201629960. arXiv: 1610.09416 [astro-ph.HE].

[140] G. Ghisellini, F. Tavecchio, and M. Chiaberge. "Structured jets in TeV BL Lac objects and radiogalaxies. Implications for the observed properties". In: *Astronomy and Astrophysics* 432 (Mar. 2005), pp. 401–410. DOI: 10.1051/0004-6361:20041404. eprint: astro-ph/0406093.

[141] J. M. Attridge, D. H. Roberts, and J. F. C. Wardle. "Radio Jet-Ambient Medium Interactions on Parsec Scales in the Blazar 1055+018". In: *The Astrophysical Journal Letters* 518 (June 1999), pp. L87–L90. DOI: 10.1086/312078. eprint: astro-ph/9903330.

[142] N. R. MacDonald et al. "Through the Ring of Fire: Gamma-Ray Variability in Blazars by a Moving Plasmoid Passing a Local Source of Seed Photons". In: *The Astrophysical Journal* 804, 111 (May 2015), p. 111. DOI: 10.1088/0004-637X/804/2/111. arXiv: 1505.01239 [astro-ph.HE].

[143] N. R. MacDonald, S. G. Jorstad, and A. P. Marscher. "Orphan γ-Ray Flares and Stationary Sheaths of Blazar Jets". In: *The Astrophysical Journal* 850, 87 (Nov. 2017), p. 87. DOI: 10.3847/1538-4357/aa92c8. arXiv: 1611.09953 [astro-ph.HE].

[144] E. A. Corbett et al. "The appearance of broad Hα in BL Lacertae". In: *Monthly Notices of the Royal Astronomical Society* 281 (Aug. 1996), pp. 737–749. DOI: 10.1093/mnras/281.3.737.

[145] A. Capetti, C. M. Raiteri, and S. Buttiglione. "Is BL Lacertae an "orphan" AGN?. Multiband and spectroscopic constraints on the parent population". In: *Astronomy and Astrophysics* 516, A59 (June 2010), A59. DOI: 10.1051/0004-6361/201014232. arXiv: 1004.2161.

[146] I. Agudo et al. "Location of γ-ray Flare Emission in the Jet of the BL Lacertae Object OJ287 More than 14 pc from the Central Engine". In: *The Astrophysical Journal Letters* 726, L13 (Jan. 2011), p. L13. DOI: 10.1088/2041-8205/726/1/L13. arXiv: 1011.6454.

[147] A. B. Pushkarev et al. "Multifrequency study of the gamma-ray flaring BL Lacertae object PKS 2233-148 in 2009-2012". In: *Monthly Notices of the Royal Astronomical Society* 482 (Jan. 2019), pp. 2336–2353. DOI: 10.1093/mnras/sty2724. arXiv: 1808.06138 [astro-ph.HE].

[148] B. G. Piner and P. G. Edwards. "Multi-epoch VLBA Imaging of 20 New TeV Blazars: Apparent Jet Speeds". In: *The Astrophysical Journal* 853, 68 (Jan. 2018), p. 68. DOI: 10.3847/1538-4357/aaa425. arXiv: 1801.00817 [astro-ph.HE].

[149] V. A. Acciari et al. "TeV and Multi-wavelength Observations of Mrk 421 in 2006-2008". In: *The Astrophysical Journal* 738, 25 (Sept. 2011), p. 25. DOI: 10.1088/0004-637X/738/1/25. arXiv: 1106.1210 [astro-ph.HE].

[150] M. L. Ahnen et al. "Long-term multi-wavelength variability and correlation study of Markarian 421 from 2007 to 2009". In: *Astronomy and Astrophysics* 593, A91 (Sept. 2016), A91. DOI: 10.1051/0004-6361/201628447. arXiv: 1605.09017.

[151] E. J. Lindfors et al. "Optical and radio variability of the northern VHE gamma-ray emitting BL Lacertae objects". In: *Astronomy and Astrophysics* 593, A98 (Sept. 2016), A98. DOI: 10.1051/0004-6361/201628420. arXiv: 1606.06431 [astro-ph.HE].

[152] M. Georganopoulos and D. Kazanas. "Decelerating Flows in TeV Blazars: A Resolution to the BL Lacertae-FR I Unification Problem". In: *The Astrophysical Journal Letters* 594 (Sept. 2003), pp. L27–L30. DOI: 10.1086/378557. eprint: astro-ph/0307404.

[153] E. Lindfors. "Very high energy gamma-rays from flat spectrum radio quasars". In: *Extragalactic Jets from Every Angle*. Ed. by F. Massaro et al. Vol. 313. IAU Symposium. Mar. 2015, pp. 27–32. DOI: 10.1017/S1743921315001817.

[154] S. Boula and A. Mastichiadis. "Expanding one-zone model for blazar emission". In: *Astronomy and Astrophysics* 657, A20 (Jan. 2022), A20. DOI: 10.1051/0004-6361/202142126. arXiv: 2110.05325 [astro-ph.HE].

[155] Stella Boula, Demosthenes Kazanas, and Apostolos Mastichiadis. "Accretion disc MHD winds and blazar classification". In: *Monthly Notices of the Royal Astronomical Society* 482.1 (Jan. 2019), pp. L80–L84. DOI: 10.1093/mnrasl/sly189. arXiv: 1810.01796 [astro-ph.HE].

[156] Susumu Inoue and Fumio Takahara. "Electron Acceleration and Gamma-Ray Emission from Blazars". In: *The Astrophysical Journal* 463 (June 1996), p. 555. DOI: 10.1086/177270.

[157] F. Tavecchio, L. Maraschi, and G. Ghisellini. "Constraints on the Physical Parameters of TeV Blazars". In: *The Astrophysical Journal* 509 (Dec. 1998), pp. 608–619. DOI: 10.1086/306526. eprint: astro-ph/9809051.

[158] A. Lähteenmäki and E. Valtaoja. "Total Flux Density Variations in Extragalactic Radio Sources. III. Doppler Boosting Factors, Lorentz Factors, and Viewing Angles for Active Galactic Nuclei". In: *The Astrophysical Journal* 521 (Aug. 1999), pp. 493–501. DOI: 10.1086/307587.

[159] T. Hovatta et al. "Doppler factors, Lorentz factors and viewing angles for quasars, BL Lacertae objects and radio galaxies". In: *Astronomy and Astrophysics* 494 (Feb. 2009), pp. 527–537. DOI: 10.1051/0004-6361:200811150. arXiv: 0811.4278.

[160] A. C. S. Readhead. "Equipartition brightness temperature and the inverse Compton catastrophe". In: *The Astrophysical Journal* 426 (May 1994), pp. 51–59. DOI: 10.1086/174038.

[161] I. Liodakis et al. "Constraining the Limiting Brightness Temperature and Doppler Factors for the Largest Sample of Radio-bright Blazars". In: *The Astrophysical Journal* 866, 137 (Oct. 2018), p. 137. DOI: 10.3847/1538-4357/aae2b7. arXiv: 1809.08249 [astro-ph.HE].

[162] M. Lyutikov and M. Lister. "Resolving Doppler-factor Crisis in Active Galactic Nuclei: Non-steady Magnetized Outflows". In: *The Astrophysical Journal* 722 (Oct. 2010), pp. 197–203. DOI: 10.1088/0004-637X/722/1/197. arXiv: 1004.2430 [astro-ph.HE].

[163] M. Ackermann et al. "Multifrequency Studies of the Peculiar Quasar 4C +21.35 during the 2010 Flaring Activity". In: *The Astrophysical Journal* 786, 157 (May 2014), p. 157. DOI: 10.1088/0004-637X/786/2/157. arXiv: 1403.7534 [astro-ph.HE].

[164] Svetlana G. Jorstad et al. "Kinematics of Parsec-scale Jets of Gamma-Ray Blazars at 43 GHz within the VLBA-BU-BLAZAR Program". In: *The Astrophysical Journal* 846.2, 98 (Sept. 2017), p. 98. DOI: 10.3847/1538-4357/aa8407. arXiv: 1711.03983 [astro-ph.GA].

[165] A. B. Pushkarev et al. "MOJAVE: Monitoring of Jets in Active galactic nuclei with VLBA Experiments. IX. Nuclear opacity". In: *Astronomy and Astrophysics* 545, A113 (Sept. 2012), A113. DOI: 10.1051/0004-6361/201219173. arXiv: 1207.5457 [astro-ph.HE].

[166] T. Savolainen et al. "Magnetic Field Structure in the Parsec Scale Jet of 3C 273 from Multi-frequency VLBA Observations". In: *Extragalactic Jets: Theory and Observation from Radio to Gamma Ray*. Ed. by T. A. Rector and D. S. De Young. Vol. 386. Astronomical Society of the Pacific Conference Series. June 2008, p. 451. arXiv: 0708.0144.

[167] T. Beckert and H. Falcke. "Circular polarization of radio emission from relativistic jets". In: *Astronomy and Astrophysics* 388 (June 2002), pp. 1106–1119. DOI: 10.1051/0004-6361:20020484. eprint: astro-ph/0112398.

[168] D. C. Homan et al. "Full Polarization Spectra of 3C 279". In: *The Astrophysical Journal* 696 (May 2009), pp. 328–347. DOI: 10.1088/0004-637X/696/1/328. arXiv: 0902.0810 [astro-ph.CO].

[169] K. Katarzyński et al. "Hard TeV spectra of blazars and the constraints to the infrared intergalactic background". In: *Monthly Notices of the Royal Astronomical Society* 368 (May 2006), pp. L52–L56. DOI: 10.1111/j.1745-3933.2006.00156.x. eprint: astro-ph/0603030.

[170] J. Aleksić et al. "Discovery of VHE γ-rays from the blazar 1ES 1215+303 with the MAGIC telescopes and simultaneous multi-wavelength observations". In: *Astronomy and Astrophysics* 544, A142 (Aug. 2012), A142. DOI: 10.1051/0004-6361/201219133. arXiv: 1203.0490 [astro-ph.HE].

[171] J. Virtanen and R. Vainio. "Simulations on the Effect of Internal Structure of Shock Fronts on Particle Acceleration (Poster)". In: *High Energy Blazar Astronomy, ASP Conference Proceedings, Vol. 299, held 17-21 June 2002 at Tuorla Observatory, Piikkio, Finland. Edited by Leo O. Takalo and Esko Valtaoja. ISBN: 1-58381-146-X. San Francisco: Astronomical Society of the Pacific, 2003, p.157*. Ed. by L. O. Takalo and E. Valtaoja. Vol. 299. July 2003, p. 157.

[172] L. Sironi and A. Spitkovsky. "Particle Acceleration in Relativistic Magnetized Collisionless Electron-Ion Shocks". In: *The Astrophysical Journal* 726, 75 (Jan. 2011), p. 75. DOI: 10.1088/0004-637X/726/2/75. arXiv: 1009.0024 [astro-ph.HE].

[173] W. J. Potter and G. Cotter. "Synchrotron and inverse-Compton emission from blazar jets - III. Compton-dominant blazars". In: *Monthly Notices of the Royal Astronomical Society* 431 (May 2013), pp. 1840–1852. DOI: 10.1093/mnras/stt300. arXiv: 1303.1182 [astro-ph.HE].

[174] A. Celotti, P. Padovani, and G. Ghisellini. "Jets and accretion processes in active galactic nuclei: further clues". In: *Monthly Notices of the Royal Astronomical Society* 286 (Apr. 1997), pp. 415–424. DOI: 10.1093/mnras/286.2.415. eprint: astro-ph/9611111.

[175] P. J. Francis et al. "A high signal-to-noise ratio composite quasar spectrum". In: *The Astrophysical Journal* 373 (June 1991), pp. 465–470. DOI: 10.1086/170066.

[176] G. Ghisellini and F. Tavecchio. "Canonical high-power blazars". In: *Monthly Notices of the Royal Astronomical Society* 397 (Aug. 2009), pp. 985–1002. DOI: 10.1111/j.1365-2966.2009.15007.x. arXiv: 0902.0793.

[177] E. Pian et al. "Ultraviolet and Multiwavelength Variability of the Blazar 3C 279: Evidence for Thermal Emission". In: *The Astrophysical Journal* 521 (Aug. 1999), pp. 112–120. DOI: 10.1086/307548. eprint: astro-ph/9906326.

[178] B. J. Wills. "Optical-infrared synchrotron emission in luminous AGN". In: *BL Lac Objects*. Ed. by L. Maraschi, T. Maccacaro, and M.-H. Ulrich. Vol. 334. Lecture Notes in Physics, Berlin Springer Verlag. 1989, p. 107. DOI: 10.1007/BFb0031151.

[179] S. Soldi et al. "The multiwavelength variability of 3C 273". In: *Astronomy and Astrophysics* 486 (Aug. 2008), pp. 411–425. DOI: 10.1051/0004-6361:200809947. arXiv: 0805.3411.

[180] M. P. Malmrose et al. "Emission from Hot Dust in the Infrared Spectra of Gamma-ray Bright Blazars". In: *The Astrophysical Journal* 732, 116 (May 2011), p. 116. DOI: 10.1088/0004-637X/732/2/116. arXiv: 1103.1682.

[181] M. Nenkova et al. "AGN Dusty Tori. I. Handling of Clumpy Media". In: *The Astrophysical Journal* 685 (Sept. 2008), pp. 147–159. DOI: 10.1086/590482. arXiv: 0806.0511.

[182] T. Minezaki et al. "Inner Size of a Dust Torus in the Seyfert 1 Galaxy NGC 4151". In: *The Astrophysical Journal Letters* 600 (Jan. 2004), pp. L35–L38. DOI: 10.1086/381364. eprint: astro-ph/0311338.

[183] M. Suganuma et al. "Reverberation Measurements of the Inner Radius of the Dust Torus in Nearby Seyfert 1 Galaxies". In: *The Astrophysical Journal* 639 (Mar. 2006), pp. 46–63. DOI: 10.1086/499326. eprint: astro-ph/0511697.

[184] C. Nigro et al. "agnpy: An open-source python package modelling the radiative processes of jetted active galactic nuclei". In: *Astronomy and Astrophysics* 660, A18 (Apr. 2022), A18. DOI: 10.1051/0004-6361/202142000. arXiv: 2112.14573 [astro-ph.IM].

[185] Ilaria Viale et al. "Development of hadronic emission processes in the open-source python package AGNpy". In: *PoS* ICRC2023 (2023), p. 1524. DOI: 10.22323/1.444.1524.

[186] Justin D. Finke, Charles D. Dermer, and Markus Böttcher. "Synchrotron Self-Compton Analysis of TeV X-Ray-Selected BL Lacertae Objects". In: *The Astrophysical Journal* 686.1 (Oct. 2008), pp. 181–194. DOI: 10.1086/590900. arXiv: 0802.1529 [astro-ph].

[187] Frank C. Jones. "Calculated Spectrum of Inverse-Compton-Scattered Photons". In: *Physical Review* 167.5 (Mar. 1968), pp. 1159–1169. DOI: 10.1103/PhysRev.167.1159.

[188] Charles D. Dermer et al. "Gamma-Ray Studies of Blazars: Synchro-Compton Analysis of Flat Spectrum Radio Quasars". In: *The Astrophysical Journal* 692.1 (Feb. 2009), pp. 32–46. DOI: 10.1088/0004-637X/692/1/32. arXiv: 0808.3185 [astro-ph].

[189] Justin D. Finke. "External Compton Scattering in Blazar Jets and the Location of the Gamma-Ray Emitting Region". In: *The Astrophysical Journal* 830.2, 94 (Oct. 2016), p. 94. DOI: 10.3847/0004-637X/830/2/94.

[190] Charles D. Dermer and Reinhard Schlickeiser. "Transformation Properties of External Radiation Fields, Energy-Loss Rates and Scattered Spectra, and a Model for Blazar Variability". In: *The Astrophysical Journal* 575.2 (Aug. 2002), pp. 667–686. DOI: 10.1086/341431. arXiv: astro-ph/0202280 [astro-ph].

[191] Omar Laurino et al. "Sherpa, Python, and Astronomy. A Successful Co-evolution." In: *Astronomical Data Analysis Software and Systems XXVI*. Ed. by Marco Molinaro, Keith Shortridge, and Fabio Pasian. Vol. 521. Astronomical Society of the Pacific Conference Series. Oct. 2019, p. 479.

[192] Charles D. Dermer and Reinhard Schlickeiser. "On the Location of the Acceleration and Emission Sites in Gamma-Ray Blazars". In: *The Astrophysical Journal Supplement Series* 90 (Feb. 1994), p. 945. DOI: 10.1086/191929.

[193] P. M. Chadwick et al. "Geomagnetic effects on atmospheric Cerenkov images". In: *Journal of Physics G Nuclear Physics* 25.6 (June 1999), pp. 1223–1233. DOI: 10.1088/0954-3899/25/6/312. arXiv: astro-ph/9904082 [astro-ph].

[194] Jamie Holder. "Atmospheric Cherenkov Gamma-ray Telescopes". In: *arXiv e-prints*, arXiv:1510.05675 (Oct. 2015), arXiv:1510.05675. DOI: 10.48550/arXiv.1510.05675. arXiv: 1510.05675 [astro-ph.IM].

[195] Gernot Maier. *Gamma-ray picture book*. Version v1.0.0. Feb. 2022. DOI: 10.5281/zenodo.6037688. URL: https://doi.org/10.5281/zenodo.6037688.

[196] A. M. Hillas. "Cerenkov Light Images of EAS Produced by Primary Gamma Rays and by Nuclei". In: *19th International Cosmic Ray Conference (ICRC19), Volume 3*. Vol. 3. International Cosmic Ray Conference. Aug. 1985, p. 445.

[197] W. Hofmann et al. "Comparison of techniques to reconstruct VHE gamma-ray showers from multiple stereoscopic Cherenkov images". In: *Astroparticle Physics* 12.3 (Nov. 1999), pp. 135–143. DOI: 10.1016/S0927-6505(99)00084-5. arXiv: astro-ph/9904234 [astro-ph].

[198] J. Aleksić et al. "Performance of the MAGIC stereo system obtained with Crab Nebula data". In: *Astroparticle Physics* 35.7 (Feb. 2012), pp. 435–448. DOI: 10.1016/j.astropartphys.2011.11.007. arXiv: 1108.1477 [astro-ph.IM].

[199] T. C. Weekes et al. "Observation of TeV Gamma Rays from the Crab Nebula Using the Atmospheric Cerenkov Imaging Technique". In: *The Astrophysical Journal* 342 (July 1989), p. 379. DOI: 10.1086/167599.

[200] T. Ashton et al. "A NECTAr-based upgrade for the Cherenkov cameras of the H.E.S.S. 12-meter telescopes". In: *Astroparticle Physics* 118, 102425 (Mar. 2020), p. 102425. DOI: 10.1016/j.astropartphys.2019.102425. arXiv: 2001.04510 [astro-ph.IM].

[201] D. Bose et al. "Ground-based gamma-ray astronomy: history and development of techniques". In: *European Physical Journal Special Topics* 231.1 (Jan. 2022), pp. 3–26. DOI: 10.1140/epjs/s11734-021-00396-3. arXiv: 2201.04719 [astro-ph.IM].

[202] H. Abe et al. "Observations of the Crab Nebula and Pulsar with the Large-sized Telescope Prototype of the Cherenkov Telescope Array". In: *The Astrophysical Journal* 956.2, 80 (Oct. 2023), p. 80. DOI: 10.3847/1538-4357/ace89d. arXiv: 2306.12960 [astro-ph.HE].

[203] F. Aharonian et al. "Observations of the Crab nebula with HESS". In: *Astronomy and Astrophysics* 457.3 (Oct. 2006), pp. 899–915. DOI: 10.1051/0004-6361:20065351. arXiv: astro-ph/0607333 [astro-ph].

[204] H. E. S. S. Collaboration et al. "The H.E.S.S. Galactic plane survey". In: *Astronomy and Astrophysics* 612, A1 (Apr. 2018), A1. DOI: 10.1051/0004-6361/201732098. arXiv: 1804.02432 [astro-ph.HE].

[205] F. Aharonian et al. "Energy Spectrum of Cosmic-Ray Electrons at TeV Energies". In: *Physical Review Letters* 101.26, 261104 (Dec. 2008), p. 261104. DOI: 10.1103/PhysRevLett.101.261104. arXiv: 0811.3894 [astro-ph].

[206] H. E. S. S. Collaboration et al. "The γ-ray spectrum of the core of Centaurus A as observed with H.E.S.S. and Fermi-LAT". In: *Astronomy and Astrophysics* 619, A71 (Nov. 2018), A71. DOI: 10.1051/0004-6361/201832640. arXiv: 1807.07375 [astro-ph.HE].

[207] T. C. Weekes et al. "VERITAS: the Very Energetic Radiation Imaging Telescope Array System". In: *Astroparticle Physics* 17.2 (May 2002), pp. 221–243. DOI: 10.1016/S0927-6505(01)00152-9. arXiv: astro-ph/0108478 [astro-ph].

[208] VERITAS Collaboration et al. "A connection between star formation activity and cosmic rays in the starburst galaxy M82". In: *Nature* 462.7274 (Dec. 2009), pp. 770–772. DOI: 10.1038/nature08557. arXiv: 0911.0873 [astro-ph.CO].

[209] E. Aliu et al. "Discovery of High-energy and Very High Energy γ-Ray Emission from the Blazar RBS 0413". In: *The Astrophysical Journal* 750.2, 94 (May 2012), p. 94. DOI: 10.1088/0004-637X/750/2/94. arXiv: 1204.0865 [astro-ph.HE].

[210] E. Aliu et al. "Multiwavelength Observations of the AGN 1ES 0414+009 with VERITAS, Fermi-LAT, Swift-XRT, and MDM". In: *The Astrophysical Journal* 755.2, 118 (Aug. 2012), p. 118. DOI: 10.1088/0004-637X/755/2/118. arXiv: 1206.4080 [astro-ph.HE].

[211] A. U. Abeysekara et al. "Gamma-Rays from the Quasar PKS 1441+25: Story of an Escape". In: *The Astrophysical Journal Letters* 815.2, L22 (Dec. 2015), p. L22. DOI: 10.1088/2041-8205/815/2/L22. arXiv: 1512.04434 [astro-ph.HE].

[212] J. Aleksić et al. "The major upgrade of the MAGIC telescopes, Part II: A performance study using observations of the Crab Nebula". In: *Astroparticle Physics* 72 (Jan. 2016), pp. 76–94. DOI: 10.1016/j.astropartphys.2015.02.005. arXiv: 1409.5594 [astro-ph.IM].

[213] F. Dazzi et al. "The Stereoscopic Analog Trigger of the MAGIC Telescopes". In: *IEEE Transactions on Nuclear Science* 68.7 (July 2021), pp. 1473–1486. DOI: 10.1109/TNS.2021.3079262.

[214] V. A. Acciari et al. "Proton acceleration in thermonuclear nova explosions revealed by gamma rays". In: *Nature Astronomy* 6 (Apr. 2022), pp. 689–697. DOI: 10.1038/s41550-022-01640-z. arXiv: 2202.07681 [astro-ph.HE].

[215] Werner Hofmann and Roberta Zanin. "The Cherenkov Telescope Array". In: *arXiv e-prints*, arXiv:2305.12888 (May 2023), arXiv:2305.12888. DOI: 10.48550/arXiv.2305.12888. arXiv: 2305.12888 [astro-ph.IM].

[216] Y. Kobayashi et al. "Camera Calibration of the CTA-LST prototype". In: *37th International Cosmic Ray Conference*. Mar. 2022, 720, p. 720. DOI: 10.22323/1.395.0720. arXiv: 2108.05035 [astro-ph.IM].

[217] J. Cortina and C. l. Project. "Status of the Large Size Telescopes of the Cherenkov Telescope Array". In: *36th International Cosmic Ray Conference (ICRC2019)*. Vol. 36. International Cosmic Ray Conference. July 2019, 653, p. 653. DOI: 10.22323/1.358.0653. arXiv: 1907.10146 [astro-ph.IM].

[218] H. Abe et al. "Performance of the joint LST-1 and MAGIC observations evaluated with Crab Nebula data". In: *Astronomy and Astrophysics* 680, A66 (Dec. 2023), A66. DOI: 10.1051/0004-6361/202346927. arXiv: 2310.01954 [astro-ph.IM].

[219] M. Shayduk and Cta Consortium. "Optimized Next-neighbour Image Cleaning Method for Cherenkov Telescopes". In: *International Cosmic Ray Conference*. Vol. 33. International Cosmic Ray Conference. Jan. 2013, p. 3000. DOI: 10.48550/arXiv.1307.4939. arXiv: 1307.4939 [astro-ph.IM].

[220] M. Punch et al. "Supercuts: An Improved Method of Selecting Gamma-rays". In: *International Cosmic Ray Conference*. Vol. 1. International Cosmic Ray Conference. Aug. 1991, p. 464.

[221] E. Aliu et al. "Improving the performance of the single-dish Cherenkov telescope MAGIC through the use of signal timing". In: *Astroparticle Physics* 30.6 (Jan. 2009), pp. 293–305. DOI: 10.1016/j.astropartphys.2008.10.003. arXiv: 0810.3568 [astro-ph].

[222] Saverio Lombardi. "Advanced stereoscopic gamma-ray shower analysis with the MAGIC telescopes". In: *International Cosmic Ray Conference*. Vol. 3. International Cosmic Ray Conference. Jan. 2011, p. 266. DOI: 10.7529/ICRC2011/V03/1150. arXiv: 1109.6195 [astro-ph.IM].

[223] J. Albert et al. "VHE γ-Ray Observation of the Crab Nebula and its Pulsar with the MAGIC Telescope". In: *The Astrophysical Journal* 674.2 (Feb. 2008), pp. 1037–1055. DOI: 10.1086/525270. arXiv: 0705.3244 [astro-ph].

[224] J. Albert et al. "Implementation of the Random Forest method for the Imaging Atmospheric Cherenkov Telescope MAGIC". In: *Nuclear Instruments and Methods in Physics Research A* 588.3 (Apr. 2008), pp. 424–432. DOI: 10.1016/j.nima.2007.11.068. arXiv: 0709.3719 [astro-ph].

[225] A. M. Hillas. "Differences between Gamma-Ray and Hadronic Showers". In: *Space Science Reviews* 75.1-2 (Jan. 1996), pp. 17–30. DOI: 10.1007/BF00195021.

[226] V. P. Fomin et al. "New methods of atmospheric Cherenkov imaging for gamma-ray astronomy. I. The false source method". In: *Astroparticle Physics* 2.2 (May 1994), pp. 137–150. DOI: 10.1016/0927-6505(94)90036-1.

[227] T. -P. Li and Y. -Q. Ma. "Analysis methods for results in gamma-ray astronomy." In: *The Astrophysical Journal* 272 (Sept. 1983), pp. 317–324. DOI: 10.1086/161295.

[228] G. Mohanty et al. "Measurement of TeV gamma-ray spectra with the Cherenkov imaging technique". In: *Astroparticle Physics* 9.1 (June 1998), pp. 15–43. DOI: 10.1016/S0927-6505(98)00005-X.

[229] F. Aharonian et al. "The Crab Nebula and Pulsar between 500 GeV and 80 TeV: Observations with the HEGRA Stereoscopic Air Cerenkov Telescopes". In: *The Astrophysical Journal* 614.2 (Oct. 2004), pp. 897–913. DOI: 10.1086/423931. arXiv: astro-ph/0407118 [astro-ph].

[230] A. Djannati-Atai et al. "Very High Energy Gamma-ray spectral properties of MKN 501 from CAT Čerenkov telescope observations in 1997". In: *Astronomy and Astrophysics* 350 (Oct. 1999), pp. 17–24. DOI: 10.48550/arXiv.astro-ph/9906060. arXiv: astro-ph/9906060 [astro-ph].

[231] M. Noethe et al. "Prototype Open Event Reconstruction Pipeline for the Cherenkov Telescope Array". In: *37th International Cosmic Ray Conference*. Mar. 2022, 744, p. 744. DOI: 10.22323/1.395.0744. arXiv: 2110.11097 [astro-ph.IM].

[232] Ruben López-Coto et al. "lstchain: An Analysis Pipeline for LST-1, the First Prototype Large-Sized Telescope of CTA". In: *Astronomical Society of the Pacific Conference Series*. Ed. by Jose Enrique Ruiz, Francesco Pierfedereci, and Peter Teuben. Vol. 532. Astronomical Society of the Pacific Conference Series. July 2022, p. 357.

[233] J. E. Ruiz et al. "LSTOSA: Onsite Processing Pipeline for the CTA Larged-Sized Telescope Prototype". In: *Astronomical Society of the Pacific Conference Series*. Ed. by Jose Enrique Ruiz, Francesco Pierfedereci, and Peter Teuben. Vol. 532. Astronomical Society of the Pacific Conference Series. July 2022, p. 369. DOI: 10.48550/arXiv.2101.09690. arXiv: 2101.09690 [astro-ph.IM].

[234] Roberta Zanin et al. "MARS, The MAGIC Analysis and Reconstruction Software". In: *International Cosmic Ray Conference*. Vol. 33. International Cosmic Ray Conference. Jan. 2013, p. 2937.

[235] Axel Donath et al. "Gammapy: A Python package for gamma-ray astronomy". In: *Astronomy and Astrophysics* 678, A157 (Oct. 2023), A157. DOI: 10.1051/0004-6361/202346488. arXiv: 2308.13584 [astro-ph.IM].

[236] Christoph Deil et al. "Open high-level data formats and software for gamma-ray astronomy". In: *6th International Symposium on High Energy Gamma-Ray Astronomy*. Vol. 1792. American Institute of Physics Conference Series. Jan. 2017, 070006, p. 070006. DOI: 10.1063/1.4969003. arXiv: 1610.01884 [astro-ph.IM].

[237] C. Nigro et al. "Towards open and reproducible multi-instrument analysis in gamma-ray astronomy". In: *Astronomy and Astrophysics* 625, A10 (May 2019), A10. DOI: 10.1051/0004-6361/201834938. arXiv: 1903.06621 [astro-ph.HE].

[238] W. D. Pence et al. "Definition of the Flexible Image Transport System (FITS), version 3.0". In: *Astronomy and Astrophysics* 524, A42 (Dec. 2010), A42. DOI: 10.1051/0004-6361/201015362.

[239] W. Cash. "Parameter estimation in astronomy through application of the likelihood ratio." In: *The Astrophysical Journal* 228 (Mar. 1979), pp. 939–947. DOI: 10.1086/156922.

[240] D. Heck et al. *CORSIKA: a Monte Carlo code to simulate extensive air showers.* 1998.

[241] Konrad Bernlöhr. "Simulation of imaging atmospheric Cherenkov telescopes with CORSIKA and sim_ telarray". In: *Astroparticle Physics* 30.3 (Oct. 2008), pp. 149–158. DOI: 10.1016/j.astropartphys.2008.07.009. arXiv: 0808.2253 [astro-ph].

[242] J. Albert et al. "FADC signal reconstruction for the MAGIC telescope". In: *Nuclear Instruments and Methods in Physics Research A* 594.3 (Sept. 2008), pp. 407–419. DOI: 10.1016/j.nima.2008.06.043. arXiv: astro-ph/0612385 [astro-ph].

[243] Maximilian Nöthe et al. *pyirf*. Zenodo. Version v0.4.0. Nov. 2020. DOI: 10.5281/zenodo.4304466.

[244] Seiya Nozaki et al. "Calibration and performance of the readout system based on switched capacitor arrays for the Large-Sized Telescope of the Cherenkov Telescope Array". In: *Ground-based and Airborne Instrumentation for Astronomy VIII*. Ed. by Christopher J. Evans, Julia J. Bryant, and Kentaro Motohara. Vol. 11447. Society of Photo-Optical Instrumentation Engineers (SPIE) Conference Series. Dec. 2020, 114470H, 114470H. DOI: 10.1117/12.2560018. arXiv: 2203.06582 [astro-ph.IM].

[245] Massimiliano Bitossi, Riccardo Paoletti, and Diego Tescaro. "Ultra-Fast Sampling and Data Acquisition Using the DRS4 Waveform Digitizer". In: *IEEE Transactions on Nuclear Science* 63.4 (Aug. 2016), pp. 2309–2316. DOI: 10.1109/TNS.2016.2578963.

[246] S. Masuda et al. "Development of the photomultiplier tube readout system for the first Large-Sized Telescope of the Cherenkov Telescope Array". In: *34th International Cosmic Ray Conference (ICRC2015)*. Vol. 34. International Cosmic Ray Conference. July 2015, 1003, p. 1003. DOI: 10.22323/1.236.01003. arXiv: 1509.00548 [astro-ph.IM].

[247] Michele Palatiello et al. "Performance of the INFN Camera calibration device of the first Large Size Telescope in the Cherenkov Telescope Array". In: *arXiv e-prints*, arXiv:1909.08475 (Sept. 2019), arXiv:1909.08475. DOI: 10.48550/arXiv.1909.08475. arXiv: 1909.08475 [astro-ph.IM].

[248] J. S. Miller, H. B. French, and S. A. Hawley. "The spectrum and magnitude of the galaxy associated with BL Lacertae." In: *The Astrophysical Journal Letters* 219 (Jan. 1978), pp. L85–L87. DOI: 10.1086/182612.

[249] K. Nilsson et al. "Long-term optical monitoring of TeV emitting blazars. I. Data analysis". In: *Astronomy and Astrophysics* 620, A185 (Dec. 2018), A185. DOI: 10.1051/0004-6361/201833621. arXiv: 1810.01751 [astro-ph.HE].

[250] M. Ackermann et al. "The Second Catalog of Active Galactic Nuclei Detected by the Fermi Large Area Telescope". In: *The Astrophysical Journal* 743.2, 171 (Dec. 2011), p. 171. DOI: 10.1088/0004-637X/743/2/171.

[251] N. Sahakyan and P. Giommi. "A 13-yr-long broad-band view of BL Lac". In: *Monthly Notices of the Royal Astronomical Society* 513.3 (July 2022), pp. 4645–4656. DOI: 10.1093/mnras/stac1011.

[252] Yu. I. Neshpor et al. "BL Lac: A New Ultrahigh-Energy Gamma-Ray Source". In: *Astronomy Reports* 45.4 (Apr. 2001), pp. 249–254. DOI: 10.1134/1.1361316.

[253] D. Kranich. "TeV Observations of BL Lac Objects (Invited Talk)". In: *High Energy Blazar Astronomy*. Ed. by Leo O. Takalo and Esko Valtaoja. Vol. 299. Astronomical Society of the Pacific Conference Series. July 2003, p. 3.

[254] J. Albert et al. "Discovery of Very High Energy γ-Ray Emission from the Low-Frequency-peaked BL Lacertae Object BL Lacertae". In: *The Astrophysical Journal Letters* 666.1 (Sept. 2007), pp. L17–L20. DOI: 10.1086/521550. arXiv: astro-ph/0703084 [astro-ph].

[255] Razmik Mirzoyan. "MAGIC detection of an increased activity from BL Lacertae at very-high-energy gamma rays". In: *The Astronomer's Telegram* 12724 (May 2019), p. 1.

[256] Oscar Blanch. "MAGIC detection of very-high-energy gamma-ray flaring activity from BL Lacertae during the current historical optical and high-energy gamma-ray flare". In: *The Astronomer's Telegram* 13963 (Aug. 2020), p. 1.

[257] Oscar Blanch. "Detection of a bright very-high-energy gamma-ray flare from BL Lac with the MAGIC telescopes". In: *The Astronomer's Telegram* 14032 (Sept. 2020), p. 1.

[258] T. S. Grishina and V. M. Larionov. "The blazar BL Lac reaches historical maximum". In: *The Astronomer's Telegram* 13930 (Aug. 2020), p. 1.

[259] Riley M. Corcoran et al. "Continued Optical Activity in the Blazar BL Lacertae". In: *The Astronomer's Telegram* 14773 (July 2021), p. 1.

[260] Natsuko Hazama et al. "Optical and near-infrared photometric and polarimetric monitoring at flaring state of BL Lacertae in 2020-2021". In: *Publications of the Astronomical Society of Japan* 74.5 (Oct. 2022), pp. 1041–1048. DOI: 10.1093/pasj/psac054.

[261] Juan Cortina and CTA LST Collaboratoin. "Detection of very-high-energy gamma-ray emission from BL Lac with the LST-1". In: *The Astronomer's Telegram* 14783 (July 2021), p. 1.

[262] Seiya Nozaki et al. "LST-1 observations of an enormous flare of BL Lacertae in 2021". In: *arXiv e-prints*, arXiv:2309.09715 (Sept. 2023), arXiv:2309.09715. DOI: 10.48550/arXiv.2309.09715. arXiv: 2309.09715 [astro-ph.HE].

[263] Oscar Blanch et al. "Detection of flaring very-high-energy gamma-ray emission from BL Lacertae with the MAGIC telescopes". In: *The Astronomer's Telegram* 14826 (Aug. 2021), p. 1.

[264] S. Abdollahi et al. "The Fermi-LAT Lightcurve Repository". In: *The Astrophysical Journal Supplement Series* 265.2, 31 (Apr. 2023), p. 31. DOI: 10.3847/1538-4365/acbb6a. arXiv: 2301.01607 [astro-ph.HE].

[265] Axel Donath et al. *gammapy/gammapy: v.0.19*. Version v0.19. Nov. 2021. DOI: 10.5281/zenodo.5721467. URL: https://doi.org/10.5281/zenodo.5721467.

[266] J. Aleksić et al. "Measurement of the Crab Nebula spectrum over three decades in energy with the MAGIC telescopes". In: *Journal of High Energy Astrophysics* 5 (Mar. 2015), pp. 30–38. DOI: 10.1016/j.jheap.2015.01.002. arXiv: 1406.6892 [astro-ph.HE].

[267] MAGIC Collaboration. *Constraints on VHE gamma-ray emission of Flat Spectrum Radio Quasars with the MAGIC telescopes*. 2024. arXiv: 2403.13713 [astro-ph.HE].

[268] G. Principe et al. "Gamma-ray emission from young radio galaxies and quasars". In: *Monthly Notices of the Royal Astronomical Society* 507.3 (Nov. 2021), pp. 4564–4583. DOI: 10.1093/mnras/stab2357. arXiv: 2107.12963 [astro-ph.HE].

[269] P. Bruel et al. "Fermi-LAT improved Pass~8 event selection". In: *arXiv e-prints*, arXiv:1810.11394 (Oct. 2018), arXiv:1810.11394. DOI: 10.48550/arXiv.1810.11394. arXiv: 1810.11394 [astro-ph.IM].

[270] M. Wood et al. "Fermipy: An open-source Python package for analysis of Fermi-LAT Data". In: *35th International Cosmic Ray Conference (ICRC2017)*. Vol. 301. International Cosmic Ray Conference. July 2017, 824, p. 824. DOI: 10.22323/1.301.0824. arXiv: 1707.09551 [astro-ph.IM].

[271] J. R. Mattox et al. "The Likelihood Analysis of EGRET Data". In: *The Astrophysical Journal* 461 (Apr. 1996), p. 396. DOI: 10.1086/177068.

[272] N. Gehrels et al. "The Swift Gamma-Ray Burst Mission". In: *The Astrophysical Journal* 611.2 (Aug. 2004), pp. 1005–1020. DOI: 10.1086/422091. arXiv: astro-ph/0405233 [astro-ph].

[273] Peter W. A. Roming et al. "The Swift Ultra-Violet/Optical Telescope". In: *Space Science Reviews* 120.3-4 (Oct. 2005), pp. 95–142. DOI: 10.1007/s11214-005-5095-4. arXiv: astro-ph/0507413 [astro-ph].

[274] Scott D. Barthelmy et al. "The Burst Alert Telescope (BAT) on the SWIFT Midex Mission". In: *Space Science Reviews* 120.3-4 (Oct. 2005), pp. 143–164. DOI: 10.1007/s11214-005-5096-3. arXiv: astro-ph/0507410 [astro-ph].

[275] Nasa High Energy Astrophysics Science Archive Research Center (Heasarc). *HEAsoft: Unified Release of FTOOLS and XANADU*. Astrophysics Source Code Library, record ascl:1408.004. Aug. 2014.

[276] P. Predehl and J. H. M. M. Schmitt. "X-raying the interstellar medium: ROSAT observations of dust scattering halos." In: *Astronomy and Astrophysics* 293 (Jan. 1995), pp. 889–905.

[277] L. O. Takalo et al. "Tuorla Blazar Monitoring Program". In: *American Institute of Physics Conference Series*. Ed. by Felix A. Aharonian, Werner Hofmann, and Frank Rieger. Vol. 1085. American Institute of Physics Conference Series. Dec. 2008, pp. 705–707. DOI: 10.1063/1.3076774.

[278] L. Costamante and G. Ghisellini. "TeV candidate BL Lac objects". In: *Astronomy and Astrophysics* 384 (Mar. 2002), pp. 56–71. DOI: 10.1051/0004-6361:20011749. arXiv: astro-ph/0112201 [astro-ph].

[279] C. M. Raiteri et al. "Spectroscopic monitoring of the BL Lac object <ASTROBJ>AO 0235+164</ASTROBJ>". In: *Astronomy and Astrophysics* 464.3 (Mar. 2007), pp. 871–878. DOI: 10.1051/0004-6361:20066599. arXiv: astro-ph/0701325 [astro-ph].

[280] Edward F. Schlafly and Douglas P. Finkbeiner. "Measuring Reddening with Sloan Digital Sky Survey Stellar Spectra and Recalibrating SFD". In: *The Astrophysical Journal* 737.2, 103 (Aug. 2011), p. 103. DOI: 10.1088/0004-637X/737/2/103. arXiv: 1012.4804 [astro-ph.GA].

[281] Christian Fruck and Markus Gaug. "Atmospheric monitoring in MAGIC and data corrections". In: *European Physical Journal Web of Conferences*. Vol. 89. European Physical Journal Web of Conferences. Mar. 2015, 02003, p. 02003. DOI: 10.1051/epjconf/20158902003.

[282] F. Schmuckermaier et al. "Correcting Imaging Atmospheric Cherenkov Telescope data with atmospheric profiles obtained with an elastic light detecting and ranging system". In: *Astronomy and Astrophysics* 673, A2 (May 2023), A2. DOI: 10.1051/0004-6361/202245787. arXiv: 2302.12072 [astro-ph.IM].

[283] Maarten Schmidt. "Large Redshifts of Five Quasi-Stellar Sources." In: *The Astrophysical Journal* 141 (Apr. 1965), p. 1295. DOI: 10.1086/148217.

[284] P. L. Nolan et al. "Observation of High-Energy Gamma Rays from the Quasi-stellar Object CTA 102". In: *The Astrophysical Journal* 414 (Sept. 1993), p. 82. DOI: 10.1086/173058.

[285] F. D'Ammando et al. "Investigating the multiwavelength behaviour of the flat spectrum radio quasar CTA 102 during 2013-2017". In: *Monthly Notices of the Royal Astronomical Society* 490.4 (Dec. 2019), pp. 5300–5316. DOI: 10.1093/mnras/stz2792. arXiv: 1910.03609 [astro-ph.HE].

[286] G. Minervini et al. "AGILE detection of enhanced gamma-ray emission from the FSRQ CTA 102". In: *The Astronomer's Telegram* 9743 (Nov. 2016), p. 1.

[287] Katie J. Chapman et al. "A Spectacular, Unprecedented Optical Flare in the Blazar CTA 102". In: *The Astronomer's Telegram* 9756 (Nov. 2016), p. 1.

[288] Thomas J. Balonek et al. "Blazar CTA 102 Reaches Historic Optical Maximum During Current Extended Period of Activity". In: *The Astronomer's Telegram* 9732 (Nov. 2016), p. 1.

[289] Stefano Ciprini. "Fermi LAT observation of renewed and strong GeV gamma-ray activity from blazar CTA 102". In: *The Astronomer's Telegram* 9869 (Dec. 2016), p. 1.

[290] G. Paturel et al. "Comparison LEDA/SIMBAD octobre 2002. Catalogue to be published in 2003." In: *LEDA* (Jan. 2002), p. 0.

[291] R. C. Hartman et al. "EGRET Detection of High-Energy Gamma Radiation from the OVV Quasar 3C 454.3". In: *The Astrophysical Journal Letters* 407 (Apr. 1993), p. L41. DOI: 10.1086/186801.

[292] M. Villata et al. "The unprecedented optical outburst of the quasar <ASTROBJ>3C 454.3</ASTROBJ>. The WEBT campaign of 2004-2005". In: *Astronomy and Astrophysics* 453.3 (July 2006), pp. 817–822. DOI: 10.1051/0004-6361:20064817. arXiv: astro-ph/0603386 [astro-ph].

[293] A. A. Abdo et al. "Early Fermi Gamma-ray Space Telescope Observations of the Quasar 3C 454.3". In: *The Astrophysical Journal* 699.1 (July 2009), pp. 817–823. DOI: 10.1088/0004-637X/699/1/817. arXiv: 0904.4280 [astro-ph.HE].

[294] A. A. Abdo et al. "Fermi Gamma-ray Space Telescope Observations of the Gamma-ray Outburst from 3C454.3 in November 2010". In: *The Astrophysical Journal Letters* 733.2 (June 2011), p. L26. DOI: 10.1088/2041-8205/733/2/L26. arXiv: 1102.0277 [astro-ph.HE].

[295] S. Vercellone et al. "The Brightest Gamma-Ray Flaring Blazar in the Sky: AGILE and Multi-wavelength Observations of 3C 454.3 During 2010 November". In: *The Astrophysical Journal Letters* 736.2, L38 (Aug. 2011), p. L38. DOI: 10.1088/2041-8205/736/2/L38. arXiv: 1106.5162 [astro-ph.HE].

[296] H. Anderhub et al. "MAGIC upper limits to the VHE gamma-ray flux of 3C 454.3 in high emission state". In: *Astronomy and Astrophysics* 498.1 (Apr. 2009), pp. 83–87. DOI: 10.1051/0004-6361/200811326. arXiv: 0811.1680 [astro-ph].

[297] Kevork N. Abazajian et al. "The Seventh Data Release of the Sloan Digital Sky Survey". In: *The Astrophysical Journal Supplement Series* 182.2 (June 2009), pp. 543–558. DOI: 10.1088/0067-0049/182/2/543. arXiv: 0812.0649 [astro-ph].

[298] S. Buson. "Fermi LAT Detection of a GeV Flare from OP 313 (B2 1308+32)." In: *The Astronomer's Telegram* 6068 (Apr. 2014), p. 1.

[299] Thomas J. Balonek et al. "ATel 12898: Rapid Optical Flaring of the Quasar 1308+326". In: *The Astronomer's Telegram* 12898 (June 2019), p. 1.

[300] Mangal Hazra, Sabyasachi Pal, and Debasish Saha. "Fermi/LAT detection of enhanced gamma-ray activity from the blazars OP 313 and 4C +01.02". In: *The Astronomer's Telegram* 14404 (Feb. 2021), p. 1.

[301] Isabelle Pâris et al. "The Sloan Digital Sky Survey Quasar Catalog: Fourteenth data release". In: *Astronomy and Astrophysics* 613, A51 (May 2018), A51. DOI: 10.1051/0004-6361/201732445. arXiv: 1712.05029 [astro-ph.GA].

[302] S. Buson. "Fermi LAT detection of a GeV flare from the FSRQ TXS 0025+197". In: *The Astronomer's Telegram* 13032 (Aug. 2019), p. 1.

[303] Michael S. Shaw et al. "Spectroscopy of Broad-line Blazars from 1LAC". In: *The Astrophysical Journal* 748.1, 49 (Mar. 2012), p. 49. DOI: 10.1088/0004-637X/748/1/49. arXiv: 1201.0999 [astro-ph.HE].

[304] L. Carrasco et al. "NIR flaring of the FRSQSO B2 2234+28A". In: *The Astronomer's Telegram* 3056 (Nov. 2010), p. 1.

[305] L. Carrasco et al. "A NIR Flare of the QSO B2 2234+28A". In: *The Astronomer's Telegram* 8572 (Jan. 2016), p. 1.

[306] V. V. Vlasyuk et al. "SAO RAS Observations of current brightening of [HB89] 0234+285 blazar". In: *The Astronomer's Telegram* 12111 (Oct. 2018), p. 1.

[307] L. Carrasco et al. "A New Fast NIR Flare of the Blazar BZQJ0237+2848". In: *The Astronomer's Telegram* 12401 (Jan. 2019), p. 1.

[308] J. M. O'Meara et al. "The Second Data Release of the KODIAQ Survey". In: *The Astronomical Journal* 154.3, 114 (Sept. 2017), p. 114. DOI: 10.3847/1538-3881/aa82b8. arXiv: 1707.07905 [astro-ph.GA].

[309] H. Spinrad and H. E. Smith. "AO 0235+164 a red BL Lacertae object." In: *The Astrophysical Journal* 201 (Oct. 1975), pp. 275–276. DOI: 10.1086/153883.

[310] Ross D. Cohen et al. "The Nature of the BL Lacertae Object AO 0235+164". In: *The Astrophysical Journal* 318 (July 1987), p. 577. DOI: 10.1086/165393.

[311] K. Nilsson et al. "The complex environment of AO 0235+164." In: *Astronomy and Astrophysics* 314 (Oct. 1996), pp. 754–762.

[312] M. Ackermann et al. "Multi-wavelength Observations of Blazar AO 0235+164 in the 2008-2009 Flaring State". In: *The Astrophysical Journal* 751.2, 159 (June 2012), p. 159. DOI: 10.1088/0004-637X/751/2/159. arXiv: 1207.2932 [astro-ph.HE].

[313] V. V. Vlasyuk et al. "Blazar AO 0235+164 optical brightening". In: *The Astronomer's Telegram* 6970 (Jan. 2015), p. 1.

[314] O. I. Spiridonova et al. "Blazars AO 0235+164, [HB89] 0716+714 and [HB89] 1633+382 are still near the maxima of the long-term light curves". In: *The Astronomer's Telegram* 7004 (Jan. 2015), p. 1.

[315] J. Aleksić et al. "Search for very high energy gamma-rays from the z = 0.896 quasar 4C +55.17 with the MAGIC telescopes". In: *Monthly Notices of the Royal Astronomical Society* 440.1 (May 2014), pp. 530–535. DOI: 10.1093/mnras/stu227. arXiv: 1402.0291 [astro-ph.HE].

[316] Amy Furniss and William McConville. "VERITAS Results from Deep Exposure on the Distant FSRQ 4C +55.17". In: *arXiv e-prints*, arXiv:1303.1103 (Mar. 2013), arXiv:1303.1103. DOI: 10.48550/arXiv.1303.1103. arXiv: 1303.1103 [astro-ph.HE].

[317] Roopesh Ojha and Bryce Carpen. "Gamma-ray flares from the blazars TXS 2241+406, Ton 599, and 4C +01.02". In: *The Astronomer's Telegram* 8319 (Nov. 2015), p. 1.

[318] Wolfgang A. Rolke, Angel M. López, and Jan Conrad. "Limits and confidence intervals in the presence of nuisance parameters". In: *Nuclear Instruments and Methods in Physics Research A* 551.2-3 (Oct. 2005), pp. 493–503. DOI: 10.1016/j.nima.2005.05.068. arXiv: physics/0403059 [physics.data-an].

[319] A. C. Genz and A. A. Malik. "Remarks on algorithm 006: An adaptive algorithm for numerical integration over an N-dimensional rectangular region". English. In: *J. Comput. Appl. Math.* 6 (1980), pp. 295–302. ISSN: 0377-0427. DOI: 10.1016/0771-050X(80)90039-X.

[320] A. C. Genz and A. A. Malik. "An imbedded family of fully symmetric numerical integration rules". English. In: *SIAM J. Numer. Anal.* 20 (1983), pp. 580–588. ISSN: 0036-1429. DOI: 10.1137/0720038.

[321] S. Sobolev. "Theory of Cubature Formulas". In: Jan. 2006, pp. 491–511. ISBN: 978-0-387-34148-4. DOI: 10.1007/978-0-387-34149-1_26.

[322] Misty C. Bentz. "AGN Reverberation Mapping". In: *Astronomy at High Angular Resolution*. Ed. by Henri M. J. Boffin et al. Vol. 439. Astrophysics and Space Science Library. Jan. 2016, p. 249. DOI: 10.1007/978-3-319-39739-9_13. arXiv: 1505.04805 [astro-ph.GA].

[323] Misty C. Bentz et al. "The Low-luminosity End of the Radius-Luminosity Relationship for Active Galactic Nuclei". In: *The Astrophysical Journal* 767.2, 149 (Apr. 2013), p. 149. DOI: 10.1088/0004-637X/767/2/149. arXiv: 1303.1742 [astro-ph.CO].

[324] H. E. S. S. Collaboration et al. "Constraints on the emission region of <ASTROBJ>3C 279</ASTROBJ> during strong flares in 2014 and 2015 through VHE γ-ray observations with H.E.S.S." In: *Astronomy and Astrophysics* 627, A159 (July 2019), A159. DOI: 10.1051/0004-6361/201935704. arXiv: 1906.04996 [astro-ph.HE].

[325] Jenny E. Greene and Luis C. Ho. "Estimating Black Hole Masses in Active Galaxies Using the Hα Emission Line". In: *The Astrophysical Journal* 630.1 (Sept. 2005), pp. 122–129. DOI: 10.1086/431897. arXiv: astro-ph/0508335 [astro-ph].

[326] Carolina Casadio et al. "The magnetic field structure in CTA 102 from high-resolution mm-VLBI observations during the flaring state in 2016-2017". In: *Astronomy and Astrophysics* 622, A158 (Feb. 2019), A158. DOI: 10.1051/0004-6361/201834519. arXiv: 1812.02194 [astro-ph.HE].

[327] B. Gendre and P. Giommi. "The ASI Science Data Center". In: *SF2A-2010: Proceedings of the Annual meeting of the French Society of Astronomy and Astrophysics*. Ed. by S. Boissier et al. Dec. 2010, p. 171.

[328] Christoph Wendel, Amit Shukla, and Karl Mannheim. "Pair Cascades at the Edge of the Broad-line Region Shaping the Gamma-Ray Spectrum of 3C 279". In: *The Astrophysical Journal* 917.1, 32 (Aug. 2021), p. 32. DOI: 10.3847/1538-4357/ac0a6e. arXiv: 2108.01028 [astro-ph.HE].

[329] H. Sol et al. "Active Galactic Nuclei under the scrutiny of CTA". In: *Astroparticle Physics* 43 (Mar. 2013), pp. 215–240. DOI: 10.1016/j.astropartphys.2012.12.005. arXiv: 1304.3024 [astro-ph.HE].

[330] T. Hassan et al. "Monte Carlo performance studies for the site selection of the Cherenkov Telescope Array". In: *Astroparticle Physics* 93 (July 2017), pp. 76–85. DOI: 10.1016/j.astropartphys.2017.05.001. arXiv: 1705.01790 [astro-ph.IM].

[331] Donald P. Schneider et al. "The Sloan Digital Sky Survey Quasar Catalog. V. Seventh Data Release". In: *The Astronomical Journal* 139.6, 2360 (June 2010), p. 2360. DOI: 10.1088/0004-6256/139/6/2360. arXiv: 1004.1167 [astro-ph.CO].